Lead-Free Piezoceramic Materials for SONAR Transducer Applications

William Gottfried Walter Schulz

Submitted in accordance with the requirements for the degree of Doctor of Philosophy

The University of Leeds

Functional Materials

School of Chemical and Process Engineering

September 2024

I confirm that the work submitted is my own and that appropriate credit has been given where reference has been made to the work of others.

Acknowledgements

I would first and foremost like to thank my supervisor Professor Andrew Bell for his valuable guidance, inspiration, and assistance throughout my PhD. His insight, knowledge, and encouragement has allowed me to grow and thrive as a researcher and person, and I am forever grateful for the opportunity he has provided me with. Additional thanks to my secondary supervisor Professor Andrew Brown for his additional support and advice in managing my PhD experience.

I would like to acknowledge EPSRC and Thales for providing the funding for the research. I would also like to give my big thanks to my industrial supervisor Dr. Laura Stoica from Thales for her assistance and support throughout my PhD and my placement at Thales, and for proofreading my thesis. Her guidance and feedback have been exceptionally valuable, and I am forever appreciative for her help.

I am eternally indebted to the help and support of Rob Simpson, whose technical knowledge and assistance have been a key factor in making my PhD run like clockwork, and whose advice have helped me develop as a scientist and as a person.

I also acknowledge the help of Dr. Faye Esat and Mo Javed for their help with the X-ray diffraction and Stuart Micklethwaite with scanning electron microscopy. I would also like to thank the rest of the electroceramics group at Leeds past and present: including but not limited to Anton, Tom H., Tom B., Chloe, Danielle, Di, Yang, Ashleigh, Harry, Teresa, and everyone else. It has been a great pleasure working with you and thank you for providing a great atmosphere in the lab and the office.

I would also like to thank the Acoustics team at Thales Templecombe, including but not limited to Dr. Phil O'Gara, Bo Tyson, Dr. Hannah Rose and of course Laura. Thank you very much for your guidance and support, and for making me feel as part of the team at Thales. Additional thanks to Dr. James Roscow of the University of Bath for his assistance with using the corona poling rig.

Thank you also to my friends in Leeds, Cambridge and across the globe, for being there for me and for keeping me entertained and my head above water this whole time. Finally, a big thanks to my parents and extended family across the globe for all the help and support they have provided me with.

Abstract

For this project, bismuth ferrite-barium titanate (BF-BT) compounds are doped with Mn and Sm and are prepared and investigated for their piezoelectric properties. A variety of processing variables are used to investigate their effect on the piezoelectricity and structure of the different compositions, which will help optimize the materials' piezoelectricity. The dielectric and piezoelectric properties of the materials are measured using piezoelectric resonance methods such as Berlincourt measurements, ferroelectric hysteresis and PRAP. A series of impedance measurements are also done to compare the conductivity between different compositions.

For Sm-doped BF-BT, the formula used was $0.67Bi_{1.03}FeO_3$-$0.33[Ba_{1-x}Sm_xTiO_3]$, where x=0.00-0.03. The best results achieved were a d_{33} of 85 pC/N and T_c of 433^{o}C, at x = 0.01.

For Mn-doping, the formula used was $0.67(Bi_{1-x}Mn_x)FeO_3$-$0.33BaTiO_3$, where x=0.01-0.02. The process of air-quenching (fast cooling from 1000^{o}C to room temperature) has reduced defects in its crystal structure and has improved its piezoelectric performance in comparison to slow-cooling. The best results achieved were for air-quenched Mn-doped BF-BT with a d_{33} of 176 pC/N and T_c of 450^{o}C, also at x=0.01. This is an improvement over slow-cooled BF-BT-Mn which recorded a d_{33} of 91pC/N with the same variables.

Co-doping BF-BT with both Mn and Sm achieved a maximum d_{33} of 161 pC/N and a T_c of 495^{o}C after air-quenching.

Impedance measurements have shown that the activation energy E_a decreases with air and water-quenched samples, and that higher conductivities correlate with lower d_{33} values, indicating electron conductivity to the limiting factor to the d_{33}.

Contents

List of Figures

List of Tables

List of Abbreviations

AC: Alternating Current

BCZT: Barium Calcium Zirconate Titanate

BF-BT/BFO-BTO: Bismuth Ferrite-Barium Titanate

CPE: Constant Phase Element

DC: Direct Current

EU: European Union

IEEE: Institute of Electrical and Electronics Engineers

IPA: 2-Isopropanol

KNN: Potassium Sodium Niobate

MPB: Morphotropic Phase Boundary

NBT: Sodium Bismuth Titanate

P-E: Polarisation-Electric Field

PPT: Polymorphic Phase Transition

PRAP: Piezoelectric Resonance Analysis Program

PZT: Lead Zirconate Titanate

SEM: Scanning Electron Microscopy

SONAR: Sound Navigation and Ranging

XRD: X-ray Diffraction

1. Introduction

1.1 Background and Motivation

Piezoelectric materials have unique structures and properties that allow them to convert mechanical energy into electrical energy, and vice versa. This makes them useful in certain applications such as sensors, actuators, and transducers, which involve this type of electromechanical energy conversion.

The most popular piezoelectric material is lead zirconate titanate, also known as PZT, as it is cheap to produce and has piezoelectric properties which exceed other materials in its class, thanks to the presence of a Morphotropic Phase Boundary (MPB) which allows it to change phases [1]. However, the introduction of EU legislation which will limit the use of lead in electronics will likely make PZT (approx. 50% lead content) [2] obsolete in the future. As a result, there has been a substantial increase in research into lead-free piezoelectric materials.

So far, efforts to find a lead-free alternative has produced several potential candidates to replace PZT. Materials such as potassium sodium niobate (KNN), sodium bismuth titanate (NBT), and bismuth ferrite-barium titanate (BFO-BTO) have formed the basis for several compounds that have produced interesting results [3] [4]. In many cases, their piezoelectric coefficients (d_{33} in particular) have been increased through doping such that the values are comparable to those produced by most PZT compounds. However, none have yet been able to make it into industry or have even been properly tested in devices and applications which utilise the piezoelectric properties of PZT.

1.2 Aims and Objectives

The main aim of this project is to investigate lead-free piezoceramic candidates that could replace PZT. After a thorough literature search, BFO-BTO has been selected as the base material for further investigation. The main objectives of this project are therefore as follows:

- Prepare and test BFO-BTO samples for their structural and electrical characteristics.

- Continually optimise the piezoelectric properties (namely the d_{33}) of BFO-BTO through Sm and Mn doping and variation in processing methods such as altering the sintering temperatures and testing different quenching methods.
- Understand the defect chemistry of the doped samples through impedance spectroscopy.
- Perform a full-matrix characterisation of the different BFO-BTO compositions.

1.3 Thesis Structure

The thesis is split into 6 chapters:

- Chapter 1 introduces the aims and objectives of the project.
- Chapter 2 provides the background science of piezoelectric perovskites and the concept of ferroelectricity.
- Chapter 3 provides a history of piezoelectric and ferroelectric materials, including the characteristics and development of PZT, and provides a literature review and trade-off summary of the main lead-free candidate materials.
- Chapter 4 summarises the experimental methodology used for the project.
- Chapter 5 discusses the results obtained from the different BFO-BTO compounds prepared for the project, including the X-ray diffraction, Berlincourt measurements, impedance spectroscopy, and the full-matrix characterisation.
- Finally, chapter 6 summarises the main conclusions of this work and discusses the future work that is suggested for this topic.

2. Structural and Electrical Properties of Ceramics

2.1 Crystal Structures

Crystal structures are arranged in a lattice, where the atoms form arrays of regular ordered patterns. The simplest way to describe lattice structures is in the form of unit cells. Unit cells consist of lengths a, b, and c, and angles α, β, and γ as shown in Figure 2.1:

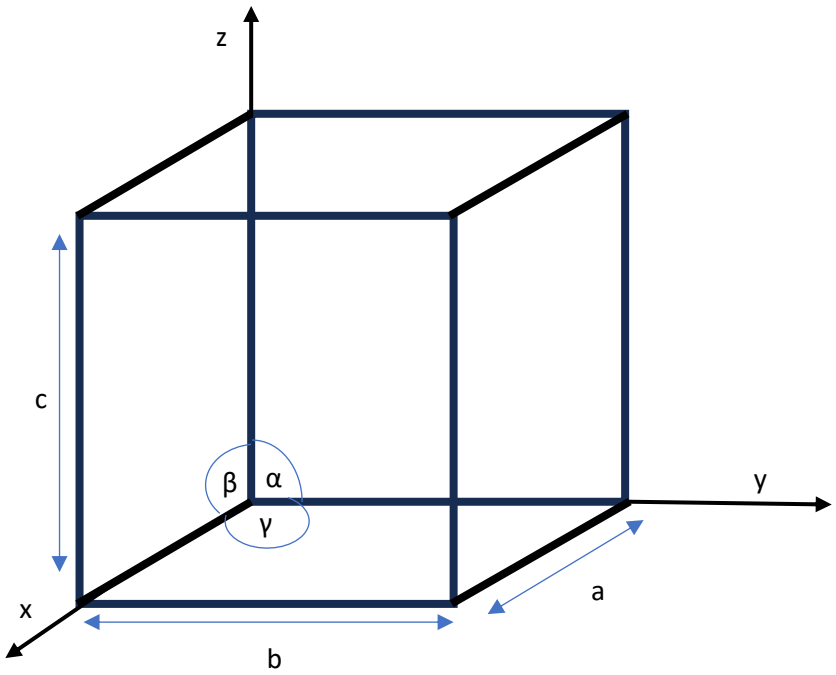

Figure 2.1: Unit cell with lengths a, b, and c, and angles α, β, and γ.

2.1.1 Bravais Lattice

The unit cell can be classified into 7 different crystal variations: cubic, tetragonal, orthorhombic, rhombohedral, hexagonal, monoclinic and triclinic. These crystal forms can be further split into 14 different classifications with body, face, and base-centred cubic forms. These are known as Bravais lattices, which were devised by French physicist Auguste Bravais in 1850. Table 2.1 highlights the parameters of the 7 crystal variations of the unit cell, and Figure 2.2 depicts the 14 Bravais lattices [6] [7]:

Table 2.1: The 7 unit cell systems and their parameters

System	Lattice Parameters
Cubic	$a = b = c$ $\alpha = \beta = \gamma = 90^o$
Tetragonal	$a = b \neq c$ $\alpha = \beta = \gamma = 90^o$
Orthorhombic	$a \neq b \neq c$ $\alpha = \beta = \gamma = 90^o$
Rhombohedral	$a = b = c$ $\alpha = \beta = \gamma \neq 90^o$
Hexagonal	$a = b \neq c$ $\alpha = \beta = 90^o; \gamma = 120^o$
Monoclinic	$a \neq b \neq c$ $\alpha = \gamma = 90^o; \beta \neq 90^o$
Triclinic	$a \neq b \neq c$ $\alpha \neq \beta \neq \gamma \neq 90^o$

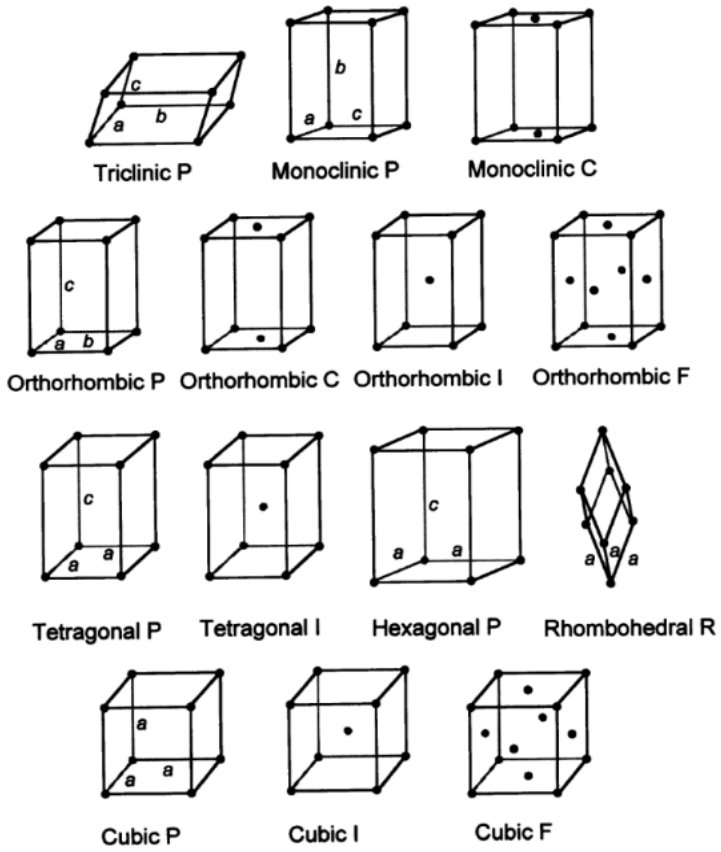

Figure 2.2: The 14 Bravais Lattice systems [6]

2.1.2 Lattice Points, Planes and Vectors

Lattice points can be located using Cartesian coordinates, and are represented as integers known as Miller indices, which are numbered relative to the origin. Figure 2.3 represents an example of how points, vectors, and planes are represented in a unit cell. Assuming the unit cell has edges of length 1, the coordinates of the origin ***O*** and point ***P*** are 000 and 011 respectively, vector ***OR*** is [111] and plane ***Q*** (pictured in amber on figure 2.3) is (100).

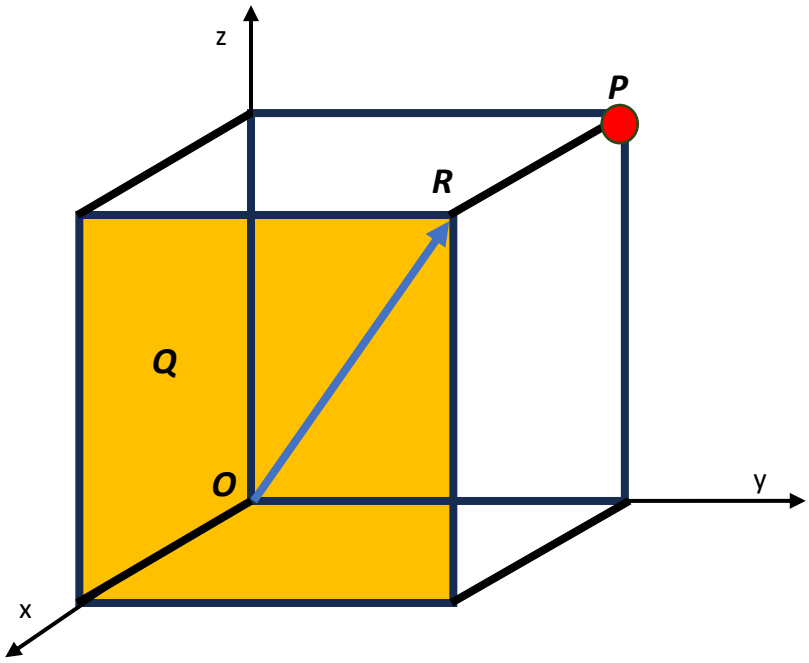

Figure 2.3: Unit cell with origin O, point P, vector OR, and plane Q.

Planes use round brackets (hkl), and vectors use square brackets [hkl]. Alternative notation includes {hkl} which represents a family of planes, and <hkl> represents a family of vectors [8]. For example:

$$\{001\} = (001), (010), (100)$$

$$< 001 > = [001], [010], [100]$$

2.1.3 Perovskite Structure

The Perovskite structure forms the basis of most piezoelectric materials. Named after Russian mineralogist Lev Perovski and first discovered in 1839 by Gustav Rose, is derived from the lattice structure of a mineral of the same name which consists of calcium titanium oxide ($CaTiO_3$). The cubic structure has ions at the vertices, in the centre of the cube, and at the centres of the planes. The general formula for a perovskite is ABO_3, where 'A' and 'B' are cations and 'O' is an anion

(typically oxygen) which forms a bond with the 2 cations. Figure 2.4 shows a diagram of the structure:

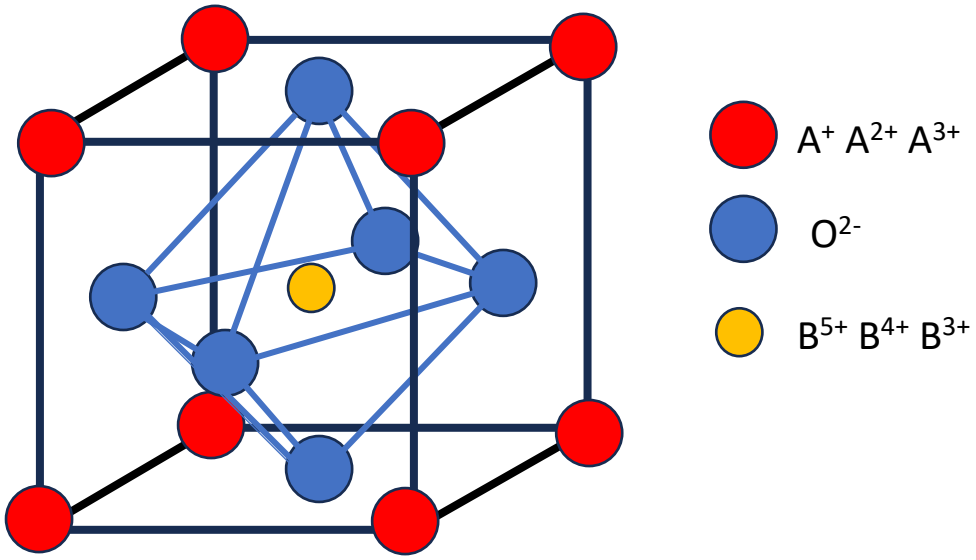

Figure 2.4: Perovskite structure. The A-site cation occupies the site at the vertices of the unit cell, the smaller B-site cation at the centre, and the O-site anion (typically oxygen) at the face centres.

As seen in figure 2.4, the smaller 'B' cation is located at the centre of the unit cell. When the material is compressed or distorted, the B-cation shifts even closer to the anion, and the opposing charges produce an electric current. For the converse piezoelectric effect, an applied electric field causes the structure to strain due to the reversing of the polarization direction [9].

2.1.4 Goldschmidt Tolerance Factor

In 1926, Norwegian mineralogist Victor Moritz Goldschmidt came up with a relationship between the radii of the ions. The derivation of the Goldschmidt equation is as follows: assuming a unit cell length a, expressing this in terms of the radii of the B-site and oxygen atom results in:

$$a = 2(r_B + r_O) \tag{1}$$

as the unit cell length crosses the full diameter of the B-site atom, and the radii of two oxygen atoms. The length of the hypotenuse of the plane which stretches between the two opposite A-site atoms is as follows:

$$\sqrt{2}a = 2(r_A + r_O) \quad (2)$$

Combining the two expressions gives:

$$\sqrt{2}(r_B + r_O) = r_A + r_O \quad (3)$$

This therefore leads to the Goldschmidt tolerance factor *t*, which is the equation below [10]:

$$t = \frac{r_A + r_O}{\sqrt{2}(r_B + r_O)} \quad (4)$$

The tolerance factor can be used to describe how well the ions pair up with each other, as the radii of the different ions could distort the lattice structure and affect the dielectric properties of the material. The ideal range of the value of t lies between 0.95-1.06, as that indicates that the cations A and B are of an ideal size [9]. An example of a material with this value is strontium titanate ($SrTiO_3$), where $t = 1$ [11].

2.1.5 Electrostriction

Displacement of the B-ion leads to phase transitions, as electrostriction causes the whole perovskite structure to change. Electrostriction is a fundamental form of electromechanical coupling where the displacement of an atom is directly proportional to the square of the electric polarization field. If we assume x to be the strain, P to be the polarization field, and Q to be the electrostriction coefficient, the phenomenon of electrostriction can be summarized in the formula below [9]:

$$x = QP^2 \quad (5)$$

2.1.6 Phase Transitions

Phase transitions are an important aspect as the rearrangement of the structure changes the properties of the material. Piezoelectric materials undergo phase transition through temperature changes. Figure 2.5 shows the phase transitions that $BaTiO_3$ goes through. The phase transitions displace the central cation, and the polarization direction can shift depending on the displacement of the central cation. Phase transitions which occur due to temperature are known as polymorphic phase transitions (PPT). For instance, in the case of $BaTiO_3$ it starts as

a non-polar simple cubic structure at temperatures above 130°C, cooling below that temperature brings it to a polarized tetragonal, polarized orthorhombic below 0°C, and polarized rhombohedral below -90°C.

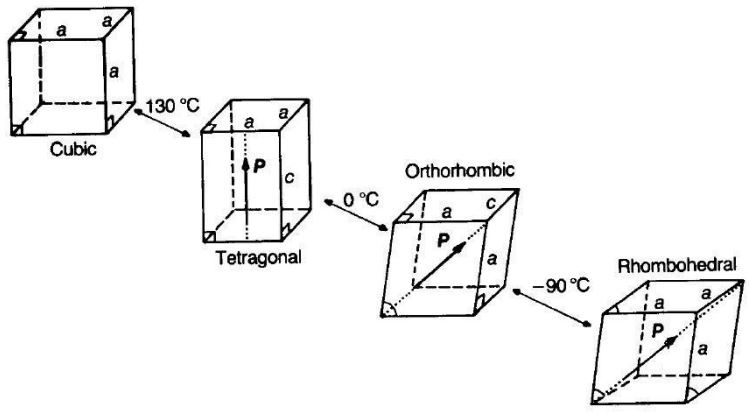

Figure 2.5: Phase transitions of $BaTiO_3$ [9]

2.1.7 Morphotropic Phase Boundary

Phase transitions can also occur due to a compositional change in the material, when either one of the A or B-site atoms are substituted for the original to induce a phase change. The transitional boundary when a new donor element is substituted for an A/B-site atom is known as a Morphotropic Phase Boundary (MPB), and it is an important aspect of research in the electroceramics field. The superior piezoelectric properties of PZT are often attributed to the presence of a MPB [12], as the compositional changes give the B-site atom more polarization directions to occupy. As a result, the vast majority of the most promising lead-free piezoelectric candidates (which will be covered later on) are materials which undergo a compositional phase transition at the MPB, examples being KNN and NBT [1].

2.1.8 Defects

An important aspect to consider regarding crystal structures is defects. Defects in crystals are divided into 2 categories: 'point' and 'line' defects. Point defects occur due to missing atoms, producing vacancies (vacancy defects), the presence of foreign atoms which have substituted normal atoms in the structure (substitutional defects), or when atoms occupy sites in a crystal structure that are normally unoccupied (interstitial defects). Line defects occur on a larger scale and

affect the periodicity of a crystal lattice structure. For this thesis, the focus will largely be concentrated on point defects. Defects in general have a significant influence on the electrical and structural properties of crystals [9].

To understand how defects in crystals occur, energy band theory needs to be considered. Band gaps are unoccupied energy states which are produced due to the fact that neighbouring electrons in atomic bonds cannot occupy the same energy levels (Pauli exclusion principle). This causes electrons to occupy different energy levels or 'bands'. There are 2 energy bands that need to be considered for the theory of conduction:

- **Valence band** – this is related to the valence shell of an atom. Typically the highest filled or partially filled band of an atom.
- **Conduction band** – this is the next highest energy band in which excited electrons can fill from the valence band.

Perovskite oxides are classed as wide band gap semiconductors, which means they have aliovalent (different valencies) impurity atoms in their structure. This allows them to add extra electrons in the conduction band (known as donors/n-type semiconductors) or trap electrons from the valence band (known as acceptors/p-type semiconductors). This improves conductivity of the perovskite and is also why doping is typically done to improve the electrical properties of materials. Figure 2.6 shows a diagram depicting the conduction of n-type and p-type semiconductors:

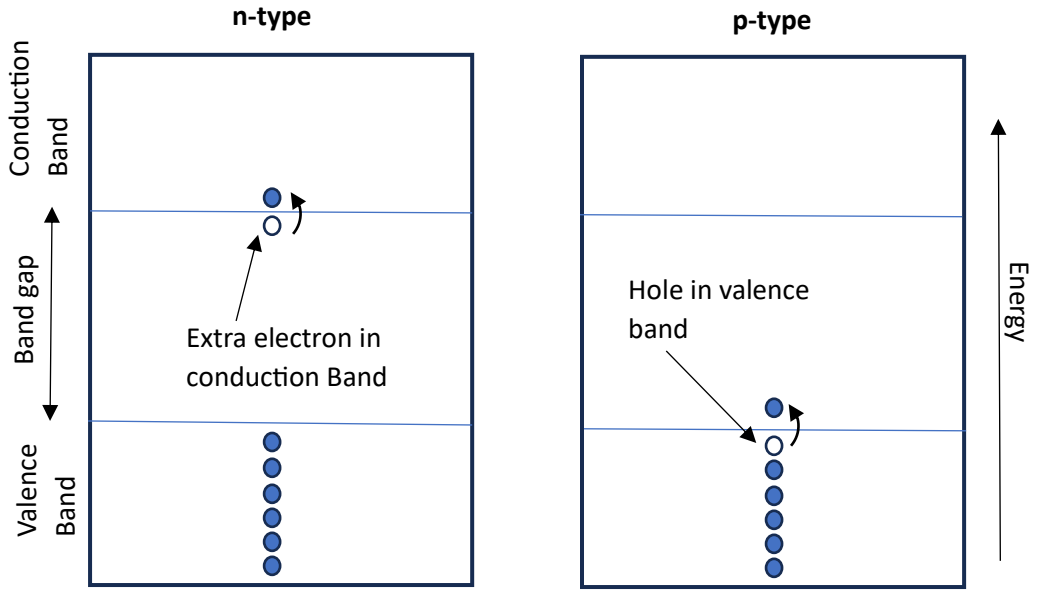

Figure 2.6: n-type (donor) semiconductors, and p-type (acceptor) semiconductors

These are examples of substitution defects, where impurity atoms occupy sites that are normally occupied by an atom of the host element in a pure, defect free crystal. Defect chemistry in this context is useful to describe the properties and characteristics of piezoelectric ceramics, which will be relevant to the topic of this thesis.

2.1.9 Kroger-Vink Notation

Kroger-Vink notation is used in defect chemistry reactions. It takes the form of $\mathrm{V_B^A}$ where V is the lattice vacancy or ion, B is the site location and A is the relative charge. For example, in the case of $\mathrm{Mn'_{Fe}}$, a manganese ion occupies an iron site with a relative negative charge represented by ' as manganese (+2) has a relative negative charge to iron (+3). In contrast, $\mathrm{Sm^{\bullet}_{Ba}}$ represents a samarium ion (+3) on a barium (+2) site with a relative positive charge (represented by •) to the host ion. Finally, $\mathrm{O_O^{\times}}$ represents an oxygen ion on its usual site, where × represents a neutral charge. The defect chemistry equations for both cases are represented below:

$$Bi_2O_3 + 2MnO \xrightarrow{2BiFeO_3} 2Bi_{Bi}^{x} + 2Mn'_{Fe} + 5O_O^x + V_O^{\bullet\bullet} \quad (6)$$

$$Sm_2O_3 + 3TiO_2 \xrightarrow{3BaTiO_3} 2Sm^{\bullet}_{Ba} + V''_{Ba} + 3Ti^x_{Ti} + 9O^x_O \quad (7)$$

2.2 Properties of Piezoelectric Materials

2.2.1 Piezoelectricity

Piezoelectric materials convert mechanical energy into electrical energy, and vice versa. As a result, the piezoelectric effect comes in 2 different forms: the direct effect occurs when a mechanical stress X_{jk} is applied to a piezoelectric material, producing a polarization P_i. The direct effect is represented by the equation below [13]:

$$P_i = d_{ijk} X_{jk} \tag{8}$$

where d_{ijk} is the piezoelectric charge coefficient.

The converse effect occurs when an electrical field E_k is applied to the material and it ends up expanding, also known as straining. The equation for this effect is represented below:

$$x_{ij} = d_{ijk} E_k \tag{9}$$

where x_{ij} is the strain.

2.2.2 Piezoelectric Coefficients and Modes

When it comes to examining the quality of piezoelectric materials, a series of coefficients, unique to every material, are used to determine the suitability of a material for a specific application. The d-coefficient, stylized as d_{ij}, is the piezoelectric charge coefficient. The units for this coefficient are pC/N, and it is used to relate the polarization P_i produced from mechanical stress X_{jk} in the direct effect, and the strain x_i produced from an applied electric field E_{jk} in the converse effect.

Another coefficient is the piezoelectric voltage coefficient, also known as the g-coefficient (g_{ij}). This is related to the d-coefficient via the following equation [9] [13]:

$$g_{ij} = \frac{d_{ij}}{\varepsilon_{ij}} \tag{10}$$

with ε_{ij} being the permittivity under constant stress. The units for the g-coefficient are Vm/N, which defines it as the ratio between the field produced and stress it experiences. This makes the g-coefficient crucial in determining the quality of a piezoelectric material for sensor applications.

Crystals are anisotropic, which means that the dipoles formed during polarization are not parallel with the electric field [14]. This leads to different properties being exhibited when measured along axes in different directions. As a result, piezoelectric coefficients need to be expressed as tensors to account for this. The ij subscripts of the coefficients represent the modes of the material. The modes are the direction of the stresses/strain experienced by the material. In a simple 3-dimensional set of axes, the x, y and z directions are represented by the numbers 1, 2 and 3 respectively, and the shears on each of those axes are represented by the numbers 4, 5 and 6 respectively. Figure 2.7 shows the graphical form of this:

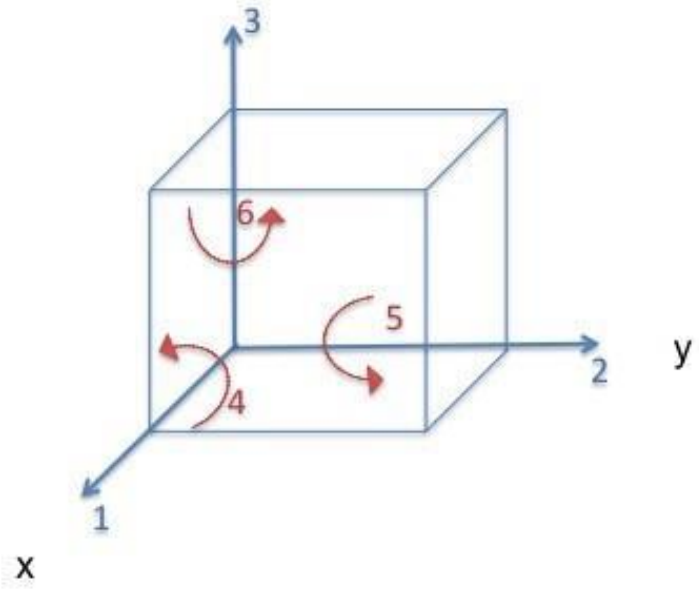

Figure 2.7: Graphical representation of directions of piezoelectric modes, axes from 1-3, and planes from 4-6. [15]

There are 3 common piezoelectric modes of operation that a material can undergo: transverse effect (d_{31}), the longitudinal effect (d_{33}), and the shear effect (d_{15}). The "i" subscript represents the direction of the electric field or dielectric displacement, and "j" is the direction of mechanical stress or strain. Therefore, the piezoelectric coefficients for the longitudinal mode are d_{33} and g_{33}, as they are defined as the coefficients for when the strain is parallel to the polarization direction. This would also make d_{31} and g_{31} the coefficients for the transverse mode (as the strain is perpendicular to the polarization). For the shear mode, the coefficients are d_{15} and g_{15} because the strain is measured along a plane rather than an axis.

Figure 2.8 shows the modes and their polarization orientation:

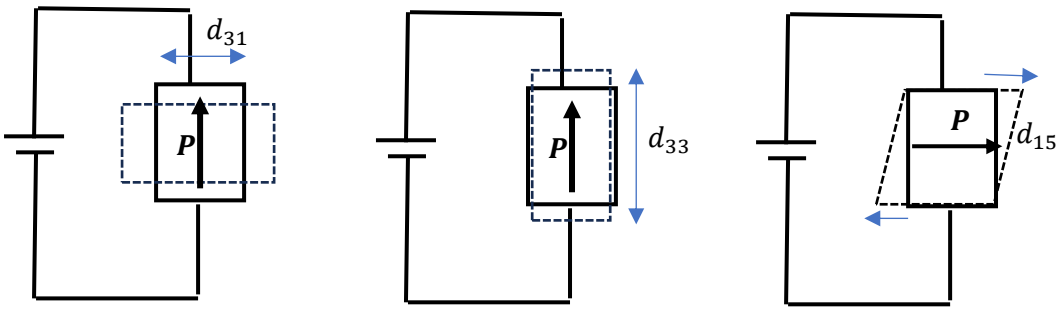

a) b) c)

Figure 2.8: 3 common piezoelectric modes. a) is transverse (d_{31}), b) is longitudinal (d_{33}), and c) is shear mode (d_{15}).

2.2.3 Electromechanical Coupling Factor

The quality of piezoelectricity from a material is determined by the electromechanical coupling coefficient, also known as k. The formulae for this coefficient are shown below [9] [13]:

$$k^2 = \frac{input\ electrical\ energy\ converted\ into\ mechanical\ energy}{input\ electrical\ energy} \quad (11)$$

$$k^2 = \frac{input\ mechanical\ energy\ converted\ into\ electrical\ energy}{input\ mechanical\ energy} \quad (12)$$

2.3 Dielectrics

Dielectrics are insulators used to create a dielectric polarization which occurs when they are placed in an electric field which rearranges electric charges slightly offset from their equilibrium position. Their main application is in capacitors as the dielectric polarization helps to store charge.

2.3.1 Dielectric Properties

The parallel plate capacitor is a common example of the functionality of dielectrics. In this capacitor a voltage, V, is applied across 2 parallel plates and a charge, q, develops over the vacuum separating the 2 plates of a distance, d. The surface area of the plates is A. As it is found that q is proportional to VA/d, the proportionality constant is known as the permittivity of free space, ε_0, whose value is 8.85×10^{-12} F m^{-1} [9]:

$$q = \varepsilon_0 \frac{VA}{d} \tag{13}$$

The capacitance, C, is the charge to voltage ratio. Therefore:

$$C = \frac{q}{V} = \varepsilon_0 \frac{A}{d} \tag{14}$$

The surface charge density, σ, is given by:

$$\sigma = \frac{q}{A} = \varepsilon_0 E \tag{15}$$

where E is the electric field. When the vacuum space is replaced with a dielectric material, the relative permittivity (ε_r), also known as the dielectric constant, increases the surface charge density and capacitance by ε_r. Therefore:

$$C = \varepsilon_0 \varepsilon_r \frac{A}{d} \tag{16}$$

$$\sigma = \varepsilon_0 \varepsilon_r E \tag{17}$$

The permittivity, ε, is the product of ε_0 and ε_r:

$$\varepsilon = \varepsilon_0 \varepsilon_r \tag{18}$$

The polarization, P, is the amount of charge distribution that is distorted by the electrical field, E:

$$P = \varepsilon_0 \chi E \tag{19}$$

where χ is defined as the magnetic susceptibility, whose relationship with ε_r is:

$$\varepsilon_r = \chi + 1 \tag{20}$$

Polarisation comes in four main mechanisms: atomic, ionic, dipolar, and diffusional as seen in figure 2.9. Atomic polarisation occurs in all materials under an applied electric field: a dipole moment is created after the displacement of an electron cloud within an atom shifts the electrons from the nucleus. Ionic polarisation occurs in ionic materials where the cations and anions are displaced relative to one another. Dipolar polarisation occurs in materials, such as water, that already have permanent dipoles which become uniformly oriented under an applied electric field. Finally, space charge or diffusional polarisation involves a dipole moment being created at a barrier, such as a defect site or a grain boundary.

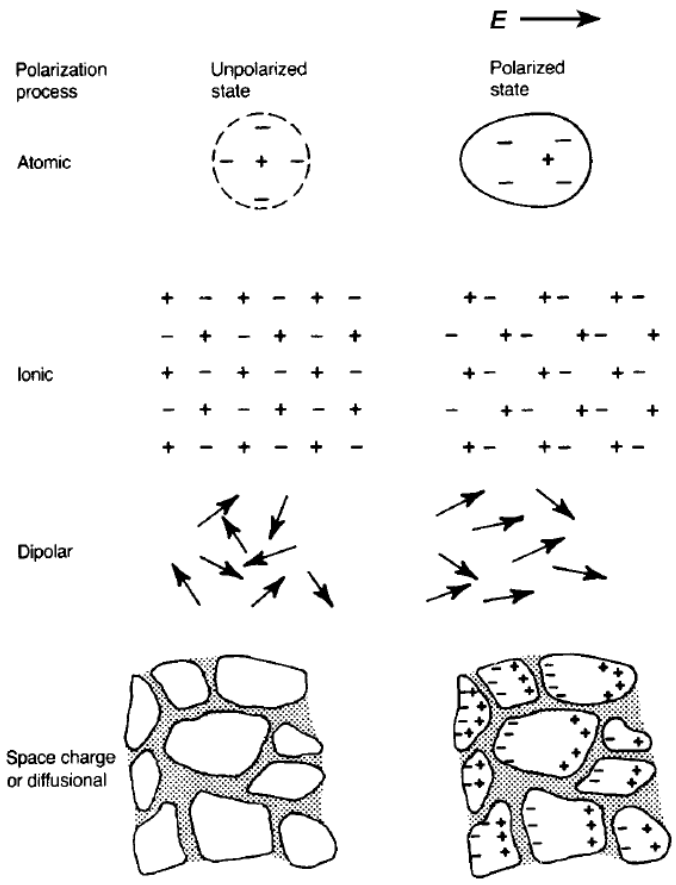

Figure 2.9: The four main polarisation mechanisms [9].

2.3.2 Dielectric Loss

Dielectrics are not perfect insulators and allow the transport of some charge to flow through. This is known as dielectric loss, and it occurs when a dielectric is exposed to a varying electric field, for example during poling.

When the dipoles in a ferroelectric ceramic start from a spontaneous polarization orientation, the application of a strong, external electric field forces the domains to arrange themselves in a uniform orientation. This process results in a dissipation of thermal energy in the form of dielectric loss.

Dielectric loss is represented as a complex formula where the permittivity is split into real and imaginary (lossy) components:

$$\varepsilon^* = \varepsilon' - j\varepsilon'' \tag{21}$$

where $j = \sqrt{-1}$, ε^*, ε', and ε'' are the complex, real, and imaginary permittivity respectively. In an ideal capacitor, the phase difference between the current and voltage is 90°, or $\pi/2$ radians. However, in practice the phase difference will be less than 90°, so an angle δ is used to determine the dissipation factor $tan(\delta)$. From the phasor diagram in Figure 2.10, it can be deduced:

$$I_c = Isin(90 - \delta) = Icos(\delta) = \varepsilon'' \tag{22}$$

$$I_R = I\cos(90 - \delta) = I\sin(\delta) = \varepsilon' \tag{23}$$

The dielectric loss or dissipation factor is determined by the ratio between the imaginary and real components of the dielectric permittivity:

$$\tan(\delta) = \frac{\varepsilon''}{\varepsilon'} \tag{24}$$

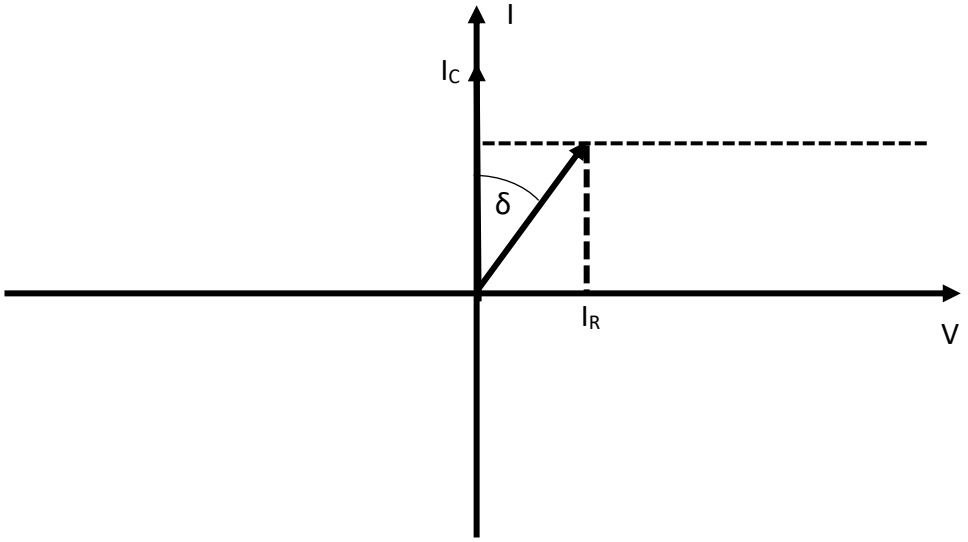

Figure 2.10: Phase diagram depicting dielectric loss. I_C is the current of an ideal capacitor and the phase difference is 90° (π/2 rads) between I_C and the voltage V. I_R is the real current produced by a lossy capacitor, which differs by an angle δ.

2.3.3 Dielectric Relaxation

After an applied alternating electric field is applied, the space charge or diffusional polarisation of a material can take time to return to an equilibrium state, or "relax". This differs from ionic or atomic polarisation which are typically instantaneous. The relaxation response of a dielectric can be expressed in terms of permittivity as a function of frequency, and the real and imaginary components of the permittivity ε are both described by the Debye equations:

$$\varepsilon' = \varepsilon'_\infty + \frac{\varepsilon'_s - \varepsilon'_\infty}{1 + \omega^2\tau^2} \tag{25}$$

$$\varepsilon'' = (\varepsilon'_s - \varepsilon'_\infty)\frac{\omega\tau}{1 + \omega^2\tau^2} \tag{26}$$

where ω is the frequency and τ is the relaxation time. The relaxation frequency, ω_r, is defined as $1/\tau$. This is also expressed as a graph in figure 2.11:

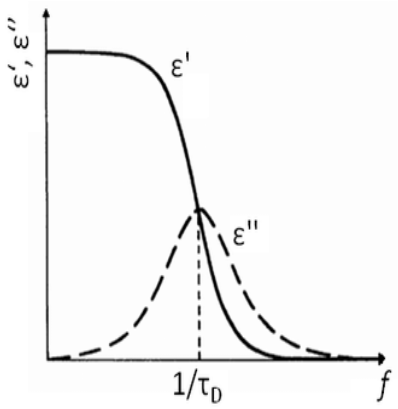

Figure 2.11: Complex permittivity expressed as a function of frequency (f) representing a dielectric exhibiting Debye relaxation [9].

Space charge and dipolar polarisation mechanisms are temperature dependent, which means that the relaxation time τ varies with temperature T:

$$\tau = \tau_0 \exp\left(-\frac{E_a}{kT}\right) \tag{27}$$

where E_a is the activation energy, k is the Boltzmann constant, and τ_0 is the relaxation constant of the material. Figure 2.12 shows how the permittivity varies with frequency based on different polarisation mechanisms:

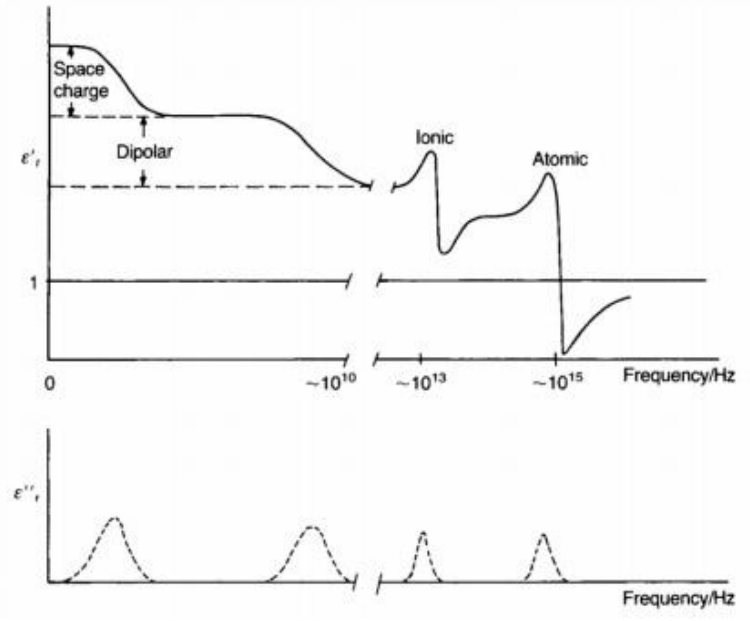

Figure 2.12: Different polarisation mechanisms undergoing Debye relaxation [9].

2.4 Ferroelectricity

Ferroelectricity is a property of materials which possess a spontaneous polarization, where the presence of a large, applied electric field is able to switch the direction of spontaneous polarization. Ferroelectricity occurs in piezoelectric and pyroelectric materials (materials which change their polarization orientation when heated or cooled).

2.4.1 Curie-Weiss Law

Ferroelectric materials display their characteristic behaviour under a certain temperature, known as the Curie point (T_c). Above this temperature, ferroelectrics revert to paraelectricity. Paraelectric materials, like ferroelectrics, also exhibit polarization under an applied electric field, except the polarization becomes zero when the field is removed. As a result, a ferroelectric material with a high T_c is desirable for commercial applications, as per the goals of this project. The relative permittivity of a material when temperature $T > T_c$ is found via the Curie-Weiss law, which is displayed in the following equation [13]:

$$\varepsilon_r = \frac{C}{T - T_0} \tag{28}$$

where ε_r is the relative permittivity, C is the Curie constant, and T_0 is the Curie-Weiss temperature. T_0 must not be confused with T_c, as $T_0 \approx T_c$, if, and only if, the phase transitions are continuous (2nd-order).

2.4.2 Hysteresis Loops

At weaker fields, the induced polarization of a material is almost exactly proportional to the applied external field (i.e. $P \approx E$) which then saturates as the field strength increases (P_{SAT}), also known as the Saturation Point. However, ferroelectric materials demonstrate a non-zero spontaneous polarization even when the electric field is 0. As ferroelectrics reverse their spontaneous polarization (P_S) in the opposite direction under an applied field, this produces a hysteresis loop, as shown in figure 2.13. When the electric field increases, the domains are oriented to align with the polarization field, at P_{SAT}. When the applied field reduces to zero, a coercive electric field, E_C, is applied to counteract the resultant remnant polarization, P_R. This allows the domains to orient themselves to align with the polarization, this time in the opposite direction. The

reversal of the field is repeated until a full hysteresis loop is complete, as figure 2.13 demonstrates.

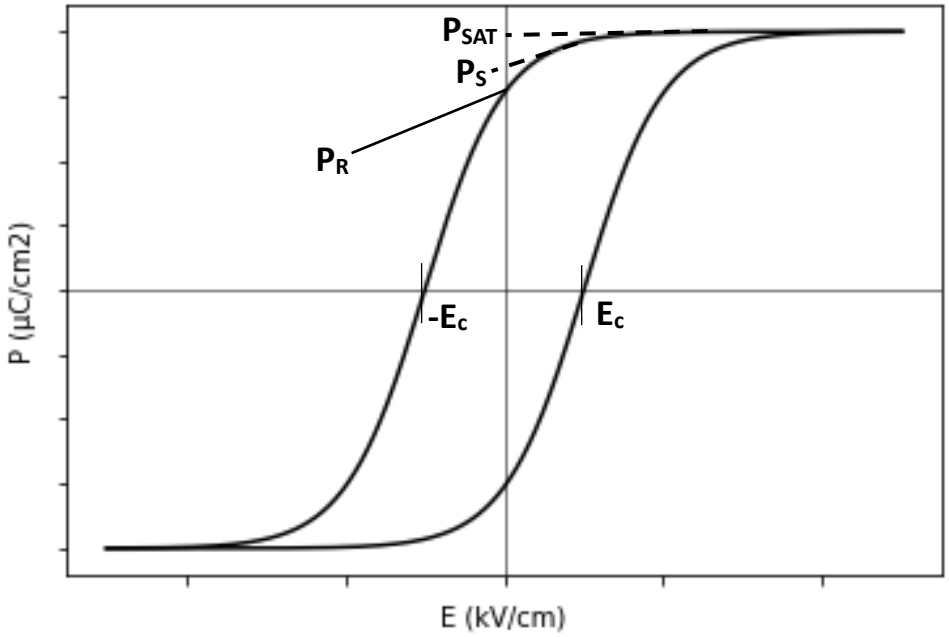

Figure 2.13: Hysteresis Loop, which is formed as the electric field is measured as a function of polarization.

2.4.3 Ferroelectric Domains

The mechanism of ferroelectric hysteresis is through domains. Domains are areas of uniform polarization direction in ferroelectric materials, and they are represented as arrows as seen on the diagram in figure 2.14. Spontaneous polarization in a material gives rise to surface charge density and a depolarizing field. Domains are there to reduce the depolarizing field by arranging themselves 180^{o} to one another, as that produces sets of opposite charges on the surface of the material, as figure 2.14 shows below:

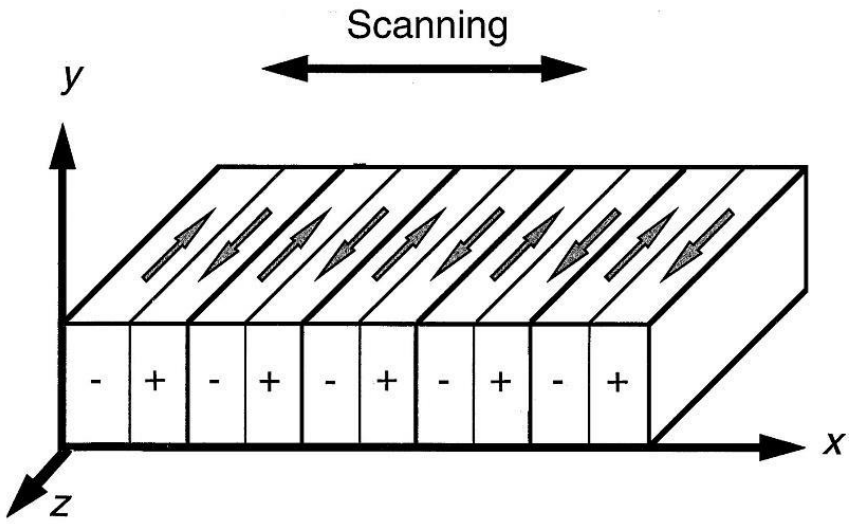

Figure 2.14: 180° domains which reduce electrostatic energy. [16]

When a ferroelectric material undergoes mechanical stresses, the domains rearrange 90° to one another to minimize the strain. This is what happens when the material (especially in the case of $BaTiO_3$) cools through the Curie point and transitions from simple cubic to tetragonal, and during the transition to rhombohedral domains of many different angles would be formed to reduce charge build-up and stress.

The distribution of the polarization directions after the formation of the domains however hinders the ability for the material to have a net polarization. This is due to the polarization directions cancelling each other out. This can be undone via a process known as poling, where an applied electric field configures the polarization directions to produce a non-zero net polarization.

In figure 2.15, the effects of applying the electric field to the material can be seen. The domains rearrange themselves in the direction of polarization, and a remanent polarization is left after the electric field is removed.

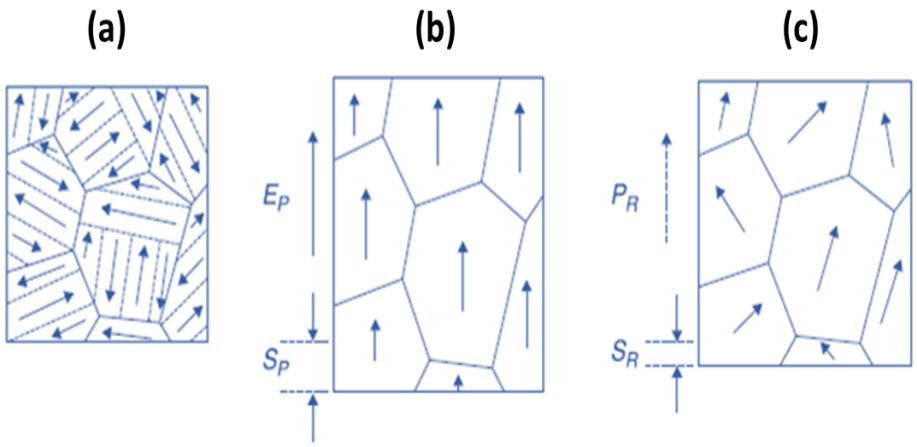

Figure 2.15: Poling a piezoelectric ceramic: a) Natural polarisation of the ceramic before poling. b) An electric field, E_P, is applied during polarisation which aligns the domain in the same direction as the electric field. S_P is the polarisation strain c) The remnant polarization, P_R, after the electric field is removed. S_R is the remnant strain. [17]

2.5 Applications

The main applications of piezoelectric and ferroelectric materials are in sensors, generators actuators, and transducers [18].

Sensors and generators convert mechanical energy into electrical energy, thus utilizing the direct piezoelectric effect. Whilst generators can convert any form of mechanical energy into any form of electrical energy, sensors can only convert mechanical stresses into electrical signals, so they both have different sets of applications. In contrast, actuators convert electrical energy into mechanical energy, thus utilizing the converse piezoelectric effect.

Sensors and actuators are both subclasses of transducer, which is generally defined as a device which can convert one form of energy into another. However, in electrical applications, transducers can also be defined as devices which can utilizes both the direct and converse piezoelectric effect in one. Table 2.2 lists examples of applications for each device which uses the piezoelectric effect:

Table 2.2: Applications of devices utilizing the piezoelectric effect [18].

Device	**Applications**
Sensors (direct effect)	• Pressure sensors • Vibration sensors
Generators (direct effect)	• High-voltage power supplies • Energy harvesting
Actuators (converse effect)	• Fuel injection • Inkjet printing • Piezoelectric pumps
Transducers (uses both effects)	• Sonar devices • Medical ultrasound • Sound amplifiers

3. Literature Review into Lead-free Piezoelectrics

3.1 A History of Piezoelectric Materials

3.1.1 Early Piezoelectric Materials

Before the discovery of piezoelectricity, pyroelectric materials (where a change in temperature produces an electric polarization in a material) were being studied. The phenomenon was first postulated by Carl Linnaeus in 1747 [19], and experimentally proven by Franz Aepinus in 1756 [20].

In the 1880s, brothers Pierre and Jacques Curie used their understanding of the pyroelectricity in crystal structures to discover piezoelectric behaviour in materials [21]. They tested several different crystals and found that quartz and Rochelle salt demonstrated the most piezoelectricity, via the direct effect [22]. This discovery led them to develop the piezoelectric quartz electrometer [23], which was a key apparatus in Pierre and Marie Sklodowska-Curie's discovery of polonium and radium in 1898.

Piezoelectric materials would first come to practical applications in WW1, when Paul Langevin helped develop a Sonar ultrasound device using a transducer made from quartz crystals [24]. After this success, piezoelectric materials were being further studied for potential applications in other areas. Subsequent applications included phonographs and ultrasonic reflectometers, which were used to find structural flaws in buildings, helping to improve their structural integrity [25]. Quartz is still used today in clocks, as their piezoelectricity produced much more accurate time keeping than mechanical clocks.

3.1.2 The Discovery of Ferroelectrics and Barium Titanate

In 1920, graduate student Joseph Valasek discovered ferroelectricity in Rochelle salt whilst developing a seismograph which utilised piezoelectricity to measure vibrations. He placed samples in an increasing electric field and observed that their polarization increased with the field via an s-shaped curve. He also discovered that the Rochelle salts exhibited hysteresis after decreasing the electric field when he found that their polarization was higher than before whilst following

the same curve in the opposite direction. Valasek and his supervisor William Swann published these findings in a paper the following year [26].

Ferroelectric materials underwent further research and development during WW2, where they were discovered to have considerably higher piezoelectric constants compared to quartz and Rochelle salt. Research conducted by teams in the USA, the Soviet Union and Japan led to the development of Barium Titanate ($BaTiO_3$) in the late 1940s [27-30]. It was the first ferroelectric perovskite material discovered and has a high dielectric constant, along with low dielectric loss. It is therefore mainly used in capacitor applications [31]. Its Curie point is 130^oC where it takes up a cubic structure, cooling to 0^oC gives it a tetragonal structure, to -90^oC it takes up an orthorhombic form, and below this it is rhombohedral. The low Curie point of $BaTiO_3$ however does limit its suitability for a wide range of other commercial applications [9] [13].

3.1.3 Lead Zirconate Titanate

The most significant breakthrough in piezoelectric materials is the development of lead zirconate titanate (PZT) at the Tokyo Institute of Technology in 1952 by Shirane and Takeda [32]. PZT is a perovskite solid solution of lead titanate ($PbTiO_3$) and lead zirconate ($PbZrO_3$), and is now the most popular piezoelectric material used in commercial applications due to its high Curie point and piezoelectricity [33]. Lead is also relatively cheap to extract compared to other elements with similar properties.

$PbTiO_3$ is a ferroelectric compound which transitions from cubic to tetragonal at around its Curie point of 490^oC. $PbZrO_3$ however is an anti-ferroelectric compound, where the electric dipoles are oriented in opposite (or antiparallel) directions (ferroelectric compounds have dipoles oriented in the same directions) [34]. $PbZrO_3$ also undergoes a phase transition from cubic to rhombohedral at its Curie point of 230^oC. Variations in the Zr:Ti ratio cause PZT to change phases, and a morphotropic phase boundary (MPB) produced at the phase boundary at Zr:Ti ≈ 52:48 has been typically attributed to the superior piezoelectric properties exhibited by PZT [33].

In their original paper published in 1952, Shirane and Takeda did not attribute the enhanced piezoelectricity of PZT to the 52:48 MPB shown in figure 3.1 [32]. Figure 3.2 shows the first phase diagram of PZT, which only included samples containing up to 20mol% of $PbTiO_3$. As a result, no shape changes were noted. However they

did discover these PZT samples exhibited anti-ferroelectricity at less than 8mol% of $PbTiO_3$, ferroelectricity at greater than 8mol%, and that increasing the $PbTiO_3$ content increases the phase-transition temperature:

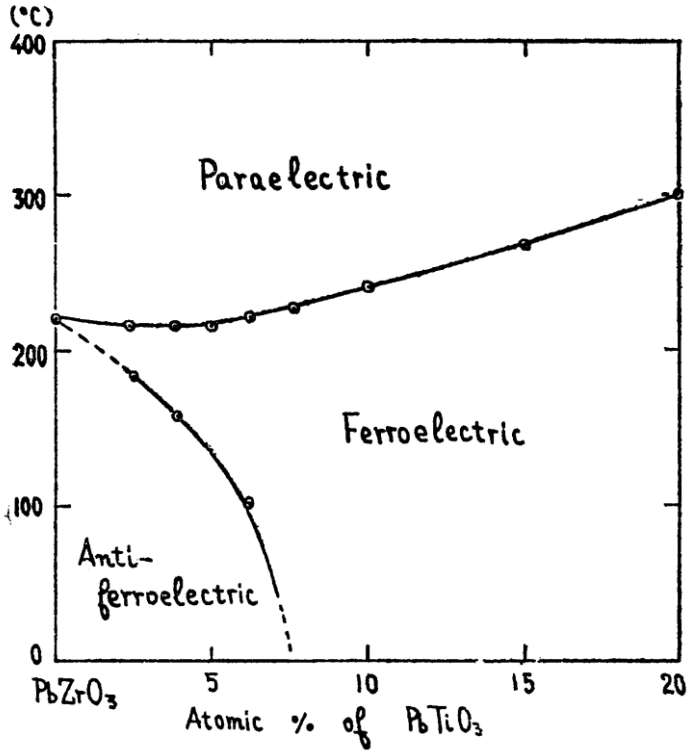

Figure 3.1: Shirane and Takeda's first phase diagram, only including up to 20mol% of $PbTiO_3$ [32].

In 1953, Etsuro Sawaguchi conducted a further study on the phase transitions of PZT, and became the first to propose the existence of the 52:48 MPB, and to identify the different phase boundaries that PZT undergoes upon temperature and compositional variations. Sawaguchi names the different phase changes as α and β phases, denoting the antiferroelectric, ferroelectric and paraelectric phases between them (Figure 3.2).

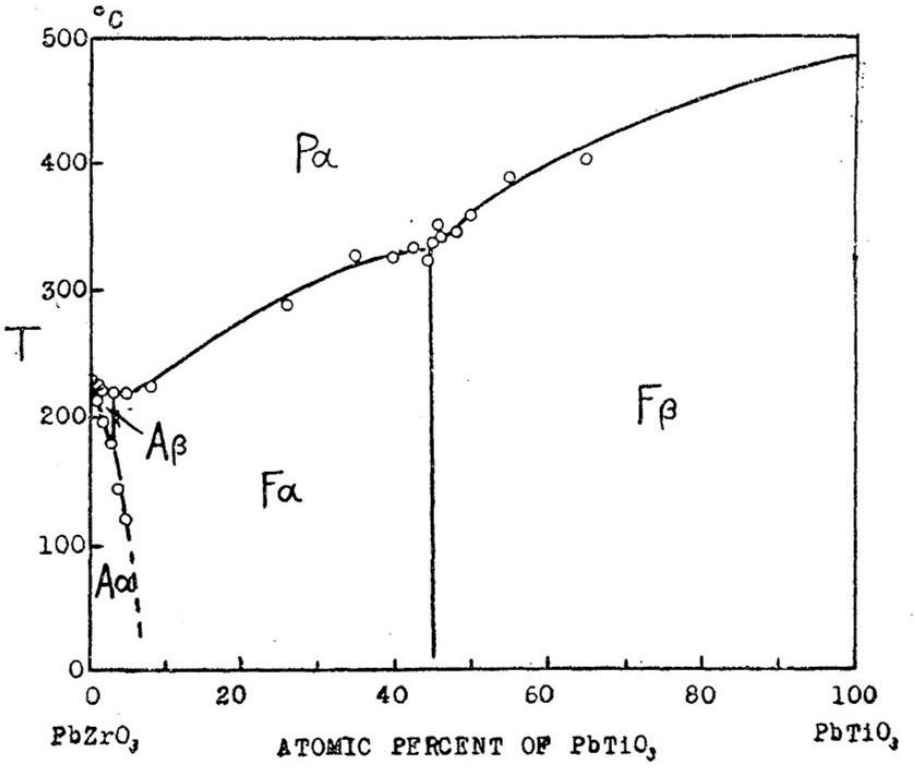

Figure 3.2: Sawaguchi's PZT diagram, the first to depict a Morphotropic Phase Boundary [34].

In 1971 Bernard Jaffe, William R. Cook and Hans Jaffe developed what came to be the generally accepted phase diagram for PZT (figure 3.3). Jaffe et al.'s phase diagram clearly defines the temperature and compositional boundaries of the different phases PZT experiences. The anti-ferroelectric phase is defined to be orthorhombic, and the rhombohedral ferroelectric phase ranging between 8mol% and 48mol% of $PbTiO_3$ is divided into high temperature and low temperature phases.

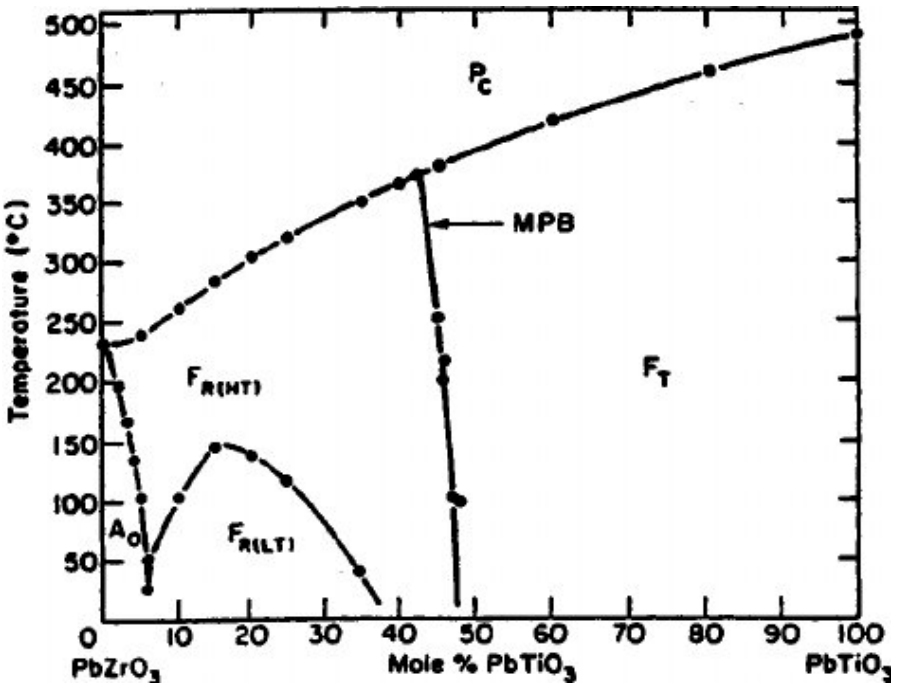

Figure 3.3: Phase diagram for PZT as proposed by Jaffe et al. (1971) [13]

The MPB as proposed by Sawaguchi indicates the phase transition between the ferroelectric rhombohedral and tetragonal phases [34]. Figure 3.4 shows the enhancement of the piezoelectric properties of PZT at the MPB:

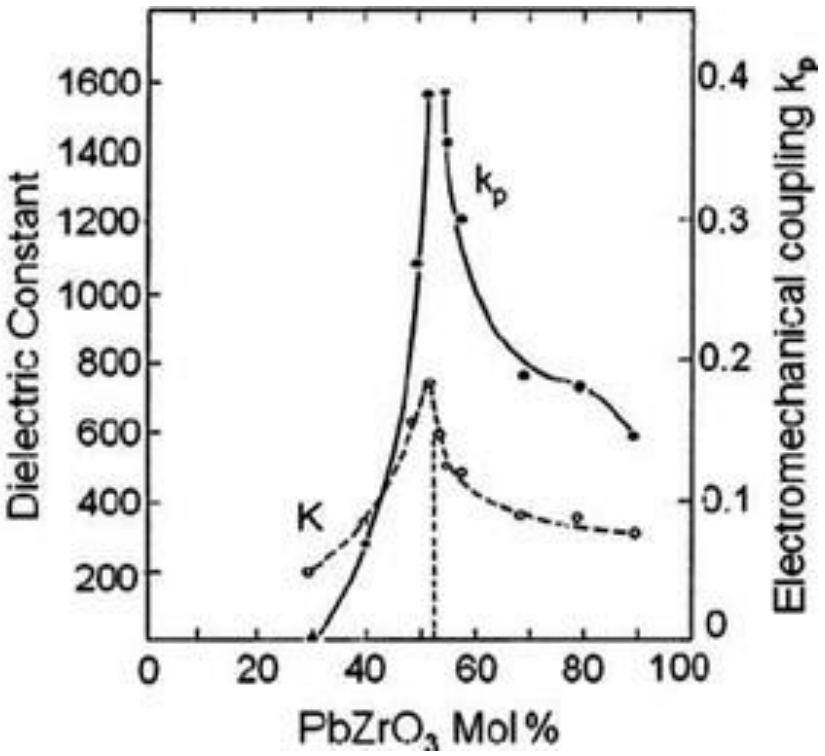

Figure 3.4: Piezoelectric enhancement at the MPB based on the dielectric constant K and the electromechanical coupling k_p [35].

Noheda et al. (1999) updated the phase diagram by Jaffe et al. by suggesting the existence of a monoclinic phase at the MPB (figure 3.5). The MPB represents the compositional change in the ratio between Zr and Ti atoms, which corresponds to the peak of the electromechanical coupling and dielectric constant on the diagram to the right. As mentioned before, the compositional changes cause the domains to reorient themselves into different directions which allows for strong poling. As a result, the electromechanical coupling factor k_p can be as high as 0.6. In addition, d_{33} values for PZT are on average measured to be 233 pC/N, the T_c is very high at over 200°C [13], and the electronic configuration for lead ([Xe] $4f^{14}$ $5d^{10}$ $6s^2$) produces a lone of valence electrons which easily forms a powerful dipole moment between the lead and oxygen ions, further enhancing its piezoelectric properties [1].

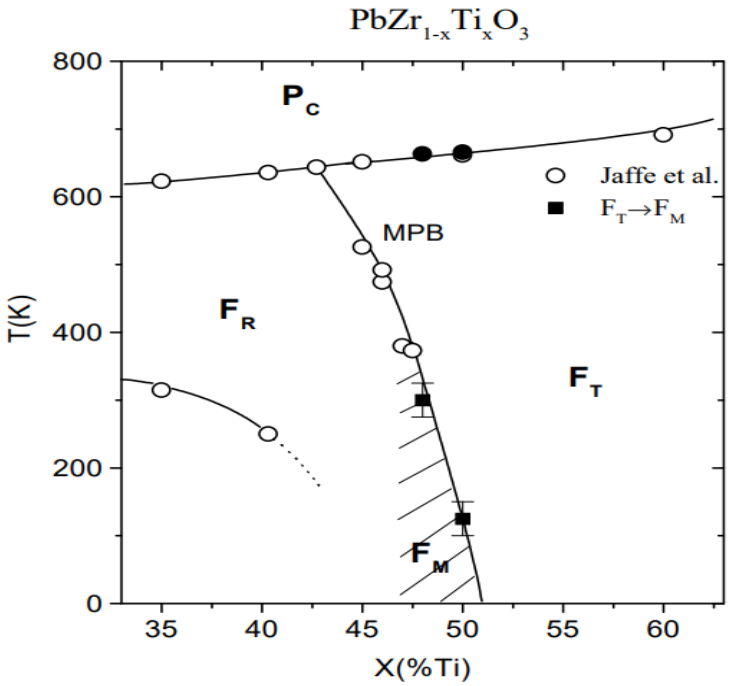

Figure 3.5: A modified version of Jaffe et al.'s phase diagram of PZT as proposed by Noheda et al. (1999), suggesting a monoclinic phase (FM) at the MPB [36].

3.1.3.1 "Hard" and "Soft" PZT

Pure PZT, of course, is not widely used in commercial applications. PZT is doped like many other compounds, and different dopants are used depending on the requirements for each application. Doped variants of PZT are divided into 2 classes, called "Hard" and "Soft" PZT [35].

Hard PZT is typically used in applications requiring high voltages or high mechanical quality factors, as they have a higher T_c (≥ 300°C), E_c and Q_M values and lower dielectric losses, at the expense of lower piezoelectric constants and dielectric constants. Hard PZTs characteristics are due to extra oxygen vacancies in its crystal structure, which are created by acceptor-doping the perovskite structure's A-site (Pb^{2+}) with Sb^{3+} and the B-site (Zr^{4+} and Ti^{4+}) with Mn^{2+} and Fe^{3+} [37]. Examples of hard PZT include Boston Piezo Optic's PZT-4 and PZT-8, which are commonly used by the US Navy in Sonar transducers, due to their strong T_c (325°C and 300°C respectively), Q_M (400 and 1000 respectively), and reasonably high d_{33} values (295 pC/N and 225 pC/N respectively) [38].

Soft PZT is used in actuators and sensors due to their high sensitivities resulting from high d_{33} values [35]. This is achieved by donor-doping the A and B-site atoms, which creates lead-vacancies and enhances their piezoelectricity and

dielectric constants, at the cost of higher dielectric losses and lower T_C values. The typical dopants for soft PZT include A-site dopants such as La^{3+} and B-site dopants such as Sb^{5+}, Nb^{5+} and Ta^{5+}[37]. The main soft PZT material developed by Boston Piezo Optics is PZT-5, which boasts a strong d_{33} of up to 585 pC/N and a high k_{33} value of 0.75, but a low Q_M of 65 and a T_c of 195°C [38].

3.1.4 European Union Restriction of Hazardous Substances

The EU directive known as the Restriction of Hazardous Substances (RoHS) restricts the lead-content in products to less than 0.1wt%, though devices are currently exempt from this restriction [2]. Devices however are often disposed of at the end of their operation lifecycle, and devices containing PZT (the market leader of piezoelectric materials) would therefore pose an environmental risk. It is therefore imperative that a suitable lead-free and environmentally friendly alternative to PZT is found. Though despite decades of research being undertaken, a suitable candidate has yet to be found [39].

3.2 Lead-free Piezoelectric Ceramics

The following section will explore the main candidates to replace PZT. Each of these materials have advantages and disadvantages, many of them have been doped in various ways to find the best performance.

In order to find a suitable candidate, researchers have tried recreating the MPB that has been found during the phase transition of PZT between the rhombohedral and tetragonal phases, as that creates a dipole coupling which allow optimum domain reorientation during electrical poling. This has been done by doping the materials with either donor or acceptor dopants; such as Mn, Sm, and Ga, depending on whether a 'hard' or 'soft' piezoelectric is required.

The main materials that have been researched include potassium sodium niobate (KNN), sodium bismuth titanate (NBT), bismuth ferrite-barium titanate (BF-BT), and barium calcium titanate zirconate (BCZT).

3.2.1 Potassium Sodium Niobate – $(K_xNa_{1-x})NbO_3$

One of the most prominent lead-free candidates is potassium sodium niobate (KNN). It is made up of the ferroelectric potassium niobate ($KNbO_3$) and the anti-ferroelectric sodium niobate ($NaNbO_3$). The two compounds were first discovered to be piezoelectric by Mathias in 1951 [40], and in 1954 their phase transitions were found to be similar to that of barium titanate [41]. The Curie temperature is 435^oC for KNN [42], making it even higher than PZT. As seen in figure 3.6, it transforms from paraelectric cubic (P_C) to a ferroelectric tetragonal (F_T) structure at around 410^oC, then transforms to orthorhombic (F_O) at 200^oC, and finally to a rhombohedral (F_R) structure on further cooling to below 0^oC.

The MPB for KNN lies between 50-60% $NaNbO_3$ content because the rhombohedral phase enters a monoclinic (F_{Mono}) phase around this area. This gives the central B-site cation more polarization directions to occupy. As a result, the piezoelectric properties are enhanced at this point, and that is the $NaNbO_3$ molar composition which forms the basis for most KNN-based piezoceramics that are currently being researched. The full phase transitions of KNN were depicted in a diagram by Jaffe et al. as seen in figure 3.6.

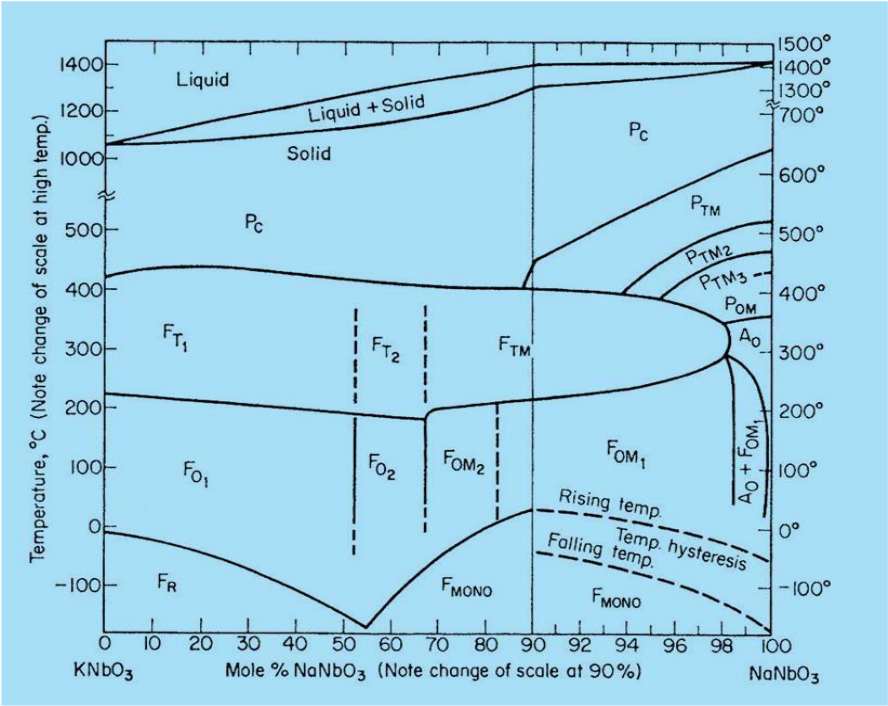

Figure 3.6: Full phase diagram of KNN by Jaffe et al. [13]

As with other ferroelectric ceramics such as PZT, KNN can be doped with many other elements and domain engineered to replicate PZT characteristics. Saito et al. doped a KNN single crystal with Lithium, Tantalum and Antimony, $(K_{0.44}Na_{052}Li_{0.04})(Nb_{0.84}Ta_{0.10}Sb_{0.06})O_3$, and were able to achieve a d_{33} value of 416 pC/N [43]. In comparison, conventional KNN ceramics fabricated by normal sintering methods achieved a maximum of 160 pC/N. PZT can achieve d_{33} values of more than 580 pC/N [13], however the progress that has been made in making KNN a more competitive lead-free alternative shows the growing potential of this material. As shown in figure 3.7, PZT still demonstrates greater piezoelectric coefficients than lead-free alternatives at a range of Curie temperatures, but KNN based piezoelectrics perform better at higher temperatures:

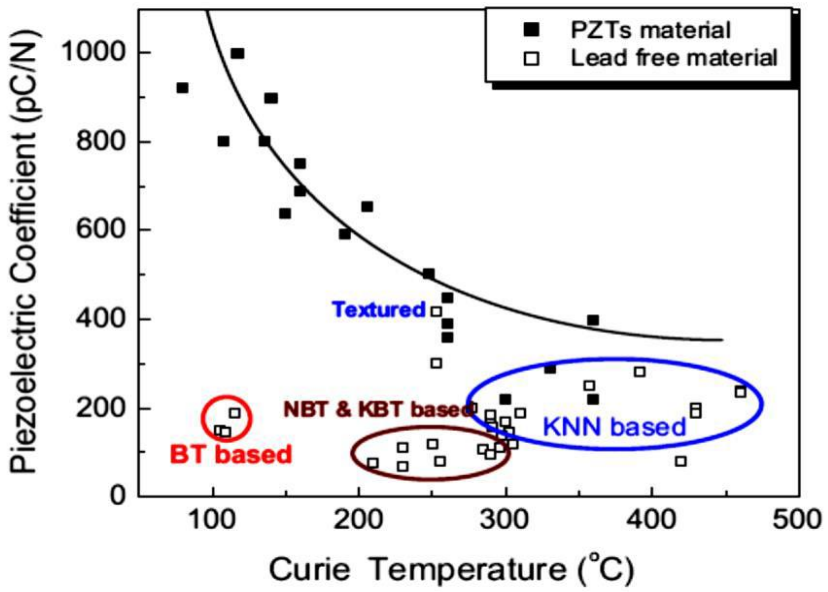

Figure 3.7: Measurement of d_{33} as a function of T_C [35]. PZT-based materials are dominant in terms of d_{33} at lower T_C, but at higher T_C KNN-based materials start to dominate in terms of d_{33}.

In PZT, the peak of piezoelectric activity is attributed to the MPB between the tetragonal and orthorhombic phases. This is normally due to polarization switching during the phase change, which is an important factor for its piezoelectric properties, as the magnitude of spontaneous polarization, P_S, is expected to be roughly proportional to the piezoelectric coefficients d and g. The P_S value in KNN ranges from between 15-25 μC/cm^2, which is a comparable range to that of PZT [44]. Egerton and Dillon (1959) were the first to investigate KNN in detail and noticed that ferroelectric and piezoelectric properties were enhanced at 0.6% and 47.5% Potassium Niobate composition (24). The piezoelectric figures for pure KNN are a d_{31} value of -49 pC/N, d_{33} of 160 pC/N, g_{31} of -0.014 Vm/N, and g_{33} of 0.045 Vm/N. The electromechanical coupling factors of k_p, k_{31}, k_{33}, k_{15} are 0.42, 0.27, 0.53, 0.60 respectively. Table 3.1 compares the coefficients of pure KNN to that of pure PZT.

PZT has superior values in all but one coefficient. However, the g_{33} coefficient is higher in KNN than in PZT, which could be significant. The g-coefficients are the piezoelectric voltage constants, which determine the amount of voltage produced when stressed. In the case of g_{33}, this represents the induced electric field in the direction parallel to that where ceramic element is polarized. This could therefore suggest that KNN's abilities as a Sonar transducer may outperform those of PZT, as

the g_{33} coefficient means that a stronger voltage is produced with the same amount of stress [18].

Table 3.1: Comparison of piezoelectric coefficients between pure PZT and KNN.

Coefficients	Pure PZT	Pure KNN
d_{31} (pC/N)	-93.5	-49
d_{33} (pC/N)	223	160
g_{31} (Vm/N)	-0.0145	-0.014
g_{33} (Vm/N)	0.0345	0.045
k_p	0.52	0.42
k_{31}	0.31	0.27
k_{33}	0.67	0.53
k_{15}	0.69	0.60

Although KNN's piezoelectric properties were discovered 60 years ago, its inferior stats compared to those of PZT have made it largely obsolete for the remainder of the 20th century. However, research into KNN resurged in 2004 when Saito et. al. published an article where they achieved a d_{33} value of up to 416 pC/N after adding lithium, tantalum, and antimony to a sample of KNN [43]. This sample, later known as LFT4, had its properties enhanced due to the presence of a MPB which was also observed to be at room temperature (approx. 25°C). The Curie temperature was also controllable within a range of 170 and 500°C, which could be shifted via the addition of the lithium and tantalum elements. For the most part, the T_C was observed at 253°C, which is lower than the original value, but still better than other lead-free piezoelectrics. For LF4T, the coupling constant k_p is 0.61, and g_{33} is 0.0299 Vm/N, which is lower than what a sample of pure KNN has. The other piezoelectric coefficients are significantly higher. However, the lower g-coefficients are largely down to the different crystal arrangements of both samples. The pure KNN sample is an example of a ceramic structure, and Saito's LB4T was grown as a single crystal. However, the overall performance of LB4T proves how much of an impact doping has on a material's performance, so modified versions of KNN are of significant interest.

KNN has been doped with $LiTaO_3$ and $LiSbO_3$ [46], and these dopants have proved to enhance the piezoelectric properties. Saito et al. doped KNN with $LiTaO_3$ and achieved a d_{33} of 230 pC/N and a k_p of 0.5, which nearly matches that of PZT [43]. Another attempt by Hollenstein et al. measured a d_{33} of 300 pC/N and a k_p of

0.52 [47]. Yang et al noticed that increasing the $LiSbO_3$ content on pure KNN increased d_{33} and k_p whilst decreasing T_C, until a maximum is reached, and these values subsequently decrease when more LS is added [48]. Saito et el also doped KNN in a ternary system of $LaTiO_3$ and $LiSbO_3$, achieving a d_{33} of 373 pC/N [43]. The reason for this superior d coefficient could be down to a MPB where the structural and compositional changes between each solution, thereby enhancing the piezoelectric properties.

Whilst KNN shows plenty of potential in replacing PZT, it does contain niobium which requires heavy mining. This is also problematic for the environment due to the processes used in extracting and purifying the material, plus the energy used to manufacture KNN exceeds that of PZT [49]. Therefore, in order to be consistent with environmental regulations and principles, another lead-free candidate other than KNN may have to be considered.

3.2.2 Sodium Bismuth Titanate – $Na_xBi_{1-x}TiO_3$

Sodium bismuth titanate (NBT) is another prominent lead-free perovskite discovered by Smolenskii et al. in 1961 [50], who discovered via X-ray diffraction that it was rhombohedral at room temperature, tetragonal when heated, and cubic at an even higher temperature [51] [52]. The d_{33} value can vary between 57-64 pC/N [53]. The T_C is also 325 ^{O}C, which is higher than $BaTiO_3$ making it more suited to commercial use. NBT has also been found to generate large piezoelectric strain, which would make it suited to actuator applications.

However, the compound also suffers from problems namely due to high leakage conductivity, which makes its abilities as a capacitor very limited, although this can be reduced by increasing the composition of bismuth. The high conductivity is problematic during the process of poling, as it hinders the ability to create a dipole moment which is a necessary component of piezoelectric materials. It also requires a high sintering temperature of at least 1200 ^{O}C [54]. The leakage conductivity is due to the high concentration of Bi^{3+} and oxygen vacancies leading to lots of ion conduction:

$$2Bi_{Bi}^{\times} + 3O_O^{\times} \rightarrow 2V_{Bi}^{'''} + 3V_{\ddot{O}} + Bi_2O_3 \qquad (29)$$

La_2O_3 has been used to dope NBT, creating $(Na_{0.5}, Bi_{0.5})_{(1-1.5x)}La_xTiO_3$ (Herabut and Safari, 2005) [55] and it has been found that d_{33} has increased from 64 to 92 pC/N

(32). This is due to a phase distortion from rhombohedral to pseudo cubic phase with increasing lanthanum dopant.

Chu et al. (2002) added $BaTiO_3$ to NBT (NBBT) and achieved d_{33} values of up to 149 pC/N near the MPB between the tetragonal and rhombohedral, more than twice the amount of pure NBT [56]. NBBT systems have also been additionally doped with La_2O_3 and CeO_2 on the A-sites and B-sites respectively, achieving d_{33} values of up to 162 pC/N (Wang et al, 2005) [57] [58].

Addition of potassium bismuth titanate (KBT) to NBT (NBT-KBT) has achieved d_{33} values going up to 192 pC/N, with T_C values ranging from 280-300°C (Sasaki et al. 1999) [59]. However, sintering conditions need to be very precise to the volatile nature of K, Na and Bi.

NBT-Ba(Ti,Zr)O3 is amongst one of the most promising doped variants of NBT, as its d33 goes up to 236 pC/N [60].

3.2.3 Bismuth Ferrite/Barium Titanate – $xBiFeO_3 – (1\text{-}x)BaTiO_3$

Bismuth Ferrite-Barium Titanate is one of the more recent candidates to replace PZT. The most notable property is its high Curie temperature (ranging from 450-636°C) [61], and a reasonably high d_{33} of at least 113 pC/N means that there is potential to increase the coefficients to a comparable level to that of PZT, whilst still maintaining a reasonably high T_C. The material utilises both Barium Titanate (one of the first perovskite piezoelectrics) with Bismuth Ferrite, a multiferroic material which is noted for its high T_C (830°C) and strong theoretical polarization (90-100 μC/cm^2). However, the latter also suffers from potential low resistivity because the Fe^{2+}/Fe^{3+} and Bi^{3+} ions evaporate during sintering and form oxygen and bismuth vacancies, leading to high dielectric losses [62]:

$$2BiFeO_3 \rightarrow 2Fe_{Fe}^{\times} + 3O_O^{\times} + 2V_{Bi}^{\prime\prime} + 3V_O^{\bullet\bullet} + Bi_2O_3 \uparrow \qquad (30)$$

At room temperature, bismuth ferrite is rhombohedral, in contrast to the tetragonal barium titanate, leading to many different crystal structures being formed as first reported by Venevtsev et al. in 1964 [63] [64]. At >67% $BiFeO_3$, the structure is found to be rhombohedral, cubic between 67-7.5%, and tetragonal at less than 7.5%, as shown in the phase diagram in figure 3.8:

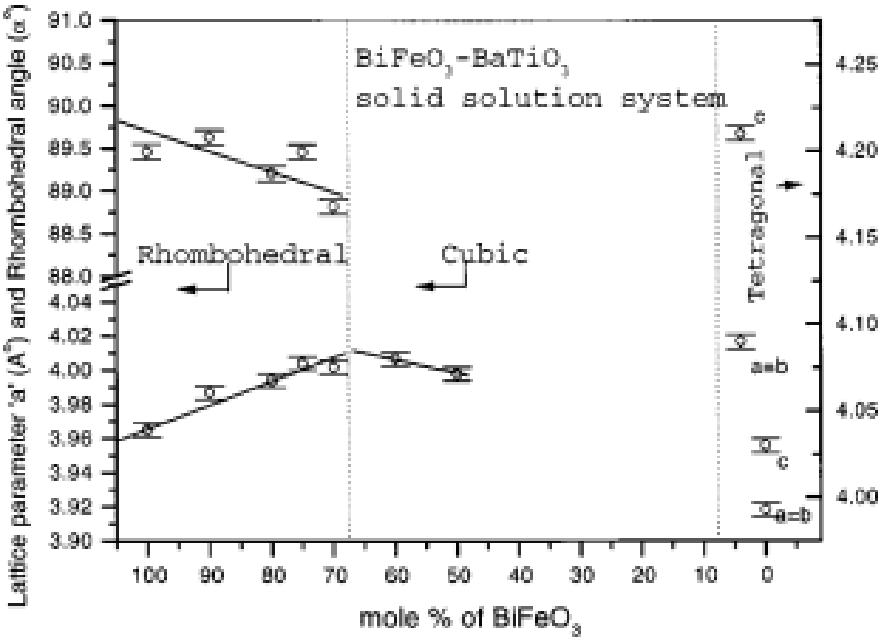

Figure 3.8: Phase diagram of the BFO-BTO system as described by Kumar et al. (1999) [65].

In 2009, Leontsev and Eitel developed the phase diagram basing it on the dielectric constant and differential scanning calorimetry (DSC) [66] measurements of the system as shown in figure 3.9:

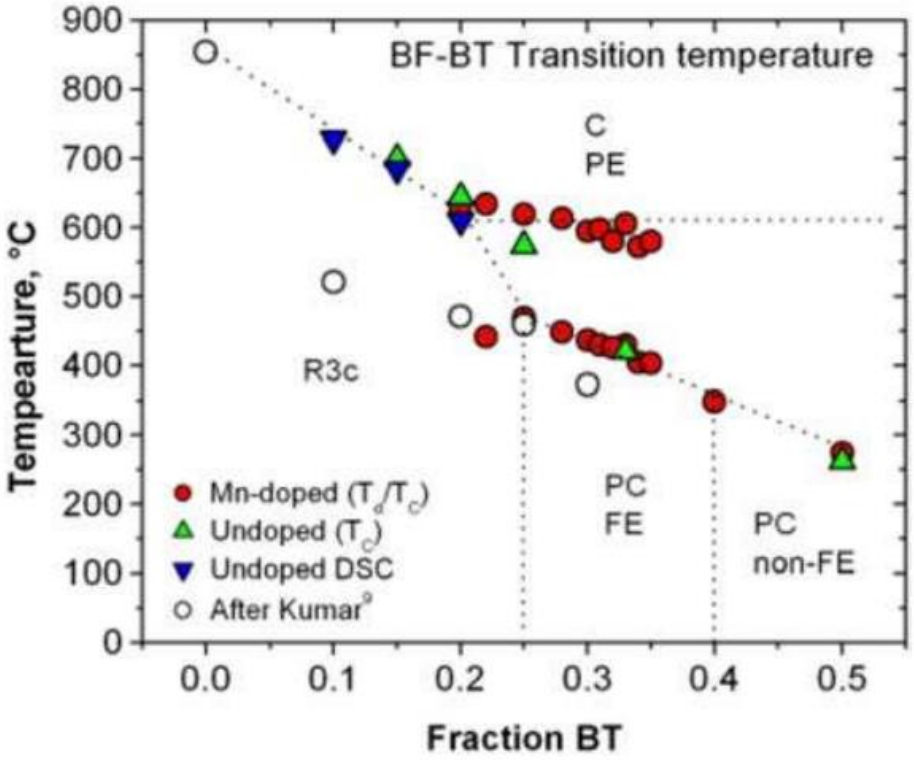

Figure 3.9: Phase diagram of BFO-BTO developed by Leontsev and Eitel (2009) [66].

Between 0.25-0.4 BT-content, they found a pseudocubic ferroelectric phase, indicating the presence of a MPB just like the one found in PZT. This was further studied by Lee et al. in 2015 [67], who subsequently revised the phase diagram to narrow the range of the MPB at approximately 0.33 BT content as shown in figure 3.10:

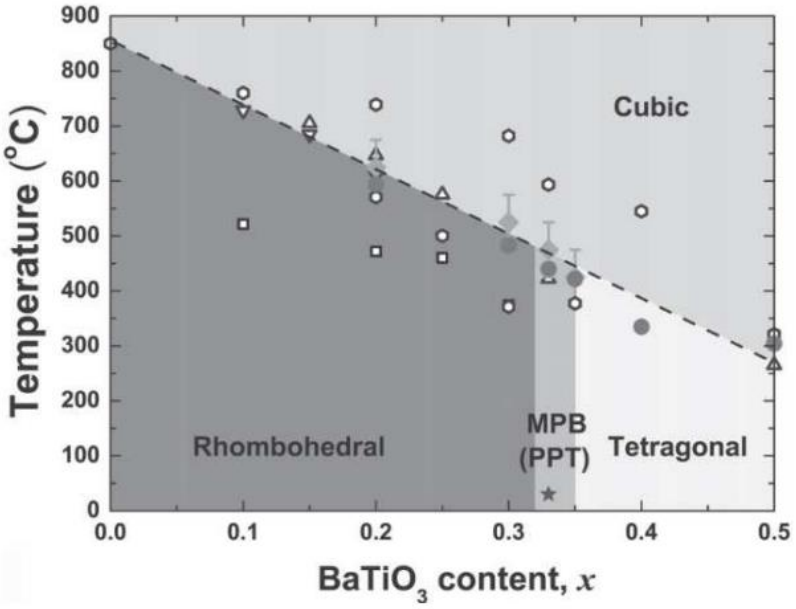

Figure 3.10: Phase diagram for BF-BT as suggested by Lee et al. (2015) [67].

To minimise the dielectric losses that BF-BT tends to suffer, various kinds of dopants have been used to minimise oxygen vacancies and to counter the Bi^{3+} and Fe^{2+}/Fe^{3+} ion losses. Manganese is one of the most common dopants used for piezoelectric used to counter these losses. Mn-doping is a form of donor doping, used to counter the Fe-losses and prevents the formation of oxygen vacancies as shown by the defect equation below [68]:

$$2MnO_2 + V_O^{\bullet\bullet} + 2Fe'_{Fe} \leftrightarrow 2Mn_{Fe}^{\times} + 4O_O^{\times} + 2Fe_{Fe}^{\times} \qquad (31)$$

Mn-doping suppresses the conductivity that is brought on by the concentration of electrons, which is seen to decrease with the introduction of MnO_2 into the reaction.

Quenching is also done to further reduce the dielectric losses by suppressing the formation of oxygen vacancies which lead to a higher concentration of electron transport. Fast cooling via quenching prevents the formation of holes as shown in equation 32 below, whereas slow-cooling from a high temperature provides extra time for oxygen vacancies and holes to form [69]:

$$V_O^{\bullet\bullet} + \frac{1}{2}O_2 \leftrightarrow O_O^{\times} + 2h^{\bullet} \qquad (32)$$

In 2013, Kim et al. Mn-doped a BF-BT ceramic on the Fe-site via quenching, achieving a maximum d_{33} of 135 pC/N and d_{33}* of 250 pm/V at 1 mol% of Mn-

dopant [68]. Jabeen et al. Mn-doped on the Ti-site, achieving a maximum d_{33} of 128 pC/N [70].

In 2014, Wan et al. modified a BFO-BTO ceramic with Sc and Mn and noticed an enhancement of the piezoelectric and ferroelectric properties. The d_{33} went up to 127-128 pC/N, and the T_C went up to 618-636°C, although the electromechanical coupling ranged between 36.6- 36.9% which is half that of some PZT ceramics [71]. Barium Zirconate Titanate (BZT) was used to dope BFO-BTO (Unruan et al. 2018) and produced a T_C of over 360°C whilst maintaining a cubic structure [72]. A low dielectric loss of 0.96 is also noted in the research. Zheng et al. (2014) used Neodymium to dope the material reaching a d_{33} of 121 pC/N with a T_C of up to 482°C [73].

Attempts to improve BFO-BTOs properties have also involved research into the way the material is prepared. For instance, Zheng and Wu (2016) were able to improve the d_{33} to 170 pC/N with a T_C of 457°C via a simple quenching process [74]. S. Lee et al. (2020) were able to achieve a d_{33} of 187 pC/N and a T_C of 422°C through optimizing the sintering conditions [75].

Sm-doping has also been carried out on the A-site, and in 2021 Habib et al. achieved a d_{33} of 334 pC/N along with a T_C of 454°C by water-quenching $0.67Bi_{1.03}FeO_3$-$0.33Ba_{1-x}Sm_xTiO_3$ [62].

By far the most promising attempt at improving BFO-BTO was done by Lee et al. (2015), in which a Ga-doped variant of BFO-BTO went up to d_{33} = 402 pC/N and T_C = 454°C [76].

Overall, quenching improves the piezoelectric properties of BF-BT and has been found to significantly distort the tetragonal-rhombohedral phases of the ceramic. Lee et al. noted that the tetragonal and rhombohedral distortions (as shown in figure 3.11) increased after water-quenching, from 1.007% to 1.0125% and 19% to 87% respectively [75]. Kim et al. also noted similar changes in the rhombohedral distortion of 0.75BF-0.25BT ceramics, where the quenched samples exhibited greater distortion compared to the slow-cooled samples [95]. These significant structural changes were considered to be driving factors in the improved piezoelectric and ferroelectric properties of the BF-BT ceramics, whilst also reducing the leakage current due to the reduction in hole concentration as mentioned previously. This suggests that the oxygen vacancy and free electron hole concentration is significantly affected by the fast-cooling effect, as observed

by Lee et al. [75] and Kim et el. [95], which therefore leads to structural alterations, reduced leakage current and, subsequently, a stronger piezoelectric response.

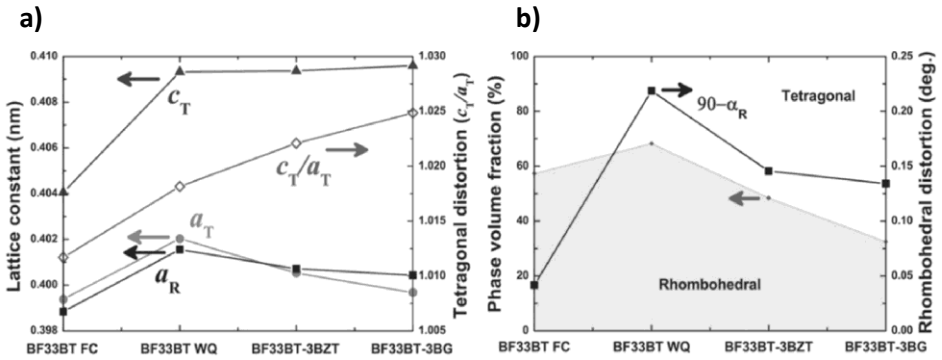

Figure 3.11: a) Tetragonal and b) Rhombohedral distortions for various BF-BT based ceramics (FC: furnace-cooled, WQ: water-quenched) [75].

3.2.4 Barium Calcium Titanate Zirconate – (Ba,Ca)(Ti,Zr)O_3

Barium calcium titanate zirconate (BCZT) has the highest d_{33} amongst all of the lead-free piezoelectric candidates. In 2009, a composition with the formula (1-x)$Ba(Ti_{0.8}Zr_{0.2})O_3$-x$(Ba_{0.7}Ca_{0.3})TiO_3$ developed by Liu and Ren was found to have an extremely high d_{33} of 620 pC/N, a value which exceeds many PZT soft ceramics [77]. The high piezoelectricity was attributed to a "triple point" MPB, where the perovskite entered a rhombohedral, tetragonal, and cubic phase at x=0.32.

Despite the impressive d_{33} of BCZT, along with high k_p and ε_r values (ranging from 0.45-0.65 and 3000-4800 respectively), the T_C of various compositions never reached 100°C, making it unsuitable for engineering applications [78].

3.2.5 Conclusion

Whilst there is an extensive range of lead-free piezoelectric materials undergoing research, the compositions listed previously are the most researched and have the best potential to emulate the performance of PZT. The graph in figure 3.12 shows the general trend amongst lead-free piezoceramic materials regarding their d_{33} and T_C. The graph shows that BF-BT based piezoceramics have some of the highest T_C values of the lead-free candidates. The high T_C values have also allowed BF-BT compositions to retain their ferroelectric properties at significantly higher temperatures, surpassing PZT in terms of d_{33}. If the losses can be accounted for using a variety of dopants and processing methods such as

quenching, BF-BT would be a very suitable candidate that should be further investigated upon [61].

In terms of the other candidates, whilst BCZT has a very high d_{33} the T_C is very low, failing to surpass 100°C, making it insufficient for engineering applications [77] [78]. KNN has been one of the most researched lead-free piezoelectric materials in recent years, however it requires sodium and potassium carbonates which are known to be highly volatile materials. This could prove problematic during sintering, where a significant amount of potassium ions would be lost and potentially make the material porous. In addition, niobium mining is a very environmentally costly procedure and is believed to cause more damage in the long term than lead-mining [3]. As the environmental sustainability is the main motivation for this project, KNN would be an unsuitable candidate for further research and investigation. Finally, NBT does have decent piezoelectric properties and a respectable T_C value [59]. However, they are significantly lower than the values for PZT and BF-BT. In conclusion, BF-BT has been proposed by the author as the selected candidate of interest.

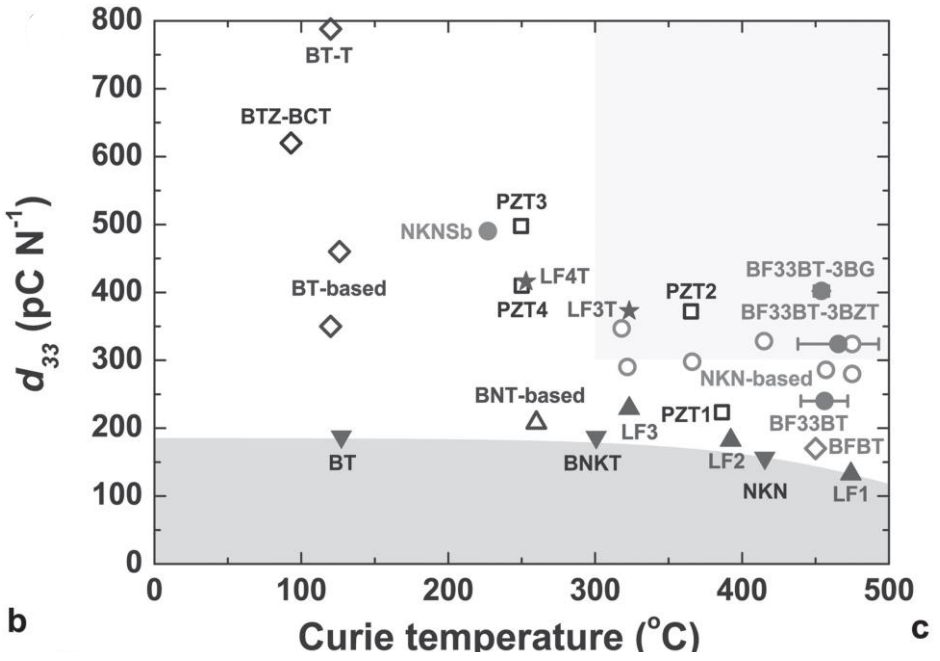

Figure 3.12: Comparison of the lead-free piezoceramic materials in terms of their T_C and d_{33}. BF-BT based ceramics dominate at the far-right end of the graph with higher d_{33} and can withstand higher temperatures [76].

4. Experimental Techniques

4.1 Material Processing

Material processing is done by solid state reaction. This involves reacting oxides and carbonates together at high temperatures to produce polycrystalline ceramics from raw oxides and carbonates. The reagents are mixed together and undergo an initial reaction stage known as calcination before the reacted powder is mixed with binder and pressed into pellets, before undergoing a densification process known as sintering. After sintering is completed, the pellets are polished and ground before being electrode and poled.

Figure 4.1 depicts a flow chart naming each step of the material processing procedure:

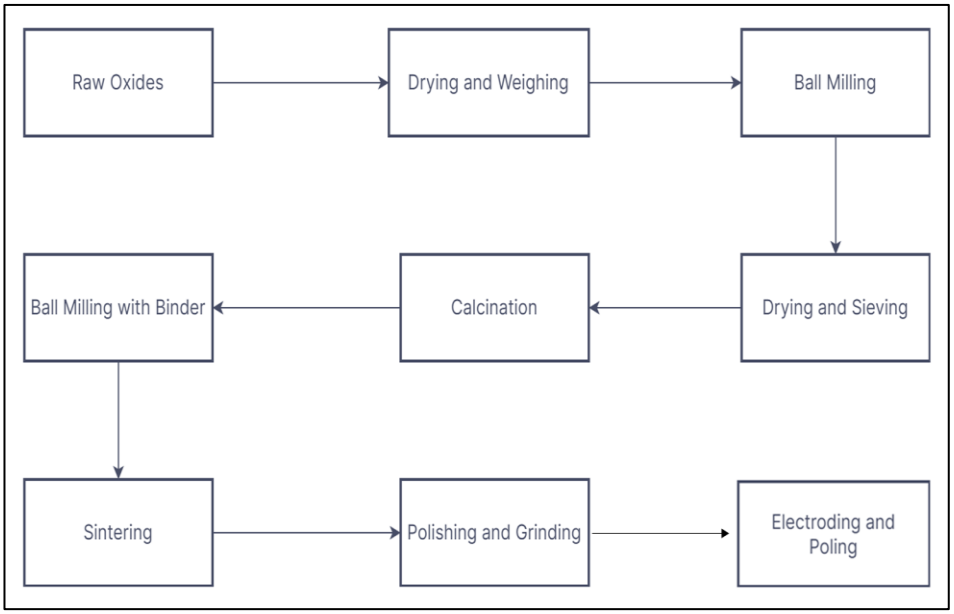

Figure 4.1: A flow chart depicting the material processing procedure.

Each stage of the material processing procedure is described in more detail below, along with the extra measures that are done to control the purity, microstructure, particle size, density and electrical properties of the material.

4.1.1 Raw Oxides

The first step is identifying the raw oxides required to produce the desired material. For example, in order to produce bismuth ferrite-barium titanate, the required reagents are bismuth (III) oxide (Bi_2O_3), iron (III) oxide (Fe_2O_3), barium carbonate ($BaCO_3$), titanium oxide (TiO_2).

Table 4.1: All the reagents used for the project.

Reagent	Molar Mass (g/mol)	Purity	Manufacturer
Bi_2O_3	465.959	99.90%	Sigma-Aldrich
Fe_2O_3	159.687	99.00%	Sigma-Aldrich
$BaCO_3$	197.340	99.00%	Alfa Aesar
TiO_2	79.866	99.80%	Alfa Aesar
Sm_2O_3	348.720	99.90%	Merck
MnO_2	86.937	99.00%	Sigma-Aldrich

4.1.2 Powder Drying and Weighing

Raw powders are then dried in ovens for at least 24 hours to prevent them from absorbing moisture. This is done to ensure accurate mass measurements when weighing them, as the absorption of excess water vapor can affect the weight of a powder. For most powders drying is done at 150^{o}C.

Stoichiometric calculations were done using the following procedure:

1. Multiplying the molar mass of each component of the product with the percentage of occupation on a particular site (A or B-site).
2. Calculating the total molar mass of the product by calculating the total of step 1.
3. Dividing the desired mass by the molar mass of the product to get the number of moles.
4. Calculating the desired mass of each reagent by multiplying the molar mass of the reagent by the number of moles for the desired mass of the product (answer to step 3), and the mass ratio of the element in question relative to the composition.

Removing the powders from the oven was done shortly before weighing where they were then transferred onto plastic boats.

4.1.3 Ball Milling

After weighing, the powders were transferred to a high-density polyethylene bottle (HDPE) with Tosoh 9.5mm yttria-stabilised zirconia beads. IPA was added to the mixture until a creamy-viscous slurry was formed in the bottle. The bottle was then placed on a rotating ball-mill for 24 hours.

Ball-milling is done to break down the particles into smaller sizes so they mix better, creating a homogenous mixture of uniform particle size and density. This makes it easier for the particles to react when calcining later. A diagram depicting the ball-milling process is shown in figure 4.2:

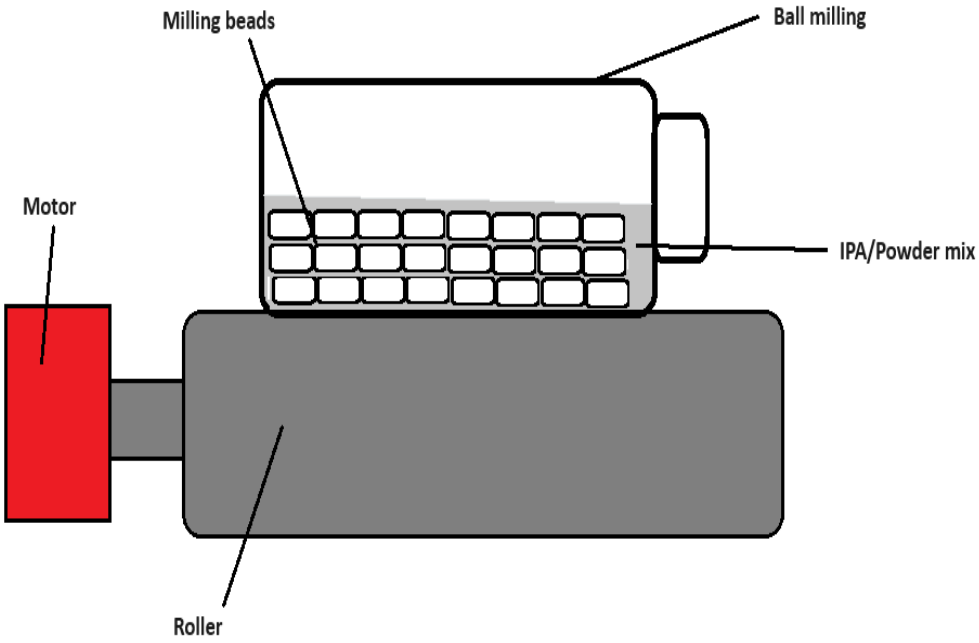

Figure 4.2: A schematic of the ball-milling process.

4.1.4 Mixing, Drying and Sieving

After 24 hours, the milled slurry is removed from the HDPE and transferred to a metal bowl which is placed on a Kenwood KM080 conductive heater (set to 90°C). The slurry is then stirred and heated for about 20 minutes until the IPA has evaporated and the slurry is reverted back into a powdery form. The powder is then transferred back to a beaker and placed in the drying oven (150°C) for 12 hours. This is done to boil any remaining IPA in the powder to make it easier to sieve.

The powder is then sieved through 300µm mesh with a pestle to break down any bits of powder that may have clumped together during stirring. Once sieving was completed, the powder was transferred to an alumina crucible for calcination.

4.1.5 Calcination

Calcination is the initial heat treatment that powders undergo, where the reagents react together to form perovskite powder, producing CO_2 as a byproduct.

The calcination regime is shown in figure 4.3. For BF-BT, the powder was heated up to 800°C in a Lenton ECF 12/10 furnace from room temperature at a ramp rate of 300°C/hr and left to dwell at the calcining temperature for 6 hours before being cooled back to room temperature at 600°C/hr.

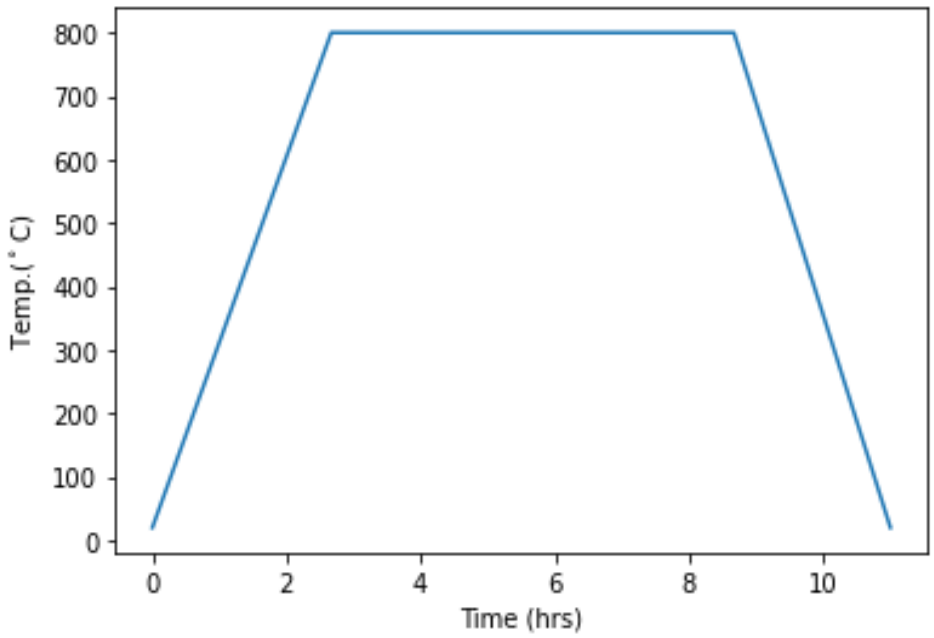

Figure 4.3: Illustration of calcination program for doped BF-BT ceramic powders at 800°C.

4.1.6 Binder and Pressing

After calcination, the powder was sieved again (as it tends to clump during the heat treatment) and transferred to a milling bottle with distilled water and left to mill for 24 hours. For the final hour, 2wt% Optapix binder was added to the slurry and left to mill for another hour.

The slurry was again transferred to the Kenwood mixer and stirred and dried at 110°C until it reverted to powder form. The powder was then dried in an oven for another 12 hours and sieved again to break down clumps of powder.

The powder was then pressed into 10mm wide cylindrical pellets using a uniaxial press. For each pellet, a 0.8g sample was weighed and poured into a 10mm steel die. 5.0kN of pressure was then applied to produce the pellet shape. For each batch, 10 pellets were typically produced.

The pellets were then placed in double layers of latex gloves in preparation for isostatic pressing (isopressing). Each pellet was placed in a finger of a latex glove,

before a vacuum pump was used to remove the air inside the glove and a knot was tied at the entrance of the glove. The first glove is then placed into a second glove with the fingers of the first glove occupying the volume of the fingers of the second glove. Again, air was removed from the second glove using a vacuum pump before a knot was tied at the glove's entrance.

The gloves were then placed in a cage container which was then submerged in a pool of mineral oil used for the isopressing process. The isopress (Stansted fluid power) then pumped the mineral oil to a pressure of 200MPa for 5 minutes. Isopressing was done to reduce the porosity of the newly produced pellets before sintering, as uniaxial pressing only concentrates the pressure down the centre of the pellet but leaves the edges brittle. As isopressing distributes the pressure around the entire volume of each pellet, this ensures that the pellets remain rigid when handling them before sintering (e.g. when measuring the green density).

After isopressing, the pellets had their geometric "green" densities measured. If the "green" densities were measured to be at least 50-60% of the composition's theoretical density, the sintering process was started.

4.1.7 Sintering

Sintering is the second heat treatment process during the solid-state reaction process. It is the main densification process where the polycrystalline grains are grown during heating. Sintering is typically done at temperatures considerably higher than the calcination process, which results in the loss or changing of states for volatile elements. Therefore, atmospheric or sacrificial powder was used to minimize losses from sintering. Each compound required a different sintering setup to account for the losses of their respective elements.

For BF-BT materials, the pellets were submerged in BF-BT powder on ceramic tiles and then covered up by alumina crucibles. This is done to minimize Bi_2O_3 losses during sintering. Figure 4.4 shows the sintering setup for BF-BT:

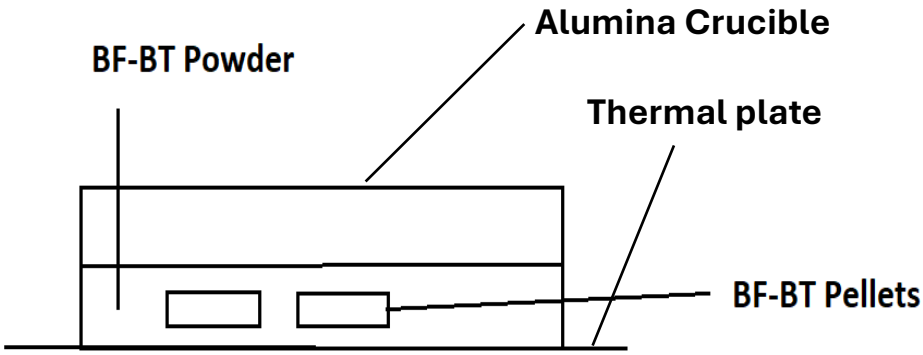

Figure 4.4: Diagram illustrating the sintering setup for BF-BT, indicating the use of atmospheric powder burying the pellets to minimise Bi losses during the process.

The pellets were then transferred to the same Lenton furnace used during calcination. The sintering program used was as follows (represented graphically in figure 4.5):

- Heat up to 350°C from room temperature at a rate of 200°C/hr.
- Dwell at 350°C for 1 hour (to burn off the binder).
- Ramp up by 300°C/hr from 350°C to 980°C/990°C/1000°C.
- Dwell at 980°C/990°C/1000°C for 2 hours.
- Cool back down to room temperature at a rate of 600°C/hr.

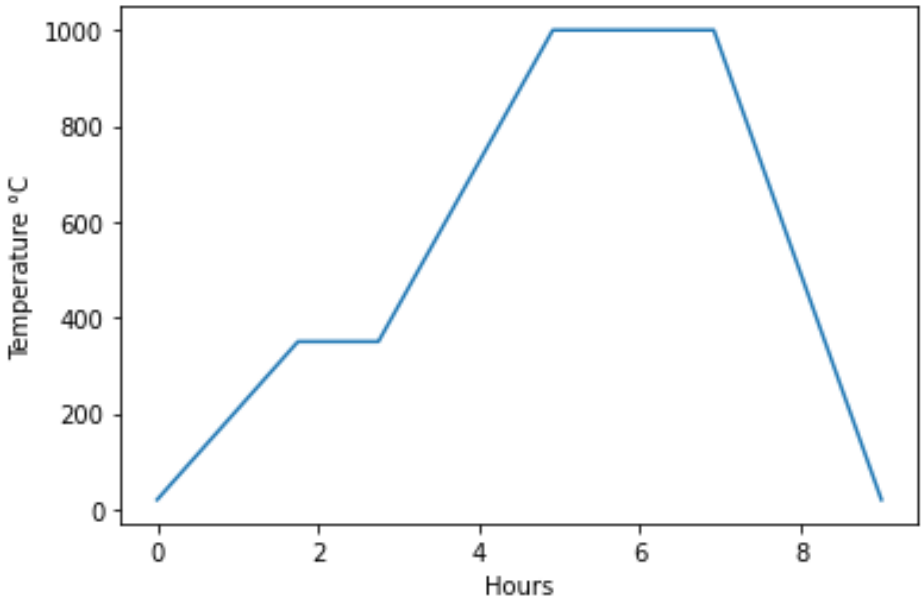

Figure 4.5: Graph representing the sintering program at 1000°C for doped BF-BT pellets. Includes a 1-hour dwell at 350°C to burn off the binder.

4.1.8 Quenching

Quenching is a fast-cooling process where the pellets are removed straight from the furnace at the sintering temperature and left to fast cool back down to room temperature. As mentioned in section 3.2.3, this is done to reduce defects and suppress the formation of oxygen vacancies, thus improving the piezoelectric properties of the material. However, quenching also risks producing cracks in the material due to thermal shock. There are 2 main ways of quenching a ceramic material: air and water quenching. Water quenching speeds up the fast-cooling process, but the material is more likely to form cracks.

Both air and water quenching were used during the processing of BF-BT samples in addition to conventional slow-cooling processes. Before the quenching round, the pellets were sintered using the main method above, except they were sintered for 1 hour. After the first round of sintering and clearing away the atmospheric powder, a few pellets were placed into a small rectangular crucible which was subsequently placed into the centre of a Lenton LTD tube furnace. The tube furnace was then ramped up to the sintering temperature of 1000^{o}C at a rate of 400^{o}C/hr, and then dwelled for 1 hour. After 1 hour had passed, a rod was used to push the crucible out of the tube furnace. For the air quenching process, the crucible was caught at the other end of the tube with pliers and left to cool in a safe area overnight. For water quenching, the pellets were tipped out of the crucible into a water bowl.

Figure 4.6 shows the first round of sintering prior to quenching, and figure 4.7 shows the second sintering regime used for the tube furnace, after which the pellet is quenched:

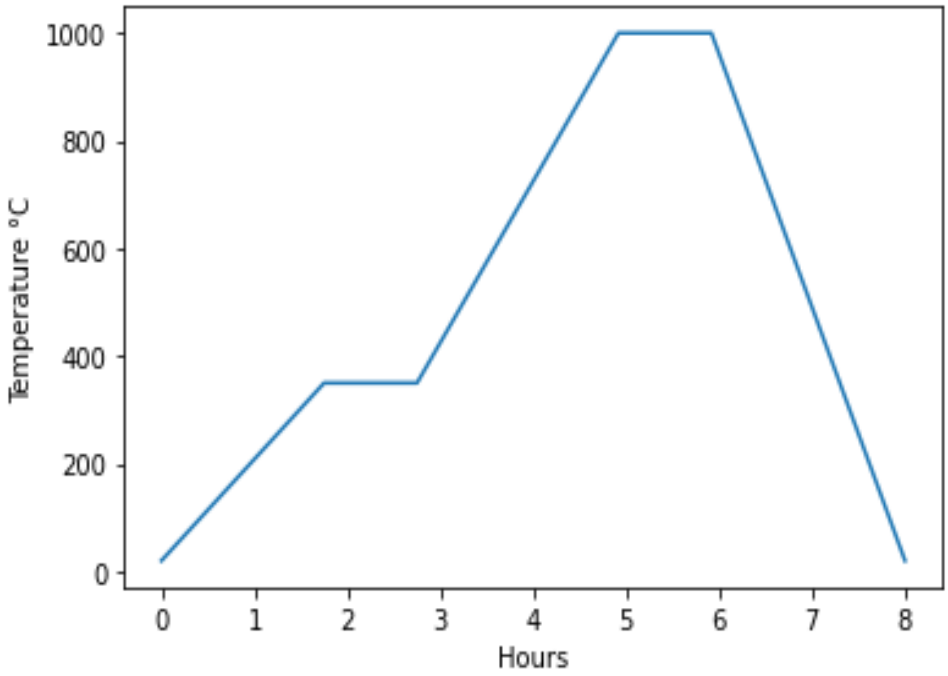

Figure 4.6: Diagram showing the first round of the quenching sintering program for BF-BT via the main furnace.

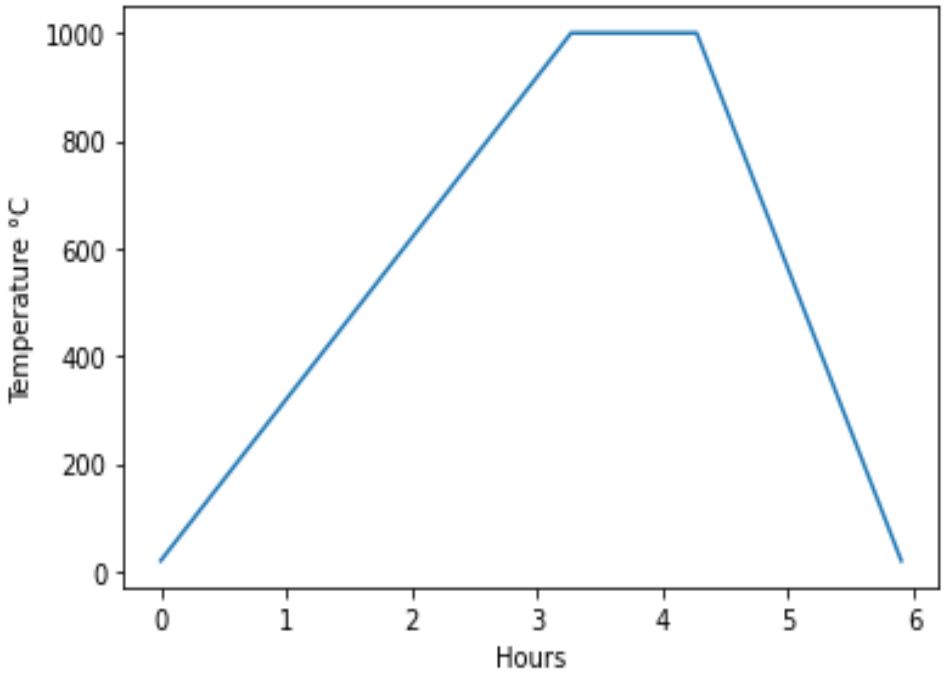

Figure 4.7: Diagram of the second round of the quenching sintering program for BF-BT via the tube furnace.

4.1.9 Grinding

Once sintering is complete, the pellets were automatically ground using Buehler P400 grinding paper to a thickness of approximately 1mm. This was done to remove any form of atmospheric powder stuck to the surface of the pellet, and to also smoothen out the surface in preparation for the electroding process.

4.1.10 Electroding

The pellets had silver electroding paint applied to one side and left to dry at 120^{o}C for 1 hour in a Carbolite electroding furnace. Once this was done, the opposite sides of each pellet were painted with silver electrodes and left to dry for the remaining duration of the program at 550^{o}C for 30 minutes. Once electroding was completed, excess electroding paint that was accidentally applied onto the sides of the pellet were removed using Buehler grinding paper (typically P600 or P800 spec) to prevent the pellets from shorting or arcing during electrical poling.

4.1.11 Poling

Electrical poling was done using a poling rig consisting of a long metal rod connected to a 10kV power supply fixed onto a fully adjustable platform that is used to contain the sample to be poled. When the sample is in place, the platform is lowered into a bowl of silicone oil placed on top of a magnetic stirrer and heater. The poling was done at room temperature, 50^{o}C and 80^{o}C, and from 1kV/mm fields which increased by 0.5kV/mm increments until sample or circuit breakdown. Figure 4.8 shows the diagram for the poling set up:

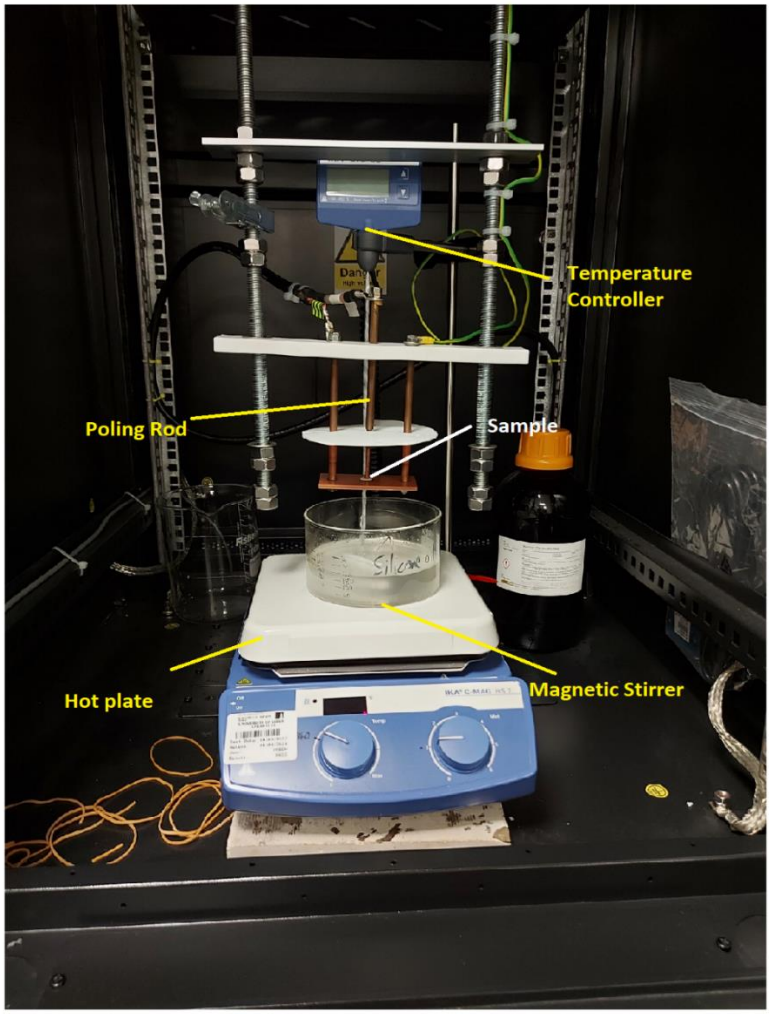

Figure 4.8: The poling rig used for electrically poling the samples. The rig was connected to a 10kV external power supply.

4.2 Crystallographic Characterisation

4.2.1 X-ray Diffraction

X-ray Diffraction (XRD) is the most common way to determine the crystallographic structure of a material. It does this by firing an X-ray beam at the material, and the diffracted beam emits a pattern that is then recorded onto a film. This technique measures the average spacings between rows of atoms, the sizes and shapes of small crystalline regions, and in general determines the crystal structures of unknown materials.

XRD techniques are largely based on the principle of Bragg's Law, in which Sir William Henry Bragg and his son Sir William Lawrence Bragg derived a relationship between the x-ray wavelength, the distance between atomic layers in crystal structures, and angle of incidence of the x-ray beam [79]. Referring to figure 4.9, the parallel x-rays of wavelength, λ, interact with two different parallel atomic planes separated by a distance d. For constructive interference to occur, the lower x-ray has to travel n number of wavelengths from A to B, then from B to C.

$$n\lambda = AB + BC \tag{33}$$

Since AB and BC are equal:

$$n\lambda = 2AB \tag{34}$$

Using basic trigonometry:

$$AB = dsin\theta \tag{35}$$

Thus, Bragg's Law is derived:

$$n\lambda = 2dsin\theta \tag{36}$$

where λ is the wavelength of the x-ray, d is the distance separating the two planes, and θ is the angle of incidence as the beam strikes the plane. The diffracted x-rays produce intensity peaks, which are detected on the film and are used to determine the d-spacing between atomic planes. The d-spacing can be calculated by rearranging Bragg's Law:

$$d = \frac{n\lambda}{2sin\theta} \tag{37}$$

The angle of incidence, θ, is adjusted by rotating the sample in the path of the x-ray beam, and diffraction peaks appear at certain angles depending on the material analysed, as different materials have different d-spacings. The d-spacing in a cubic structure is:

$$\frac{1}{d^2} = \frac{h^2 + k^2 + l^2}{a^2} \tag{38}$$

The letters h, k, l, represent the different planes in a cubic structure (known as Miller indices), and a is the unit cell length. Structures with multiple unit cell lengths will produce multiple diffraction peaks, also known as peak splitting

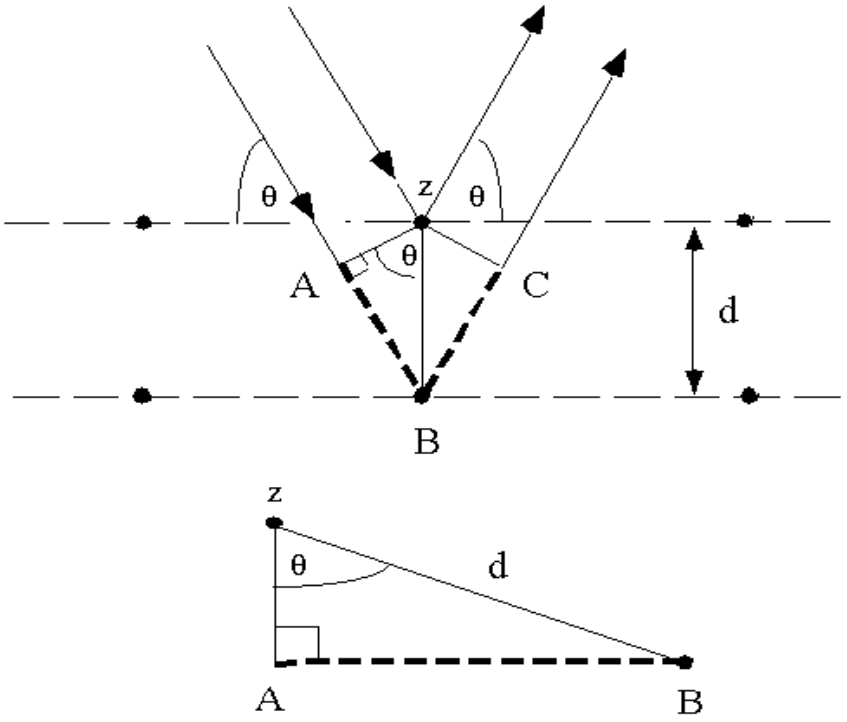

Figure 4.9: Diagram of the interaction between the x-ray beams and atomic planes used to derive Bragg's Law [80].

The phase of the material can be determined by studying the peak splitting distribution and the intensity of the peaks. Table 4.2 shows the number of peaks from peak splitting in simple perovskite systems:

Table 4.2: Number of peaks from peak splitting for simple perovskites [81].

h	k	l	Cubic	Tetragonal	Orthorhombic	Rhombohedral
1	0	0	1	2	2	1
1	1	0	1	2	3	2
1	1	1	1	1	2	2
0	0	2	1	2	2	1
0	1	2	1	3	4	2
1	1	2	1	2	4	3
2	2	0	1	2	3	2
0	0	3	1	2	2	1
2	2	1	1	2	4	3
1	0	3	1	3	4	2
2	2	2	1	1	2	2
1	2	3	1	3	6	4
3	3	0	1	2	3	2

After sintering, one pellet is selected for XRD and is crushed into powder form using a pestle and mortar and then poured into a sample holder and flattened into a smooth surface.

The X-ray diffractometer used for this project is a Bruker D8. The 2θ positions were between 20-80^{o}, the scan step was 0.033425^{o}, the wavelength of the X-rays was 1.5406 angstroms and the total scan time was 20mins.

4.2.2 Scanning Electron Microscopy

A Scanning Electron Microscope (SEM) scans a beam of high-energy electrons on a surface to reveal an image of the material's topography and composition [82]. An SEM consists of an electron gun which directs a beam of high-energy electrons into a vacuum chamber, where an anode accelerates the electrons. An electromagnetic condenser lens then controls the resolution of the electron beam (by varying the current applied to the coils in the lens), before an objective lens focuses the beam onto the surface. Figure 4.10 shows a diagram of an SEM:

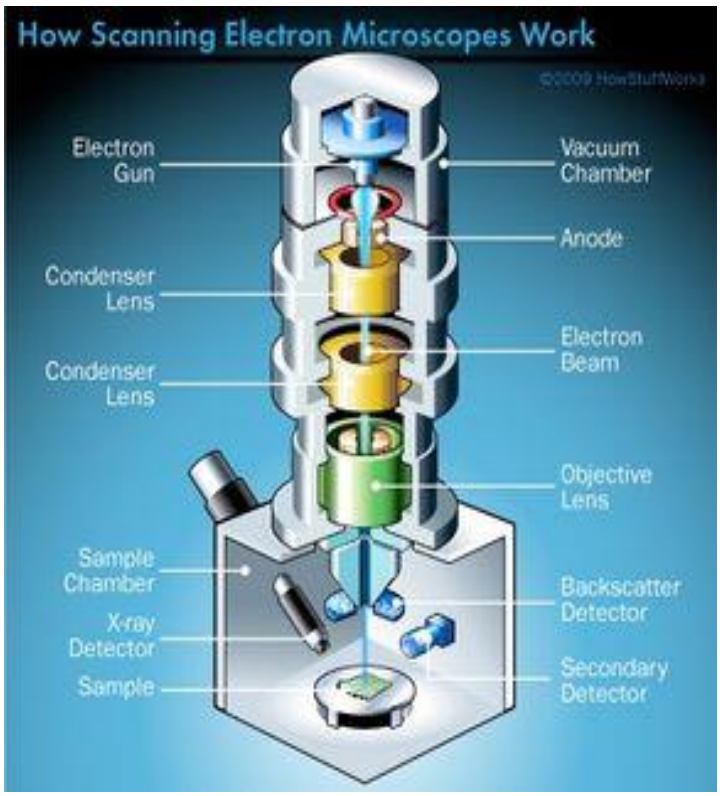

Figure 4.10: Cross section of a Scanning Electron Microscope [82].

The interaction between the electron beam and the surface atoms produces two types of electrons that are detected. Secondary electrons (SE) are the result of inelastic collision, where the incoming electron moves into the valence band of the atom, causing a valence electron to eject. It is then attracted to an Everhart-Thornley detector, which determines the composition of the surface material.

The other type of electron detected is a backscattered electron (BSE) which results from elastic collisions between the electron beam and the surface atoms. BSEs are detected by conventional solid-state detectors, which in-turn produces an image of the structure of the surface material. Figure 4.11 shows how BSEs and SEs are formed as a result of SEM:

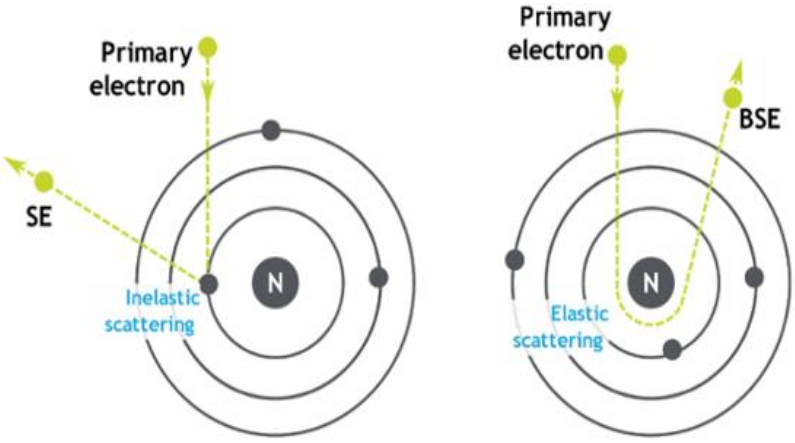

Figure 4.11: The formation of secondary electrons (left), and backscattered electrons (right) [83].

The SEM used was a Hitachi TM3030Plus, and the pellets placed in the sample holder were as fired samples (straight out of the furnace). Quenched samples, due to the two-step sintering process as mentioned in section 4.1.8, undergo a form of thermal etching, where the grain boundaries equilibrate with the free surface of the sample and reveal clear grain-boundaries under microscopy [96]. Figure 4.12 shows how grain-boundaries appear after thermal etching:

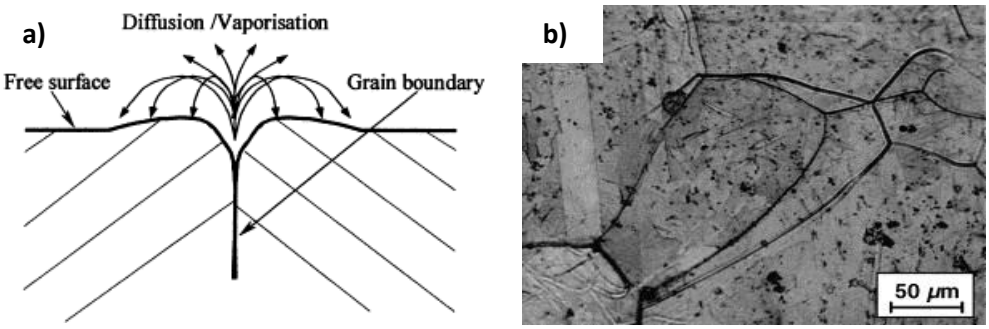

Figure 4.12: a) A diagram showing how thermal etching causes the grain-boundaries and free surfaces to equilibriate under vaporisation, clearly revealing the emergence of those grain boundaries as shown in b) [96].

4.3 Electrical Characterisation

4.3.1 Permittivity – Temperature Measurements

Permittivity vs Temperature measurements were carried out to monitor the phase changes of a sample and can also be used to determine the Curie point of a material.

The samples were placed into a tube furnace consisting of a thermocouple connected to a Hewlett-Packard 4284A and a National Instruments USB-TC01. The furnace was heated up to 600°C at a rate of 2°C/min.

The permittivity was measured as a function of temperature and frequency, and the maximum permittivity can determine the Curie point of the material.

4.3.2 Berlincourt Method

The simplest method to measure the piezoelectric coefficients of a ceramic is via direct methods, where a ceramic is in an applied electric field or undergoes external stress.

In the direct piezoelectric effect, a voltage from the ceramic is produced when it is stressed, in which a voltage is developed from a charge in between the electrodes, creating a polarization, P. The polarization is a product of the d_{ij} coefficient and the stress X:

$$P = d_{ij}X \tag{38}$$

The Berlincourt method involves using a Berlincourt meter to measure the d_{33} of a ceramic. A Berlincourt meter exerts stress on a sample nestled between two vibrating contacts, and measures the voltage produced by the sample under stress. Figure 4.13 shows a diagram of a Piezotest d_{33} PiezoMeter Berlincourt meter.

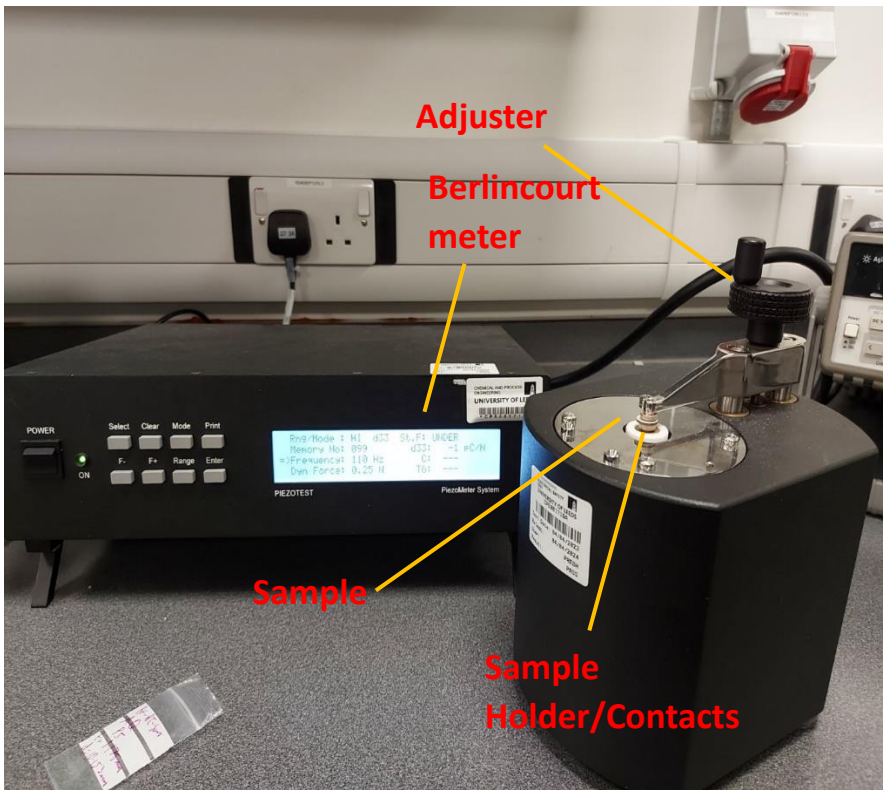

Figure 4.13: Diagram of a Berlincourt meter. On the right is the sample holder, which holds the sample between two vibrating contacts under an applied electric field. The measured voltage is then passed to the analyser on the left, which gives a d_{33} reading on the screen.

4.3.3 Resonance Methods

When a ceramic is vibrated at a certain frequency, it gives insight into the properties of the material. The ceramic will either excite at a series resonance frequency f_s, or a parallel resonance frequency f_p. The impedance of the ceramic is at its peak at f_m and at a minimum at f_n. For simplicity in explaining the concept of resonance measurements, the electrical reactance is assumed to be zero. Therefore, two additional frequencies will be used: the resonance frequency, f_r, and the anti-resonance frequency, f_a [83]. The IEEE Standard 177 clarifies that in many cases, one can assume that $f_m = f_s = f_r$ and that $f_n = f_p = f_a$ [84]. For this section, this assumption is used.

When a piezoelectric ceramic is in an applied electric field, the shape changes dimensions cyclically and approaches the resonant frequency at f_r, where the impedance is a minimum and the element vibrates most efficiently converting electrical energy into mechanical energy. As the cycling frequency increases the impedance changes dramatically and reaches a maximum at f_a. Typically, the thinner an element is the higher the frequency [18].

The relationship between the impedance and frequency is described in figure 4.14 below [83].

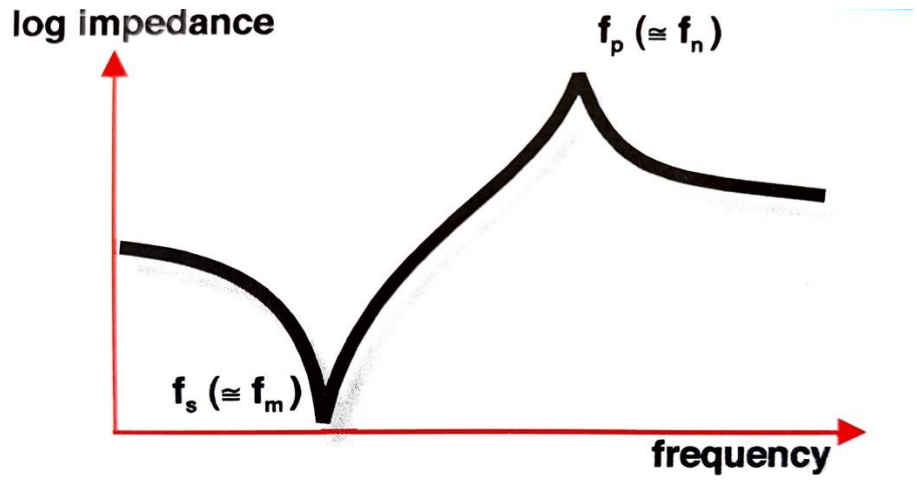

Figure 4.14: Impedance as a function of frequency. [18]

The frequencies can be used to calculate the electromechanical coupling coefficients, k_p, k_{31}, and k_{33}. To ensure that the relevant mode is the lowest frequency mode, the ceramic is cut into certain geometric shapes which is used to measure for different coefficients. Figure 4.15 and table 4.3 show the different sample geometries and the corresponding properties they are used to measure:

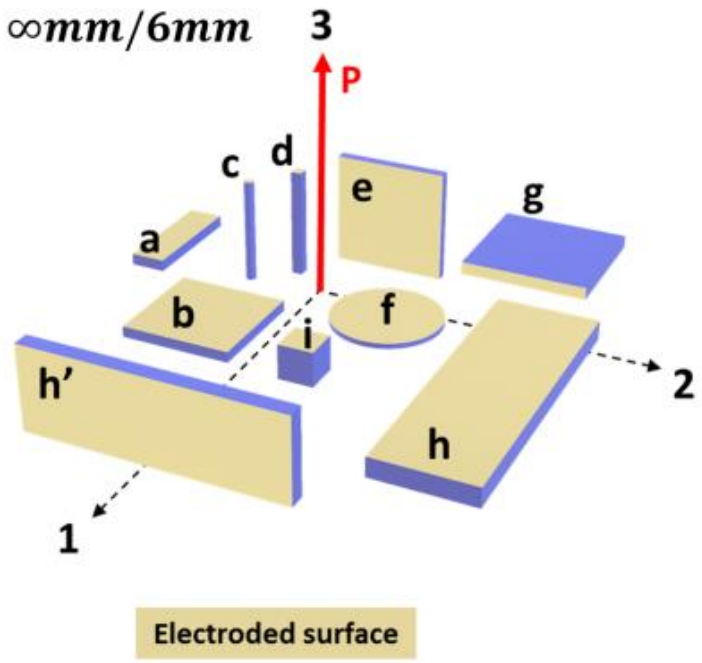

Figure 4.15: Sample geometries for resonance measurements. The geometries of interest are the longitudinal thickness extensional (LTE) bar a), the length extensional (LE) bar d), and the radial extensional (RE) disk f) [85].

Table 4.3: The properties each of the sample geometries in figure 4.2 measure (44), where ε_{33}^{x} is the relative permittivity, $tan(\delta)$ is the phase difference, the s-coefficients are the elastic coefficients, and Q_M is the mechanical quality factor [85].

Shape (from Fig. 4.14)	d)	a)	f)
Dimensional requirements	l > 3d/w	l > 3.5t, l > w	d > 10t
Poling dimension	Length-poled	Thickness-poled	Thickness-poled
Properties measured	ε_{33}^{X}, k_{33}, $\tan(\delta)$, s_{33}^{D}, s_{33}^{E}, d_{33}, g_{33}, Q_M	ε_{33}^{X}, k_{31}, $\tan(\delta)$, s_{11}^{D}, s_{11}^{E}, d_{31}, g_{31}, Q_M	ε_{33}^{X}, k_p, $\tan(\delta)$, Q_M

The equations used to calculate the properties from the frequencies are listed below [83-85]:

$$k_p \approx \frac{f_a^2 - f_r^2}{f_r^2} \tag{39}$$

$$k_{31}^2 = \frac{\psi}{1+\psi} \tag{40}$$

$$k_{33}^2 = \frac{\left(\frac{\pi}{2}\right)}{\left(1+\frac{(f_a-f_r)}{f_r}\right)} tan\left\{\frac{\frac{\pi(f_a-f_r)}{2f_r}}{1+\frac{(f_a-f_r)}{f_r}}\right\} \tag{41}$$

where:

$$\psi = \frac{\pi}{2}\left(1+\frac{f_a-f_r}{f_r}\right) tan\left(\frac{\pi(f_a-f_r)}{2f_r}\right) \tag{42}$$

sonance measurements are done using software called the Piezoelectric Resonance Analysis Program (PRAP), in which a sample is placed between two electrodes connected to an impedance analyser which measures the frequencies. The PRAP software receives the data and fits a model to it, where it calculates the desired coefficients using the equations above.

4.3.4 Measurement of Material Properties

Capacitors are often used in circuits that measure piezoelectric properties, as the capacitance can be used to calculate the relative permittivity ε_r, which is the ratio between the permittivity of the material, ε, and the permittivity of free space, ε_0, whose value is 8.85 x 10^{-12} F/m. The full equation is given below [83-85]:

$$\varepsilon_r = \frac{\varepsilon}{\varepsilon_0} = \frac{tC}{\varepsilon_0 A} \tag{43}$$

where t is the distance between the electrodes connecting the piezoelectric ceramic in meters, A is the area of each electrode in meters squared, and C is the capacitance. $\varepsilon_{33}^x$is also used to calculate a variety of other coefficients such as the d-coefficients and g-coefficients. It is also used to calculate the elastic constants which describe the stress in relation to the strain of a material when exposed to an externally applied electric field. The following equations describe how to calculate the elastic constants [13]:

$$s_{33}^D = \frac{1}{4\rho f_a^2 l^2} \tag{44}$$

$$s_{33}^E = \frac{s_{33}^D}{1-k_{33}^2} \tag{45}$$

$$s_{11}^E = \frac{1}{4\rho f_r^2 w^2} = \frac{s_{11}^D}{1-k_{31}^2} \tag{46}$$

where ρ is the density of the piezoelectric material in kg/m^3, l is the distance between electrodes in meters, w is the width of the ceramic (also in meters), and the superscripts D and E denote the constant electric displacement for an open circuit and short circuit respectively. The d-coefficients are calculated in the following equations [83-85]:

$$d_{33} = k_{33}\sqrt{\varepsilon_0 \varepsilon_{33}^X s_{33}^E} \tag{47}$$

$$d_{31} = k_{31}\sqrt{\varepsilon_0 \varepsilon_{33}^X s_{11}^D} \tag{48}$$

The d-coefficients can be subbed into the following equations to calculate the g-coefficients:

$$g_{33} = \frac{d_{33}}{\varepsilon_0 \varepsilon_{33}^X} \tag{49}$$

$$g_{31} = \frac{d_{31}}{\varepsilon_0 \varepsilon_{33}^X} \tag{50}$$

The mechanical quality factor (Q_M) is the ratio of the initial energy stored in the resonator to the energy lost in one radian of the cycle of oscillation. The formula is given below [86]:

$$Q_M = \frac{1}{2\pi f_r Z_m C_0}\left(\frac{f_a^2}{f_a^2 - f_r^2}\right) \tag{51}$$

where Z_m is the minimum impedance.

4.3.5 Electrical Impedance Spectroscopy

Electrical impedance measurements were done with a Ametek Solartron Analyzer, and analysed using Modulab XM MTS software. The analyser was connected to a tube furnace which was heated at a temperature range of 150-600^{o}C in 50^{o}C intervals. The Modulab software fitted a model to the experimental data which was used to calculate parameters such as the activation energy, conductivity, and Rayleigh coefficient.

Impedance is generally defined as the opposition to alternating current, and differs from electrical resistance in the sense that it is dependent on frequency and possesses both magnitude and phase (whereas resistance only has magnitude and is independent of frequency). It is represented by Z and its unit of measurement is Ω (Ohm).

Impedance is quantitatively defined as the ratio between the sinusoidal voltage and current of a system. The voltage and current are represented as sinus functions of time (t) as represented by the following two equations and the graph in figure 4.15 [87]:

$$V = |V| \sin(\omega t) \tag{52}$$

$$I = |I| \sin(\omega t + \Phi) \tag{53}$$

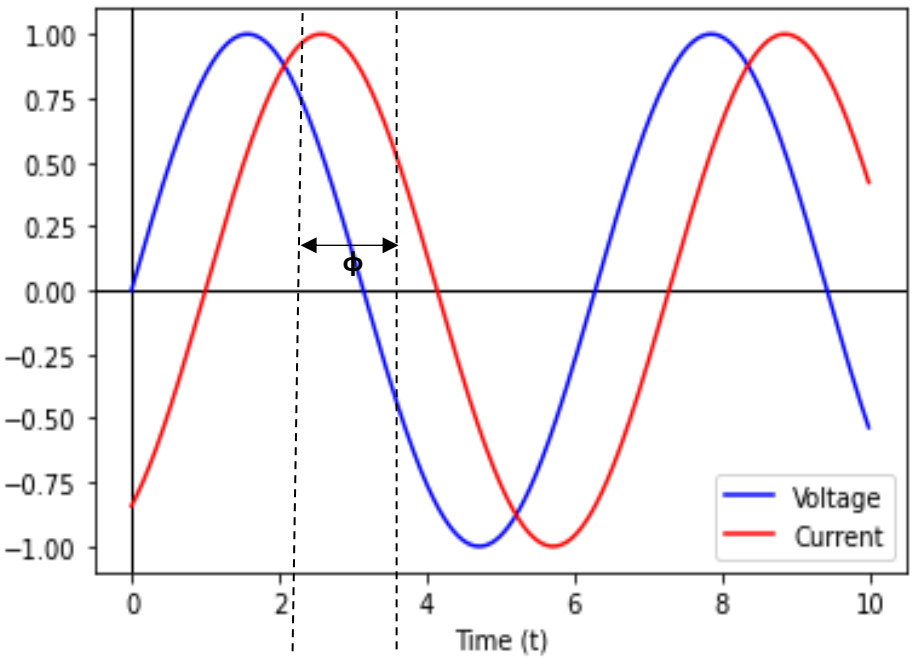

Figure 4.16: AC voltage and current as sinusoidal functions of time t, separated by a phase shift ϕ between them.

From the equations, V is the voltage at time t, $|V|$ is the amplitude of the voltage, I is the current at time t, $|I|$ is the amplitude of the current, ω is the angular frequency of the signal ($\omega = 2\pi f$), and Φ is the phase shift of the current signal from the voltage signal.

As the impedance, Z, is the ratio between the voltage and the current, the resulting equation can be derived as follows:

$$Z = \frac{V}{I} = \frac{|V| \sin(\omega t)}{|I| \sin(\omega t + \Phi)} = |Z| \frac{\sin(\omega t)}{\sin(\omega t + \Phi)} \tag{54}$$

Impedance calculations are also simplified by describing them as complex equations, where the sinusoidal voltage and currents are represented as complex formulae [88]:

$$V = |V| e^{j\omega t} \tag{55}$$

$$I = |I|e^{j\omega t - \Phi} \tag{56}$$

where $j = \sqrt{-1}$. The derivation for the complex equation of impedance can be done using Euler's formula (in terms of θ):

$$e^{j\theta} = \cos(\theta) + jsin(\theta) \tag{57}$$

Thus, the complex impedance Z^* can be derived as follows:

$$Z^* = \frac{V}{I} = \frac{|V|e^{j\omega t}}{|I|e^{j\omega t - \Phi}} = |Z|e^{j\Phi} = |Z|[\cos(\Phi) + jsin(\Phi)] = Z' + jZ'' \tag{58}$$

It can therefore be seen that the impedance possesses both a 'real' (Z') and 'imaginary' (Z'') component.

Cole-Cole plots are produced to show the relationship between the real and imaginary components, resulting in a semi-circle. An equivalent circuit can then be produced to model the raw data, which can be used to extract the capacitance and resistance of a material. The Cole-Cole plot of complex impedance (Z' vs Z'') in figure 4.17 and the corresponding equivalent RC circuit in 4.18 represent an ideal, well-made homogenous sample, that has a single relaxation time after a voltage is applied. This is typically the case for single crystals.

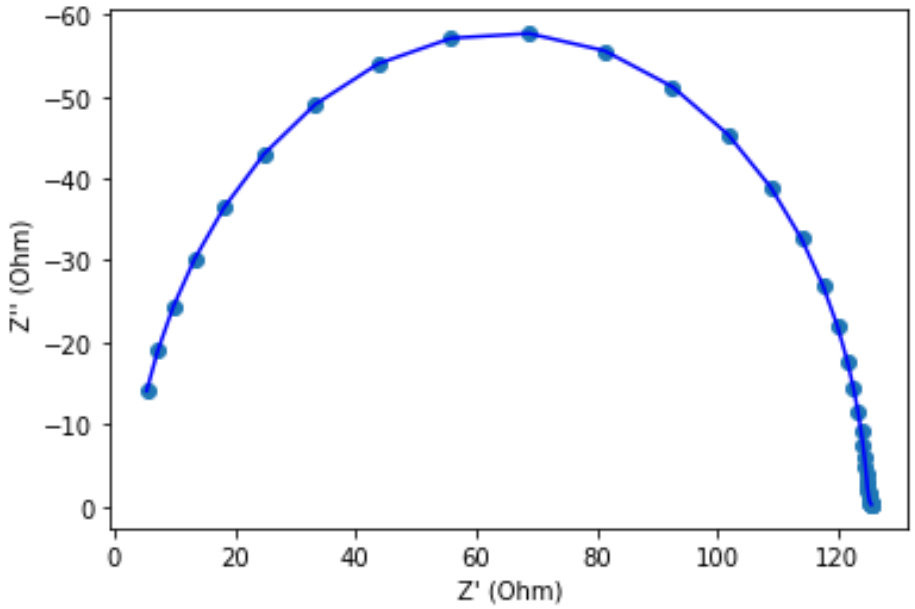

Figure 4.17: Cole-Cole plot of complex impedance for a BFO-BTO sample at 400°C: Z' vs Z''

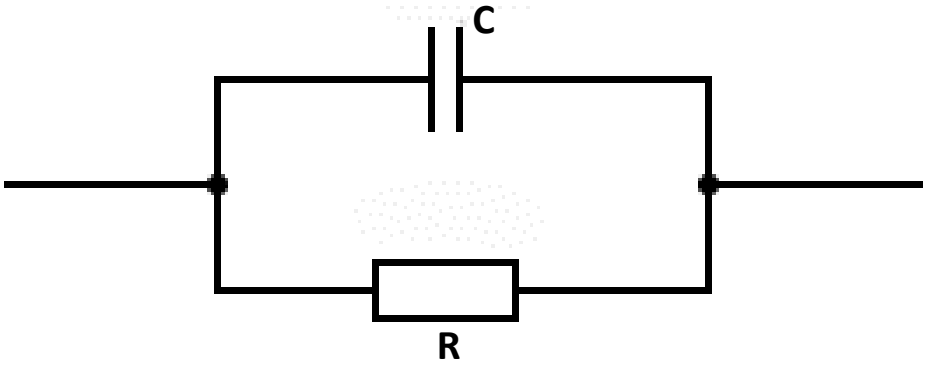

Figure 4.18: The equivalent RC circuit to figure 4.17 consisting of capacitor C and resistor R.

However, not all samples will exhibit this behaviour and polycrystalline samples will go through several relaxation phases before decaying to zero. This is due to grain boundary contributions that are not present in single crystals, leading to more semicircles. Modelling the complex impedance for these samples would require a different equivalent circuit, such as a series-parallel RC circuit (as depicted in figure 4.19), depending on the response that is shown:

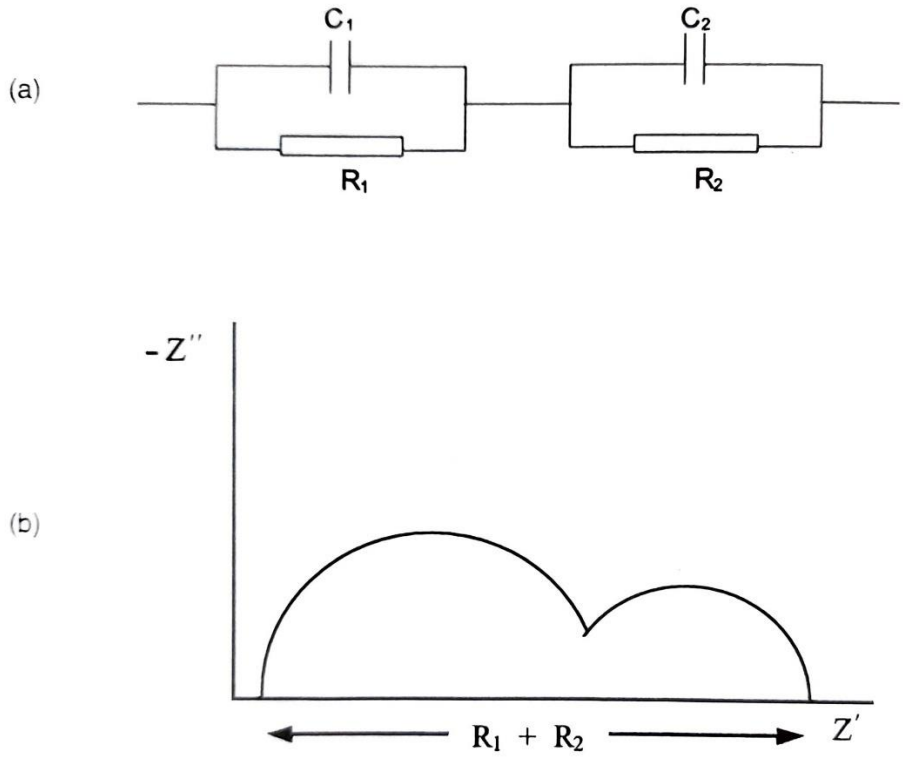

Figure 4.19: (a) series-parrallel RC equivalent circuit and (b) the corresponding Nyquist plot that fits the model [9].

In practice, a material will not act as an ideal capacitor, and therefore a constant phase element (CPE) is typically used in place of a capacitor in an equivalent circuit model to better fit the data. The equation for the complex impedance of the CPE is shown below [89]:

$$Z^*_{CPE} = [B(j\omega)^m]^{-1} \tag{59}$$

where $B = \gamma/\cos(\frac{m\pi}{2})$, γ=constant and m is a constant between 0 and 1. If $m = 0$, the CPE acts as an ideal resistor, and acts as an ideal capacitor at $m = 1$.

Another type of plot used is the Bode plot, which plots the complex components against the frequency, as seen in figure 4.20:

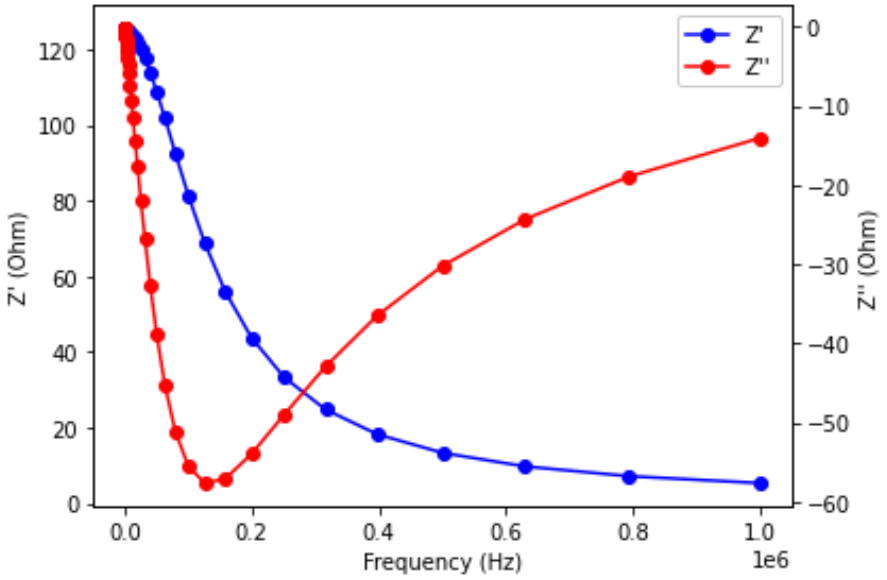

Figure 4.20: Bode plot for a BF-BT sample showing the Z' and Z'' components over frequency (Hz)

Impedance spectroscopy provides a better insight into the electrical characterisation of a material, and can lead to the calculation of many other parameters such as admittance Y^*:

$$Y^* = \frac{1}{Z^*} = Y' + jY'' \tag{60}$$

And the electric modulus M^*:

$$M^* = j\omega C Z^* = M' + jM'' \tag{61}$$

Figure 4.21 shows a full table of complex relationships:

	Z^*	Y^*	C^*	M^*
$Z^*=$	Z^*	$\frac{1}{Y^*}$	$\frac{1}{i\omega C^*}$	$\frac{M^*}{i\omega C_0}$
$Y^*=$	$\frac{1}{Z^*}$	Y^*	$i\omega C^*$	$\frac{i\omega C_0}{M^*}$
$C^*=$	$\frac{1}{i\omega Z^*}$	$\frac{Y^*}{i\omega}$	C^*	$\frac{C_0}{M^*}$
$M^*=$	$i\omega C_0 Z^*$	$\frac{i\omega C_0}{Y^*}$	$\frac{C_0}{C^*}$	M^*

Figure 4.21: Complex relationships used for impedance spectroscopy [89].

Processing the impedance data and modelling the raw data against that of the selected equivalent circuit can determine the resistance R and capacitance C [90]:

$$\omega_{max}RC = 2\pi f_{max}RC = 1 \quad (62)$$

This allows the conductivity σ and resistivity ρ to be calculated via the following equations:

$$\rho = \frac{RA}{L} \quad (63)$$

$$\sigma = \frac{1}{\rho} \quad (64)$$

where A is the surface area and L is the length (or thickness) of the sample being measured.

Obtaining the conductivity allows the activation energy E_a to be calculated as follows [91]:

$$\sigma = \sigma_0 \exp\left(-\frac{E_a}{kT}\right) \quad (65)$$

$$\ln(\sigma) = -\frac{E_a}{kT} + \ln(\sigma_0) \quad (66)$$

where k is the Boltzmann constant (1.380649 x 10^{-23} J K^{-1}), T is the temperature in K, and σ_0 is the conductivity at the x-intercept. As the final equation takes up the form of a linear equation, the natural log of conductivity $ln(\sigma)$ can be plotted against $1/T$, and the gradient of the best fit line could be used to estimate the activation energy of the conduction mechanisms of the material [91].

4.3.6 Ferroelectric Polarization – Electric field Hysteresis

As mentioned in section 2.4.2, a ferroelectric material can switch between two states when an electric field is applied, producing a hysteresis loop. Measuring the polarization as a function of electric field is done to assess the materials ferroelectric properties (also known as P-E loops) [13].

P-E loops were measured using a Radiant technologies Precision LC analyser, with a Trek model 5/80 high voltage amplifier providing the voltage. The measurements were done using Radiant technologies Vision 4.2 software, and the P-E loops were measured between 1.0kV/mm to 5.0kV/mm or sample breakdown in 0.5kV/mm increments. Double bipolar measurements were carried out with 1000μs loops.

5. $BiFeO_3$-$BaTiO_3$ based Materials

$BiFeO_3$-$BaTiO_3$ (BFO-BTO) has been heavily researched as a potential lead-free candidate and have been noted for their high T_C and wide scope for compositional changes to optimise its piezoelectric characteristics. In this chapter Sm, Mn, and Mn-Sm doping techniques are investigated for their effect on the materials piezoelectricity. The effect of air and water quenching the materials is also covered, and a matrix characterisation of a select few compositions for their piezoelectricity in different dimensions is done.

5.1 Sm-doped BFO-BTO

The first portion of this chapter will look at the effects of Sm-doped BFO-BTO, specifically a composition prepared by Habib et al. (2021) [62]: $0.67Bi_{1.03}FeO_3$-$0.33Ba_{1-x}Sm_xTiO_3$. According to the literature a d_{33} of 334 pC/N along with a T_C of 454°C were obtained after water-quenching the material from a sintering temperature ranging between 980-1000°C. For this analysis, different compositions where x = 0.000, 0.010, 0.015, 0.020, 0.030 were prepared and compared. The effects of air-quenching are also investigated for the composition containing x = 0.010 as this was the best performing composition.

A lot of research has been done into Sm-doping due to its ability to suppress oxygen vacancy concentration and produce many electron vacancies. The defect chemistry of the Sm^{3+} donor doping on the Ba^{2+}-site is shown below [62]:

$$Sm_2O_3 + 3TiO_2 \rightarrow 3Ti_{Ti}^{x} + 2Sm_{Ba}^{\bullet} + V_{Ba}'' + 9O_O^x \qquad (67)$$

creating electron vacancies on the Ba-site. The defect chemistry of the Bi_2O_3 during sintering is written as below:

$$2BiFeO_3 \rightarrow 2Fe_{Fe}^{x} + 3O_O^x + 2V_{Bi}''' + 3V_O^{\bullet\bullet} + Bi_2O_3 \uparrow \qquad (68)$$

5.1.1 Sample synthesis

The material was again prepared using conventional solid-state reaction as highlighted in chapter 4. As BFO-BTO can suffer from dielectric loss due to the evaporation of Bi^{2+} ions during sintering, an extra 3mol% of bismuth was added to minimise the dielectric losses as was done by Habib et al.

Table 5.1 outlines the reagents and their weights for each composition (x = 0.000, 0.010, 0.015, 0.020 and 0.030). The stoichiometry is for 50g batches:

Table 5.1: Stoichiometric table of reagents for Sm-doped BFO-BTO

Material	Molar Mass (g/mol)	Weight Used (x=0.000)	Weight Used (x=0.010)	Weight Used (x=0.015)	Weight Used (x=0.020)	Weight Used (x=0.030)
Bi_2O_3	465.96	27.6452	27.6404	27.6390	27.6371	27.6331
Fe_2O_3	159.69	9.1997	9.1981	9.1975	9.1970	9.1957
$BaCO_3$	197.34	11.7025	11.0851	11.0285	10.9719	10.8583
TiO_2	79.866	4.7361	4.5316	4.5314	4.5311	4.5304
Sm_2O_3	348.72	n/a	0.1979	0.2968	0.3957	0.5934

The calcining and sintering programs were outlined in sections 4.1.5 and 4.1.7 respectively, where the sintering temperature was 1000°C.

5.1.2 Scanning Electron Microscopy

Figures 5.1 to 5.4 show the SEM images of the as-fired surfaces of BF-BT-Sm samples including x=0.01 (both air-quenched and unquenched), x=0.015 and x=0.03. The samples containing x=0.00 and x=0.02 Sm-content are omitted due to poor image quality.

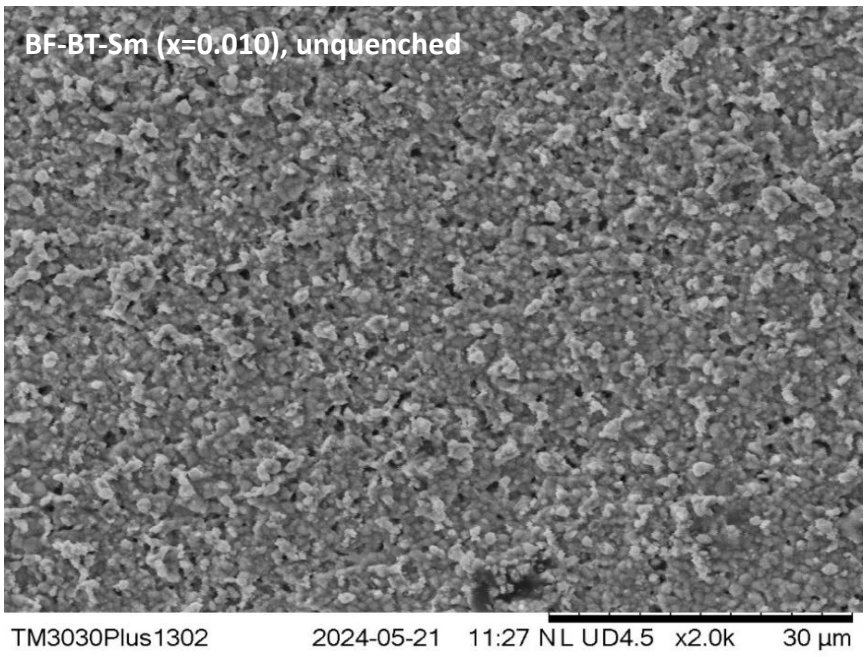

Figure 5.1: SEM image of unquenched BF-BT-Sm (x=0.01)

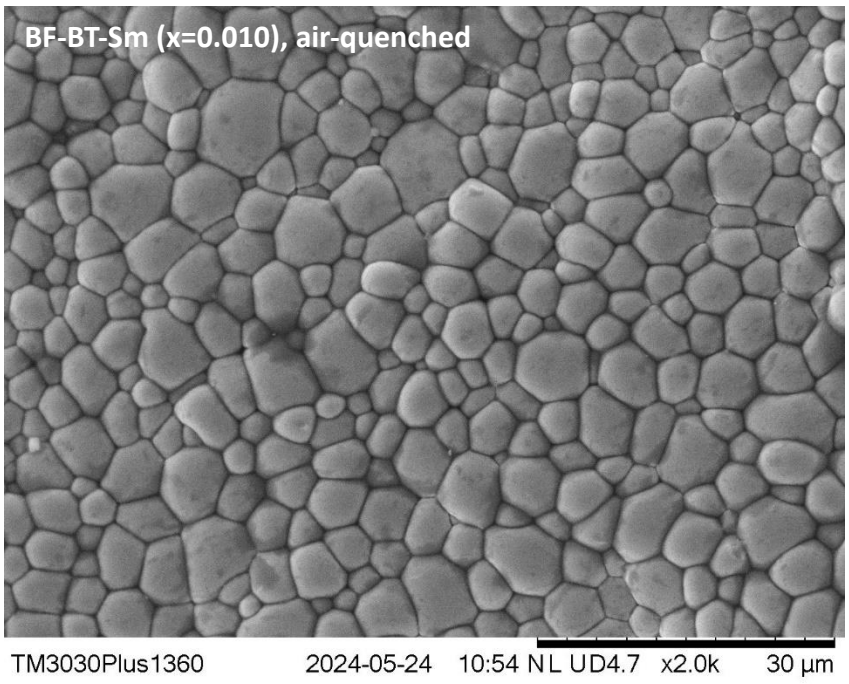

Figure 5.2: SEM image of air-quenched BF-BT-Sm (x=0.01)

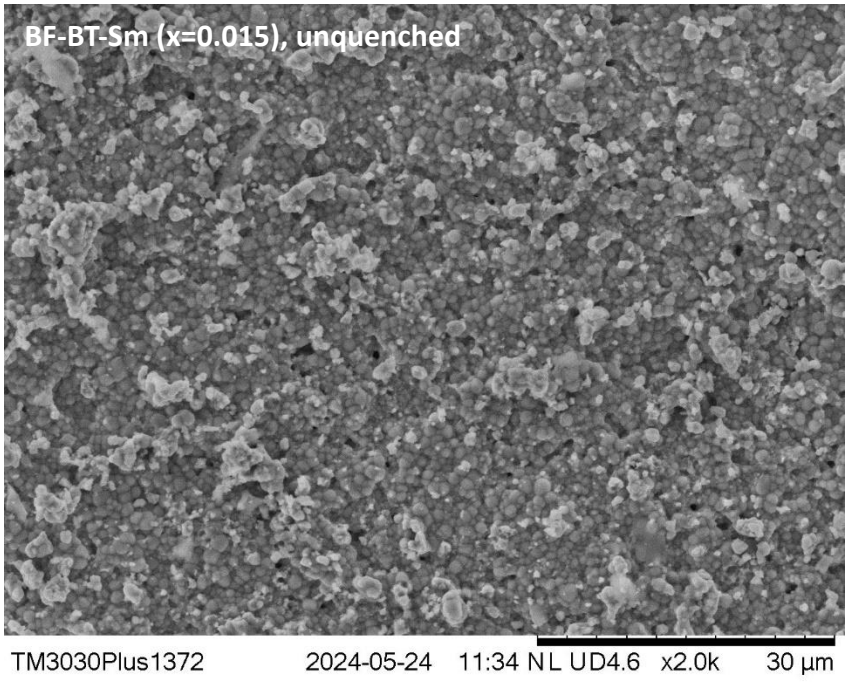

Figure 5.3: SEM image of BF-BT-Sm (x=0.015)

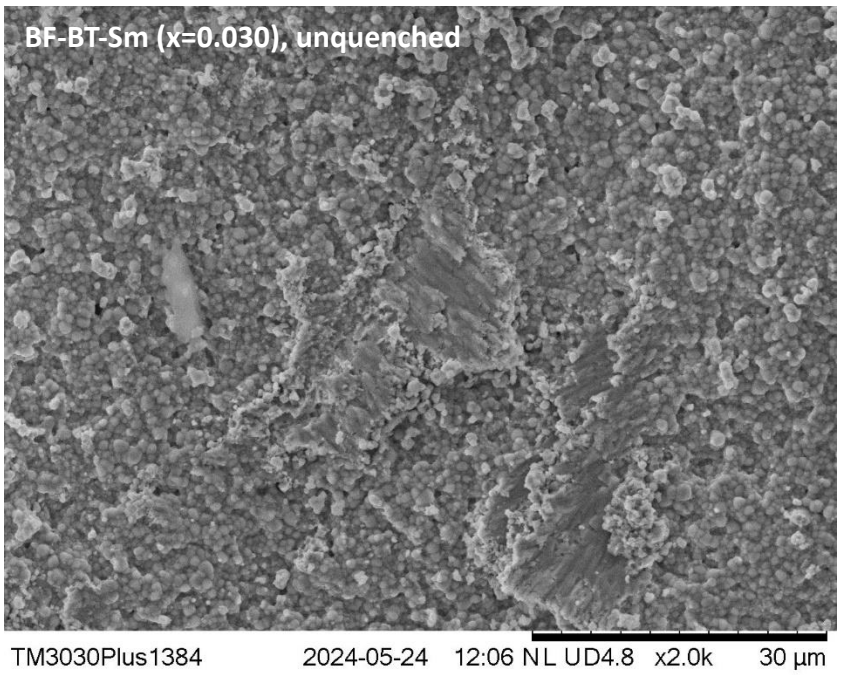

Figure 5.4: SEM image of BF-BT-Sm (x=0.03)

The air quenched sample in figure 5.2 has considerably larger grains (≈6µm wide) than the unquenched samples (<1µm). This is possibly due to the double sintering regime necessary for the quenching process, which causes the grains to grow and densify twice. It is therefore unlikely for the grain size increase to be caused by the air-quenching, and it is unexpected for that to happen as grain size is usually altered by chemical composition. No significant defects can be seen in the microstructure of the air-quenched sample, which is to be expected as air-quenching and other fast-cooling methods suppress the growth of defects due to the fast shrinkage of the grains due to fast heat loss.

5.1.3 X-ray diffraction results

Figure 5.5 shows the XRD results of the different Sm-doped BFO-BTO compositions:

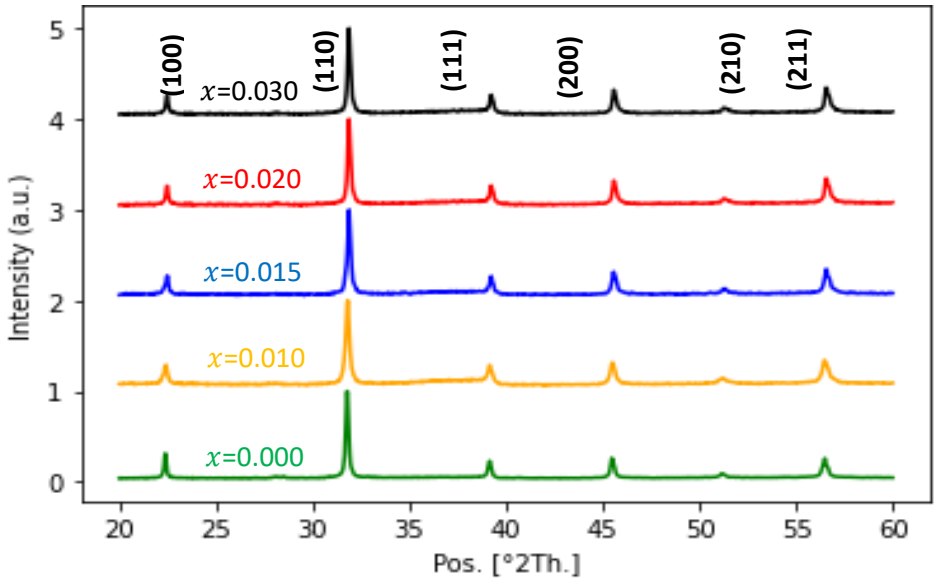

Figure 5.5: XRD Pattern of crushed BF-BT-Sm (x=0.000-0.030) pellets after sintering

Figure 5.5 shows that BF-BT is a pure perovskite, with the amount of SmO_2 dopant having a minimal effect on the XRD pattern. After sintering at 1000°C, the single peaks suggest that the material is in a pseudocubic structure. This differs from the XRD graph found in the literature by Habib et al., who found additional peaks at the (100) peak at 2θ≈21-22° for x=0.010. Figure 5.6 shows the XRD pattern obtained by Habib et al. The additional (001) peaks obtained by Habib et al. when x=0.005 and x=0.010 indicates a secondary phase for their prepared BF-BT-Sm samples, although this is likely induced by surface grinding instead of phase changes in the bulk material. For x > 0.010, a broad shoulder can be observed on the (100) peak, which is likely formed due to the formation of a distorted surface region [97] [98]. As the BF-BT-Sm used in present study is as-sintered (straight out of the furnace) and polished/grinded, but crushed and flattened into the sample holder, no additional phase distortions are found in figure 5.5.

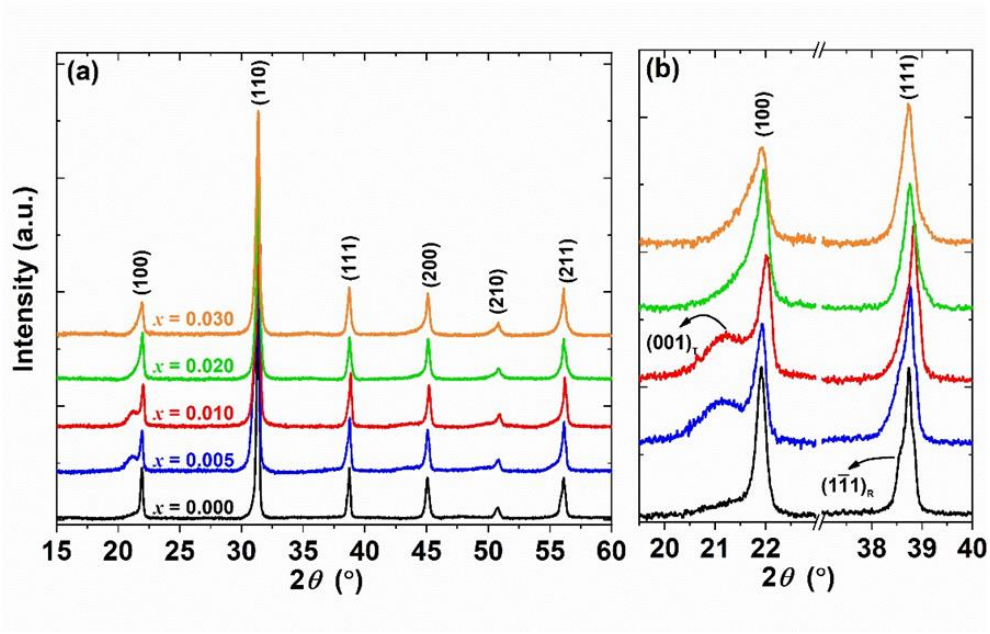

Figure 5.6: XRD Pattern for BF-BT-Sm obtained by Habib et al. (a), including a close up of the peak splitting at the (100) peak (b) [62]

Figure 5.7 compares the XRD patterns of the air-quenched and unquenched samples of BF-BT-Sm (x=0.010). Figure 5.7 shows that air-quenching seems to have smoothed out the XRD pattern compared to the unquenched samples, possibly due to the reduction of defects in its crystal structure. The post-calcined/pre-sintered sample shows peak splitting at most peaks, most notably at the (110) and (211) peaks, where secondary phases are identified. The secondary phases in the calcined powder are likely due to incomplete reaction of the reagents, which is then completed during the sintering phases as seen in the XRD patterns for the sintered samples.

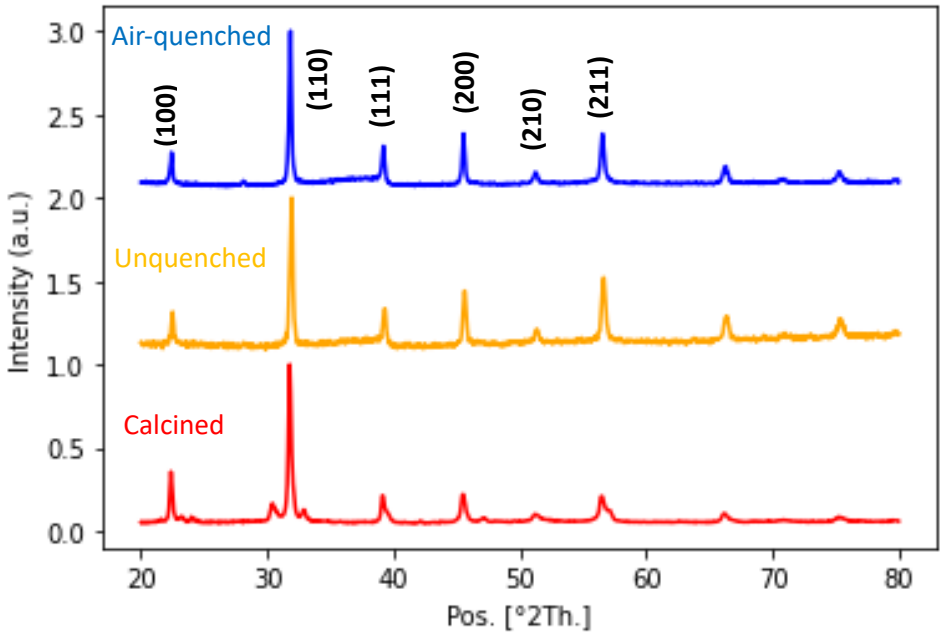

Figure 5.7: XRD pattern for BF-BT-Sm (x=0.010) depicting calcined (red), unquenched (amber) and air-quenched (blue).

5.1.4 Permittivity-Temperature Measurements

The main change made to the Permittivity-temperature measuring procedure was lowering the maximum furnace temperature to 600°C. This was done to prevent damage to the components in the tube furnace at higher temperatures, as was the fact that the theoretical T_c for BFO-BTO materials is below 500°C. Figure 5.8 shows the Permittivity-temperature graph recorded for BF-BT-Sm:

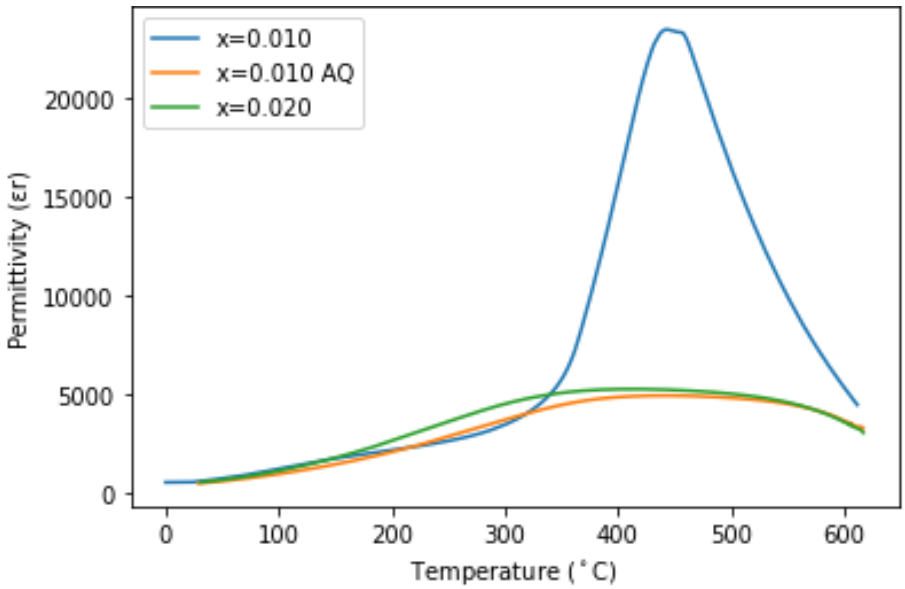

Figure 5.8: Permittivity-temperature measurement for BF-BT-Sm, measured at 1000 kHz.

From the data, T_C ≈ 433°C for the unquenched sample at x=0.010. The Perm-T graphs for the air-quenched sample and x=0.020 fail to show a significant permittivity peak, where the permittivity appears to plateau between 400-500°C. This could be due to a fault with the thermocouple as multiple runs were done with little improvement in the results.

Figure 5.9 shows the $tan\delta$ for BF-BT-Sm:

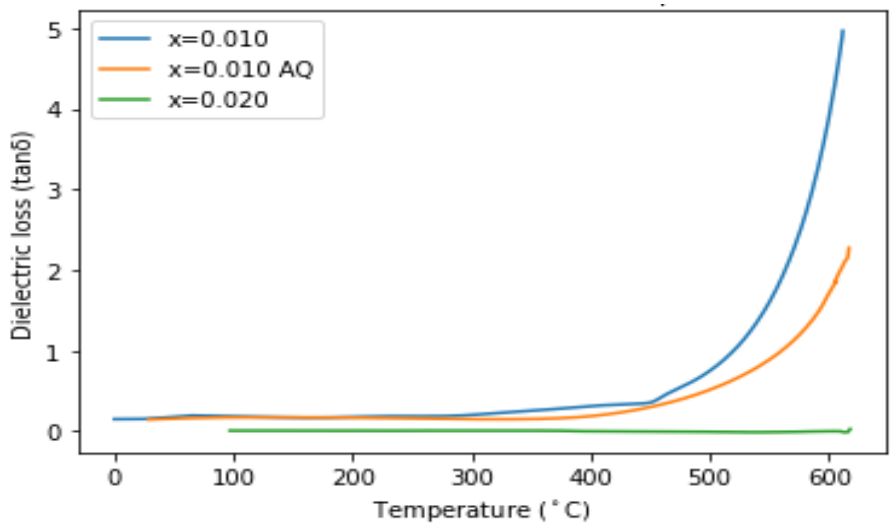

Figure 5.9: Dielectric loss - temperature measurement for BF-BT-Sm (x=0.010), also measured at 1000 kHz.

5.1.5 Polarization-Electric Field Loops

The P-E hysteresis loops for the different BF-BT-Sm samples were measured from 1000 kV/mm to 5000 kV/mm at 500 kV/mm increments. Figure 5.10 shows the P-E loops recorded at 5000 kV/mm for the different samples:

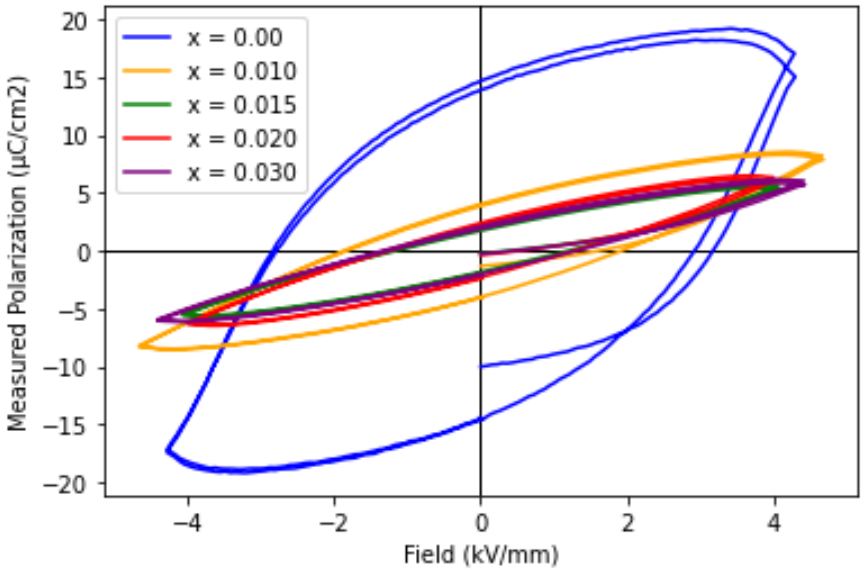

Figure 5.10: P-E Hysteresis for BF-BT-Sm (x = 0.00 - 0.03)

For better clarity, Figure 5.11 shows the same graph excluding the P-E hysteresis for undoped BF-BT (x=0.00):

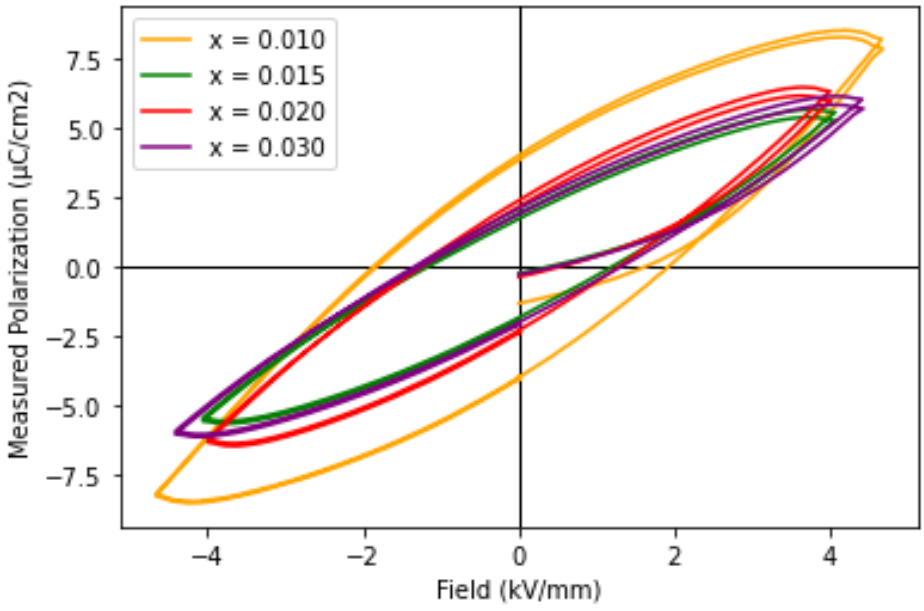

Figure 5.11: P-E Hysteresis for BF-BT-Sm (x = 0.01 - 0.03)

As seen from figure 5.10, the undoped BF-BT has an abnormally higher polarization compared to the doped samples, indicating a high number of electric dipole moments under an applied electric field. The P_{Max} of the undoped BF-BT is measured to be 17.05 µC/cm^2 and the P_R is 14.66 µC/cm^2. In contrast, the largest measured polarization for a Sm-doped sample (at x=0.010 Sm content) is 8.21 µC/cm^2 and the P_R is 4.02 µC/cm^2. Increasing the Sm-content decreases the P_{Max} and P_R along with the E_C, though between the remaining samples there seems to be little variation in the polarization coefficients.

Figure 5.12 shows the instantaneous current of the BF-BT samples as a function of electric field, suggesting the huge increase in electrical polarization is due to high conductivity:

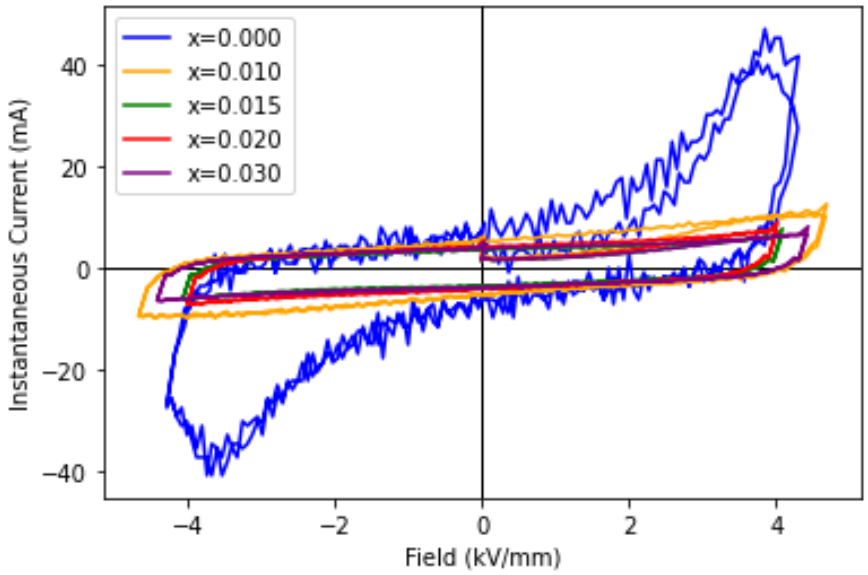

Figure 5.12: Instantaneous Current vs Field (in kV/mm) for BF-BT-Sm

And figure 5.13 shows the same graph excluding the undoped sample for better clarity:

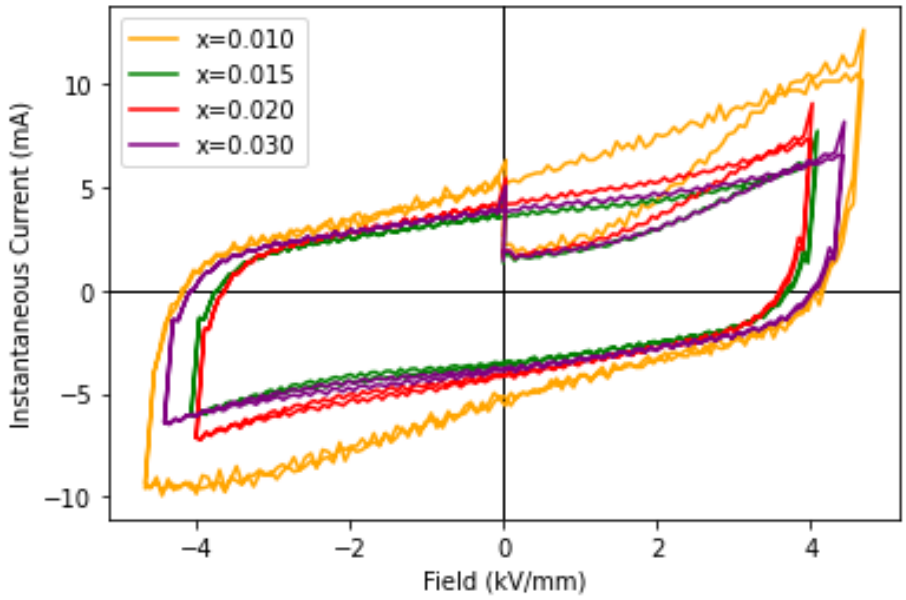

Figure 5.13: Instantaneous Current vs Field for BF-BT-Sm (x=0.01-0.03)

As seen from both graphs, all samples are shown to be ferroelectric but very conductive, as the undoped BF-BT has an instantaneous current 4 times as large as that of the Sm-doped samples.

Figure 5.14 compares the air-quenched BF-BT-Sm at x=0.010 to that of its unquenched counterpart:

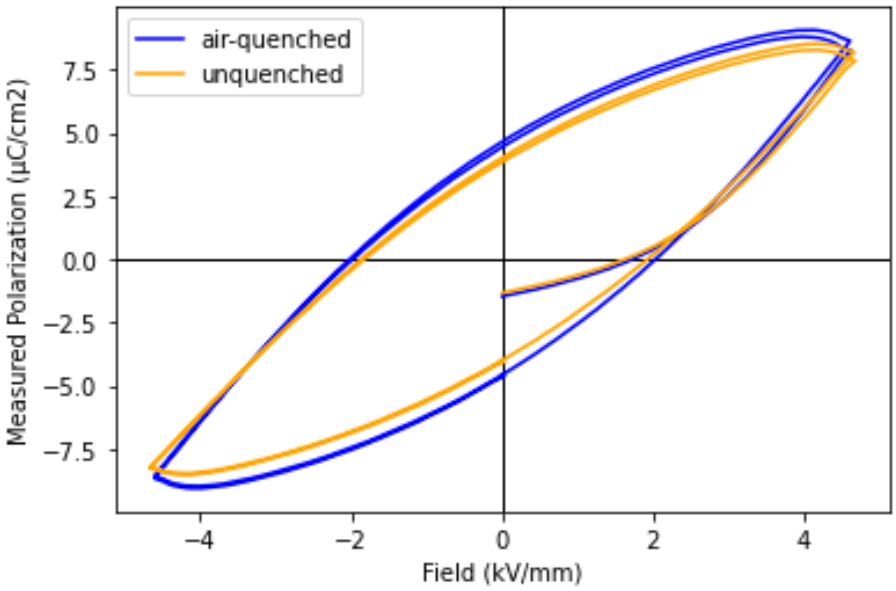

Figure 5.14: P-E loops of air-quenched vs unquenched BF-BT-Sm (x=0.01)

The instantaneous current over field for the air-quenched and unquenched samples is shown in figure 5.15:

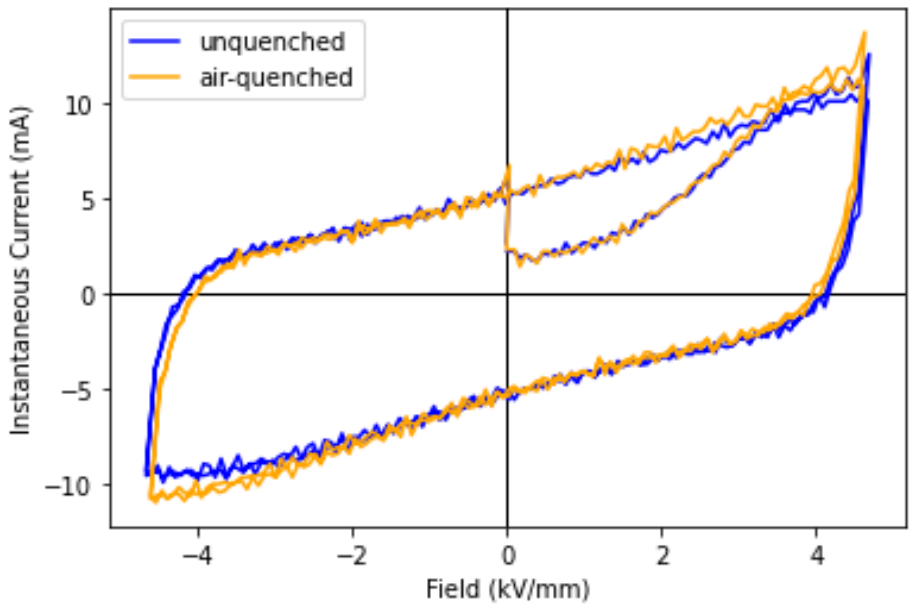

Figure 5.15: Instantaneous Current over Field, air-quenched vs unquenched.

In terms of electrical polarization, air-quenching has slightly improved the polarization values of the sample (P_{Max} = 8.655 µC/cm^2, P_R = 4.651 µC/cm^2), and the instantaneous current indicates a slightly higher conductivity than the unquenched sample.

5.1.6 Poling and Characterisation

The BF-BT-Sm samples were poled at a range of electrical polarization fields from 1 kV/mm up to 8 kV/mm at 0.5 kV/mm increments, until the sample breaks or the power supply cuts out. Each set of compositions was poled at room temperature (≈25°C) and 80°C to see how the temperature affects the piezoelectric response.

5.1.6.1 Undoped-BF-BT

No poling/piezoelectric data has been obtained for the undoped BF-BT sample, because of sample breakage at weak fields at room temperature. This is possibly due to the high leakage currents observed during poling and as predicted by the P-E loops in the previous section. It can therefore be concluded that Sm-doping has significantly reduced the leakage current by reducing the defects in the crystal structure.

5.1.6.2 BF-BT-Sm (x=0.01)

This subsection covers both the unquenched and air-quenched sets of BF-BT-Sm with 1% Sm-content. Poling studies were done for both sets to get a wide range of

values and find the relationship between piezoelectricity, field strength and processing variables.

Table 5.2 shows the poling study for unquenched BF-BT-Sm at room temperature:

Table 5.2: Poling results for unquenched BF-BT-Sm (x=0.01) at room temperature

Field (kV/mm)	d_{33} (pC/N)	$tan(\delta)$
1.0	43	0.0806
1.5	25	0.0814
2.0	39	0.0826
2.5	50	0.0845
3.0	67	0.0863
3.5	60	0.0875
4.0	85	0.0904

Table 5.3 shows the poling study for the same samples at 80°C:

Table 5.3: Poling results for unquenched BF-BT-Sm (x=0.01) at 80°C

Field (kV/mm)	d_{33} (pC/N)	$tan(\delta)$
1.0	25	0.0845
1.5	58	0.0912
2.0	63	0.0870

The samples broke at 4.5 kV/mm at room temperature and broke at 2.5 kV/mm after poling at 80°C. The maximum d_{33} achieved for the samples poled at room temperature was 85 pC/N at 4 kV/mm, and 63 pC/N at 2 kV/mm for samples poled at 80°C. However, the d_{33} for the room temperature-poled sample at 2kV/mm was 39 pC/N, which shows that poling at a higher temperature induces a stronger piezoelectric response and a higher dielectric loss.

The poling results for the air-quenched samples at room temperature are shown in Table 5.4:

Table 5.4: Poling results for air-quenched BF-BT-Sm (x=0.01) at room temperature

Field (kV/mm)	d_{33} (pC/N)	$tan(\delta)$
1.0	10	0.0923
1.5	15	0.0934
2.0	28	0.0957
2.5	41	0.0949
3.0	41	0.0924
3.5	43	0.1007
4.0	95	0.0916
4.5	92	0.0939

No data has been obtained from poling at 80°C, due to sample breakage at that temperature. The maximum d_{33} obtained from the air-quenched samples was 95 pC/N, which is 10 pC/N greater than the maximum obtained from the un-quenched samples. The $tan\delta$ dielectric loss has also increased with the air-quenched samples, likely due to greater electrical conductivity within the material, as seen in the previous section.

5.1.6.3 BF-BT-Sm (x=0.015)

Table 5.5: Poling for results for BF-BT-Sm (x=0.015) at room temperature

Field (kV/mm)	d_{33} (pC/N)	$tan(\delta)$
1.0	1	0.0731
1.5	3	0.0745
2.0	4	0.0755
2.5	5	0.0744
3.0	6	0.0753
3.5	7	0.0760
4.0	7	0.0741
4.5	9	0.0762
5.0	8	0.0745
5.5	8	0.0748
6.0	11	0.0768
6.5	13	0.0770

As seen in table 5.5, the adding of 0.5% extra Sm has significantly reduced the d_{33} coefficients, achieving a maximum of 13 pC/N after poling at 6.5 kV/mm at room temperature before sample breakage at 7.0 kV/mm.

Table 5.6: Poling results for BF-BT-Sm (x=0.015) at 80°C

Field (kV/mm)	d_{33} (pC/N)	$tan(\delta)$
5.0	6	0.0676
5.5	7	0.0671
6.0	7	0.0668

From table 5.6, increasing the poling temperature to 80°C did not induce a stronger piezoelectric response, achieving a maximum d_{33} of 7 pC/N at 6.0 kV/mm. Fields below 5.0 kV/mm are omitted due to low readings.

5.1.6.4 BF-BT-Sm (x=0.02)

Table 5.7: Poling results for BF-BT-Sm (x=0.02) at room temperature

Field (kV/mm)	d_{33} (pC/N)	$tan(\delta)$
1.0	3	0.0712
1.5	4	0.0720
2.0	4	0.0722
2.5	6	0.0714
3.0	7	0.0741
3.5	8	0.0703
4.0	8	0.0706
4.5	9	0.0711
5.0	9	0.0698
5.5	10	0.0691
6.0	12	0.0701
6.5	17	0.0704
7.0	14	0.0693
7.5	13	0.0691
8.0	16	0.0686

2% Sm-content slightly improved the d_{33} compared to 1.5% Sm-content (17 pC/N at 6.5 kV/mm at room temperature as seen in table 5.9) but is still significantly lower compared to 1% Sm-content. Poling at 80°C only produced a maximum of 13 pC/N at 6.5 kV/mm (table 5.8).

Table 5.8: Poling results for BF-BT-Sm (x=0.02) at 80°C

Field (kV/mm)	d_{33} (pC/N)	$tan(\delta)$
6.0	12	0.0691
6.5	13	0.0687

5.1.6.5 BF-BT-Sm (x=0.03)

Table 5.9: Poling results for BF-BT-Sm (x=0.03) at room temperature

Field (kV/mm)	d_{33} (pC/N)	$tan(\delta)$
1.0	3	0.0709
1.5	3	0.0706
2.0	4	0.0714
2.5	5	0.0711
3.0	5	0.0709
3.5	5	0.0715
4.0	6	0.0724
4.5	7	0.0711
5.0	7	0.0727
5.5	8	0.0716
6.0	8	0.0731
6.5	7	0.0718

BF-BT-Sm (x=0.03) has the lowest average piezoelectric performance of all the compositions, producing a maximum of 8 pC/N (at 5.5 kV/mm for room temperature and 4.5 kV/mm for 80°C).

Table 5.10: Poling results for BF-BT-Sm (x=0.03) at 80°C

Field (kV/mm)	d_{33} (pC/N)	$tan(\delta)$
4.0	6	0.0668
4.5	8	0.0720
5.0	5	0.0662

5.1.7 Discussion and Conclusion

Figure 5.16 shows a graph depicting the overall trend between Sm-content and d_{33} performance:

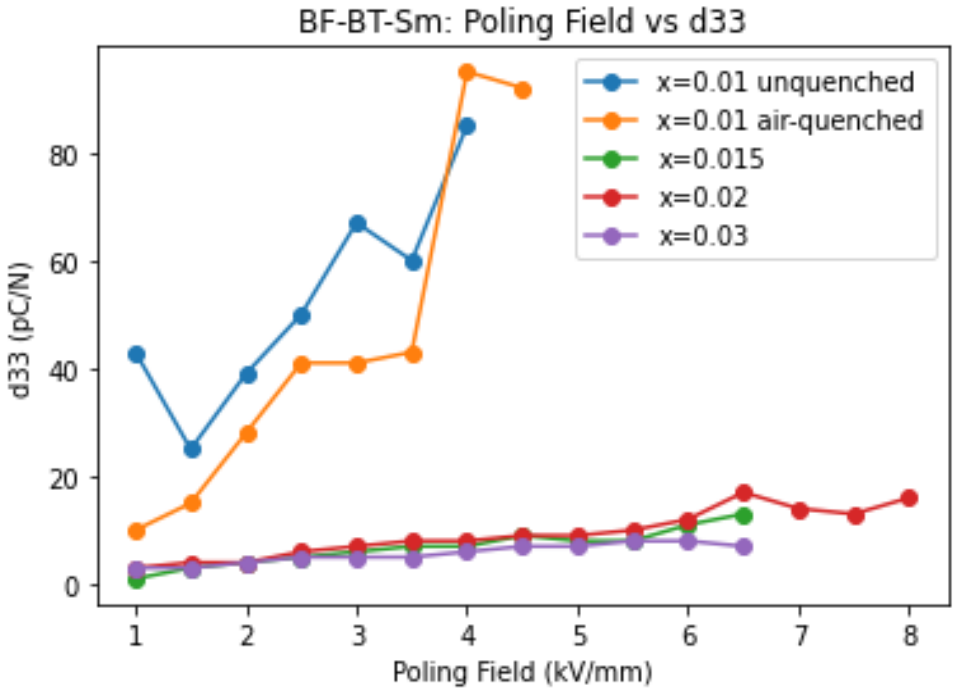

Figure 5.1: Overall poling study of BF-BT-Sm compositions.

Overall, a lower amount of Sm-dopant contributes to a higher d_{33} coefficient, although compositions with a higher amount of Sm-content can withstand stronger electric fields. Air-quenching has produced a higher maximum d_{33} compared to its unquenched counterpart, however the d_{33} for the air-quenched samples is lower at weaker fields. The obtained d_{33} values however are significantly lower than the ones obtained by Habib et al., where the maximum they obtained was 334 pC/N, which is more than 300% of the value obtained here (95 pC/N). The T_C reached by Habib et al. was also higher at approximately 454°C (compared to 433°C) [62], despite using the same solid-state sintering method that Habib et al. used. Air-quenching has also not improved the performance of the sample by much and seems to make the sample more fragile as poling at 80°C immediately broke the samples. Although the sample tested by Habib et al. was water-quenched, the lack of a significant increase in piezoelectric activity from air-quenching suggests that water-quenching may not make a noticeable improvement in piezoelectric performance.

The Sm-dopant seems to have decreased the conductivity of the BF-BT composition from the undoped variant, however the conductivity and dielectric loss remains very high and therefore causes the piezoelectric performance to be significantly lower than expected. It is possible that due to the reduction in conductivity from Sm-doping the BF-BT sample that oxygen vacancy reduction is a significant defect mechanism present in the process as demonstrated below:

$$Sm_2O_3 \overset{BaTiO_3}{\longleftrightarrow} 2Sm_{Ba}^{\bullet} + V_{Ba}'' + 3O_O^x \tag{69}$$

$$Sm_2O_3 + V_O^{\bullet\bullet} \overset{BaTiO_3}{\longleftrightarrow} 2Sm_{Ba}^{\bullet} + 3O_O^x \tag{70}$$

As the conductivity is shown to have decreased upon Sm-doping, this indicates that hole or oxygen vacancy reduction is likely the dominant mechanism. Equations (69) and (70) show that oxygen vacancy formation in $BaTiO_3$ is inhibited by the introduction of Sm_2O_3.

This investigation therefore suggests that Sm-doping BF-BT may not be the best solution to make the material suitable for transducer applications, and calls into question the credibility of various scientific articles citing high d_{33} coefficients from Sm-doped BF-BT. Whilst Sm-doping needs to be further investigated, other dopants may prove to be better to work with and may, in practice, prove to be better alternatives for engineering applications.

5.2 Mn-doped BF-BT

In this section, the effects of Mn-doping on different perovskite B-sites are investigated. For this reason, two different formulas are compared to one another. A composition prepared by Kim et al. (2013): $0.67Bi(Fe_{1-x}Mn_x)O_3$-$0.33BaTiO_3$ is used as a platform to investigate the effects of Mn-doping on the Fe-site [68]. The maximum d_{33} obtained by Kim et al. was 135 pC/N with 1% (x=0.01) Mn-content.

For the Ti-site, the formula $0.67BiFeO_3$-$0.33Ba(Ti_{1-x}Mn_x)O_3$, based on one prepared by Jabeen et al. (2022), is investigated [70]. The d_{33} as quoted in the literature reached a maximum of 128 pC/N at x=0.01. For each formula, samples containing x=0.01, x=0.02, x=0.03 and x=0.04 Mn-content are prepared and tested. To ensure a more thorough comparison between doping on the Fe-site and Ti-site atoms, the mass of the MnO_2 remains the same for each x value.

5.2.1 Sample Synthesis

The stoichiometry for both the Fe-site and Ti-site doped compositions is given in tables 5.11 and 5.12 respectively:

Table 5.11: Stoichiometry for BF-BT-Mn (Fe-site doped)

Material	Molar Mass (g/mol)	Weight Used (g) (x=0.010)	Weight Used (g) (x=0.020)	Weight Used (g) (x=0.030)	Weight Used (g) (x=0.040)
Bi_2O_3	465.96	28.224	27.224	28.224	27.224
Fe_2O_3	159.69	9.576	9.524	9.382	9.329
$BaCO_3$	197.34	10.245	10.245	10.245	10.245
TiO_2	79.866	4.146	4.146	4.146	4.146
MnO_2	86.937	0.053	0.105	0.158	0.211

Table 5.12: Stoichiometry for BF-BT-Mn (Ti-site doped)

Material	Molar Mass (g/mol)	Weight Used (g) (x=0.010)	Weight Used (g) (x=0.020)	Weight Used (g) (x=0.030)	Weight Used (g) (x=0.040)
Bi_2O_3	465.96	28.216	28.216	28.216	28.216
Fe_2O_3	159.69	9.670	9.670	9.670	9.670
$BaCO_3$	197.34	10.243	10.342	10.243	10.243
TiO_2	79.866	4.096	4.074	3.998	3.949
MnO_2	86.937	0.053	0.105	0.158	0.211

The calcination and sintering programs used for these compositions were the same ones used for the BF-BT-Sm materials (calcining temperature at 750^{o}C and sintering temperature at 1000^{o}C). The air-quenching regime used for BF-BT-Mn is exactly the same one used for BF-BT-Sm (sinter for 1 hour in conventional furnace at 1000^{o}C, and for 1 hour at the same temperature in a tube furnace before removing and allowing it to fast cool at room temperature). Water-quenching used the same regime as air-quenching, except the fast cooling was done by dropping the pellets from the tube furnace into a water container.

5.2.2 SEM Results

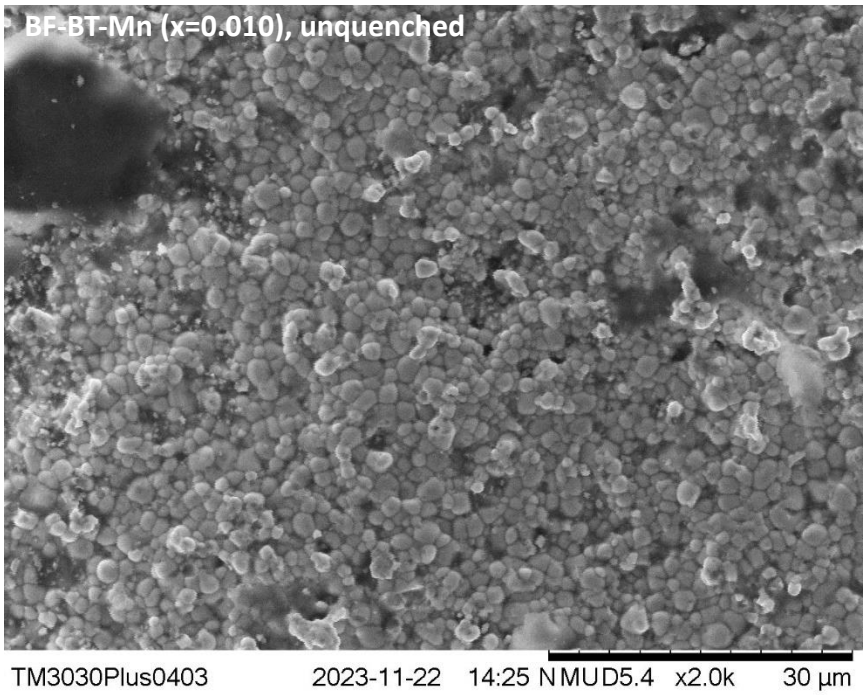

Figure 5.17: SEM image of unquenched BF-BT-Mn (Fe-site) at x=0.010

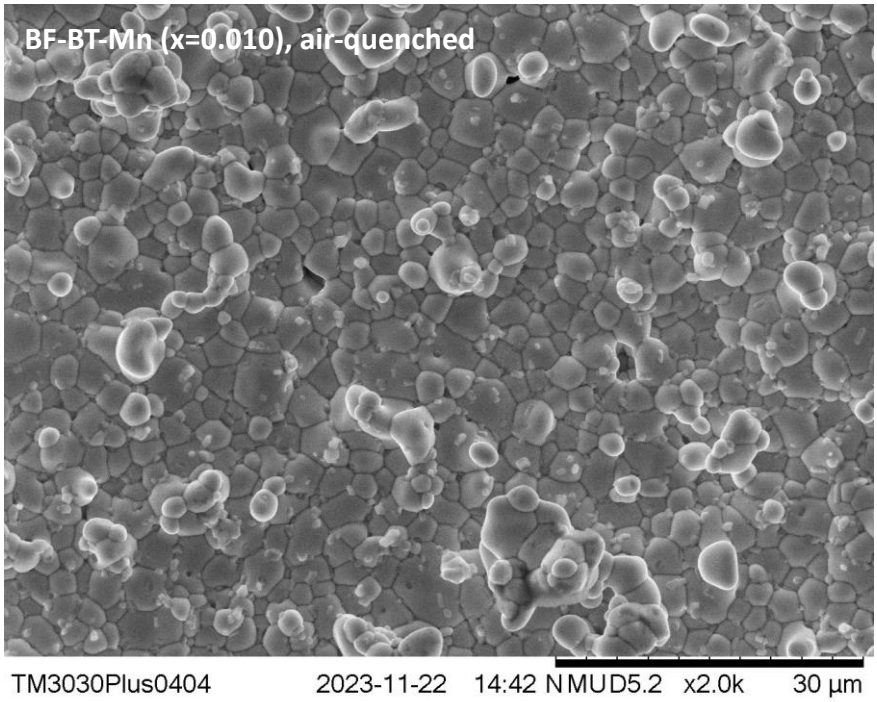

Figure 5.18: SEM image of air-quenched BF-BT-Mn (Fe-site) at x=0.010

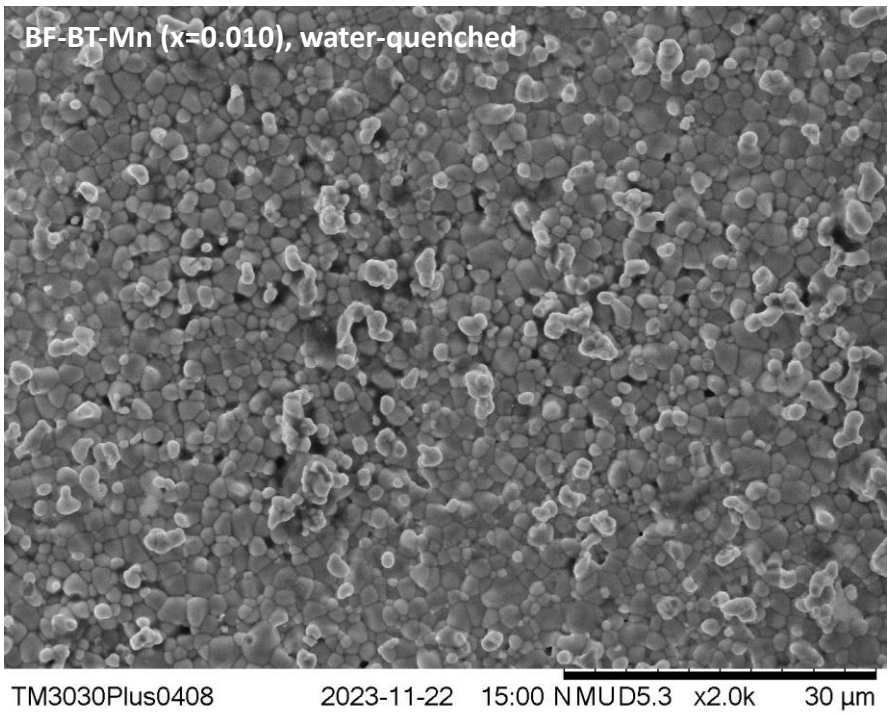

Figure 5.19: SEM image of water-quenched BF-BT-Mn (Fe-site) at x=0.010

All of the SEM images in figures 5.17, 5.18, and 5.19 are of the Fe-site doped samples at x=0.010, and are comparisons between the unquenched, air-quenched and water-quenched samples to show the effects on the microstructures.

From figure 5.18, the air-quenched sample has the largest grains in comparison to the other two samples, with an average grain size of approximately 3µm. This could also be due to the double-sintering regime for the quenching process, causing the pellet to densify twice (as is the case with the air-quenched BF-BT-Sm samples). However, the water-quenched sample in figure 5.19 shows a microstructure with grain sizes similar to the ones for the unquenched sample in figure 5.17 (approximately 1µm). The air-quenched sample also has significantly fewer defects compared to the unquenched sample, where one defect (as seen in figure 5.17) is approximately 20µm wide. The water-quenched sample in figure 5.19 is shown to have several smaller defects scattered around the microstructure (approximately 1µm wide on average), suggesting water-quenching likely produces breakages in the microstructure due to the faster-cooling rate compared to air-quenching.

5.2.3 XRD Results

Figures 5.20 and 5.21 show the XRD patterns for both $0.67Bi(Fe_{1-x}Mn_x)O_3$-$0.33BaTiO_3$ and $0.67BiFeO_3$-$0.33Ba(Ti_{1-x}Mn_x)O_3$ respectively:

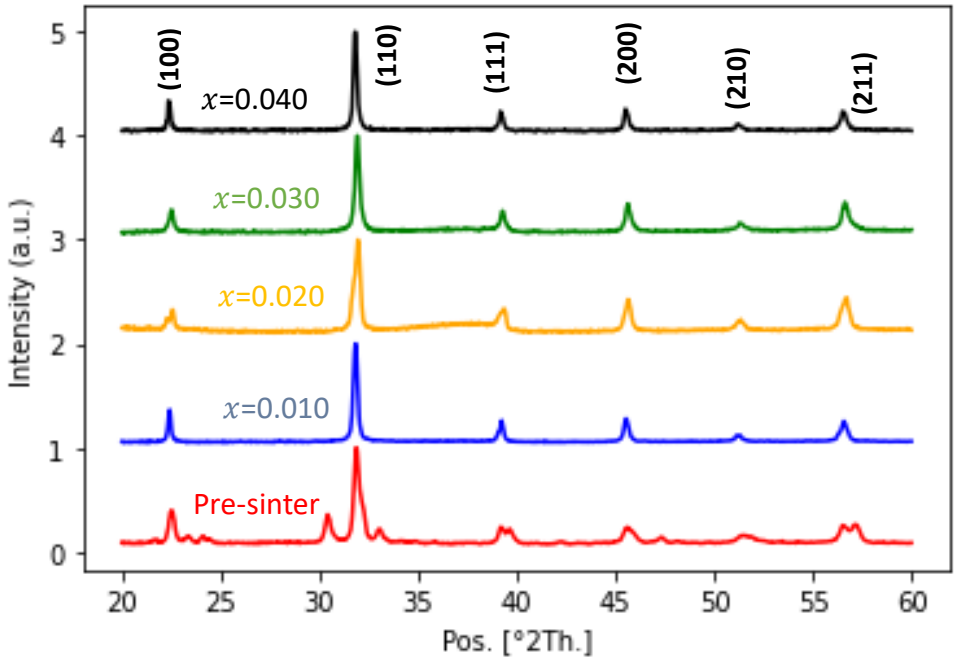

Figure 5.20: XRD pattern for BF-BT-Mn (Fe-site)

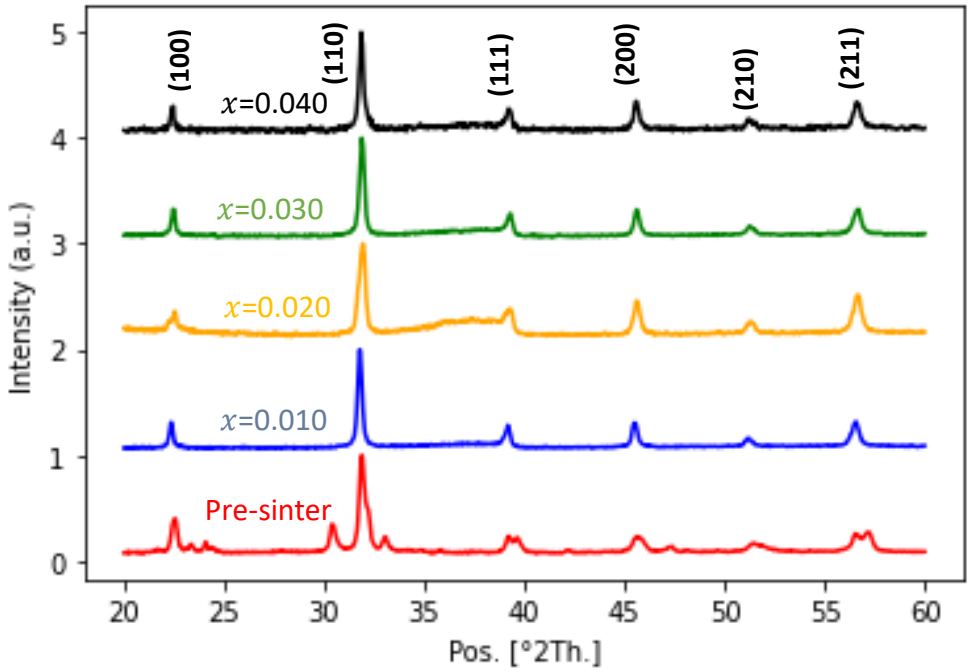

Figure 5.21: XRD pattern for BF-BT-Mn (Ti-site)

Both XRD patterns reveal pure perovskite structures, and the pre-sintered patterns for both formulas reveal phase changes as evidenced by the peak splitting. At the (110) peak at 2θ=32° the phase seems to change from orthorhombic to cubic

during sintering, and the (111) peak at 2θ=39° seems to change from orthorhombic to cubic or tetragonal. For both formulas, the (100) peak at 2θ=23° for the x=0.020 samples seems to be undergoing a phase change, as shown in figure 5.22:

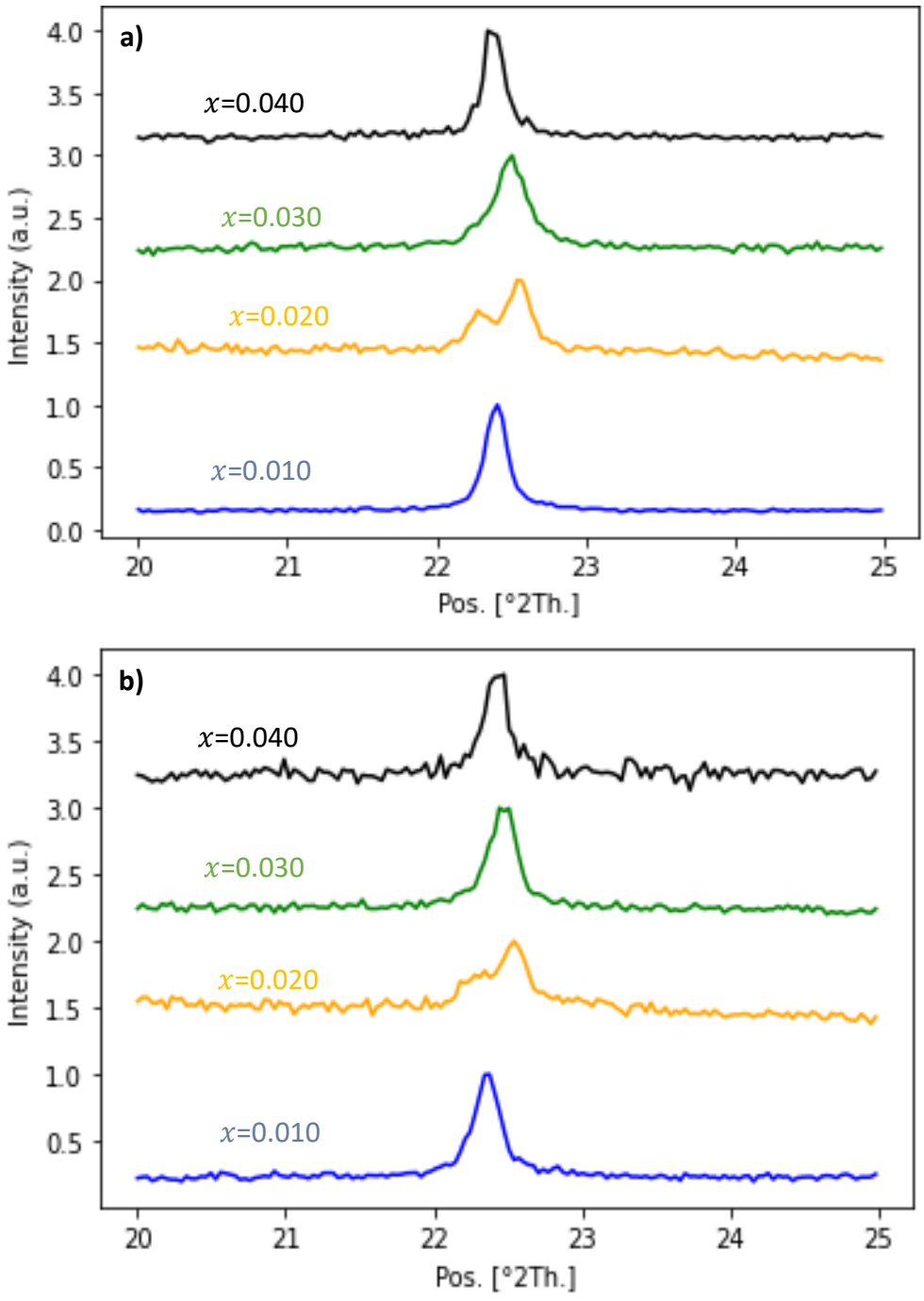

Figure 5.22: The (100) peak for the Fe-site, a), and Ti-site, b)

At x=0.020 for the Fe-site doped material, the (100) peak splits into 2 clear peaks and is then reverted to one peak at x=0.030. It seems to switch to a tetragonal phase when 2% Mn-dopant is added. For the Ti-site doped sample, the secondary peak seems to be flatter than the one for the Fe-site doped sample, though this

could be due to the powder distribution in the sample holder. Overall, the peak positions shift to a slightly higher angle with increasing Mn-content due to the decreasing unit cell volume.

5.2.4 Permittivity vs Temperature measurements

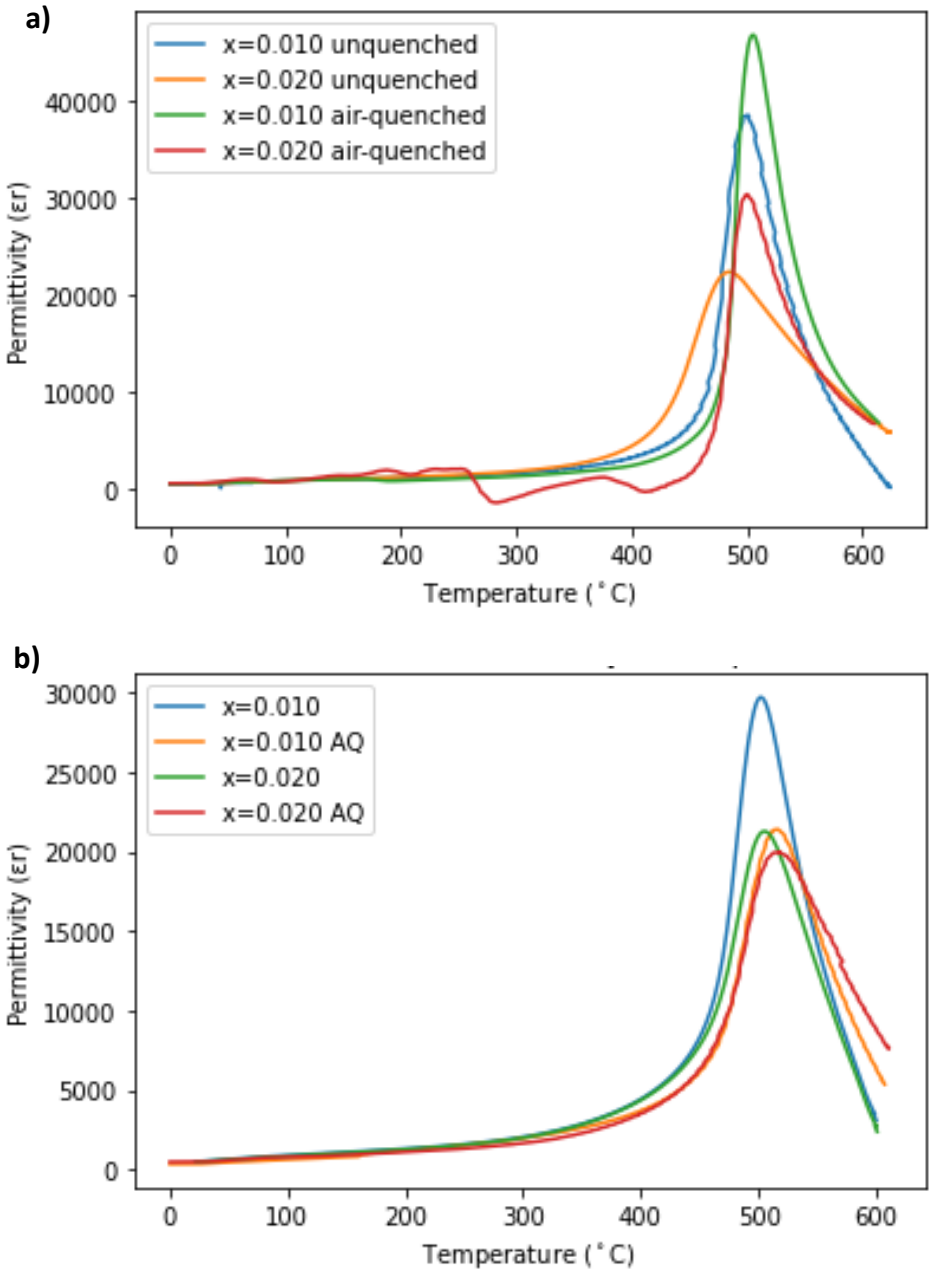

Figure 5.23: Permittivity vs Temperature for BF-BT-Mn. (a): Fe-site, b): Ti-site)

In Figure 5.23, the T_C for the Fe-site doped BF-BT-Mn obtained is 499°C at both x=0.010 and x=0.020, though the recorded maximum permittivity is higher at x=0.010. For the samples doped on the Ti-site atom, the recorded T_C is 517°C at both x=0.010 and x=0.020, though the permittivity is lower than the Fe-site doped samples.

Figure 5.24 shows the dielectric loss ($tan\delta$) against temperature for both Fe-site and Ti-site doped samples:

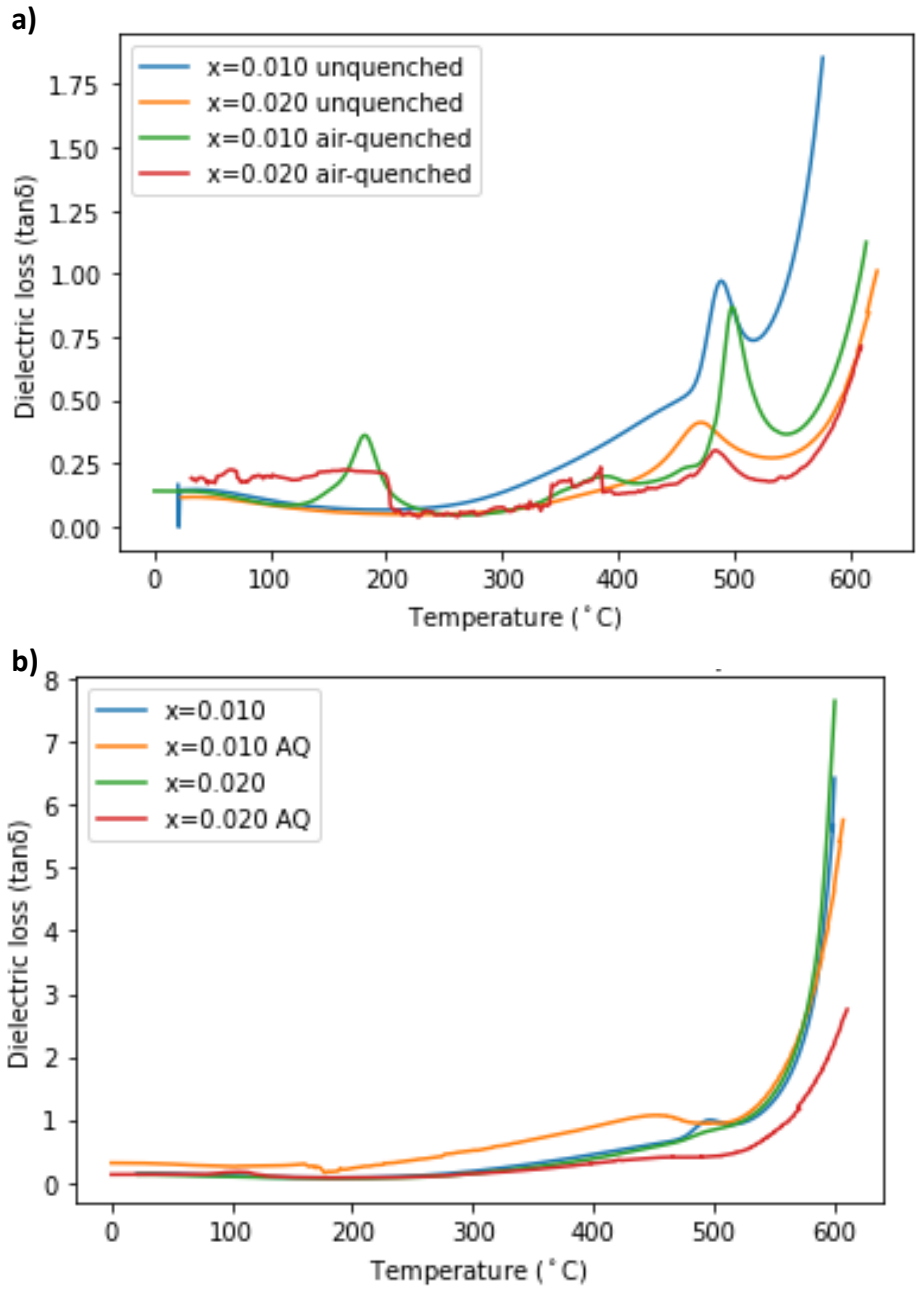

Figure 5.2: Dielectric temperature vs temperature for BF-BT-Mn. a): Fe-site, b): Ti-site

For both sets of samples, the $tan\delta$ peaks at the Curie point in sync with the Permittivity-temperature graphs, before decreasing again and rapidly increasing at around 550°C. The rate of dielectric loss for the Ti-site doped samples is significantly higher than the Fe-site doped samples past 550°C, indicating that Ti-site doping results in significantly higher losses than the latter. The air-quenched Fe-site doped sample at x=0.010 produces a few peaks throughout the plot, possibly due to short circuiting on the contacts in the tube furnace, rather than an

indication of phase changes (the Permittivity-temperature graph in figure 5.23 shows no extra peaks). The air-quenched sample at x=0.020 in the same graph shows a rough plot, which is likely due to noise recorded by the analyser.

5.2.5 Polarization-Electric Field

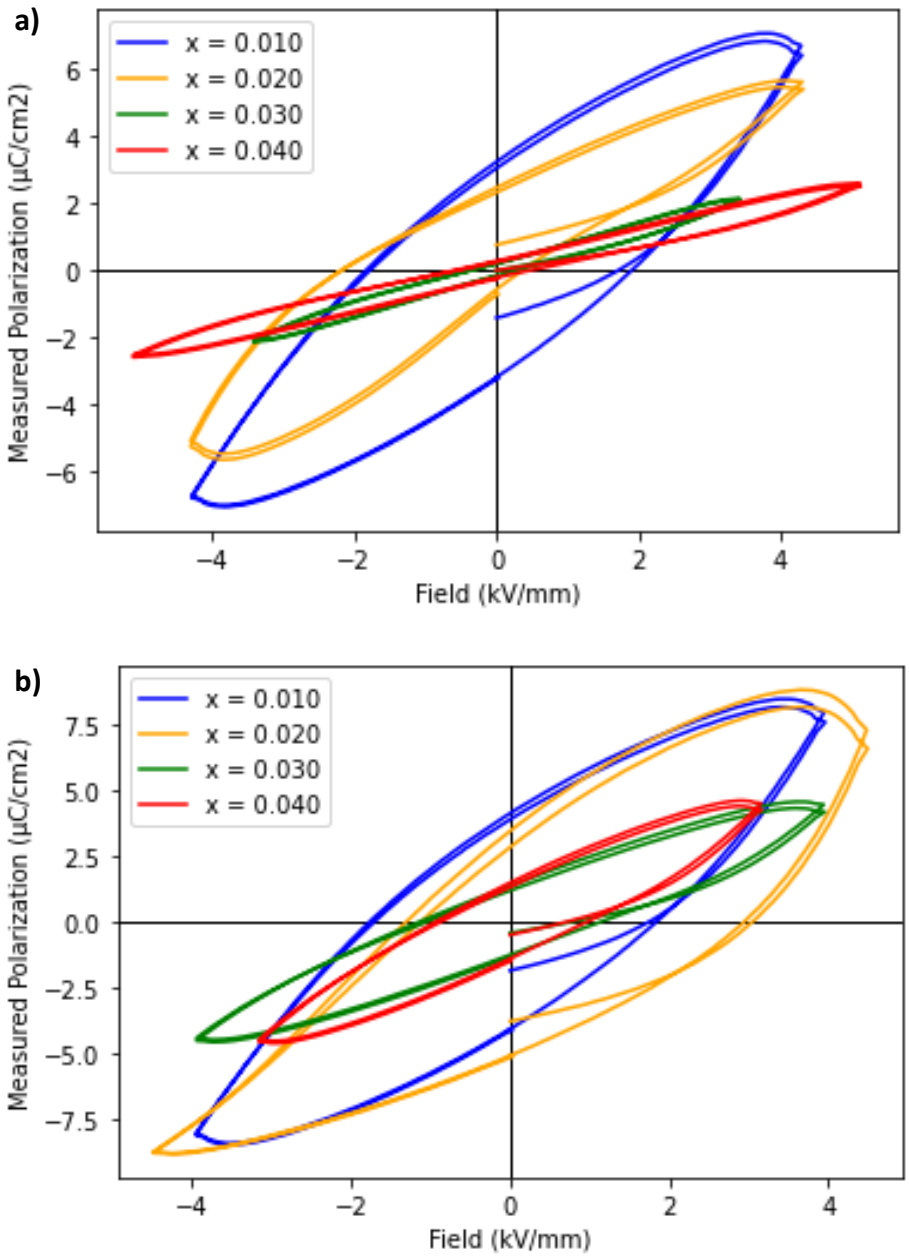

Figure 5.25: P-E hysteresis loops for BF-BT-Mn from x=0.010 to 0.040. a): Fe-site, b): Ti-site

The hysteresis loops as depicted in figure 5.25 show a general trend in greater polarization over increasing electrical fields with decreasing Mn content for the Fe-site doped samples (top). However, for the Ti-site doped samples the polarization range seems to be greater for x=0.020 Mn-content compared to x=0.010, indicating higher conductivity. This is shown in figure 5.26:

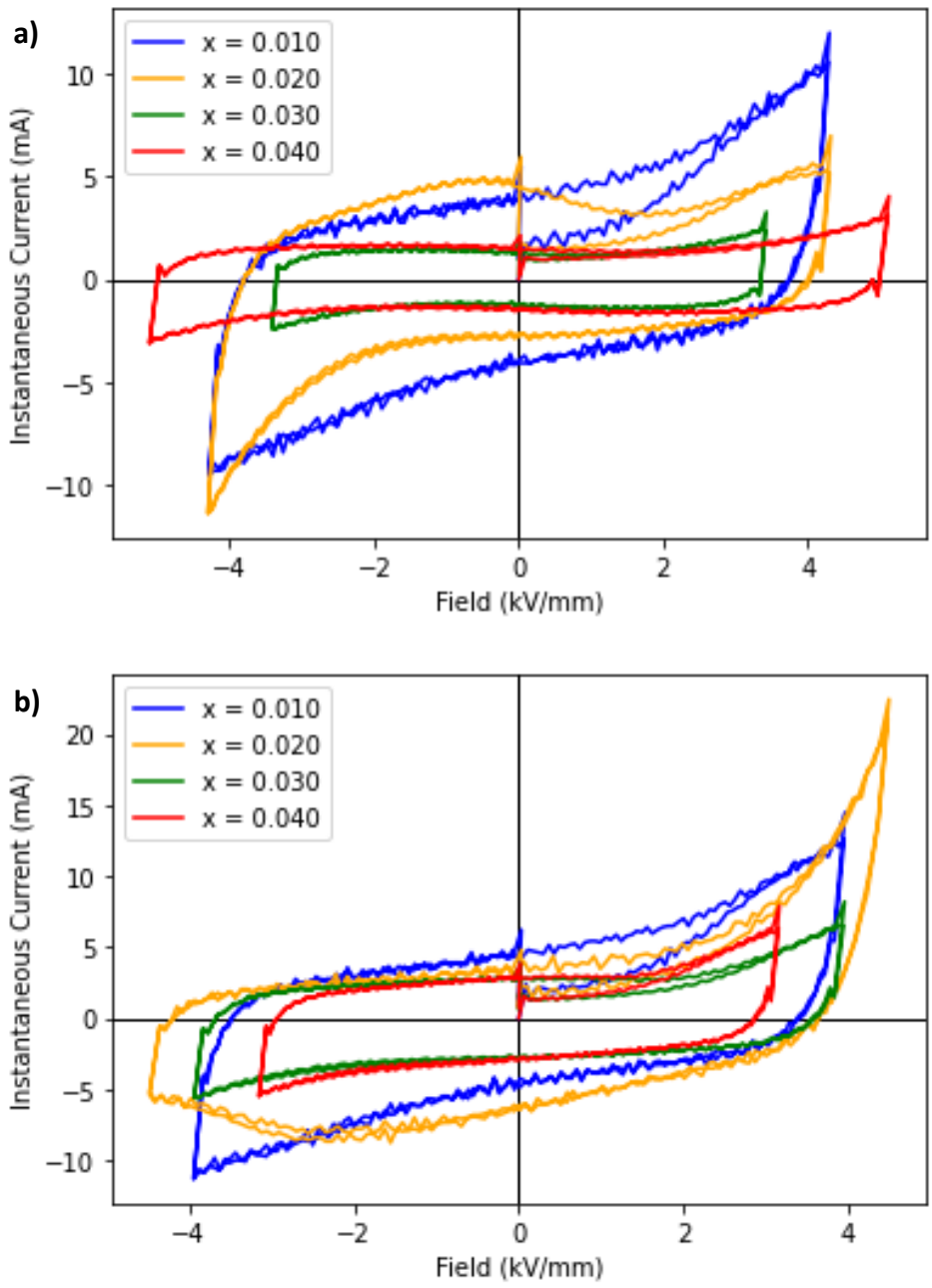

Figure 5.3: Instantaneous current over electric field for BF-BT-Mn. a): Fe-site, b): Ti-site

Towards the right of the bottom graph, the conductivity for x=0.020 in terms of the instantaneous current is considerably higher than that of x=0.010.

Figure 5.27 compares the P-E hysteresis between unquenched and air-quenched samples:

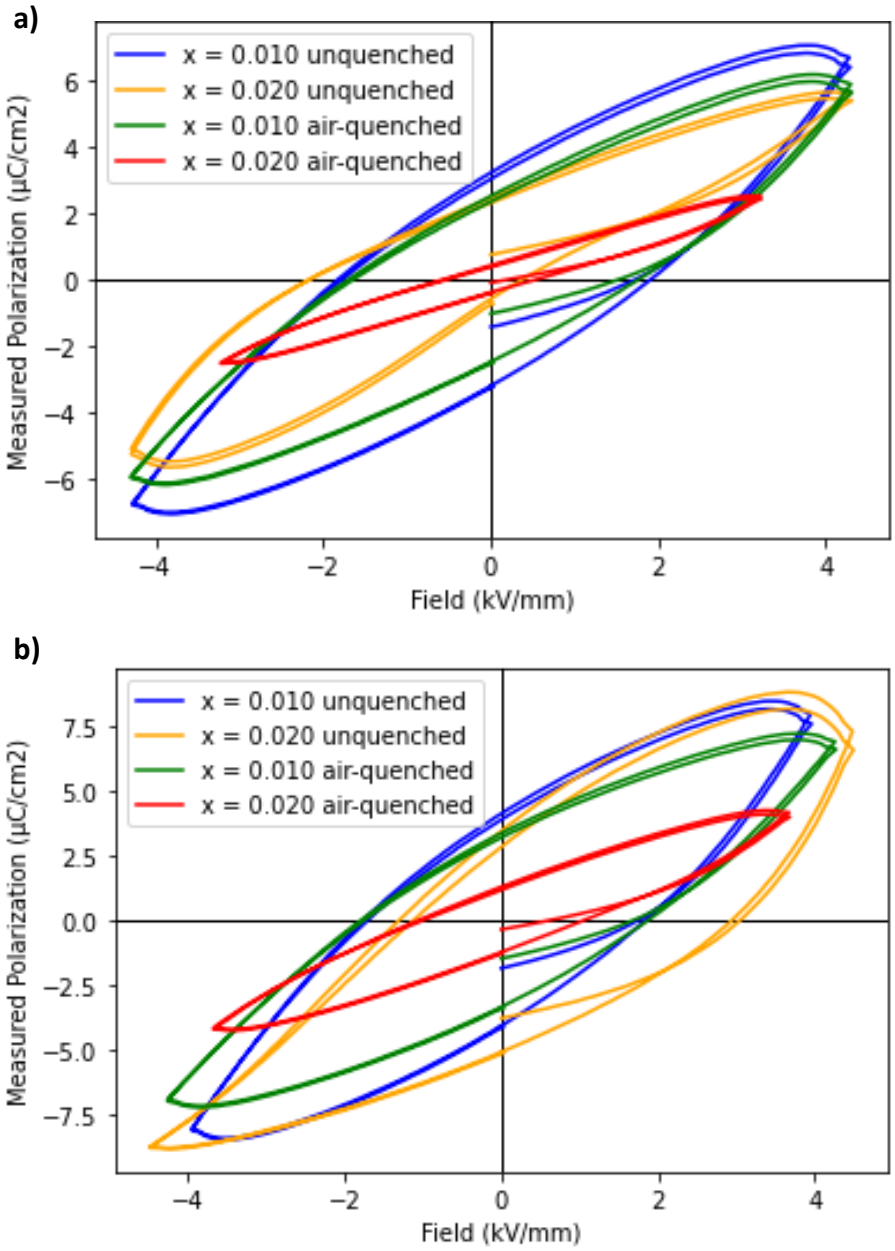

Figure 5.27: P-E hysteresis between unquenched and air-quenched BF-BT-Mn. a): Fe-site, b): Ti-site

The air-quenched samples have a lower maximum polarization compared to their unquenched counterparts, possibly due to the reduction in defects which prevents leakage current from occurring. The difference between the air-quenched/unquenched samples at x=0.020 Mn-content is significantly greater than the samples at x=0.010 for both Fe-site and Ti-site doping.

Tables 5.13 and 5.14 show the polarization coefficients for all of the samples:

Table 5.13: Polarization coefficients for BF-BT-Mn (Fe-site) samples at 5kV

BF-BT-Mn (Fe-site)

x	P_{Max} (μC/cm²)	P_R (μC/cm²)	E_C (kV/mm)
0.01	6.677	3.209	1.907
0.01 (AQ)	5.876	2.513	1.763
0.02	5.601	2.451	2.17
0.02 (AQ)	2.522	0.43	0.5345
0.03	2.134	0.191	0.34
0.04	2.591	0.265	0.482

Table 5.14: Polarization coefficients for BF-BT-Mn (Ti-site) samples at 5kV.

BF-BT-Mn (Ti-site)

x	P_{Max} (μC/cm²)	P_R (μC/cm²)	E_C (kV/mm)
0.01	7.965	4.112	2.078
0.01 (AQ)	6.899	3.361	1.873
0.02	7.295	3.444	2.941
0.02 (AQ)	4.169	1.292	1.056
0.03	4.453	1.372	1.133
0.04	4.504	1.483	1.22

The Ti-site doped samples possess significantly higher maximum-polarization coefficients than the Fe-site doped samples, along with greater remnant polarization and coercive electric fields.

5.2.6 Poling Study and d_{33} coefficients

Poling studies were carried out for each sample, with poling rounds done for each composition at room temperature and at 80°C. Each composition had 8 pellets produced for poling, which were initially poled at room temperature and each pellet was poled at a specific field starting at 1.0 kV/mm and increasing at 0.5 kV/mm increments until sample breakage or the circuit tripping. Pellets were re-poled if necessary. The Berlincourt measurements are then carried out 24 hours after being poled. The process is then repeated for measurements at 80°C using the same pellets.

The full tables can be found in the supplemental material in the appendix, but the following figures and tables list the maximum d_{33} values of each sample and their respective $tan\delta$ and capacitances:

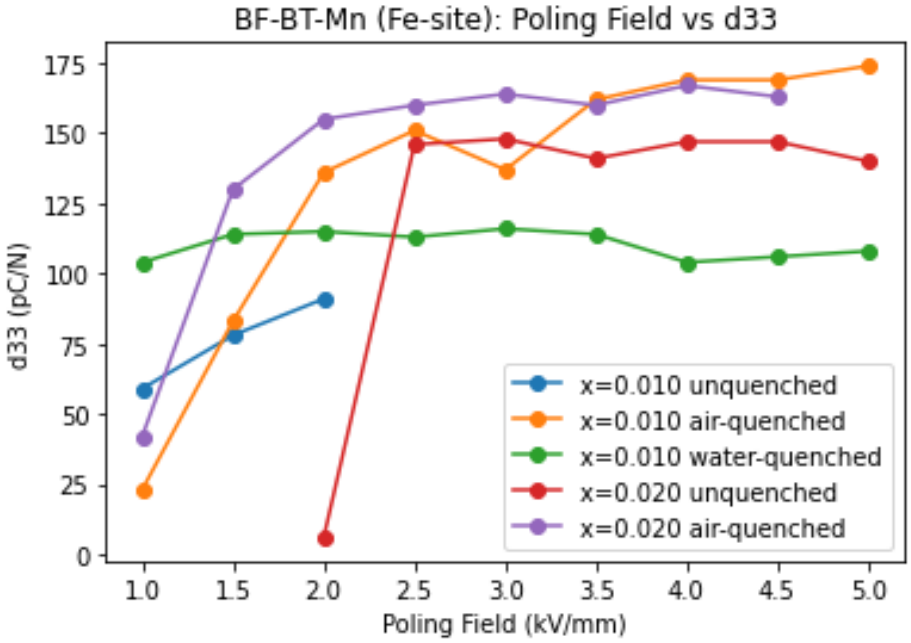

Figure 5.28: d_{33} coefficients vs Poling field (kV/mm) for BF-BT-Mn (Fe-site)

Table 5.15: d_{33} coefficients, capacitance and $tan\delta$ dielectric loss for BF-BT-Mn (Fe-site)

x	d_{33} (pC/N)	$tan(\delta)$
0.01	91	0.0534
0.01 (AQ)	174	0.0398
0.01 (WQ)	114	0.063
0.02	148	0.0357
0.02 (AQ)	167	0.0319
0.03	72	0.035
0.04	10	0.0381

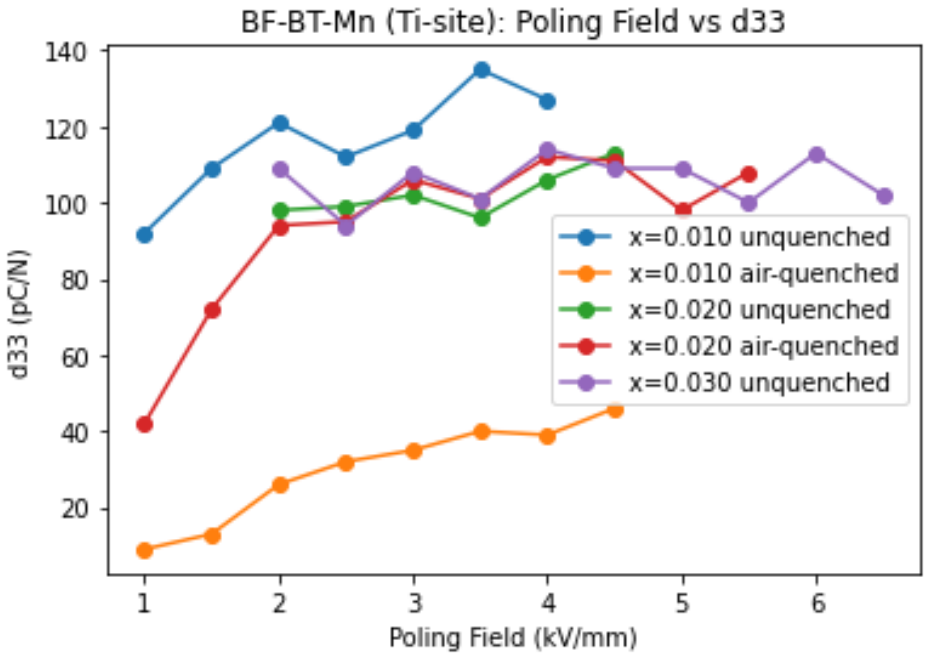

Figure 5.29: d_{33} vs Poling field for BF-BT-Mn (Ti-site)

Table 5.16: d_{33} coefficients, capacitance and $tan\delta$ dielectric loss for BF-BT-Mn (Ti-site)

x	d_{33} (pC/N)	$tan(\delta)$
0.01	135	0.049
0.01 (AQ)	46	0.068
0.02	113	0.0471
0.02 (AQ)	112	0.0405
0.03	114	0.0389
0.04	63	0.0429

The highest d_{33} achieved was 174 pC/N for the air-quenched Fe-site with 1% Mn-content. Air-quenching has massively improved the performances of the Fe-site samples, whilst the opposite is true for the Ti-site samples. This could be due to structural breakage resulting from the air-quenching process, leading to more leakage current as suggested by the dramatic drop in d_{33} found in table 5.16 at x=0.01, which corresponds to an increase in $tan\delta$ dielectric loss. In general, Fe-site doping has produced a lower dielectric loss than Ti-site doped whilst also having significantly higher d_{33} coefficients at lower Mn-content. The only exceptions are the unquenched and water-quenched samples at x=0.01, as seen in table 5.15, due to their low d_{33} coefficients coupled with their high $tan\delta$ values.

5.3 Co-doped BF-BT (Mn and Sm)

After seeing the effects of Mn and Sm doping on BF-BT ceramics, in this section the effects of co-doping BF-BT samples by using Mn-dopant on the Fe-site, and Sm-dopant on the Ba-site. Using co-doping on different sites could produce significantly more electron vacancies which in turn should theoretically improve the d_{33} and other piezoelectric values.

The formula used to examine the performance of Mn and Sm-doped BF-BT is a combination of the formulas used by Kim et al. and Habib et al. [62] [68]: $0.7Bi(Fe_{1-x}Mn_x)O_3$-$0.3(Ba_{1-y}Sm_y)TiO_3$. For the Mn-doped site, the amount of Mn-content ranged from x=0.01 to 0.02, whereas the Sm-content remained the same at y=0.01.

5.3.1 Sample synthesis

Table 5.17: Stoichiometry of BF-BT-Mn-Sm

Material	Molar Mass (g/mol)	Weight Used (g) (x=0.010, y=0.010)	Weight Used (g) (x=0.020, x=0.010)
Bi_2O_3	465.96	28.219	28.219
Fe_2O_3	159.69	9.530	9.477
$BaCO_3$	197.34	10.141	10.141
TiO_2	79.866	4.146	4.146
MnO_2	86.937	0.053	0.105
Sm_2O_3	348.72	0.091	0.091

The material synthesis for BF-BT-Mn-Sm is exactly the same as the one used for all previous BF-BT samples. Slow-cooling, air and water quenching processes are also used and remain the same as before too.

5.3.2 SEM Results

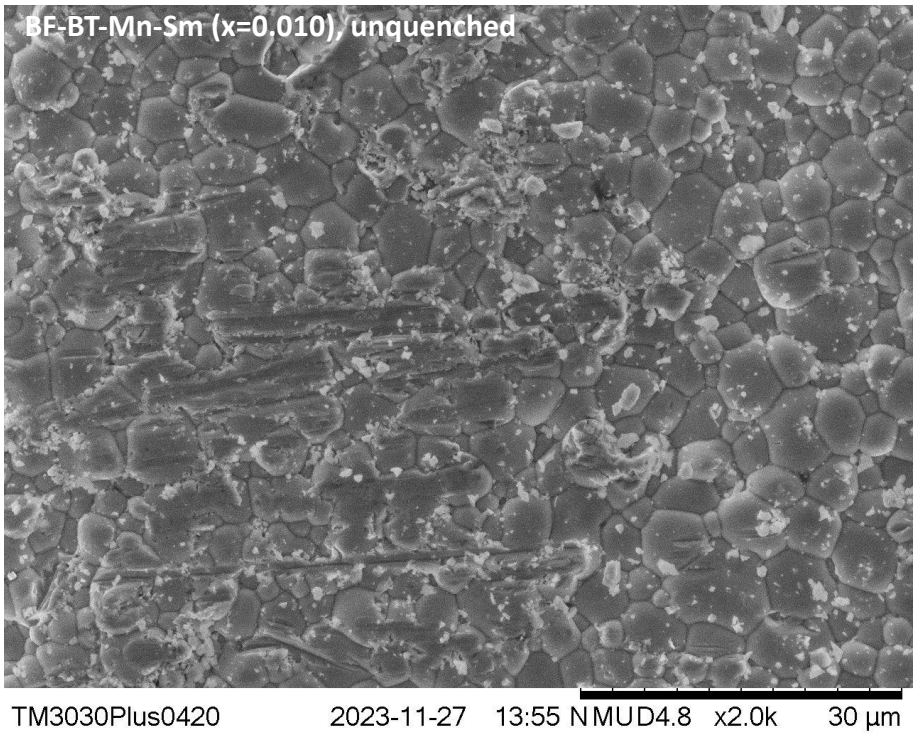

Figure 5.30: SEM image of unquenched BF-BT-Mn-Sm (x and y =0.010)

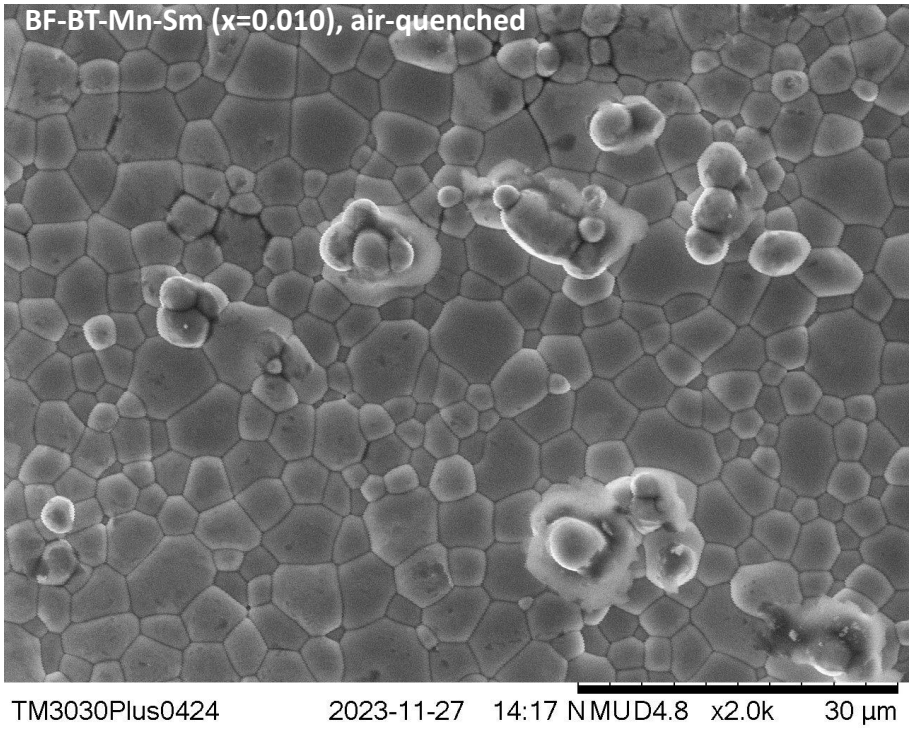

Figure 5.31: SEM image of air-quenched BF-BT-Mn-Sm (x and y =0.010)

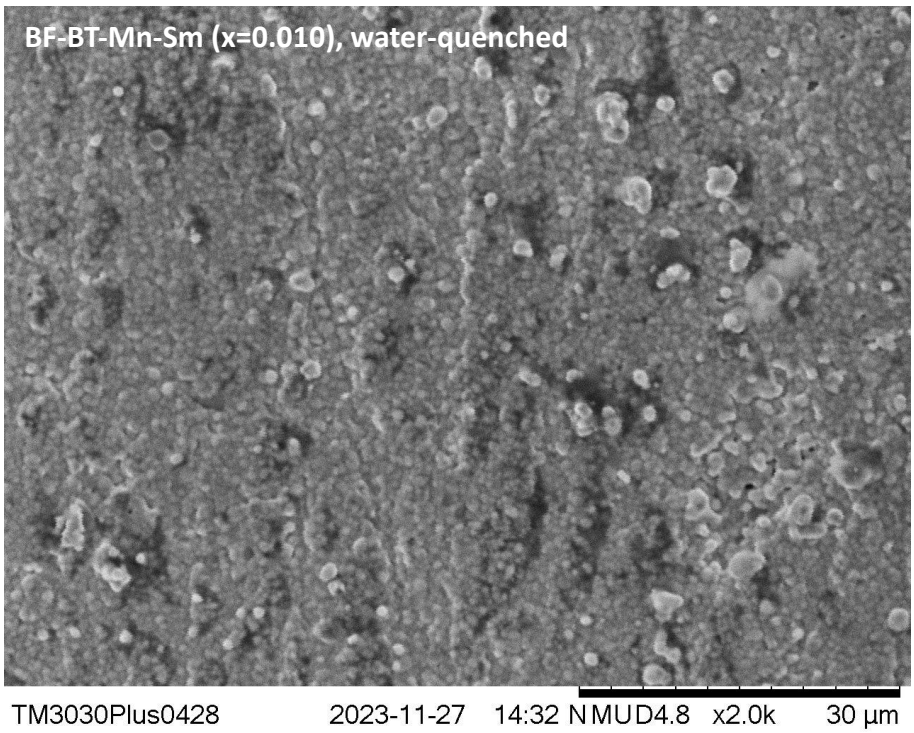

Figure 5.32: SEM image of water-quenched BF-BT-Mn-Sm (x and y = 0.010)

The SEM image of the unquenched BF-BT-Mn-Sm sample in figure 5.30 suggests the presence of impurities in its microstructure, as evidenced by the amount of brightly coloured streaks in the image. However, it can be seen that the grain sizes of the composition are approximately 5-6µm in diameter, with few significant defects found in the microstructure. The SEM of the air-quenched samples microstructure (figure 5.31) shows a clearer image, with similarly sized grains to the unquenched sample. Again, no significant defects are found, though the brightly coloured grains are likely to be oxygen vacancies, though there are fewer compared to the microstructure of the air-quenched BF-BT-Mn in figure 5.18. This probably suggests that the presence of Sm-dopant on the Ba-site reduces the amount of oxygen vacancies formed. The water-quenched sample in figure 5.32 has much smaller grains (less than 1µm), and more defects, suggesting the microstructure suffered breakages during water-quenching.

5.3.3 XRD Results

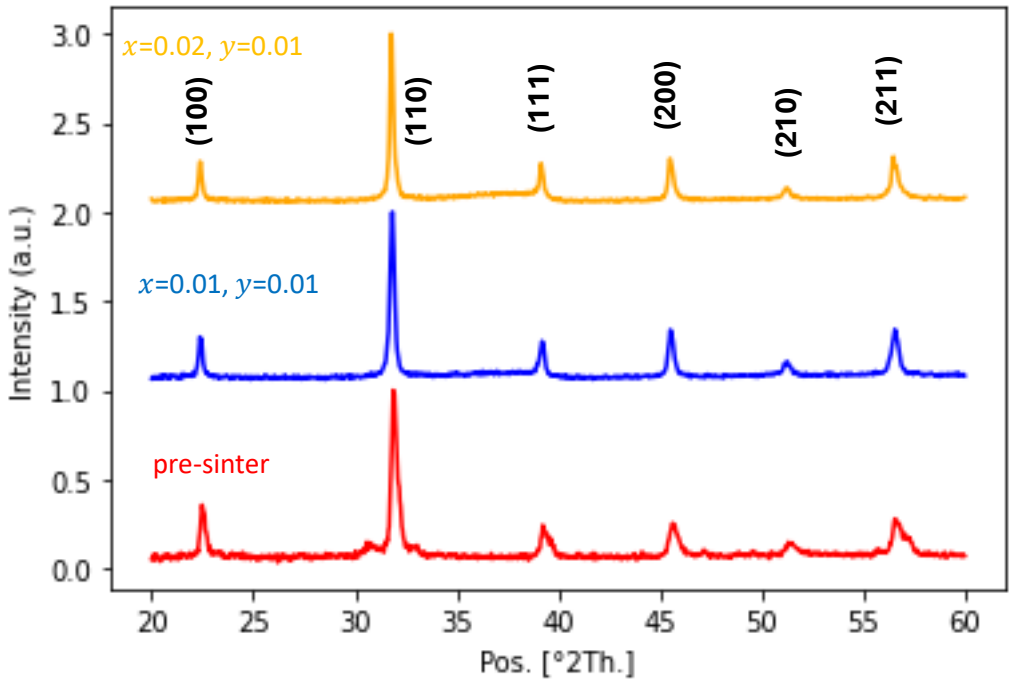

Figure 5.33: XRD patterns for BF-BT-Mn-Sm

The difference between the samples with x=0.010 and x=0.020 Mn-content seems to be very minimal, with possible minor peak shifts due to increasing Mn-content. The pre-sintered sample has secondary peaks, most notably at the [110] and [211] peak, which could indicate a transition between orthorhombic and tetragonal phases. After sintering, all XRD patterns smooth out indicating cubic phases throughout. The phase transitions with co-doped Mn-Sm BF-BT seem to be less prominent compared to purely Mn-doped samples.

5.3.4 Permittivity-temperature Results

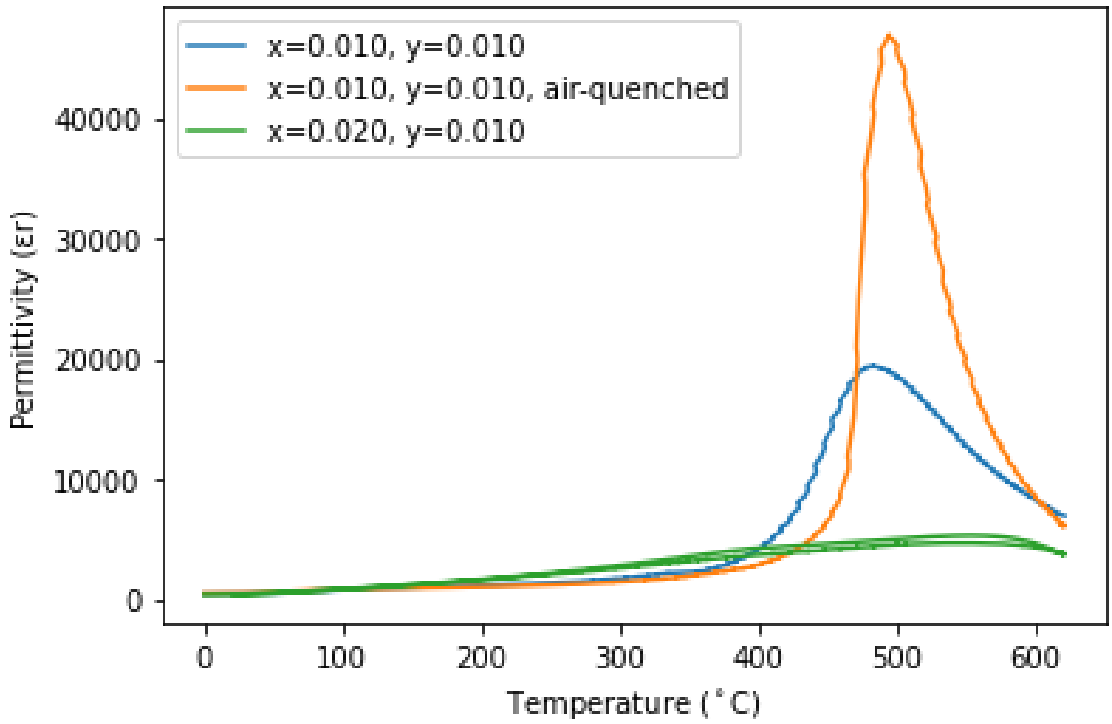

Figure 5.34: Permittivity-temperature of BF-BT-Mn-Sm

As seen from figure 5.34, the air-quenched sample at x=0.010 and y=0.010 increases the relative permittivity by over 100% compared to its unquenched counterpart. Increasing the Mn-content to x=0.020 significantly lowers the relative permittivity to less than half that of x=0.010. The T_C for the unquenched sample at x=0.010 is approximately 483.32°C. Air-quenching the sample increases it to 494.96°C and increasing the Mn-content to x=0.020 increases it to approximately 553.88°C. However, the relative permittivity is significantly lower compared to the samples with x=0.010 Mn-content. The T_C decreased for the co-doped samples at x=0.010 Mn-content, but significantly increased at x=0.020 Mn-content at the expense of a significantly lower relative permittivity.

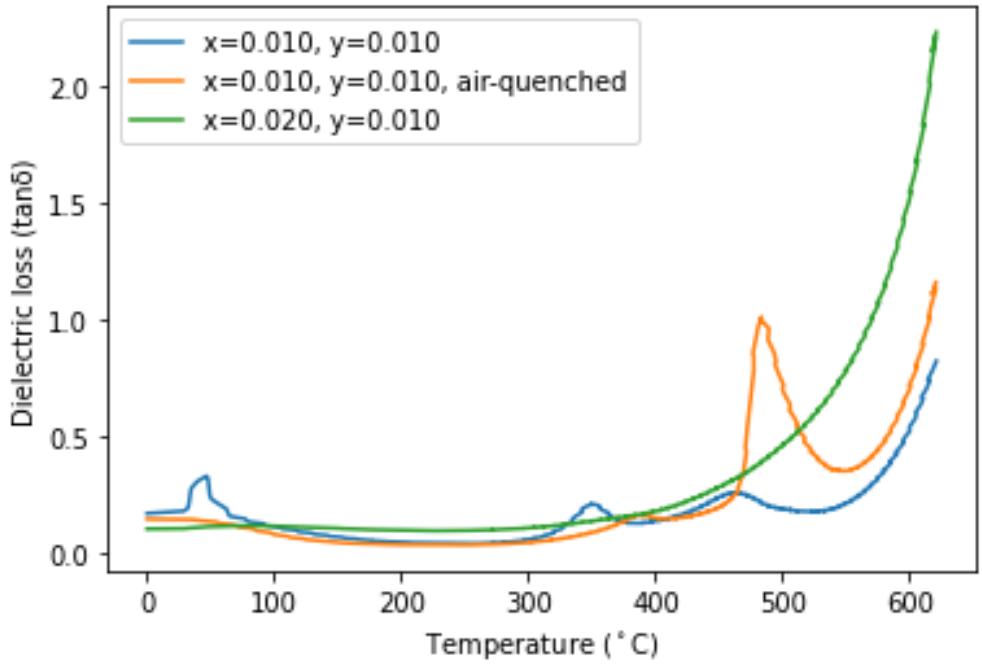

Figure 5.35: Dielectric loss of BF-BT-Mn-Sm samples

From figure 5.35, the dielectric loss experienced by the unquenched sample at x=0.010 is generally lower than the other samples, though there are a few peaks distributed throughout the plot which indicate either noise or conduction. The air-quenched sample has a peak at around the T_C, which indicates significant conductivity at that point. The sample at x=0.020 generally experiences a steady $tan\delta$ loss before significantly increasing after 400°C.

5.3.5 P-E Hysteresis

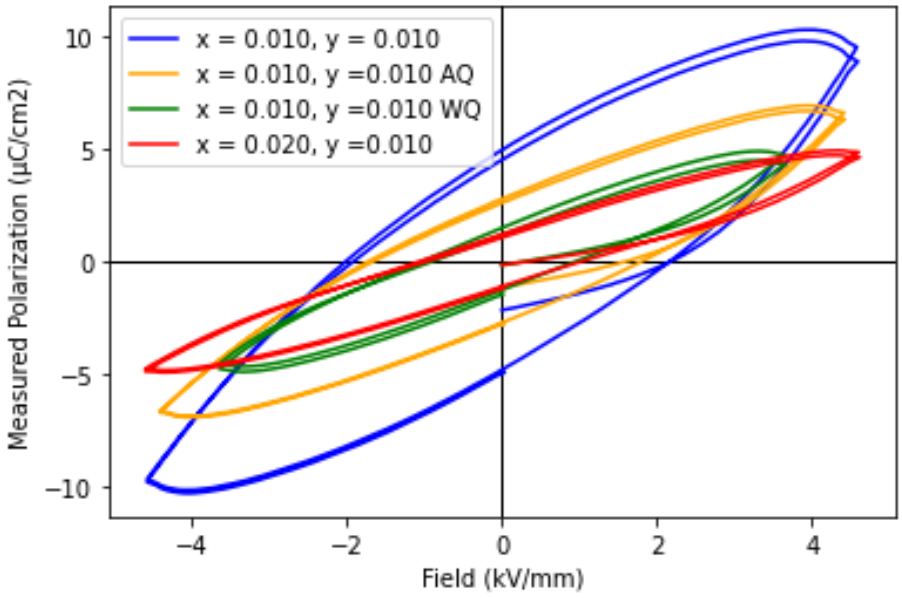

Figure 5.36: P-E Hysteresis for BF-BT-Mn-Sm samples

The P-E hysteresis as seen in figure 5.36 shows the largest polarization range being exhibited by the unquenched sample at x=0.010, with the air-quenched and water-quenched samples showing lower polarization ranges. The full figures exhibited by the samples are shown in table 5.18:

Table 5.18: Polarization coefficients for BF-BT-Mn-Sm samples

x	y	P_{Max} (µC/cm^2)	P_R (µC/cm^2)	E_C(kV/mm)
0.01	0.01	9.562	4.961	2.168
0.01 (AQ)	0.01 (AQ)	6.636	2.794	1.803
0.01 (WQ)	0.01 (WQ)	4.76	1.494	0.951
0.02	0.01	4.881	1.211	1.028

The unquenched sample at x=0.010 has the highest polarization but has also got the highest remnant polarization and coercive field required to correct it. Increasing Mn-content does lower the P_{Max} to half its original value, but is slightly higher than the water-quenched sample at x=0.010. Quenching the samples in general significantly reduces the polarization values: air-quenching reduces the P_{Max} by around a third and water quenching reduces the P_{Max} of the former by another third and the E_C by around half. The polarization is generally higher than the single Mn-doped samples in the previous section (especially compared to the

Fe-site doped samples), which might indicate higher conduction under an externally applied electric field.

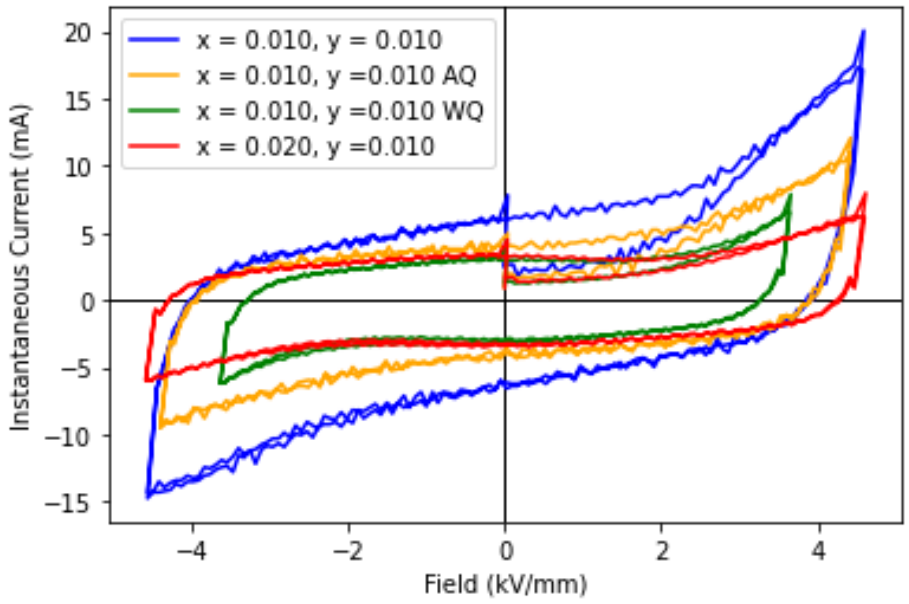

Figure 5.37: Instantaneous Current vs Field for BF-BT-Mn-Sm

Figure 5.37 confirms the significantly greater instantaneous current experienced by the unquenched sample at x=0.010, which is almost twice as much experienced by the air-quenched sample, and almost 4 times as much experienced by the water-quenched sample and sample at x=0.020.

5.3.6 Piezoelectric Results

The same procedure for poling the BF-BT-Mn samples was used for the BF-BT-Mn-Sm samples. The full results can be found in the supplementary material in the appendix, but the main results (max piezoelectric coefficients and their respective capacitances and tanδ values) are shown in table 5.19 and figure 5.38:

Table 5.19: Piezoelectric table for BF-BT-Mn-Sm

x	y	Field (kV/mm)	d_{33} (pC/N)	$tan(\delta)$	Temp. (°C)
0.01	0.01	5.0	150	0.0445	80
0.01 (AQ)	0.01 (AQ)	3.5	161	0.0413	80
0.01 (WQ)	0.01 (WQ)	3.5	18	0.0537	25
0.02	0.01	6.0	11	0.0346	80

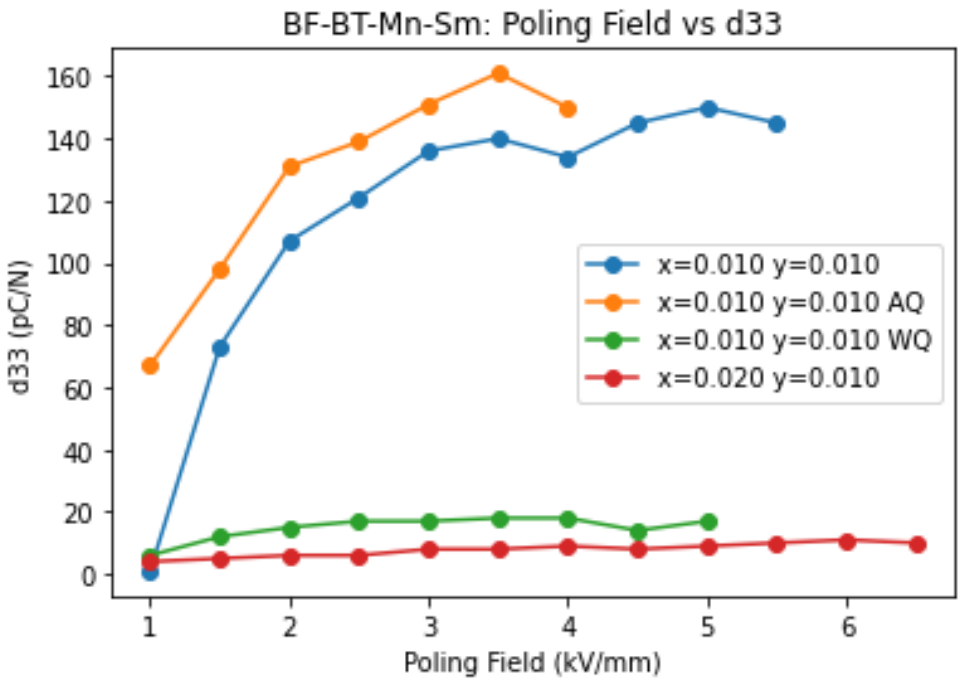

Figure 5.38: d_{33} coefficients vs electrical poling fields for BF-BT-Mn-Sm

The highest d_{33} achieved for BF-BT-Mn-Sm are the air-quenched samples, with a maximum of 161 pC/N at a poling field of 3.5 kV/mm before breaking at 4.5 kV/mm. The unquenched samples achieved a maximum of 150 pC/N at 5.0 kV/mm before breaking at 6.0 kV/mm. The water-quenched samples and the samples with x=0.020 Mn-content performed poorly, achieving a maximum d_{33} of 18 pC/N and 11 pC/N at 5.0 kV/mm and 6.0 kV/mm respectively. The water-quenched samples were also the only ones to perform slightly better after poling at room temperature compared to poling at 80°C, which deviates from the general trend where a higher temperature would initiate a larger piezoelectric response due to the greater kinetic energy obtained by the electrons. The water-quenched samples also exhibited greater $tan\delta$ losses compared to the other sets of samples, which coupled with the low d_{33} values may be symptoms of structural breakage during the water-quenching process which results in low efficiency.

The air-quenched samples however exhibited lower $tan\delta$ losses than the unquenched samples, which coupled with the greater d_{33} results hint that the air-quenching process has successfully reduced the defects. In general, the air-quenched samples consistently exhibited better d_{33} values at fields up to 4.0 kV/mm, where both sets of samples experienced a dip in performance which could be an anomaly (134 pC/N and 150 pC/N for the unquenched and air-quenched samples respectively).

5.4 Impedance Measurements

After completing the poling studies for BF-BT samples, the best performing sets of samples were selected for further testing and measurements. In this case, BF-BT-Mn (x=0.010) and BF-BT-Mn-Sm (x=0.010, y=0.010) and all of their unquenched, air-quenched and water-quenched samples have been selected for further measurements for their impedance spectroscopy and piezoelectric resonance. The impedance spectroscopy of undoped BF-BT was also measured to compare and demonstrate the effect of the addition of Mn and Sm dopants to the sample.

The first part of this section will focus on the impedance spectroscopy using the Solartron, and the second part focuses on their matrix characterisation via Piezoelectric Resonance Analysis Program (PRAP).

5.4.1 Solartron Spectroscopy

As mentioned in chapter 4, the Solartron was connected to a tube furnace where the sample was placed. The impedances of each material were measured at temperatures between 200^{o}C and 600^{o}C at 50^{o}C increments. The impedance data is then fitted to an equivalent circuit, which is selected via trial and error. The equivalent circuits used to fit the impedance data are depicted in figure 5.39:

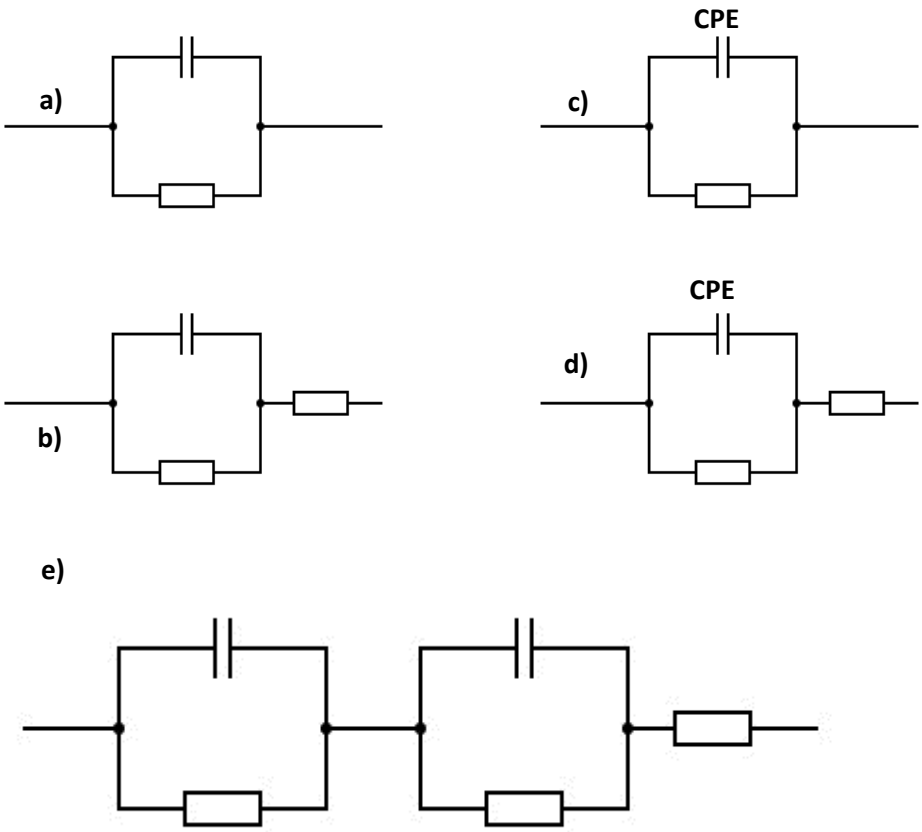

Figure 5.39: Equivalent circuit diagrams used to model the Cole-Cole plots for the complex impedance. Circuit a) is a standard RC with a capacitor or CPE for circuit c). Circuits b) and d) add a secondary resistor connected in series, with a capacitor and CPE respectively. Circuit e) is two RC circuits with an additional resistor for materials with two different relaxation constants.

5.4.1.1 Undoped BF-BT

Figure 5.40 shows the impedance spectroscopy of undoped BF-BT at 200°C. The remaining spectroscopies at different temperatures are in the appendix (Figures B1 and B2, Appendix B1). At lower temperatures up to 200°C, the Cole-Cole and Bode plots depict two relaxation peaks, implying different relaxation times. This is possibly due to electron hopping at lower temperatures or significant charge transport. However, over increasing temperatures the M'' and Z'' peaks become more in sync with one another suggesting that the material behaves like an "ideal" capacitor at higher temperatures.

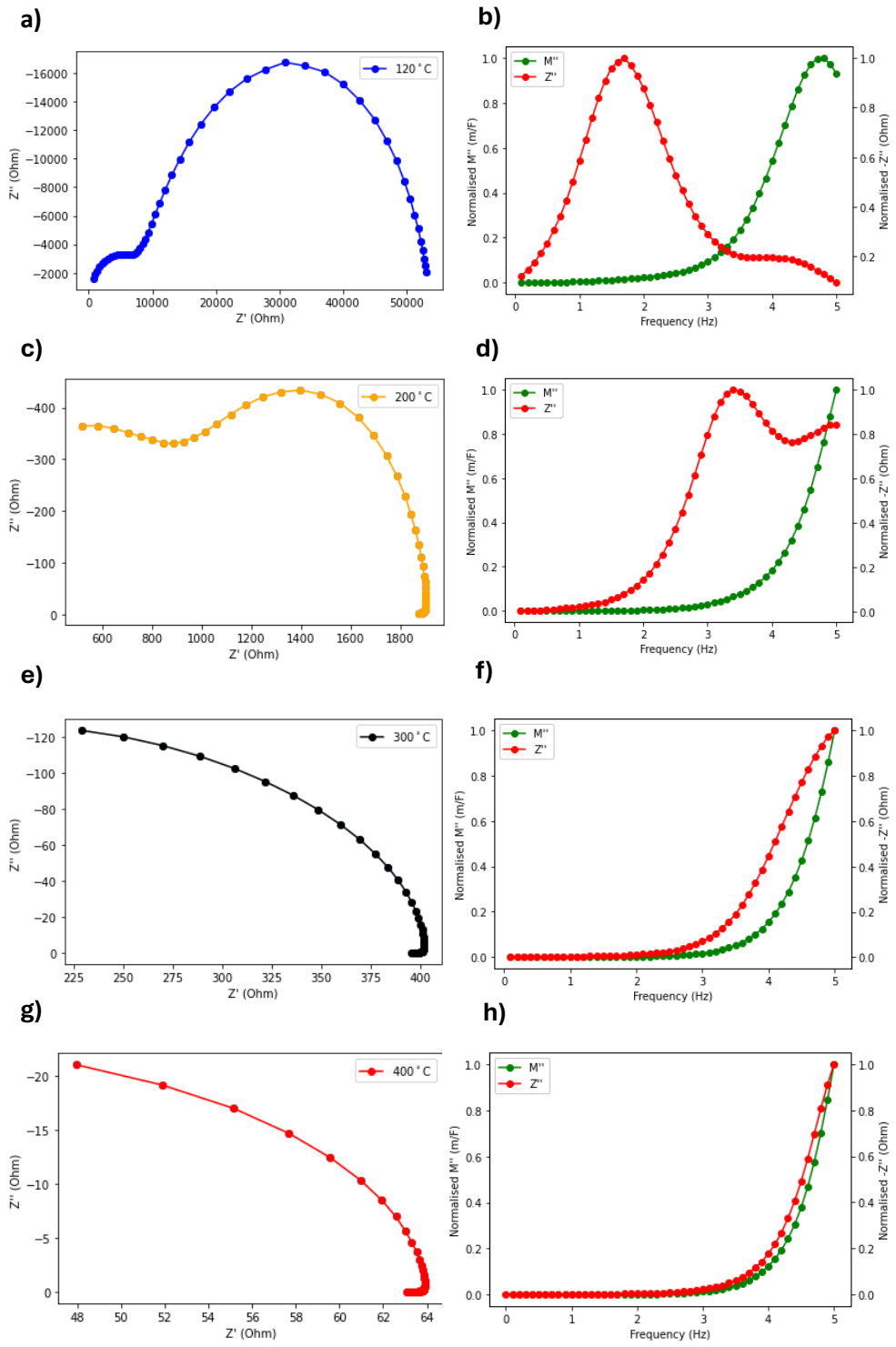

Figure 5.40: Impedance Spectroscopies of undoped BF-BT. First row: The Cole-Cole (a) and Bode (b) plots at 120°C. Second row: The Cole-Cole (c) and Bode (d) plots at 200°C. Third row: The Cole-Cole (e) and Bode (f) plots at 300°C. Fourth row: The Cole-Cole (g) and Bode (h) plots at 400°C.

Table 5.20 shows the resistances and conductivities obtained for undoped BF-BT:

Table 5.20: Resistances and conductivities from the impedance spectroscopy of BF-BT

Temp. (K)	$R1$ (Ohm)	$R2$ (Ohm)	circuit	σ_1 (S/cm)	σ_2(S/cm)
120	3.42×10^{3}	4.80×10^{4}	e	4.42×10^{-5}	3.15×10^{-6}
150	3.21×10^{3}	9.42×10^{3}	e	4.71×10^{-5}	1.61×10^{-5}
200	3.33×10^{2}	1.56×10^{3}	e	4.54×10^{-4}	9.70×10^{-5}
250	1.87×10^{2}	5.46×10^{2}	e	8.09×10^{-4}	2.77×10^{-4}
300	1.77×10^{2}	2.23×10^{2}	e	8.53×10^{-4}	6.79×10^{-4}
350	3.72×10^{1}	1.18×10^{2}	e	4.07×10^{-3}	1.28×10^{-3}
400	1.14×10^{1}	5.23×10^{1}	e	1.32×10^{-2}	2.89×10^{-3}
450	1.34×10^{1}	2.00×10^{1}	e	1.13×10^{-2}	7.58×10^{-3}

At lower temperatures below 300°C, the Cole-Cole plots had two semicircles conjoined together, implying that the grain cores and boundaries each have different capacitive contributions whilst maintaining similar conduction mechanisms. As a result, equivalent circuit e) from figure 5.39 was required to fit the data. This then resulted in two separate sets of resistances ($R1$ and $R2$) and conductivities (σ_1 and σ_2) which were used in the Arrhenius calculations, which are shown in figure 5.41. The conductivity over temperature was then used to calculate the activation energies using the following equation as mentioned in chapter 4 [91]:

$$\ln(\sigma) = -\frac{E_a}{kT} + \ln(\sigma_0) \qquad (71)$$

where k is the Boltzmann constant (1.380649×10^{-23} J K^{-1}), T is the temperature in K, and σ_0 is the conductivity at the y-intercept.

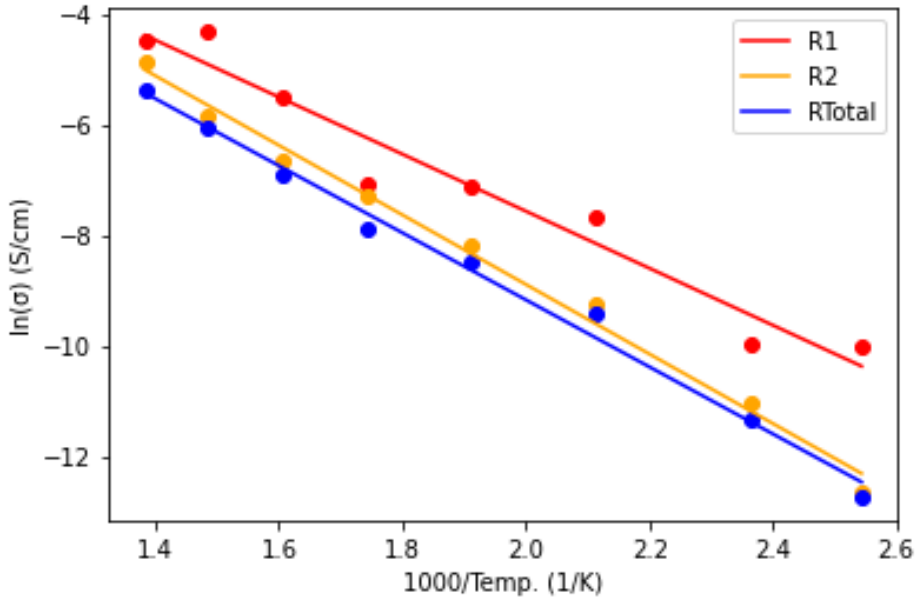

Figure 5.41: Arrhenius plot of undoped BF-BT

Figure 5.41 includes the Arrhenius plot for the total resistance (R_{Total}) at each temperature. Table 5.21 shows the E_a and conductivities for all sets of resistances, where σ_{80} is the conductivity at 80°C, and σ_{20} is the conductivity at room temperature:

Table 5.21: Activation energy and conductivities for undoped BF-BT.

	E_a (eV)	σ_0 (S/cm)	σ_{80} (S/cm)	σ_{20} (S/cm)
$R1$	0.44	15.45	8.12 x 10^{-6}	4.21 x 10^{-7}
$R2$	0.54	39.56	7.34 x 10^{-7}	1.93 x 10^{-8}
R_{Total}	0.52	18.89	1.79 x 10^{-6}	2.17 x 10^{-8}

The activation energies average around 0.5 eV, which suggests that electron hopping dominates the conduction [92].

5.4.1.2 BF-BT-Mn

The impedance of the unquenched, air-quenched and water-quenched samples of BF-BT-Mn (x=0.010) are compared to one another. Figures 5.42, 5.43 and 5.44 show the respective impedance spectroscopies of unquenched, air-quenched and water-quenched samples at a range of temperatures. The full impedance spectroscopies can be found in the appendix (figures B3, B4, B5, B6, B7 and B8 in appendix B2). As with the undoped BF-BT, the unquenched BF-BT-Mn in figure 5.42 acts like an ideal capacitor at higher temperatures from 400-600°C, as the

Bode plots show that the M'' and Z'' peaks get closer to overlapping each other with increasing temperature. At lower temperatures (150-350^{o}C) the peaks move further from each other with decreasing temperature (except for 250^{o}C where the peaks are only slightly offset), again implying the presence of electron hopping. At 150-200^{o}C the plots show more outliers than at higher temperatures, which is likely to be noise recorded by the Solartron. The Cole-Cole plots show a more complete semi-circle between 250-450^{o}C, implying a "lossy" capacitor between those temperatures [93]. The remaining temperatures outside this range show a slower relaxation of the complex impedance. Overall, this trend correlates with the Permittivity-temperature graph shown in figure 5.24.

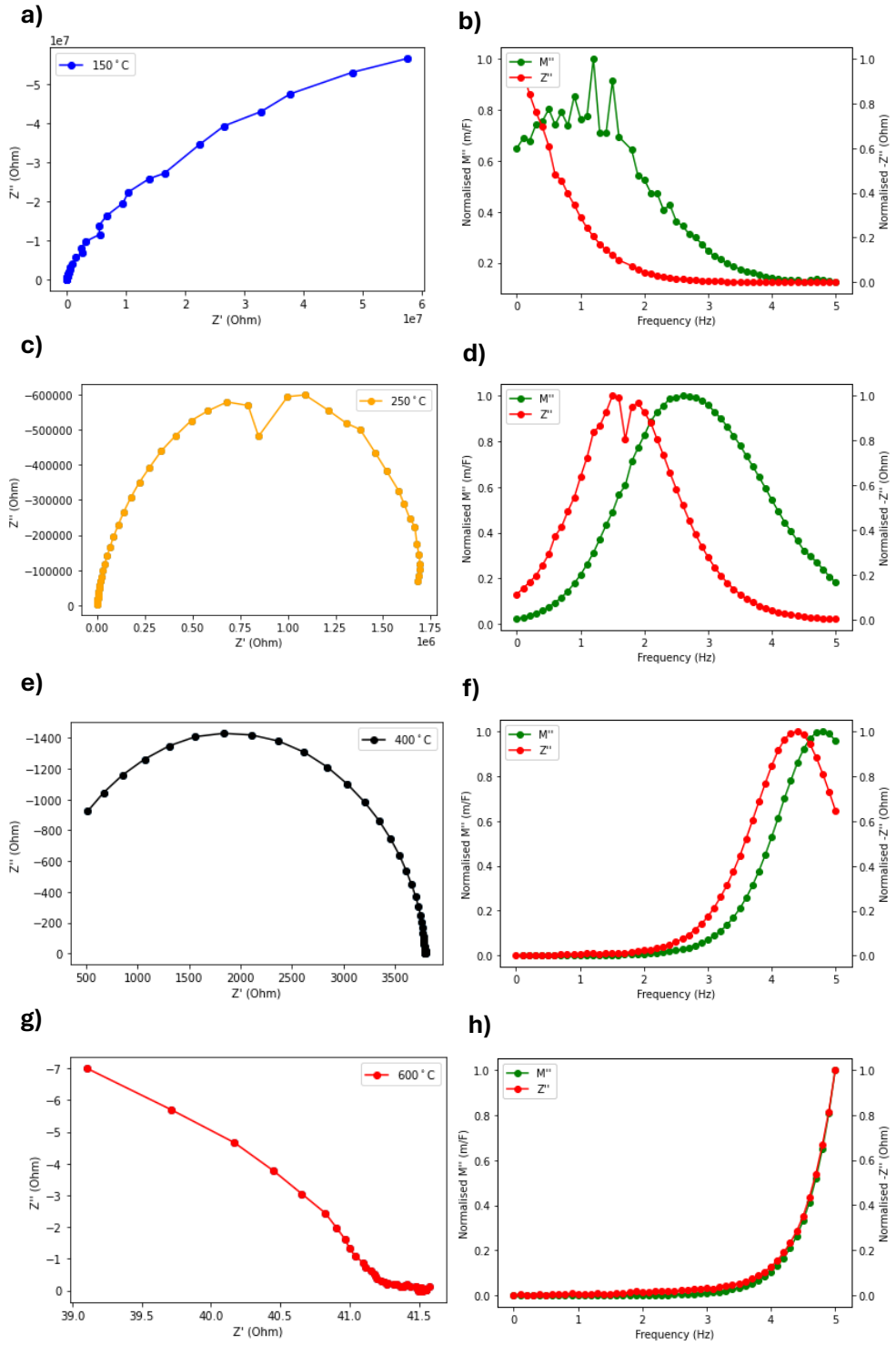

Figure 5.42: Impedance Spectroscopies of unquenched BF-BT-Mn. First row: The Cole-Cole (a) and Bode (b) plots at 150°C. Second row: The Cole-Cole (c) and Bode (d) plots at 250°C. Third row: The Cole-Cole (e) and Bode (f) plots at 400°C. Fourth row: The Cole-Cole (g) and Bode (h) plots at 600°C.

The air-quenched BF-BT-Mn as seen in figure 5.43 shows a single semi-circle in the Cole-Cole plot, and slightly offset M'' and Z'' peaks in the Bode plot at 400°C. The remaining temperatures show full semi-circle plots at the higher temperatures,

with longer relaxations depicted at lower temperatures (below 300°C). The M'' and Z'' peaks are also shown to be no more than slightly offset from one another throughout all temperatures, although at 550°C it is shown that there is a secondary M'' peak forming outside of the frequency range, and at lower temperatures the M'' relaxation is longer compared to that of the Z'' curve.

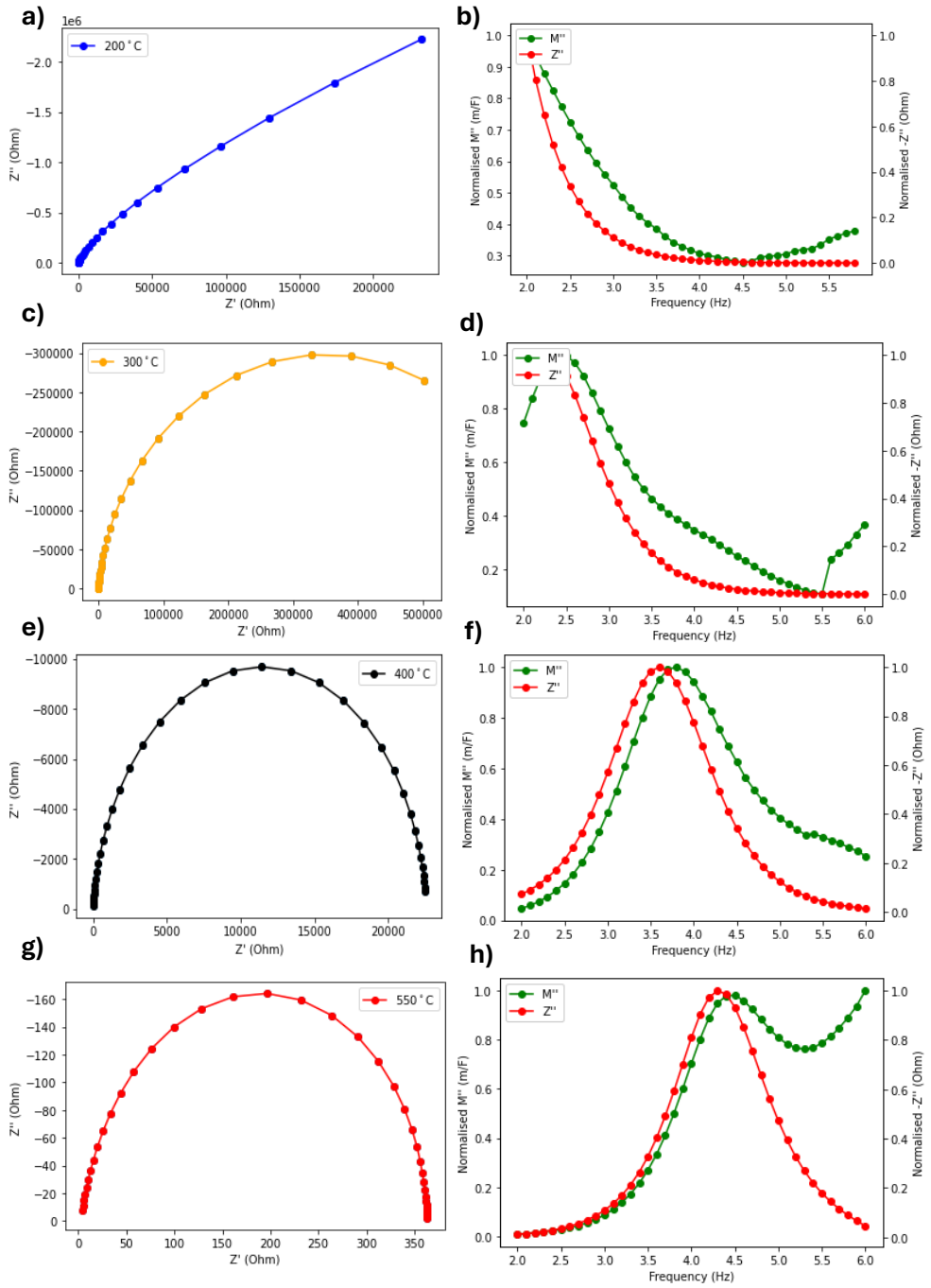

Figure 5.43: Impedance Spectroscopies of air-quenched BF-BT-Mn. First row: The Cole-Cole (a) and Bode (b) plots at 200°C. Second row: The Cole-Cole (c) and Bode (d) plots at 300°C. Third row: The Cole-Cole (e) and Bode (f) plots at 400°C. Fourth row: The Cole-Cole (g) and Bode (h) plots at 550°C.

In figure 5.44, the water-quenched BF-BT-Mn sample shows similar impedance spectroscopy to the air-quenched variant. The Cole-Cole plots also show single semi-circles at higher temperatures and longer hyperbolic curves at temperatures below 250°C. The Bode plots also mostly show the M'' and Z'' curves slightly offset at the higher temperatures, however at 450°C and 500°C the Bode plot

reveals a secondary M'' peak forming beyond the frequency range. At the lowest temperature of 150°C, the M'' and Z'' peaks are completely offset from one another, implying possible electron hopping at that temperature [94].

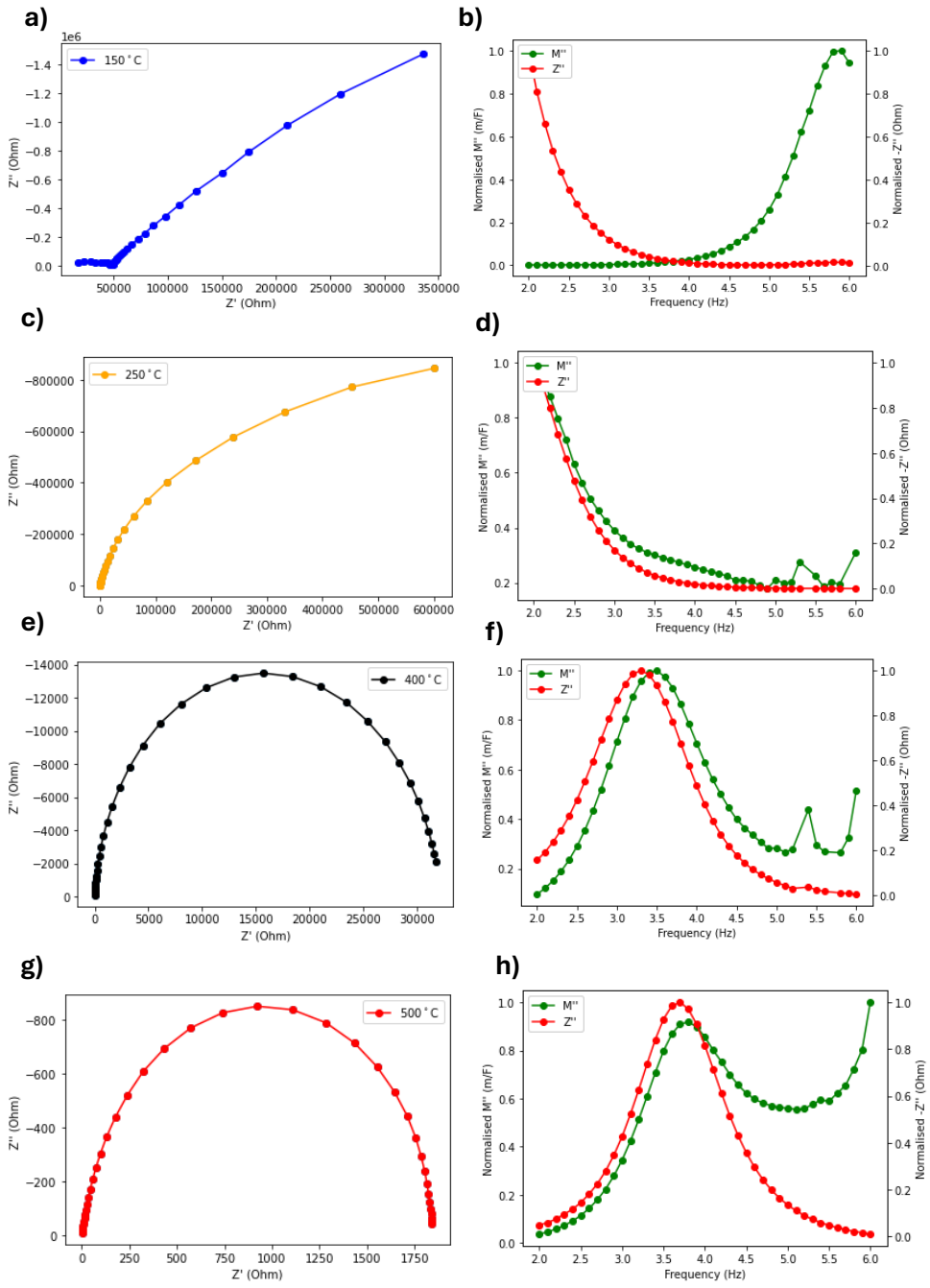

Figure 5.44: Impedance Spectroscopies of water-quenched BF-BT-Mn. First row: The Cole-Cole (a) and Bode (b) plots at 150°C. Second row: The Cole-Cole (c) and Bode (d) plots at 250°C. Third row: The Cole-Cole (e) and Bode (f) plots at 400°C. Fourth row: The Cole-Cole (g) and Bode (h) plots at 500°C.

As seen from the impedance graphs, the unquenched BF-BT-Mn is shown to have a longer relaxation time compared to the air and water-quenched samples. It also requires two resistors in its equivalent circuit for the data to have a better fit, implying it to be more lossy compared to the quenched samples. In contrast both of the quenched samples use one resistor in their equivalent circuit models and exhibit higher resistances than the unquenched sample.

Figure 5.45 shows the Arrhenius plots for the unquenched, air-quenched and water-quenched BF-BT-Mn samples respectively:

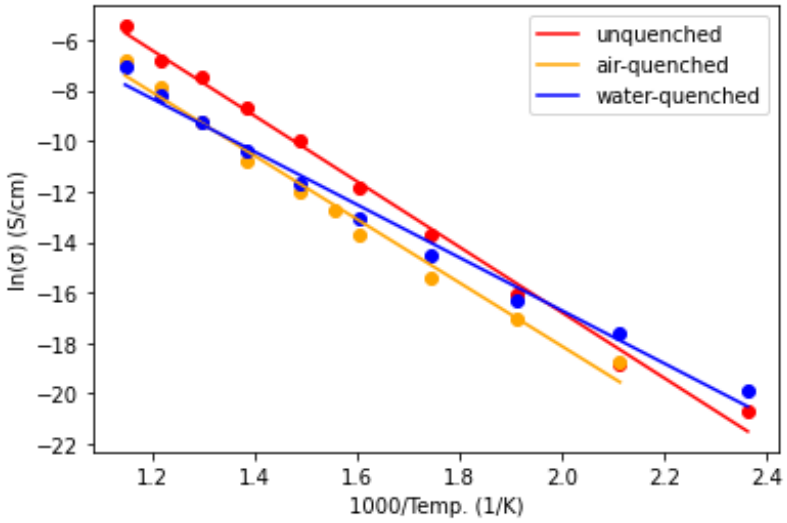

Figure 5.45: Arrhenius plot of BF-BT-Mn

Table 5.22 shows the calculated activation energies for the BF-BT-Mn samples, which were calculated from the gradients of the best fit lines for each plot, and then converted into eV:

Table 5.22: Activation energies for BF-BT-Mn samples

Material	**E_a (eV)**	**σ_0 (S/cm)**	**σ_{80} (S/cm)**	**σ_{20} (S/cm)**	**Max. d_{33} (pC/N)**
BF_BT_Mn_001	1.116	9051.5	1.11×10^{-12}	5.89×10^{-16}	91
BF_BT_Mn_001_AQ	1.081	1048.4	4.11×10^{-13}	2.72×10^{-16}	174
BF_BT_Mn_001_WQ	0.902	67.3	9.39×10^{-12}	2.09×10^{-14}	114

The unquenched, slow-cooled BF-BT-Mn sample has the largest activation energy of 1.116 eV, and the water-quenched sample has the smallest activation energy of

0.902 eV. The general trend seems to be that the faster the cooling rate of the BF-BT-Mn material, the lower the activation energy. Referring to the values for the undoped sample, Mn-doping has increased the activation energy to approximately twice the value, which would explain the high leakage current experienced by the undoped sample during electrical poling, resulting in the breakage of samples.

The unquenched sample also has the largest σ_0 value at 9051.5, which is approximately 9 times the value of the air-quenched sample. This also corresponds to the highest conductivity (σ_{80}) at 80°C (the poling temperature), resulting in the lowest d_{33} value. Between the air-quenched and water-quenched samples the σ_0 is 15-times larger for the former. However, at 80°C the conductivity for the water-quenched sample is greater than its air-quenched counterpart. Overall, the σ_{80} value has a negative correlation with the d_{33} coefficient. The larger E_a for the unquenched sample combined with the offset M'' and Z'' peaks are likely due to the large number of oxygen vacancies formed during slow cooling which results in larger energies being required to displace the ions and vacancies, so oxygen vacancies dominate the electron conduction [92]. As quenching largely prevents oxygen vacancies from forming within the structure due to the fast-cooling nature, this results in a lower activation energy. For the water-quenched samples, the offset M'' and Z'' peaks combined with the lowest activation energy suggests electron hopping may start to dominate conduction.

5.4.1.2 BF-BT-Mn-Sm

The impedance spectroscopy analysis methodology is the same one used in the previous section for BF-BT-Mn. Figurea 5.46, 5.47 and 5.48 show the impedance graphs in Cole-Cole and Bode formats over a range of temperatures. The full impedance spectroscopy data can be found in the appendix (figures B9, B10, B11, B12, B13 and B14 in appendix B3).

The Cole-Cole plots for the unquenched sample show a general trend of slow relaxation curves with increasing temperature, and semi-circle plots at temperatures below 300°C. The Bode plots show the M'' and Z'' curves in general overlapping with one another, with the peaks shown to be in sync with one another at lower temperatures.

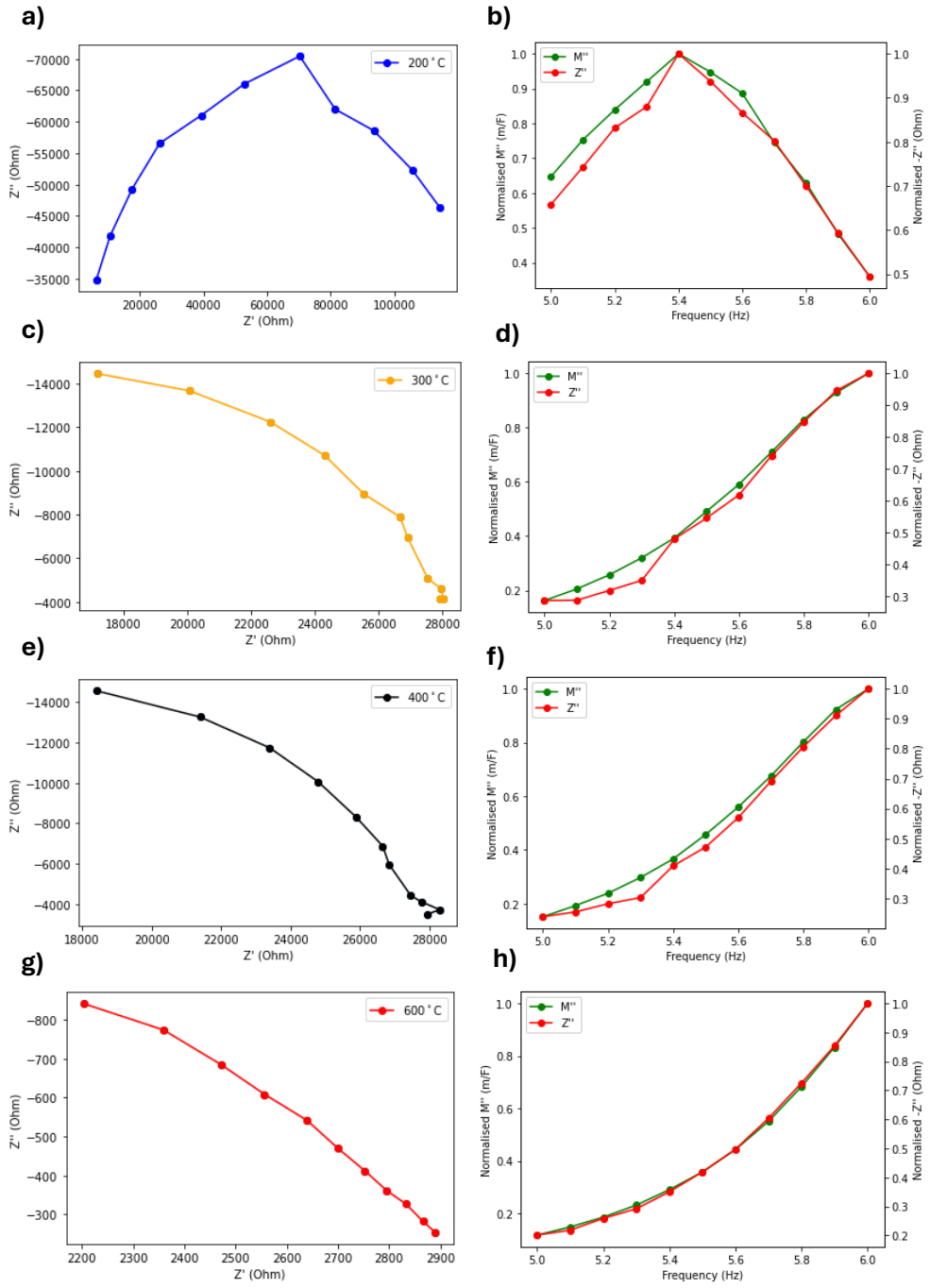

Figure 5.46: Impedance Spectroscopies of unquenched BF-BT-Mn-Sm. First row: The Cole-Cole (a) and Bode (b) plots at 200°C. Second row: The Cole-Cole (c) and Bode (d) plots at 300°C. Third row: The Cole-Cole (e) and Bode (f) plots at 400°C. Fourth row: The Cole-Cole (g) and Bode (h) plots at 600°C.

The air-quenched BF-BT-Mn-Sm sample however shows a significantly different trend in its impedance spectroscopy. The Bode plots depict a significant offset between the Z'' and M'' peaks which only increases with decreasing temperatures, possibly implying electron hopping between vacancies. The Cole-

Cole plots show slower relaxation curves at lower temperatures (below 300°C), whilst showing semi-circles at higher temperatures.

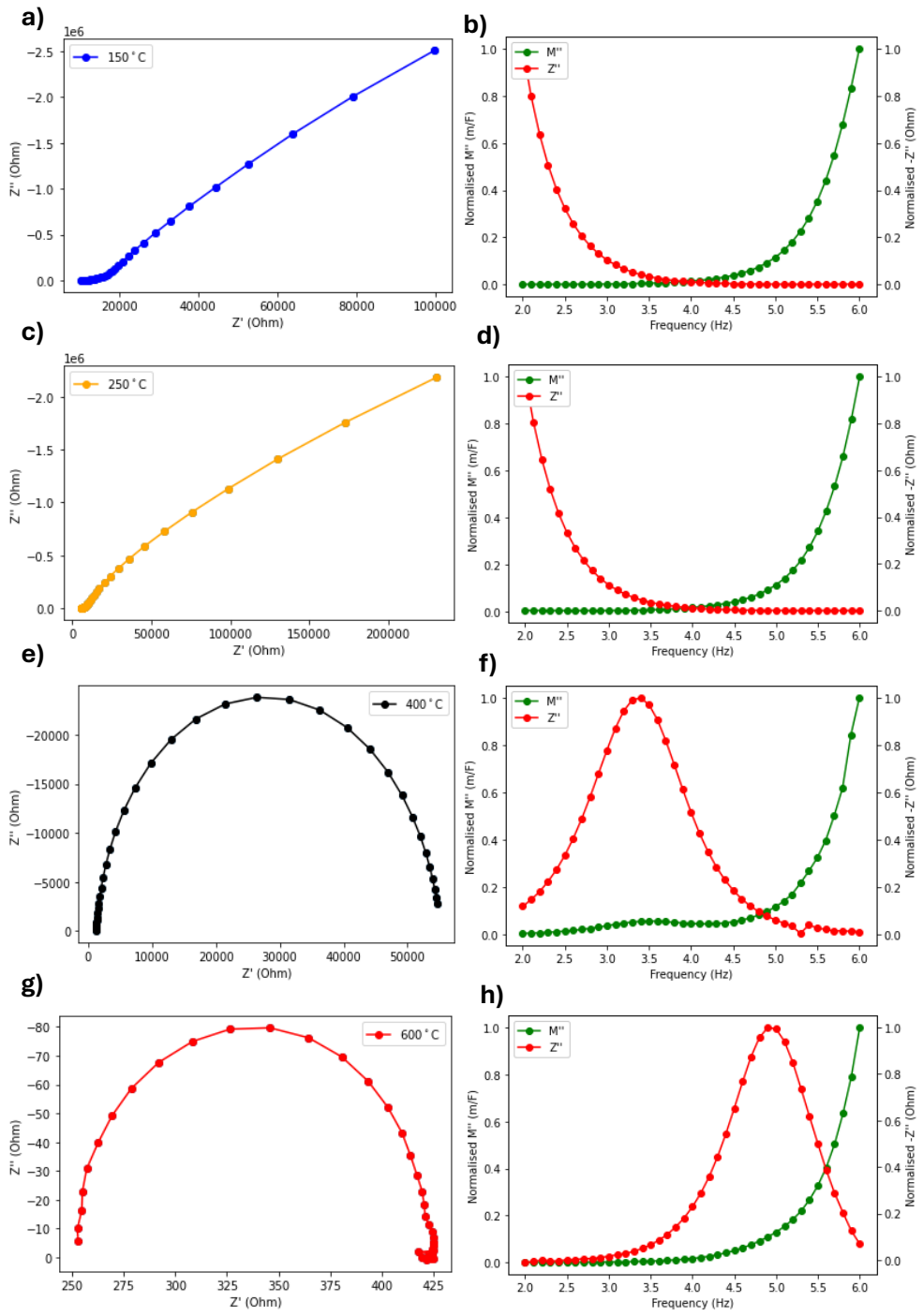

Figure 5.47: Impedance Spectroscopies of air-quenched BF-BT-Mn-Sm. First row: The Cole-Cole (a) and Bode (b) plots at 150°C. Second row: The Cole-Cole (c) and Bode (d) plots at 250°C. Third row: The Cole-Cole (e) and Bode (f) plots at 400°C. Fourth row: The Cole-Cole (g) and Bode (h) plots at 600°C.

The water-quenched sample shows a similar trend amongst the Cole-Cole plots, but the Bode plots show the M'' and Z'' peaks aligning with each other at higher

temperatures and becoming more offset as the temperature decreases. A significant number of outlier points were observed at the lower temperatures, likely to be noise recorded by the Solartron.

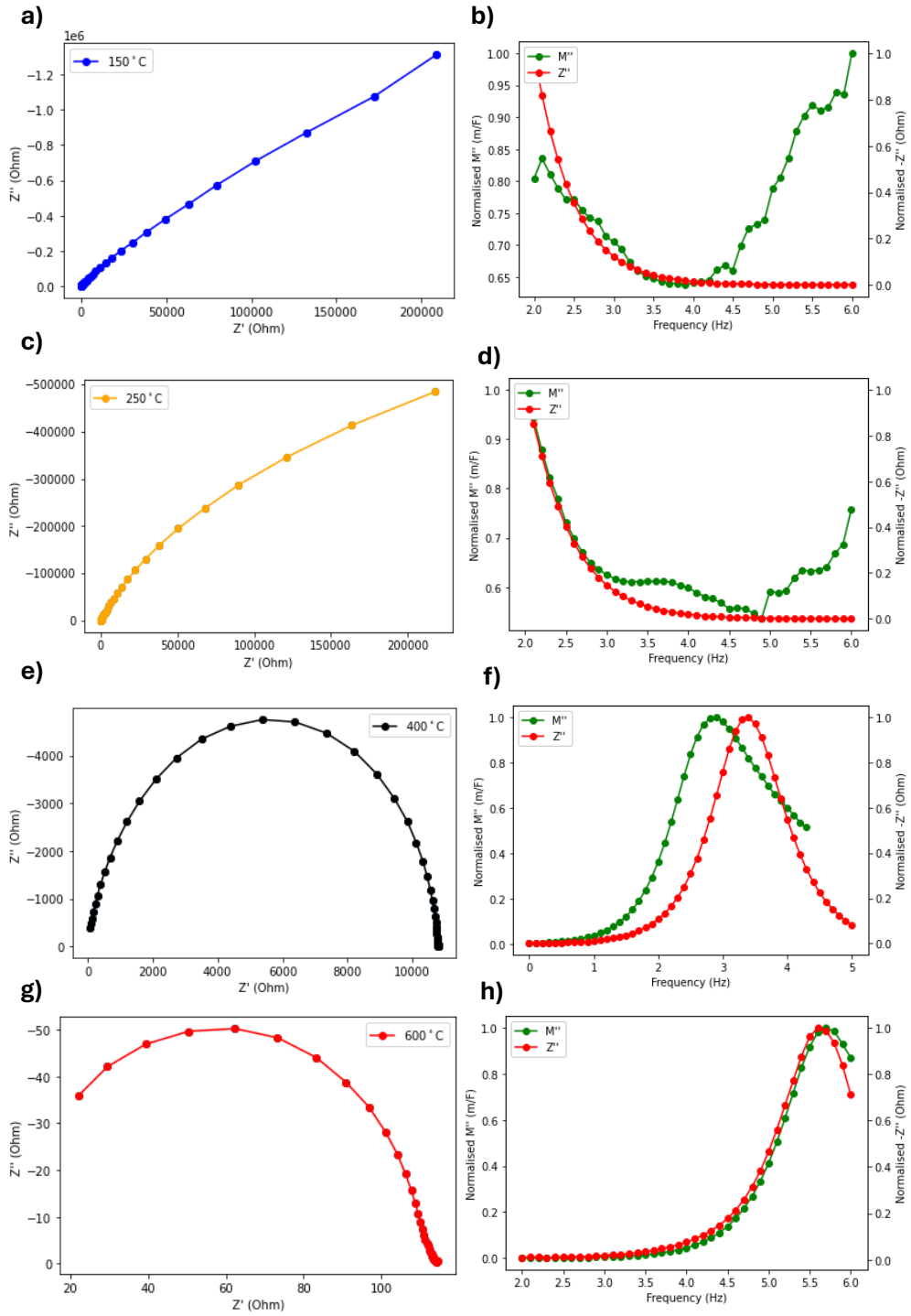

Figure 5.48: Impedance Spectroscopies of water-quenched BF-BT-Mn-Sm. First row: The Cole-Cole (a) and Bode (b) plots at 150°C. Second row: The Cole-Cole (c) and Bode (d) plots at 250°C. Third row: The Cole-Cole (e) and Bode (f) plots at 400°C. Fourth row: The Cole-Cole (g) and Bode (h) plots at 600°C.

As opposed to the single Mn-doped BF-BT samples, the co-doped BF-BT-Mn-Sm samples require a variety of equivalent circuits that required either one or two resistors. The unquenched sample mainly required circuits (a) and (c) which only consisted of one resistor connected in parallel to the capacitor or CPE, the only exception being the impedance at 550°C which required equivalent circuit (b), consisting of a capacitor and two resistors (one connected in parallel, the other in series). The air-quenched sample required double-resistor equivalent circuits (b) and (d) at 450°C at higher temperatures, and the single resistor equivalent circuit (c) from 400°C onwards (with one exception being the capacitor-based circuit (a) at 200°C). The water-quenched samples largely required circuit (b) at the highest temperatures, whilst best-fitting circuit (c) from 500°C onwards (the exception being 400°C which again required circuit (b)).

The Arrhenius plot for BF-BT-Mn-Sm is depicted in figure 5.49:

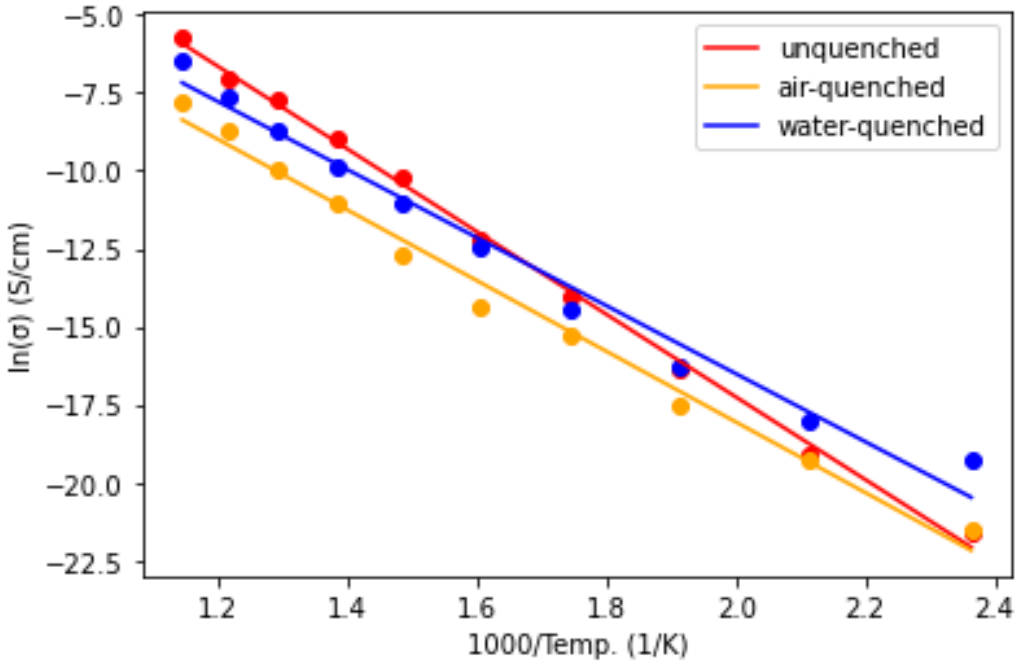

Figure 5.49: Arrhenius plots of BF-BT-Mn-Sm

The calculated activation energies for the BF-BT-Mn-Sm samples are given in table 5.23. As with the BF-BT-Mn samples, the E_a is highest for the unquenched sample and lowest for the water-quenched sample. The σ_0 value is also the highest for the unquenched sample, however the σ_{80} value is the lowest and corresponds to the second highest d_{33} value. The air-quenched sample has the lowest σ_0 value, but a higher σ_{80} value compared to the unquenched sample, whilst also possessing the

largest d_{33} value at 161 pC/N. The water-quenched sample has the highest σ_{80} value (almost 8 times as much as the air-quenched sample), which corresponds to the lowest d_{33} value at 18 pC/N, which is approximately 11% of the value of the air-quenched sample.

Table 5.23: Activation energies for the BF-BT-Mn-Sm samples

Material	E_a (eV)	σ_0 (S/cm)	σ_{80} (S/cm)	σ_{20} (S/cm)	Max. d_{33} (pC/N)
BF_BT_Mn_Sm_001	1.143	10701.1	5.49 x 10^{-13}	2.39 x 10^{-16}	150
BF_BT_Mn_Sm_001_AQ	0.978	102.01	1.16 x 10^{-12}	1.57 x 10^{-15}	161
BF_BT_Mn_Sm_001_WQ	0.941	206.6	8.02 x 10^{-12}	1.37 x 10^{-14}	18

5.4.1.3 Solartron Results Discussion and Conclusion

In general, it can be seen that the faster cooling regimes decrease the activation energy for each composition. This would likely be attributed to the reduced time period for oxygen vacancies formed during the quenching process along with the closer packing of the ions in the perovskite structure. This would make it easier for electron conduction to occur between ions, resulting in lower activation energies for the quenched samples.

The undoped BF-BT possesses a significantly lower set of E_a values (approximately half the values of the Mn and co-doped samples), which would largely be attributed to electron hopping dominating the conduction. The two semi-circles depicted in the Cole-Cole plots imply that there are two different spatially separate regions with different capacitive contributions, possibly from the grain cores and grain boundaries [94]. The conductivity at 20°C and 80°C for the undoped sample is significantly higher (by a factor of at least 10^6) than the doped samples, implying that Mn-doping inhibits the conduction by electron trapping [92].

5.4.2 Full Matrix Characterisation

5.4.2.1 Sample Preparation

The compositions used for the matrix characterisation are the unquenched and air-quenched versions of BF-BT-Mn (x=0.010) and BF-BT-Mn-Sm (x=0.010, y=0.010). As mentioned in chapter 5, different geometries were required to measure different parameters over different planes. The three different types of geometries used were the length extensional (LE), longitudinal thickness extensional (LTE), and radial extensional (RE).

20mm diameter pellets were produced for each material, which were then stuck onto aluminium substrates using adhesives and left to dry for at least 12 hours. After drying, the geometries were drawn out onto each pellet as shown in figure 5.50:

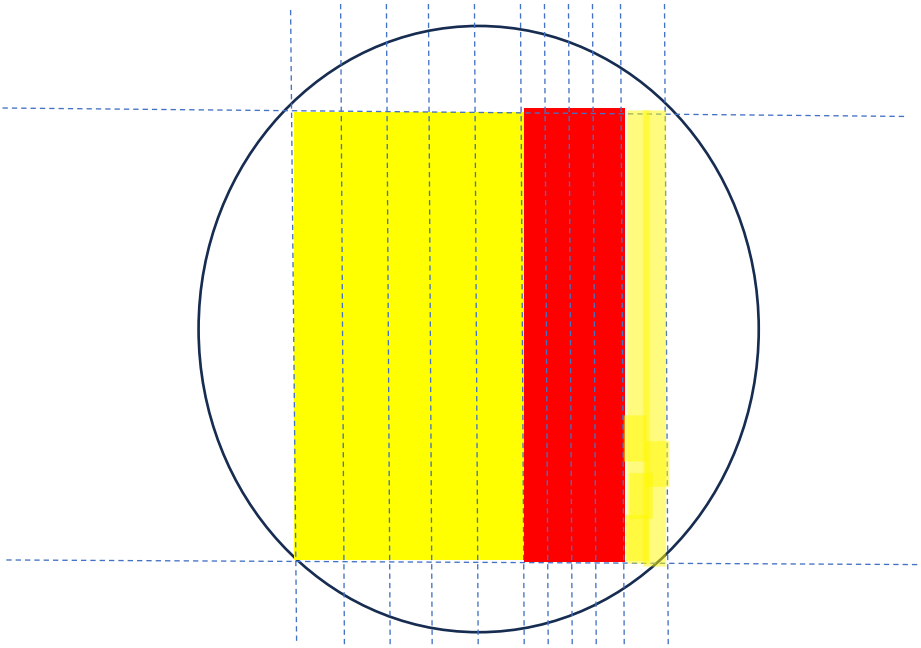

Figure 5.50: Cutting regime for full-matrix characterisation. The yellow geometries are LE samples, and the red geometries are LTE samples.

Table 5.24 shows the dimensions used for each mode:

Table 5.24: Dimensions of geometries used for different modes

Mode	Length (mm)	Width (mm)	Thickness (mm)	Diameter (mm)
Length Extensional (LE)	12.0	2.0	2.0	N/A
Longitudinal Thickness Extensional (LTE)	11.0	2.0	0.5	N/A
Radial/Thickness Extensional (RE/TE)	N/A	N/A	1.0	15.0

The dimensions for the geometries were determined by the requirements mentioned in chapter 4, which are also in line with the IRE Standards on Piezoelectric Crystals (Jaffe. et al. 1961). The pellets were then cut into the geometries using a Struers Accutom-5 precision cutter. The speed of the blade was 3000rpm and the feed was 0.025mm/s. The radial mode geometry was exempt from this process as it was already a circular pellet, and was instead polished before the electroding process. After the cutting process, silver electroding paint was applied to every sample and electrode at 550°C, as per the process described in chapter 4. Figure 5.51 shows a photo of the cut samples:

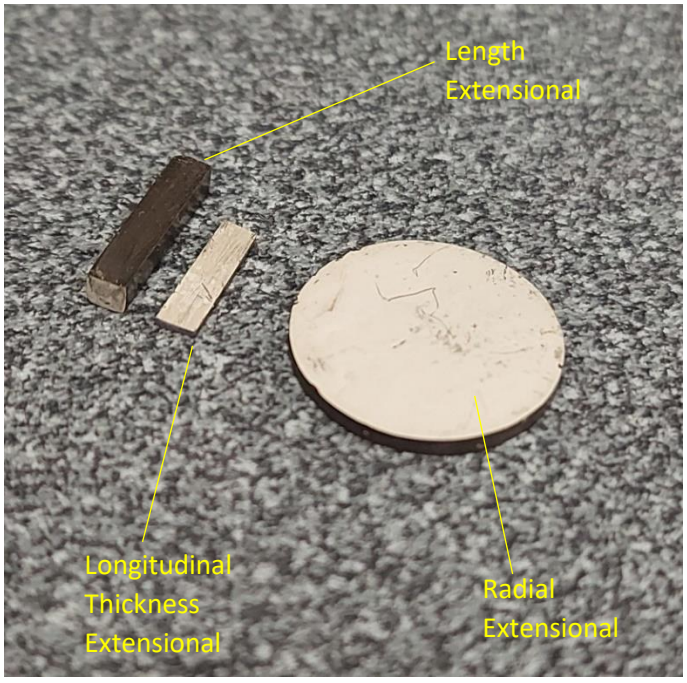

Figure 5.51: The cut samples used for the matrix characterisation.

To maintain consistency, the samples were all poled at a 2.0kV/mm field at room temperature. However, as the poling rig at the University of Leeds could only go up to a maximum voltage of 10kV, the LE geometries were poled using a rig at Thales UK's site at Templecombe that could go up to 40kV, allowing them to be poled at 24kV or 2.0kV/mm due to their 12mm length.

5.4.2.2 PRAP Measurements

An Agilent 4294a was used to carry out the resonance measurements and was connected to a laptop which was running the piezoelectric resonance analysis program (PRAP) to calculate the different piezoelectric parameters using the equations depicted in chapter 4. The impedance analyser was calibrated using an open and closed-circuit procedure before measurements took place. An average of 10 sweeps were done for each sample, with a sweep time of 50 seconds and 500 points taken per sweep.

The impedance curve was measured as a function of frequency, and the curve had a resonant frequency f_r (the minimum point) and an anti-resonant frequency, f_a, which was the maximum point. Those two frequencies can be used to calculate many piezoelectric parameters that are depicted in table 5.25:

Table 5.25: Piezoelectric parameters which were calculated from different modes.

Length Extensional (LE)	Longitudinal Thickness Extensional (LTE)	Radial Extensional (RE)
d_{33}, g_{33}, k_{33}, s^{D}_{33}, s^{E}_{33}, ε^{X}_{33}, $\varepsilon^{S3=0}_{33}$	k_{31}, s^{E}_{11}, ε^{X}_{33}, d_{31}, g_{31}	k_t, c^{D}_{33}, c^{E}_{33}, k_p, ε^{X}_{33}, s^{E}_{11}, s^{E}_{12}, ε^{P}_{33}, c^{P}_{11}, σ^{p}, e^{p}_{31}, s^{E}_{66}, c^{E}_{66}

5.4.2.3 BF-BT-Mn (unquenched) Results

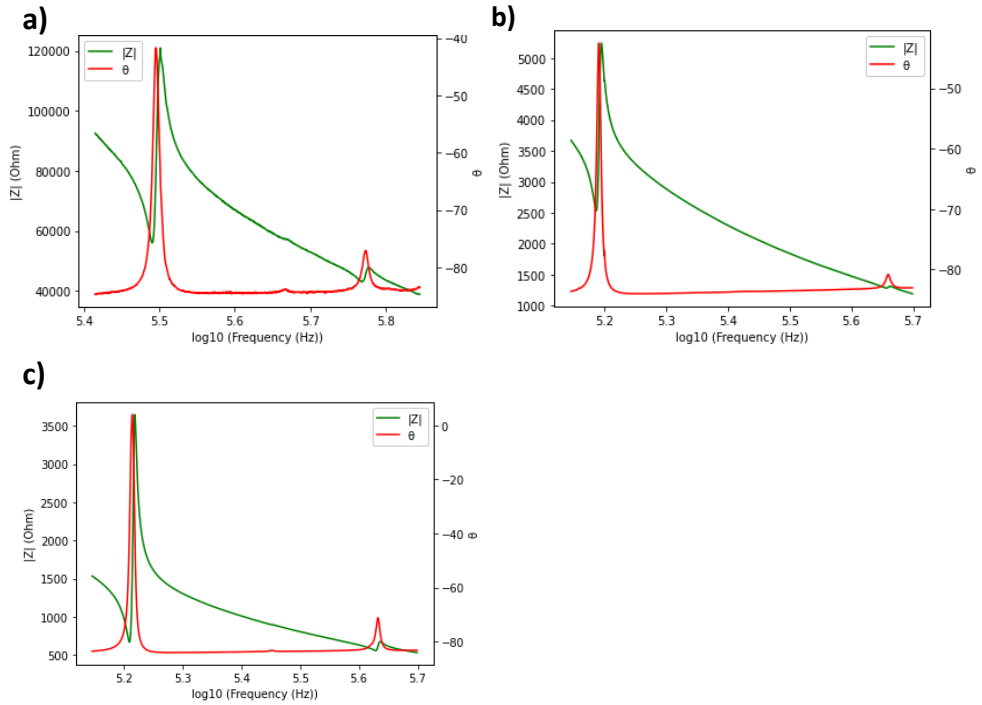

Figure 5.52: PRAP graphs for unquenched BF-BT-Mn; a) Length Extensional b) Length Thickness Extensional c) Radial Extensional

Figure 5.52 shows the LE, LTE and RE modes respectively for the unquenched BF-BT-Mn samples. The data obtained from PRAP is listed in table 5.26:

Table 5.26: Full matrix of unquenched BF-BT-Mn

Length Extensional	
f_a (Hz)	3.143 x 10^5
f_r (Hz)	3.117 x 10^5
k_{33}	0.1443
d_{33} (C/N)	6.831 x 10^{-11}
g_{33} (Vm/N)	1.122 x 10^{-3}
Longitundinal Thickness Extensional	
f_a (Hz)	7.78547 x 10^5
f_r (Hz)	7.78589 x 10^5
k_{31}	0.01674
d_{31} (C/N)	1.798 x 10^{-13}
g_{31} (Vm/N)	-5.533 x 10^{-4}
Radial Extensional	
f_{r1} (Hz)	1.626 x 10^5
f_{a1} (Hz)	1.6503 x 10^5
f_{r2} (Hz)	4.287 x 10^5
d_{31} (C/N)	3.367 x 10^{-11}
k_p	0.1915
σ^p	0.291

The d_{33} that was calculated from PRAP is 68.31 pC/N, which is greater than the measured d_{33} for unquenched BF-BT-Mn poled at 2.0 kV/mm at room temperature (46 pC/N), and more closely resembles the values obtained at 2.5 kV/mm and 3.0 kV/mm (61 and 73 pC/N respectively). The electromechanical coupling factors (the k coefficients) all show very low values, including a k_{33} of 0.1443 and a k_p of 0.1915, indicating that no more than 3.6% of its input energy is produced as useful output energy (as k^2 represents the ratio between input and output energy). There is a huge disparity in k-coefficients between the LE and RE dimensions, and the LTE cut as the k_{31} value is 0.01674. The LTE sample has performed especially poorly with regards to the PRAP measurements, indicating that the sample used is of subpar quality, as the d_{31} measurement is 0.1798 pC/N, significantly lower than the d_{31} measurement.

5.4.2.4 BF-BT-Mn (air-quenched) Results

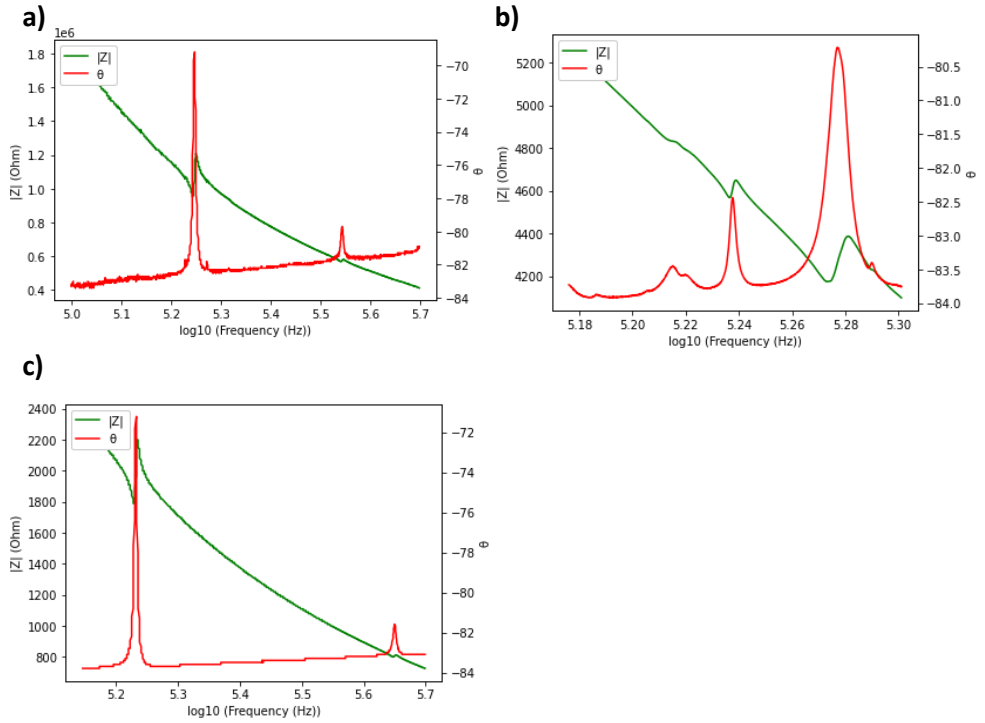

Figure 5.53: PRAP graphs for air-quenched BF-BT-Mn; a) Length Extensional b) Length Thickness Extensional c) Radial Extensional

The d_{33} recorded for air-quenched BF-BT-Mn is 180.5 pC/N which is abnormally high for this material given the poling conditions. From the poling study in section 5.2.4, the recorded d_{33} for 2.0 kV/mm at room temperature was 39 pC/N, and the maximum d_{33} achieved by the air-quenched BF-BT-Mn was 174 pC/N poled at 5.0 kV/mm at 80°C. The k_{33} is 0.1888 and the k_{31} is 0.1048, which are both higher than the unquenched sample, however the k_p is only 0.05705. The d_{31} recorded for the RE sample was 6.719 pC/N, which is less than 2% the value obtained during the poling study. The reason for some of the values calculated are possibly down to abnormalities in the geometries or an error in the program, which result in incorrect readings being calculated. In the case of the LE sample, the former is more likely, as that would have been caused by an error in the cutting process as it is difficult to finely cut samples accurately to the desired geometries (thicknesses of ≈1mm). For the RE sample, this could also be down to a case of a poor-quality sample. However, as seen in figure 5.53, the plots are shown to not be smooth and somewhat jagged: this is due to the impedance analyser recording the impedances in whole numbers instead of integers, which could be the result of an error in the equipment.

Table 5.27: Full matrix of air-quenched BF-BT-Mn.

Length Extensional	
f_a (Hz)	1.6504×10^5
f_r (Hz)	1.6262×10^5
k_{33}	0.1888
d_{33} (C/N)	1.805×10^{-10}
g_{33} (Vm/N)	2.676×10^{-4}
Longitundinal Thickness Extensional	
f_a (Hz)	1.398×10^5
f_r (Hz)	1.396×10^5
k_{31}	0.1048
d_{31} (C/N)	1.04×10^{-9}
g_{31} (Vm/N)	0.02005
Radial Extensional	
f_{r1} (Hz)	1.705×10^5
f_{a1} (Hz)	1.707×10^5
f_{r2} (Hz)	4.465×10^5
d_{31} (C/N)	6.719×10^{-12}
k_p	0.05705
σ^p	0.3165

5.4.2.5 BF-BT-Mn-Sm (unquenched)

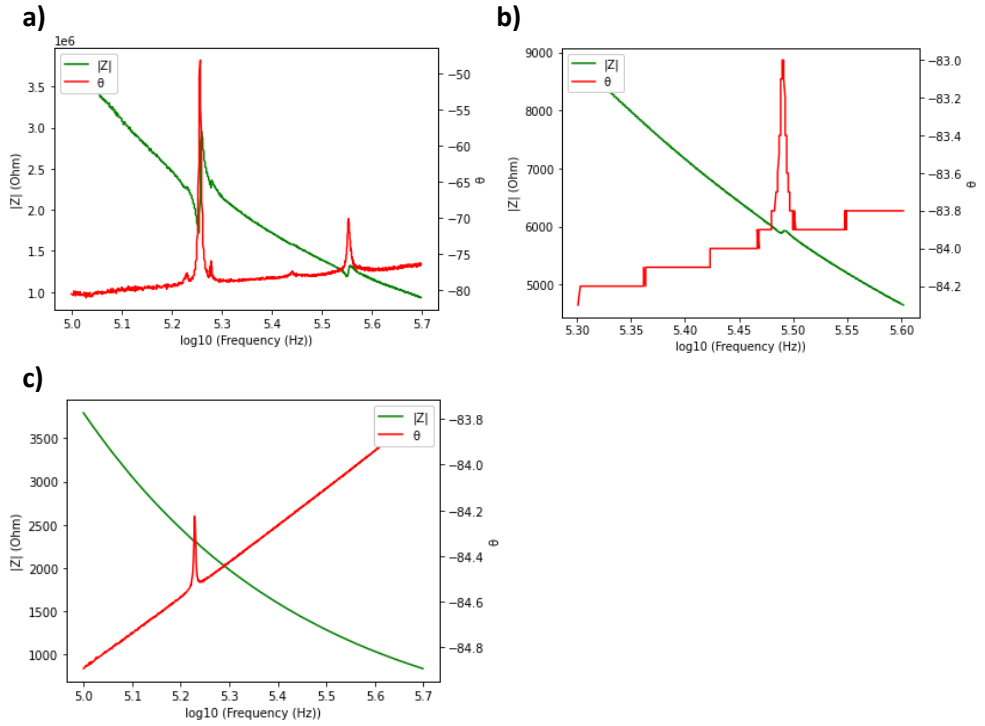

Figure 5.54: PRAP graphs for unquenched BF-BT-Mn-Sm. a) Length Extensional, b) Length Thickness Extensional, c) Radial Extensional

Table 5.28: Obtained matrix of unquenched BF-BT-Mn for the LE mode. The LTE and RE modes were unavailable due to the lack of resonant and anti-resonant frequencies in the PRAP measurements.

Length Extensional	
f_a (Hz)	1.809 x 10^5
f_r (Hz)	1.802 x 10^5
k_{33}	0.0948
d_{33} (C/N)	3.529 x 10^{-12}
g_{33} (Vm/N)	3.627

For the unquenched BF-BT-Mn-Sm sample, only the LE matrix of results was obtained. The other two samples failed to show a resonant and anti-resonant frequency as seen in figure 5.54. Poling all samples at 2.0 kV/mm at room temperature induced a very poor piezoelectric response and poling at higher fields or temperatures only resulted in sample breakages. For the LTE sample, the phase measurements were only recorded by the impedance analyser in whole numbers, resulting in another plot with sharp edges.

The LE sample showed a very poor d_{33} of 3.529 pC/N (the value for the same conditions as measured during the poling study was 19 pC/N), and k_{33} of 0.0948. The g_{33} value was recorded as 3.627, which is significantly larger by magnitude compared to the values obtained for the BF-BT-Mn samples. This could be down to an error in the measurement process (either due to the program or the sample may have clamped down too firmly), or the quality of the sample was poor, due to an error that occurred during the cutting process.

5.4.2.6 BF-BT-Mn-Sm (air-quenched) Results

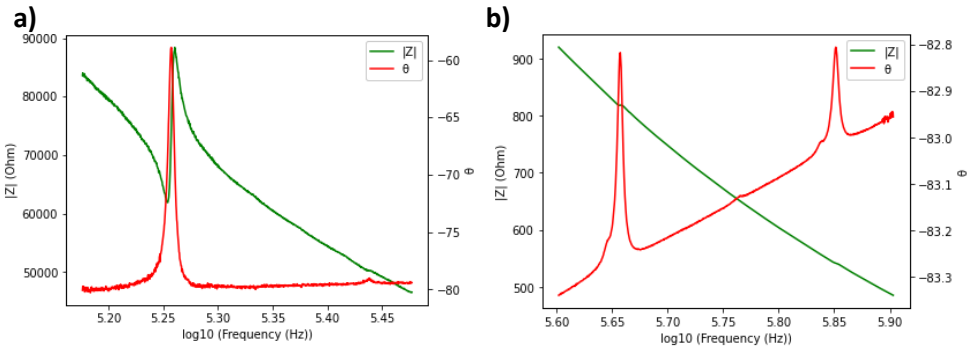

Figure 5.55: PRAP graphs for air-quenched BF-BT-Mn-Sm. a) Length Extensional, b) Radial Extensional

Table 5.29: Obtained matrix for LE mode of air-quenched BF-BT-Mn-Sm, as the lack of a significant f_r and fa value for the RE mode made matrix calculations impossible.

Length Extensional	
f_a (Hz)	1.812 x 10^5
f_r (Hz)	1.806 x 10^5
k_{33}	0.0835
d_{33} (C/N)	9.556 x 10^{-11}
g_{33} (Vm/N)	7.93 x 10^{-4}

No data was obtained for the LTE due to sample breakages at low poling fields. No resonant or anti-resonant peak was detected for the RE sample, making it impossible to calculate piezoelectric coefficients. The d_{33} calculated for the LE sample was 95.56 pC/N, which is almost 3 times the value obtained in the poling study (36 pC/N). The k_{33} was 0.0835, which is lower than the other materials.

5.4.2.7 PRAP Results Conclusion

Overall, the PRAP measurements have been shown to be inconsistent in terms of the d_{33} values obtained from the Berlincourt measurements and the poling study. Both BF-BT-Mn samples and the air-quenched BF-BT-Mn-Sm sample had d_{33} values that were significantly greater in PRAP than they were during the Berlincourt measurements, whereas the unquenched BF-BT-Mn-Sm sample had a PRAP-measured d_{33} that was less than 20% of the value obtained from the Berlincourt meter. The k-coefficients for all materials failed to exceed 0.20, with some dimensions even failing to reach 0.10. The unreliability of the results calls into question the validity of the other coefficients, as the formulae use the d-coefficients to calculate them.

One reason for the irregularities in the values obtained could be the quality of the sample cuts. This might be due to the saw of the precision cutter not producing a smooth cut because of alignment issues or the saw being blunt at the edge. Smoother cuts were noticeably harder to produce for smaller lengths (≈0.5 mm) and have even resulted in sample breakages during cutting. The small lengths were required to match the IEEE sample geometry standards for piezoelectric characterisation measurements and be within the electrical poling limitations of the equipment that was available.

It is also probable that the PRAP software used is not suitable for lead-free systems due to it being primarily developed for testing PZT, using assumptions based on data that relies heavily on PZT [81].

6. Summary and Conclusion

$BiFeO_3$-$BaTiO_3$ is one of the most researched lead-free candidates to replace PZT, due to its high T_c, reasonable piezoelectric coefficients, and high thermal stability. BFO-BTO is found to have a morphotropic phase boundary, similar to the one found within the phase transitions of PZT. The high T_c of $BiFeO_3$ also provides better piezoelectricity at higher temperatures than PZT. In addition, the production of BFO-BTO provides a significantly smaller environmental cost than that of PZT, making it more sustainable for production in the long run. BFO-BTO also does not possess any material that is limited by EU environmental legislation, making it a very suitable candidate to replace PZT.

The main aims and objectives of this work, as stated in chapter 1, are to:

- Prepare and test BFO-BTO samples for their structural and electrical characteristics.
- Continually optimise the piezoelectric properties of BFO-BTO through Sm and Mn doping and variation in processing methods such as altering the sintering temperatures and testing different quenching methods.
- Measure the impedance spectroscopy and perform a full-matrix characterisation of the different BFO-BTO compositions.

The first composition studied was BF-BT-Sm based on a formula developed by Habib et al. (2021), with a claimed d_{33} of 334 pC/N and T_c of 454°C [62]. After conducting permittivity vs temperature measurements and poling studies, the highest d_{33} achieved was 95 pC/N along with a T_c of 433°C. Although Habib et al. water-quenched their samples to get the best d_{33}, air-quenching BF-BT-Sm in this work failed to significantly improve the d_{33}, thereby calling into question the feasibility of reproducing this composition. It is possible that air-quenching may have damaged the microstructure in some ways, however there is no significant evidence from the SEM to suggest that this was the case. Another suggestion may be that there is a significant amount electron conduction present in the material, which inhibits the piezoelectricity. It is suggested therefore that a more thorough investigation of Sm-doping should be done, for example: preparing and testing smaller increments of Sm-dopant concentration (i.e. x=0.001 increments), more SEM to be done to further observe the microstructure and perform X-ray photoelectron spectroscopy (XPS) to check the chemical state of the material.

Mn-doping BF-BT was then studied, and different doping sites (Fe and Ti sites) were compared to one another. Doping on the Ti-site was shown to have increased the T_c to 517°C (compared to 499°C for the Fe-site doped samples), however doping on the Fe-site (especially after air-quenching) was shown to have significantly improved the piezoelectricity during the poling study, achieving a maximum d_{33} of 174 pC/N. This figure is shown to be significantly higher than the literature value quoted by Kim et al. (2013), which was 135 pC/N [68]. The Ti-site doped samples achieved a maximum d_{33} of 135 pC/N, which was also higher than the literature value (Jabeen et al. 2022) of 128 pC/N [70].

Impedance spectroscopy of BF-BT-Mn (Fe-site doped) has shown that both E_a and σ_0 decrease with a faster cooling rate. The conductivity at the poling temperature 80°C (σ_{80}) is also significantly higher for the unquenched sample, and lowest for the air-quenched sample, which corresponds to the lowest and highest d_{33} values respectively. In this case, d_{33} seems to be limited by conductivity, as a higher conductivity results in a lower d_{33}. From the impedance spectroscopy, it is suggested that oxygen vacancy conduction dominates the conductivity for the unquenched sample, resulting in a higher E_a. Quenching prevents oxygen vacancies from forming and therefore reduces the E_a for the samples. In comparison to the impedance spectroscopy of the undoped BF-BT sample, Mn-doping seems to reduce the conductivity and double the activation energy. This could be due to the Mn-dopants trapping electrons and preventing excess conduction.

A novel BF-BT composition compromising of Mn-dopant on the Fe-site and Sm-dopant on the Ba-site was also prepared and tested. The maximum d_{33} achieved was 161 pC/N after air-quenching, with a T_c of 494°C. In general, for all samples it was found that air-quenching significantly improved the T_c and d_{33} and produced a microstructure with significantly fewer defects according to the scanning electron microscopy. The E_a values are similar to the ones of BF-BT-Mn, with a similar trend of E_a decreasing with a faster cooling rate. However, the conductivity for the unquenched sample is the lowest, and highest for the water-quenched sample. This also correlates with a significantly higher d_{33} for the unquenched sample, and a poor value for the water-quenched sample. For both BF-BT-Mn and BF-BT-Mn-Sm, it can be seen that higher conductivities correspond with lower d_{33}, indicating that conductivity is the limiting factor in d_{33} coefficients.

PRAP measurements were done for BF-BT-Mn and BF-BT-Mn-Sm with the aim of obtaining a full-matrix characterisation. However, the results obtained were inconsistent and unrealistic, which suggested that PRAP may not be a reliable way of measuring piezoelectric coefficients.

Table 6.1 lists the best piezoelectric values between the BF-BT compositions produced during this project (along with the values from the literature), and the values from Boston Piezo Optic's hard-piezoelectric materials, PZT-4 and PZT-8 (due to their comparable applications) [38]:

Material	**T_c (°C)**	**d_{33} (pC/N)**
BF-BT-Mn (Schulz)	499	174
BF-BT-Mn (Kim et al.) [68]	n/a	135
BF-BT-Mn-Sm (Schulz)	495	161
BF-BT-Sm (Schulz)	433	95
BF-BT-Sm (Habib et al.) [62]	454	334
PZT-4 [38]	325	295
PZT-8 [38]	300	225

Table 6.1: T_c and d_{33} values of BF-BT samples produced for this work and from the literature, and the values for PZT-4 and PZT-8.

BF-BT-Mn has very strong potential to become a candidate to compete with PZT, due to having a higher T_c value compared to the PZT compositions listed in table 6.1. The research done here suggests that BF-BT-Mn should continue to be a significant piezoelectric material of interest, and more research will need to be done to explore its full capabilities.

6.1 Future Work

BF-BT provides a very strong platform for future work in the field of lead-free piezoceramics, and there are a number of suggestions for future opportunities to explore the material's full capabilities and potential.

The first would be to understand the mechanisms of BF-BT by undertaking a more rigorous approach to the study of the materials microstructure. For this work, SEM has only been carried out on the Fe-site doped samples, and more SEM undertaken on samples that have been doped on the Ti-site and consist of higher amounts of dopant would provide a more thorough insight into the effects on grain-growth of the BF-BT system. XRD calorimetry would also be a useful measurement to undertake, to gain a better understanding as to how the crystal structure varies with temperature variables. More research is also needed in order to better understand the effects of quenching and the reason why the material performs better after this process.

Material optimisation of BF-BT is also a strong area of future work. Performing various studies on the effects of sintering temperature and time, annealing and other forms of heat treatment, and trying out different milling methods along with other processing variables would be essential in optimising the piezoelectricity of BF-BT. Testing out different dopants such as Ga is another solution, as well as looking at different concentrations of Mn-dopant for a more thorough investigation of the electronic to oxygen vacancy conduction.

Another future aim would be to test BF-BT in devices, such as Sonar transducer devices, and compare their performances to devices containing PZT. There are very few papers that conduct research on BF-BT's performance in transducer applications, and testing the material in devices would improve understanding as to how BF-BT performs in different environments.

Bibliography

[1] Rodel, J., Jo, W., Seifert, K. T. P., Anton, E. M. and Granzow, T. 2009. *Perspective on the Development of Lead-free Piezoceramics.* J. Am. Ceram. Soc., **92** (6), pp. 1153-1177.

[2] *Official Journal of the European Union.* 2011. **65**, pp.10-12

[3] Panda, P. K. 2009. *Review: Environmental Friendly Lead-free Piezoelectric Materials*. J. Mater Sci, **44**, pp.5049-5062.

[4] Zheng, T., Wu, J., Xiao, D. and Zhu, J. 2018. *Recent Development in Lead-free Perovskite Piezoelectric Bulk Materials.* Progress in Materials Science. **98**, pp. 552-624.

[5] Mauguin, C. 1931. *Sur le Symbolisme des Groupes de Répetition ou de Symétrie des assemblages Cristallins. Zeitschrift für Kristallographie.* Crystalline Materials. **76**, p.16.

[6] Hammond, C. 2009. *The Basics of Crystallography and Diffraction, 3rd edition*. New York: Oxford University Press Inc.

[7] Suryanarayana, C. and Norton, M. G. 2013. *X-Ray Diffraction: A Practical Approach, 2nd edition.* New York: Springer Science & Business Media.

[8] Ashcroft, N. W. and Mermin, N. D. 1976. *Solid State Physics*. New York: Holt, Rinehart and Winston.

[9] Moulson, A. J. and Herbert, J. M. 2003. *Electroceramics. 2nd ed.* John Wiley and Sons.

[10] Goldschmidt, V. M. 1926. *Die Gesetze der Krystallochemie.* Naturwissenschaften. **14**(21), p. 9.

[11] Kronmuller, H., Parkin, S. S. P., Johnsson, M. and Lemmens, P. 2007. *Handbook of Magnetism and Advanced Magnetic Materials.* Hoboken, NJ: John Wiley & Sons.

[12] Ahart, M., Somayazulu, M., Cohen, R. E., Ganesh, P., Dera, P., Mao, H. K., Hemley, R. J., Ren, Y., Liermann, P. and Wu, Z. 2008. *Origin of morphotropic phase boundaries in ferroelectrics.* Nature, **451**(7178), pp.545-548.

[13] Jaffe, B., Cook Jr., W. R., and Jaffe, H. 1971 *Piezoelectric Ceramics.* London and New York: Academic Press.

[14] Hartmann, E. 1984. *An Introduction to Crystal Physics.* Cardiff: University College Cardiff Press.

[15] Holterman, J. and Groen, P. 2012. *An Introduction to Piezoelectric Materials and Components.* Stichting Applied Piezo.

[16] Lu, Y., Wei, T., Duewer, F., Lu, Y., Ming, N. B., Schultz, P. G. and Xiang, X. D. 1997. *Nondestructive Imaging of Dielectric-Constant Profiles and Ferroelectric Domains with a Scanning-Tip Microwave Near-Field Microscope.* Science. **276** (5321), pp. 2004-2006.

[17] Cochran, S. 2012. *Piezoelectricity and Basic Configurations for Piezoelectric Ultrasonic Transducers. Ultrasonic Transducers: Materials and Design for Sensors, Actuators and Medical Applications*. Woodhead Publishing Series in Electronic and Optical Materials, pp. 3-35.

[18] *Piezoelectric Ceramics: Principles and Applications*. 2006. APC International Ltd.

[19] Linnaeus, C. 1747. *Flora Zeylanica: Sistens Plantas Indicas Zeylonae Insulae [The Flora of Ceylon: consisting of Indian plants of the island of Ceylon]* (Stockholm ("Holmiae"), Sweden: Laurentii Salvii.

[20] Aepinus, F. 1756. *Memoire concernant quelques nouvelles experiences électriques remarquables [Memoir concerning some remarkable new electrical experiments],* Histoire de l'Académie royale des sciences et des belles lettres (Berlin) **12**, pp. 105-121.

[21] Curie, J. and Curie, P. 1880. *Développement par compression de l'électricité polaire dans les cristaux hémièdres à faces inclines.* Bulletin de la Société Minéralogique de France. **3** (4), pp. 90-93.

[22] Curie, J. and Curie, P. 1881. *Contractions et dilatations produites par des tensions dans les cristaux hémièdres à faces inclinées [Contractions and expansions produced by voltages in hemihedral crystals with inclined faces].* Comptes Rendus. **93**, pp. 1137–1140.

[23] Molinie, P. and Boudia, S. 2009. *Mastering Picocoloumbs in the 1890s: The Curies' Quartz-Electrometer Instrumentation, and how it shaped early Radioactivity History.* Journal of Electrostatics. **67** (2-3), pp. 524-530.

[24] Katzir, S. 2012. *Who knew piezoelectricity? Rutherford and Langevin on submarine detection and the invention of sonar.* Notes Rec. R. Soc. **66** (2), pp. 141–157.

[25] Mason, W. P. 1981. *Piezoelectricity, its history and applications.* Journal of the Acoustical Society of America. **70**(6).

[26] Valasek, J. 1921. *Piezo-Electric and Allied Phenomena in Rochelle Salt*. Physical Review. **17** (4), pp. 475–481.

[27] Thurnauer, H., Deaderick, J. W. and Badger, A. E. 1944. *Ceramic electrical insulation.* Digest of Literature on Dielectrics, Washington, DC, USA. **8**, pp. 96-101.

[28] Wainer, E. and Salomon, N. 1943. *Electrical Reports Titanium Alloys Manufacturing Division, National Lead Co.* Reports No. 8, 9, 10.

[29] Ogawa, S. 1946. *On Polymorphic Change of Barium Titanate.* J. Phys. Soc. Jpn. **1** (1), pp. 32-33.

[30] Wul, B. M. and Goldman, I. M. 1954. *Dielectric Constants of Titanates of Metals of the Second Group* Dokl. Akad. Nauk. SSSR. **46** (154)

[31] Cross, L. E., Newnham, R. E. 1987. *History of Ferroelectrics.* The American Ceramic Society, **3**.

[32] Shirane, G., Takeda, A. 1952. *Phase Transitions in Solid Solutions of $PbZrO_3$ and $PbTiO_3$ (I) Small Concentrations of $PbTiO_3$.* Journal of the Physical Society of Japan, **7** (1), pp. 5-11

[33] Jaffe, B., Roth, R. S., Marzullo, S. 1954. *Piezoelectric Properties of Lead Zirconate-Lead Titanate Solid Solution Ceramics.* Journal of Applied Physics. **25** (6), pp. 809-810.

[34] Sawaguchi, E. 1953. *Ferroelectricity versus Antiferroelectricity in the Solid Solutions of $PbZrO_3$ and $PbTiO_3$.* Journal of the Physical Society of Japan. **8** (5), pp. 615-629.

[35] Shrout, T. R. and Zhang, S. J. 2007. *Lead-free Piezoelectric Ceramics: Alternatives for PZT?* Journal of Electroceramics. **19**, pp. 113-126.

[36] Noheda, B., Cox, I. M., Shirane, G., Gonzalo, J. A., Cross, L. E. and Park, S. E. 1999. *A monoclinic ferroelectric phase in the Pb(Zr1−xTix)O3 solid solution.* Applied Physics Letters. **74** (14), pp. 2059-2061.

[37] Horchidan, N., Ciomaga, C. E., Frunza, R. C., Capiani, C., Galassi, C., Mitoseriu, L. 2016. *A Comparative Study of Hard/Soft PZT-based Ceramic Composites.* Ceramics International, **42** (7), pp. 9125-9132.

[38] Boston Piezo Optics Inc. 2021. *Ceramic Materials PZT.* [Online]. [Accessed 16 January 2021] Available at: https://www.bostonpiezooptics.com/ceramic-materials-pzt

[39] Hong, C. H., Kim, H. P., Choi B. Y., Han, H. S., Son, J. S., Ahn, C. W., Jo, W. 2016. *Lead-free Piezoceramics-Where to Move On?* J Materiomics **2**, pp. 1-24.

[40] Matthias, B. T., Remeika, B. T. 1951. *Dielectric Properties of Sodium and Potassium Niobates.* Physical Review, **82** (5), pp. 727-729.

[41] Shirane, G., Newnham, R. and Pepinsky, R. 1954. *Dielectric properties and phase transition of $NaNbO_3$ and (Na,K)NbO_3.* Phys Rev. **96** (3), pp. 581-588.

[42] Wood, E. A. 1950. *Polymorphism in Potassium Niobate, Sodium Niobate, and other ABO_3 Compounds.* Acta Crystal **1951** (4), pp. 353-362.

[43] Saito, Y., Takao, H., Tani, T., Nonoyama, T., Takatori, K., Homma, T., Nagaya, T., and Nakamura, M. 2004. *Lead-Free Piezoceramics*. Nature. **432**, pp. 84-87.

[44] Kosec, M., Malic, B., Bencan, A., and Rojac, T. 2008. *KNN-Based Piezoelectric Ceramics. Piezoelectric and Acoustic Materials for Transducer Applications.* Boston: Springer US, pp. 81-102.

[45] Egerton, L. and Dillon, D. M. 1959. *Piezoelectric and Dielectric Properties of Ceramics In The System Potassium-Sodium Niobate.* Journal of the American Ceramic Society. **42** (9), pp. 438-442.

[46] Zhang, S., Xia, R., Shrout, T. R., Zang, G., and Wang, J. 2006. *Characterization of Lead Free (K0.5Na0.5)NbO3-LiSbO3 Piezoceramic.* Solid State Communications. **141** (12), pp. 675- 679.

[47] Hollenstein, E., Damjanovic, D., and Setter, N. 2007. *Temperature Stability of the Piezoelectric Properties of Li-Modified KNN Ceramics.* Journal of the European Ceramic Society. **27** (13), pp. 4093-4097.

[48] Yang, J., Zhang, F., Yang, Q., Liu, Z., Li, Y., Liu, Y., and Zhang, Q. 2016. *Large Piezoelectric Properties in KNN-Based Lead-free Single Crystals.* Applied Physics Letters. **108**, 182904.

[49] Gagliardi, M. 2019. *Lead-Free Piezoelectric Ceramics: Technologies and Global Opportunities.* BCC Publishing.

[50] Smolenskii, G., Isupov, V., Agranovskaya, A. and Krainik, N. 1961. *New ferroelectrics of complex composition.* Sov. Phys. Solid State. **2**, pp. 2651–2654.

[51] Zvirgzds, J.A., Kapostin, P.P., Zvirgzde, J.V. and Kruzina, T.V. 1982. *X-ray study of phase transitions in ferroelectric $Na_{0.5}Bi_{0.5}TiO_3$.* Ferroelectrics. **40** (1), pp. 75–77.

[52] Bousquet, M., Duclere, J.R., Orhan, E., Boulle, A., Bachelet, C. and Champeaux, C. 2010. *Optical properties of an epitaxial $Na_{0.5}Bi_{0.5}TiO_3$ thin film grown by laser ablation: Experimental approach and density functional theory calculations.* J. Appl. Phys. **107** (10), pp. 104107–104113

[53] Takenaka, T., Maruyama, K. I., and Sakata, K. 1991. *System for Lead-Free Piezoelectric Ceramics.* The Japan Society of Applied Physics. **30** (2236), pp. 2236-2239.

[54] Supriya, S., Kalainathan, S. and Swaroop, S. 2010. *Synthesis and Characterization of NBT Powders by Stearic Acid Gel Method.* Archives of Applied Science Research. **2** (5), pp. 386-391.

[55] Herabut, A., Safari, A. 2005. *Processing and Electromechanical Properties of $(Bi_{0.5}Na_{0.5})_{(1-1.5x)}La_xTiO_3$.* Ceramics. 80(11), pp. 2954-2958.

[56] Chu, B. J., Chen, D. R., Li, G. R. and Yin, Q. R. 2002. *Electrical Properties of Na0.5Bi0.5TiO3 Ceramics.* Journal of the European Ceramic Society. **22** (13), pp. 2115-2121.

[57] Wang, X., Chan, H. L. W. and Choy, C. L. 2003. *Piezoelectric and dielectric properties of CeO2-added (Bi0.5Na0.5)0.94Ba0.06TiO3 lead-free ceramics*. Solid State Communications. **125**(7), pp.395-399.

[58] Wang, X., Chan, H. L. W. and Choy, C. L. 2005. *(Bi0.5Na0.5)0.94Ba0.06TiO3 lead-free ceramics with simultaneous addition of CeO2 and La2O3.* Applied Physics A. **80**(2), pp.333- 336.

[59] Sasaki, A., Chiba, T., Mamiya, Y. and Otsuki, E. 1999. *Dielectric and Piezoelectric Properties of (Bi0.5Na0.5)TiO3–(Bi0.5K0.5)TiO3 Systems.* Japanese Journal of Applied Physics. **36**, p.4.

[60] Yu, Z., Ang, C., Guo, R., and Bhalla, A. S. 2002. *Piezoelectric and Strain Properties of Ba(Ti1-XZrx)O3 Ceramics.* Journal of Applied Physics. **92** (3), pp. 1489-1493.

[61] Wang, D., Wang, G., Murakami, S., Fan, Z., Feteira, A., Zhou, D., Sun, S., Zhao, Q. and Reaney, I. M. 2018. *$BiFeO_3$-$BaTiO_3$: A New Generation of Lead-free Electroceramics.* Journal of Advanced Dielectrics. **8**(6), pp. 1830004-1830004

[62] Habib, M., Ahmad, P., Akram, F., Iqbal, M., Karoui, A., Kim, M. H., Lee, S., Yeo, H., Khandaker, M., Song, T. K. 2021. *Large and temperature-insensitive piezoelectric performance in the lead-free Sm-doped BiFeO3-BaTiO3 ceramics with high Curie temperature.* Ceramics International **48**(18), pp. 22608-26617.

[63] Fedulov, S. A., Ladyzhinskii, P. B., Pyatigorskaya, I. L. and Venevtsev, Y.N. 1964. *Complete Phase Diagram of the PbTiO3-BiFeO3 System.* Sov. Phys. Solid State, **6**(2), pp. 375-378.

[64] Fedulov, S. A. and Venevtsev, Y. N. 1962. *Investigation of the structure and dielectric properties of solid solutions of (Pb,Sr)(Ti,Zr)O3.* Sov. Phys. Solid State, **3** (11), pp. 2447-2450.

[65] Kumar M. M., Srinivas, A. and Suryanarayana, S. V. 1999 *Structure property relations in BiFeO3/BaTiO3 solid solutions.* Journal of Applied Physics. **87** (2), pp. 855.

[66] Leontsev, S. O., Eitel, R. E. 2009. *Dielectric and Piezoelectric Properties in Mn-Modified (1-x)$BiFeO_3$-x$BaTiO_3$ Ceramics.* Journal of the American Ceramic Society, **92** (12), pp.2957-2961.

[67] Lee, M. H., Kim, D. J., Park, J. S., Kim, S. W., Song, T. K., Kim, M. H., Kim, W. J., Do, D. and Jeong, I. K. 2015. *High-Performance Lead-free Piezoceramics with High Curie Temperatures.* Advanced Materials. **2015** (27), pp. 6976-6982.

[68] Kim D. J., Lee M. H., Park J. S., Kim M. H. T., Song K., Kim S. W., Kim W. J., Jang K. W., Kim S. S. and Do D. 2014. *Ferroelectric and piezoelectric properties of Mn-modified BiFeO3-BaTiO3 ceramics.* J Electroceram. **2014** (33), pp. 37-41

[69] Lalitha, K. V., Wang, B., Ren, P., Hall, D. A., Rojac, T. 2022. *Quenching Effects and Mechanisms in Bismuth-based Perovskite Ferroelectrics.* Open Ceramics **10** (2022), pp. 100259

[70] Jabeen F., Shahid R., Shahid Khan M. and Pandey R. 2022. *Effect of Mn doping on the structural, spectral, electrical, ferromagnetic and piezoelectric properties of 0.7BFO-0.3BTO lead-free ceramics.* Journal of Alloys and Compounds. **917** (2022), 165303

[71] Wan, Y., Li, Y., Li, Q., Zhou, W., Zheng, Q., Wu, X., Xu, C., Zhu, B., and Lin, D. 2014. *Microstructure, Ferroelectric, Piezoelectric, and Ferromagnetic Properties of ScModified BiFeO3-BaTiO3 Multiferroic Ceramics with MnO2 Addition.* Journal of the American Ceramic Society. **97** (6), pp. 1809-1818.

[72] Unruan, S., Yimnirun, R., Unruan, M., and Tipakontitikul, R. 2019. *Effect of BaZr0.4Ti0.6O3 Addition on Electrical and Magnetic Properties of Multiferroic (1-x)BiFeO3-xBaTiO3 Ceramics.* Ferroelectrics. **534** (1), pp. 103-109.

[73] Zheng, Q., Luo, L., Lam, K. H., Jiang, N., Guo, Y., and Lin, D. 2014. *Enhanced Ferroelectricity, Piezoelectricity, and Ferromagnetism in Nd-modified BiFeO3-BaTiO3 Lead-free Ceramics.* Journal of Applied Physics. **116** (2014), 184101.

[74] Zheng, T. and Wu, J. 2016. *Quenched Bismuth Ferrite-Barium Titanate Lead-free Piezoelectric Ceramics.* Journal of Alloys and Compounds. **676** (2016), pp. 505-512.

[75] Ahmed, T., Khan, S. A., Akram, F., Bae, J., Choi, S. Y., Hussain, A., Song, T. K., Sung, Y. S., Kim, M. H., and Lee, S. 2020. *Enhanced Electromechanical Properties of 0.65Bi1.05FeO3- 0.35BaTiO3 Ceramics through Optimizing Sintering Conditions.* Phys. Status Solidi. **2020** (217), 1900970.

[76] Lee, M. H., Kim, D. J., Park, J. S., Kim, S. W., Song, T. K., Kim, M. H., Kim, W. J., Do, D., and Jeong, I. K. 2015. *High-Performance Lead-free Piezoceramics with High Curie Temperatures*. Advanced Materials. **2015** (27), pp. 6976-6982.

[77] LIU, W. and REN, X. 2009. *Large piezoelectric effect in Pb-free ceramics*. Phys Rev Lett. **103**(25), p.257602.

[78] Ji, X., Wang, C., Harumoto, T., Zhang, S., Tu, R., Shen, Q. and Shi, J. 2020. *Structure and Electrical Properties of BCZT Ceramics Derived from Microwave-*

assisted Sol-Gel-Hydrothermal Synthesized Powders. Scientific Reports, **10** (2020), 20352.

[79] Bragg, W. H. and Bragg, W. L. 1913. *The Reflexion of X-rays by Crystals*. Proceedings of the Royal Society A. **88** (605), pp. 428-438.

[80] SERC. 2010. *Bragg's Law Derivation Diagram*. [Online]. [Accessed 30 May 2021]. Available at: https://serc.carleton.edu/details/images/20375.html

[81] Parry, S. J. 2019. *KN-based Lead-free Ferroelectric Materials for Sonar Applications.* Ph.D. thesis, University of Leeds.

[82] Atteberry, J. 2021. *HowStuffWorks: How Scanning Electron Microscopes Work.* [Online]. [Accessed 30 May 2021]. Available at: https://science.howstuffworks.com/scanningelectron-microscope1.htm

[83] Jordan, T. L. and Ounaies, Z. 2001. *Piezoelectric Ceramics Characterization.* NASA ICASE Report. ICASE Report No. 2001-28.

[84] *IEEE Standard Definitions and Methods of Measurement for Piezoelectric Vibrators*. 1966. IEEE Std. 177.

[85] Fenu, N. G., Giles-Donovan, N., Sadiq, M. R. and Cochran, S. 2021. *Full Set of Material Properties of Lead-Free PIC 700 for Transducer Designs.* IEEE Transactions on Ultrasonics, Ferroelectrics, and Frequency Control, **68** (5), pp. 1797-1807.

[86] Cain, M. G. and Stewart, M. 2001. *Piezoelectric Resonance.* National Physical Laboratory: Measurement Good Practice Guide. 33.

[87] Magar, H.S., Hassan, R.Y.A. and Mulchandani, A. 2021. *Electrochemical Impedance Spectroscopy (EIS): Principles, Construction, and Biosensing Applications.* Sensors, **21,** 6578.

[88] Gerhardt, R. 1994. *Impedance and Dielectric Spectroscopy Revisited: Distinguishing Localized Relaxation from Long-Range Conductivity.* J. Phys. Che. Solids. **55** (12), pp.1491-1506.

[89] Schmidt, R. 2007. *Impedance Spectroscopy of Electroceramics.* Ceramic Materials Research Trends 2007, pp.321-351.

[90] Irvine, J. T. S., Sinclair, D. C. and West, A. R. 1990. *Electroceramics: Characterization by Impedance Spectroscopy.* Advanced Materials. **2**(3), pp.132-138.

[91] Li, Y., Borbely, M. and Bell A. 2020. *The Influence of Oxygen Vacancies on Piezoelectricity in Samarium-doped $Pb(Mg_{1/3}Nb_{2/3})O_3$-$PbTiO_3$ Ceramics.* Journal of the American Ceramic Society. **2021**, pp.1-11

[92] Bell, A. J., Schlegel, T., Alduraibi, M., Khan, M. A., Comyn, T. P. and Rodel, J. 2006.
Impedance Spectroscopy of Mn-doped BiFeO3-PbTiO3 Ceramics. 2006 15th IEEE International Symposium on the Applications of Ferroelectrics, pp. 128-131.

[93] Almond, D. P. and West, A. R. 1982. *Impedance and Modulus Spectroscopy of "Real" Dispersive Conductors.* Solid State Ionics **11** (1983), pp.57-64.

[94] Hodge, I. M., Ingram, M. D. and West, A. R. 1976. *Impedance and Modulus Spectroscopy of Polycrystalline Solid Electrolytes.* J. Electroanal. Chem., **74** (1976). pp. 125-143.

[95] Kim, S., Khanal, G.P., Nam, H.W., Fujii, I., Ueno, S., Moriyoshi, C., Kuroiwa, Y. and Wada, S. 2017. *Structural and electrical characteristics of potential candidate lead-free $BiFeO_3$-$BaTiO_3$ piezoelectric ceramics*. Journal of Applied Physics. **122**(2017), pp. 0-8.

[96] Garcia de Andres, C., Caballero, F. G., Capdevila, C. and San Martin, D. 2002. *Revealing austenite grain boundaries by thermal etching: advantages and disadvantages.* Materials Characterization **49**(2), pp. 121-127.

[97] Nam, H. W., Kim, S. W., Khanal, G. P., Fujii, I., Ueno, S. and Wada, S. 2019. *Thermal annealing induced recovery of damaged surface layer for enhanced ferroelectricity in Bi-based ceramics*. Journal of Applied Physics. **58**, SLLD04.

[98] Kong, S., Kumar, N., Checchia, S., Cazorla C. and Daniels, J. 2019. *Defect-Driven Structural Distortions at the Surface of Relaxor Ferroelectrics.* Advanced Functional Materials **2019**(29), 1900344.

Appendix A: Supplementary Poling Study Data

Appendix A.1: BF-BT-Mn (Fe-site)

Table A.1: Data for BF-BT-Mn (x=0.010) poled at room temperature

Field (kV/mm)	d33 (pC/N)	tan(δ)
1	14	0.0544
1.5	21	0.0515
2	46	0.0461
2.5	61	0.0449
3	73	0.0508
3.5	76	0.0567
4	77	0.0567
4.5	78	0.0511

Table A.2: Data for BF-BT-Mn (x=0.010) poled at 80°C

Field (kV/mm)	d33 (pC/N)	tan(δ)
1	59	0.0562
1.5	78	0.0553
2	91	0.0534

Table A.3: Data for air-quenched BF-BT-Mn (x=0.010) poled at room temperature

Field (kV/mm)	d33 (pC/N)	tan(δ)
1	3	0.0352
1.5	10	0.0345
2	39	0.0338
2.5	64	0.0344
3	76	0.0365
3.5	88	0.0352
4	90	0.0377
4.5	93	0.0373
5	97	0.0372
5.5	113	0.037

Table A.4: Data for air-quenched BF-BT-Mn (x=0.010) poled at 80°C

Field (kV/mm)	d33 (pC/N)	tan(δ)
1	23	0.035
1.5	83	0.0358
2	136	0.0348
2.5	151	0.0351
3	137	0.0373
3.5	162	0.0353
4	169	0.0384
4.5	169	0.0382
5	174	0.0398

Table A.5: Data for water-quenched BF-BT-Mn (x=0.010) poled at room temperature

Field (kV/mm)	d33 (pC/N)	tan(δ)
1	23	0.0592
1.5	90	0.0611
2	112	0.0621
2.5	111	0.0612
3	114	0.0625
3.5	114	0.063
4	112	0.0627
4.5	113	0.0631
5	110	0.0616

Table A.6: Data for water-quenched BF-BT-Mn (x=0.010) poled at 80°C

Field (kV/mm)	d33 (pC/N)	tan(δ)
1	104	0.061
1.5	114	0.0608
2	115	0.0618
2.5	113	0.0606
3	116	0.0617
3.5	114	0.063
4	104	0.0621
4.5	106	0.0629
5	108	0.0635

Table A.7: Data for BF-BT-Mn (x=0.020) poled at room temperature

Field (kV/mm)	d33 (pC/N)	tan(δ)
1	1	0.0416
1.5	10	0.0336
2	27	0.0341
2.5	54	0.0349
3	75	0.0352
3.5	6	0.0404
4	105	0.0346
4.5	116	0.035
5	117	0.0355
5.5	121	0.0354
6	135	0.0351
6.5	138	0.0351

Table A.8: Data for BF-BT-Mn (x=0.020) poled at 80°C

Field (kV/mm)	d33 (pC/N)	Capacitance (pF)	tan(δ)
2	6	275	0.0396
2.5	146	315	0.0358
3	148	317	0.0357
3.5	141	313	0.0361
4	147	308	0.0353
4.5	147	315	0.0354
5	140	311	0.0358

Table A.9: Data for air-quenched BF-BT-Mn (x=0.020) poled at room temperature

Field (kV/mm)	d33 (pC/N)	tan(δ)
1	4	0.0295
1.5	12	0.0294
2	31	0.0298
2.5	63	0.0302
3	87	0.0311
3.5	107	0.0314
4	117	0.032
4.5	127	0.0311
5	125	0.0328

Table A.10: Data for air-quenched BF-BT-Mn (x=0.020) poled at 80°C

Field (kV/mm)	d33 (pC/N)	tan(δ)
1	42	0.0302
1.5	130	0.0312
2	155	0.0315
2.5	160	0.0314
3	164	0.0317
3.5	160	0.0314
4	167	0.0319
4.5	163	0.0313

Table A.11: Data for BF-BT-Mn (x=0.040) poled at room temperature

Field (kV/mm)	d33 (pC/N)	tan(δ)
1	2	0.0371
1.5	3	0.0385
2	5	0.0373
2.5	7	0.038
3	7	0.0375
3.5	7	0.038
4	8	0.0378
4.5	7	0.0374
5	9	0.0387
5.5	9	0.0379
6	9	0.0385
6.5	10	0.0381

Appendix A2: BF-BT-Mn (Ti-site)

Table A.12: Data for BF-BT-Mn (x=0.010) poled at room temperature

Field (kV/mm)	d33 (pC/N)	tan(δ)
1	7	0.0538
1.5	19	0.0492
2	41	0.0541
2.5	57	0.0487
3	68	0.0498
3.5	78	0.0463
4	83	0.0512
4.5	84	0.0567
5	91	0.0516
5.5	93	0.0562

Table A.13: Data for BF-BT-Mn (x=0.010) poled at 80°C

Field (kV/mm)	d33 (pC/N)	tan(δ)
1	92	0.0564
1.5	109	0.0522
2	121	0.0566
2.5	112	0.0517
3	119	0.0519
3.5	135	0.049
4	127	0.0535

Table A.14: Data for air-quenched BF-BT-Mn (x=0.010) poled at room temperature

Field (kV/mm)	d33 (pC/N)	tan(δ)
1	9	0.062
1.5	13	0.087
2	26	0.073
2.5	32	0.067
3	35	0.062
3.5	40	0.7
4	39	0.085
4.5	46	0.068

Table A.15: Data for air-quenched BF-BT-Mn (x=0.010) poled at 80°C

Field (kV/mm)	d33 (pC/N)	tan(δ)
1	20	0.063
1.5	23	0.088
2	38	0.0785
2.5	38	0.0725
3	44	0.067
3.5	45	0.081

Table A.16: Data for BF-BT-Mn (x=0.020) poled at room temperature

Field (kV/mm)	d33 (pC/N)	tan(δ)
1	4	0.0425
1.5	12	0.0407
2	35	0.0404
2.5	48	0.0442
3	62	0.0442
3.5	74	0.0437
4	83	0.0443
4.5	84	0.0462
5	90	0.0447
5.5	93	0.0443
6	91	0.0472
6.5	96	0.0466
7	102	0.0459

Table A.17: Data for BF-BT-Mn (x=0.020) poled at 80°C

Field (kV/mm)	d33 (pC/N)	tan(δ)
2	98	0.0472
2.5	99	0.0456
3	102	0.0458
3.5	96	0.0283
4	106	0.048
4.5	113	0.0471

Table A.18: Data for air-quenched BF-BT-Mn (x=0.020) poled at room temperature

Field (kV/mm)	d33 (pC/N)	tan(δ)
1	5	0.0368
1.5	15	0.0354
2	27	0.0355
2.5	45	0.0364
3	65	0.0358
3.5	69	0.0431
4	81	0.0384
4.5	86	0.0404
5	93	0.0397
5.5	105	0.0394
6	104	0.0396

Table A.19: Data for air-quenched BF-BT-Mn (x=0.020) poled at 80°C

Field (kV/mm)	d33 (pC/N)	tan(δ)
1	42	0.039
1.5	72	0.0391
2	94	0.0392
2.5	95	0.0393
3	106	0.0382
3.5	101	0.0423
4	112	0.0405
4.5	111	0.0393
5	98	0.0426
5.5	108	0.0405

Table A.20: Data for BF-BT-Mn (x=0.040) poled at room temperature

Field (kV/mm)	d33 (pC/N)	tan(δ)
1	5	0.042
1.5	14	0.0426
2	24	0.0397
2.5	39	0.0426
3	45	0.0434
3.5	51	0.0445
4	49	0.0464
4.5	54	0.0429
5	48	0.0435
5.5	62	0.0401
6	63	0.0429
6.5	63	0.0428

Appendix A3: BF-BT-Mn-Sm

Table A.21: Data for BF-BT-Mn-Sm (x=0.010, y=0.010) poled at room temperature

Field (kV/mm)	d33 (pC/N)	tan(δ)
1	10	0.0409
1.5	9	0.0402
2	19	0.0396
2.5	42	0.0399
3	51	0.0415
3.5	66	0.0418
4	69	0.0415
4.5	76	0.0424

Table A.22: Data for BF-BT-Mn-Sm (x=0.010, y=0.010) poled at 80°C

Field (kV/mm)	d33 (pC/N)	tan(δ)
1	1	0.041
1.5	73	0.042
2	107	0.0431
2.5	121	0.0437
3	136	0.0453
3.5	140	0.0442
4	134	0.0425
4.5	145	0.0429
5	150	0.0445
5.5	145	0.0443

Table A.23: Data for air-quenched BF-BT-Mn-Sm (x=0.010, y=0.010) poled at room temperature

Field (kV/mm)	d33 (pC/N)	tan(δ)
1	3	0.0379
1.5	12	0.0376
2	36	0.038
2.5	47	0.0382
3	66	0.0387
3.5	72	0.039
4	80	0.0345

Table A.24: Data for air-quenched BF-BT-Mn-Sm (x=0.010, y=0.010) poled at 80°C

Field (kV/mm)	d33 (pC/N)	tan(δ)
1	67	0.0387
1.5	98	0.0389
2	131	0.0393
2.5	139	0.0406
3	151	0.0392
3.5	161	0.0413
4	150	0.0412

Table A.25: Data for water-quenched BF-BT-Mn-Sm (x=0.010, y=0.010) poled at room temperature

Field (kV/mm)	d33 (pC/N)	tan(δ)
1	6	0.0535
1.5	12	0.0534
2	15	0.0528
2.5	17	0.0538
3	17	0.0586
3.5	18	0.0537
4	18	0.0537
4.5	14	0.0548
5	17	0.0548

Table A.26: Data for water-quenched BF-BT-Mn-Sm (x=0.010, y=0.010) poled at 80°C

Field (kV/mm)	d33 (pC/N)	tan(δ)
2	11	0.0516
2.5	14	0.0517
3	14	0.0517
3.5	14	0.0519
4	15	0.0517
4.5	12	0.0519
5	14	0.0528

Appendix B: Supplementary Impedance Data

Appendix B1: Undoped BF-BT

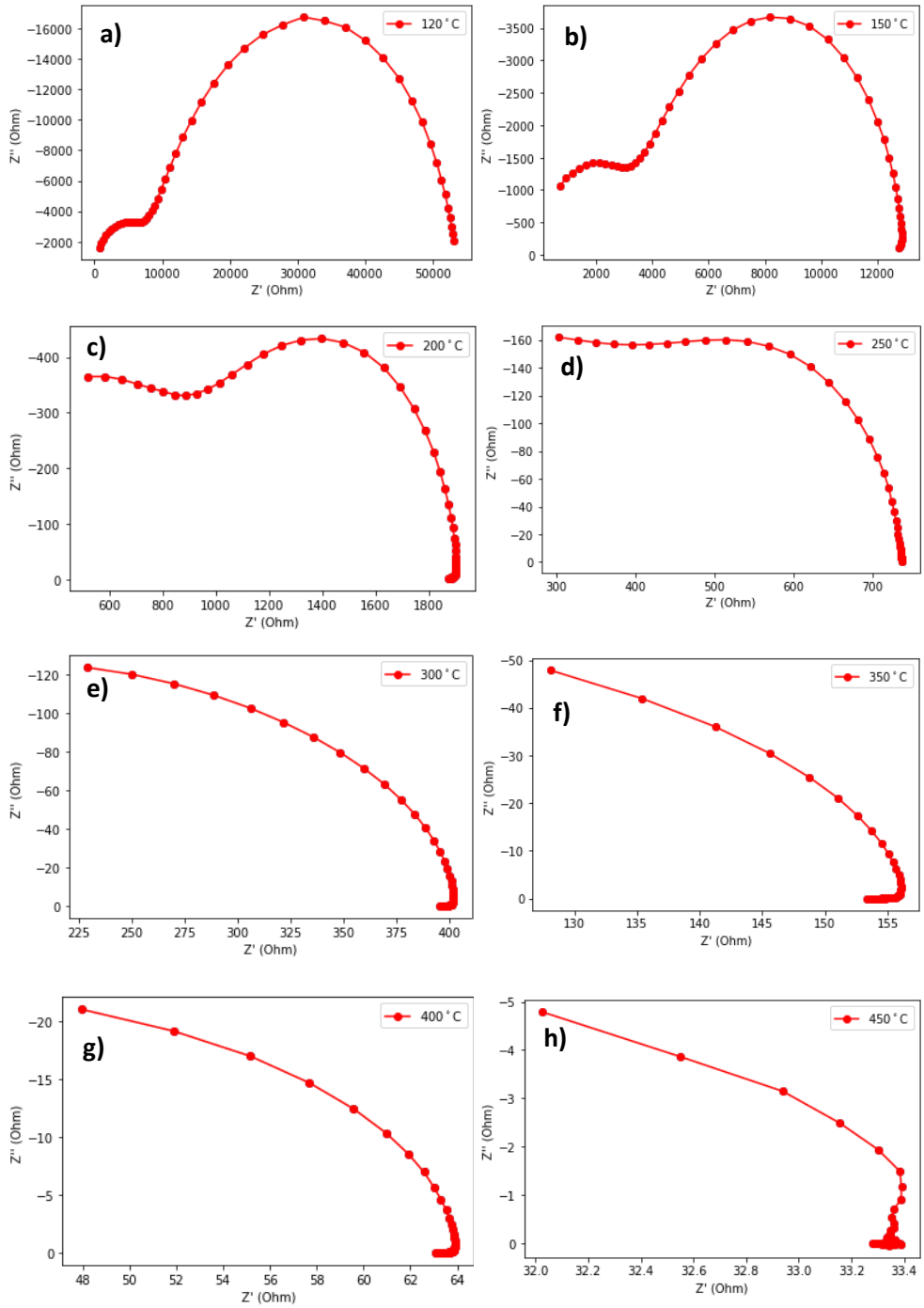

Figure B.1: Cole-Cole Impedance Plots of undoped BF-BT taken at different temperatures. a) 120°C, b) 150°C, c) 200°C, d) 250°C, e) 300°C, f) 350°C, g) 400°C and h) 450°C.

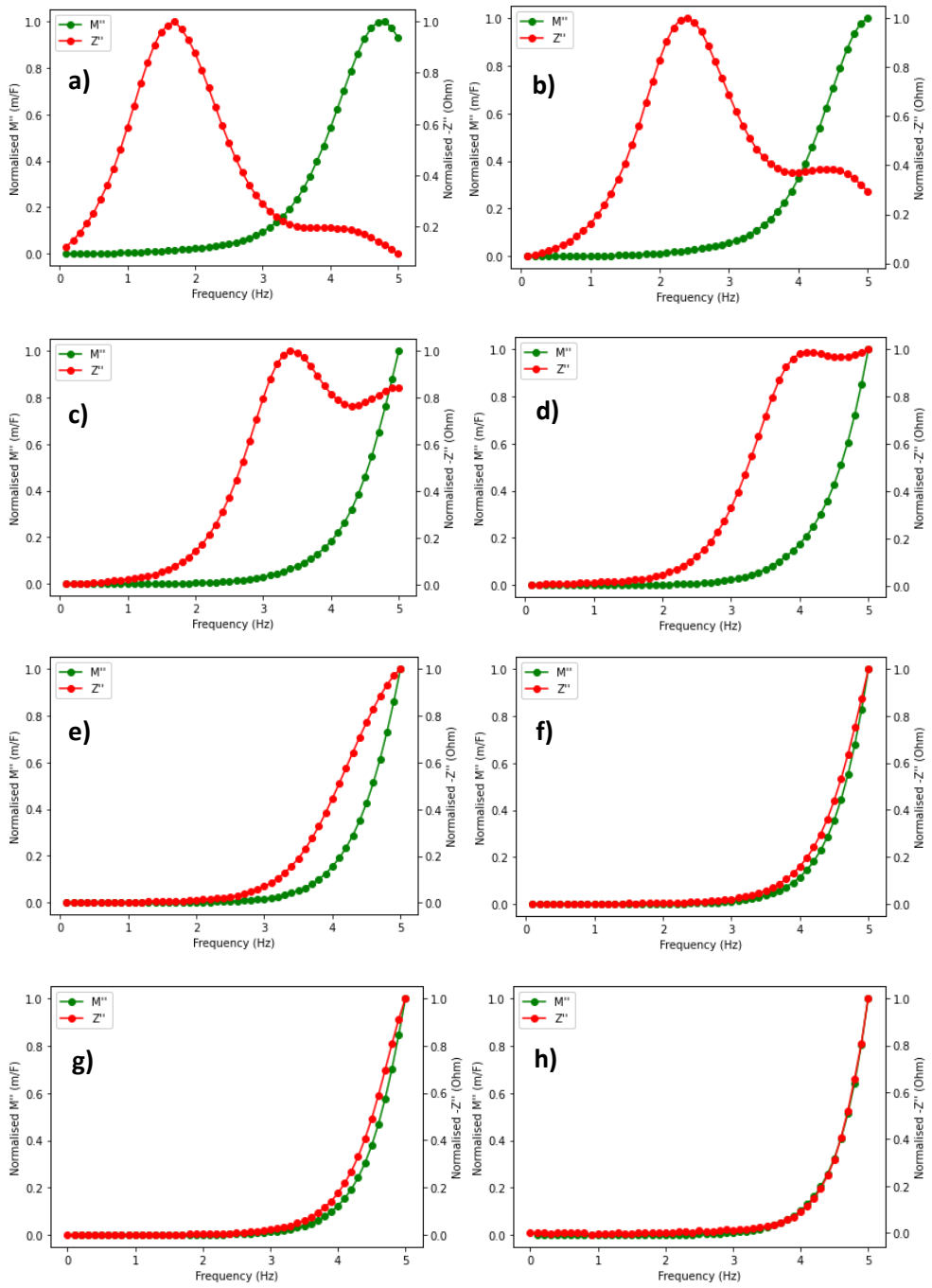

Figure B.2: Bode plots for undoped BF-BT taken at different temperatures. a) 120°C, b) 150°C, c) 200°C, d) 250°C, e) 300°C, f) 350°C, g) 400°C and h) 450°C.

Appendix B2: BF-BT-Mn

Table B.1: Resistances obtained from impedance spectroscopy for unquenched BF-BT-Mn

Temp. (°C)	Resistance (Ohm)	Circuit	Conductivity (S/cm)
150	1.74×10^{8}	d	1.02×10^{-9}
200	2.62×10^{7}	d	6.75×10^{-9}
250	1.69×10^{6}	d	1.05×10^{-7}
300	1.60×10^{5}	d	1.10×10^{-6}
350	2.52×10^{4}	d	7.02×10^{-6}
400	3.80×10^{3}	b	4.66×10^{-5}
450	1.01×10^{3}	b	1.76×10^{-5}
500	3.08×10^{2}	b	5.75×10^{-4}
550	1.60×10^{2}	d	1.11×10^{-3}
600	4.14×10^{1}	d	4.28×10^{-3}

Table B.2: Resistances obtained from impedance spectroscopy for air-quenched BF-BT-Mn

Temp. (K)	Resistance (Ohm)	Circuit	Conductivity (S/cm)
200	1.92×10^{7}	a	7.43×10^{-9}
250	3.70×10^{6}	c	3.85×10^{-8}
300	6.95×10^{5}	c	2.05×10^{-7}
350	1.29×10^{5}	c	1.11×10^{-6}
370	4.85×10^{4}	c	2.94×10^{-6}
400	2.27×10^{4}	c	6.28×10^{-6}
450	6.69×10^{3}	c	2.13×10^{-5}
500	1.48×10^{3}	c	9.64×10^{-5}
550	3.62×10^{2}	a	3.94×10^{-4}
600	1.25×10^{2}	c	1.14×10^{-3}

Table B.3: Resistances obtained from impedance spectroscopy for water-quenched BF-BT-Mn

Temp. (K)	Resistance (Ohm)	Circuit	Conductivity (S/cm)
150	7.89×10^{7}	c	2.27×10^{-9}
200	7.96×10^{6}	c	2.25×10^{-8}
250	2.09×10^{6}	c	8.56×10^{-8}
300	3.69×10^{5}	c	4.85×10^{-7}
350	8.50×10^{4}	c	2.10×10^{-6}
400	2.21×10^{4}	c	8.10×10^{-6}
450	5.96×10^{3}	c	3.00×10^{-5}
500	1.86×10^{3}	c	9.62×10^{-5}
550	6.23×10^{2}	a	2.87×10^{-4}
600	2.12×10^{2}	c	8.44×10^{-4}

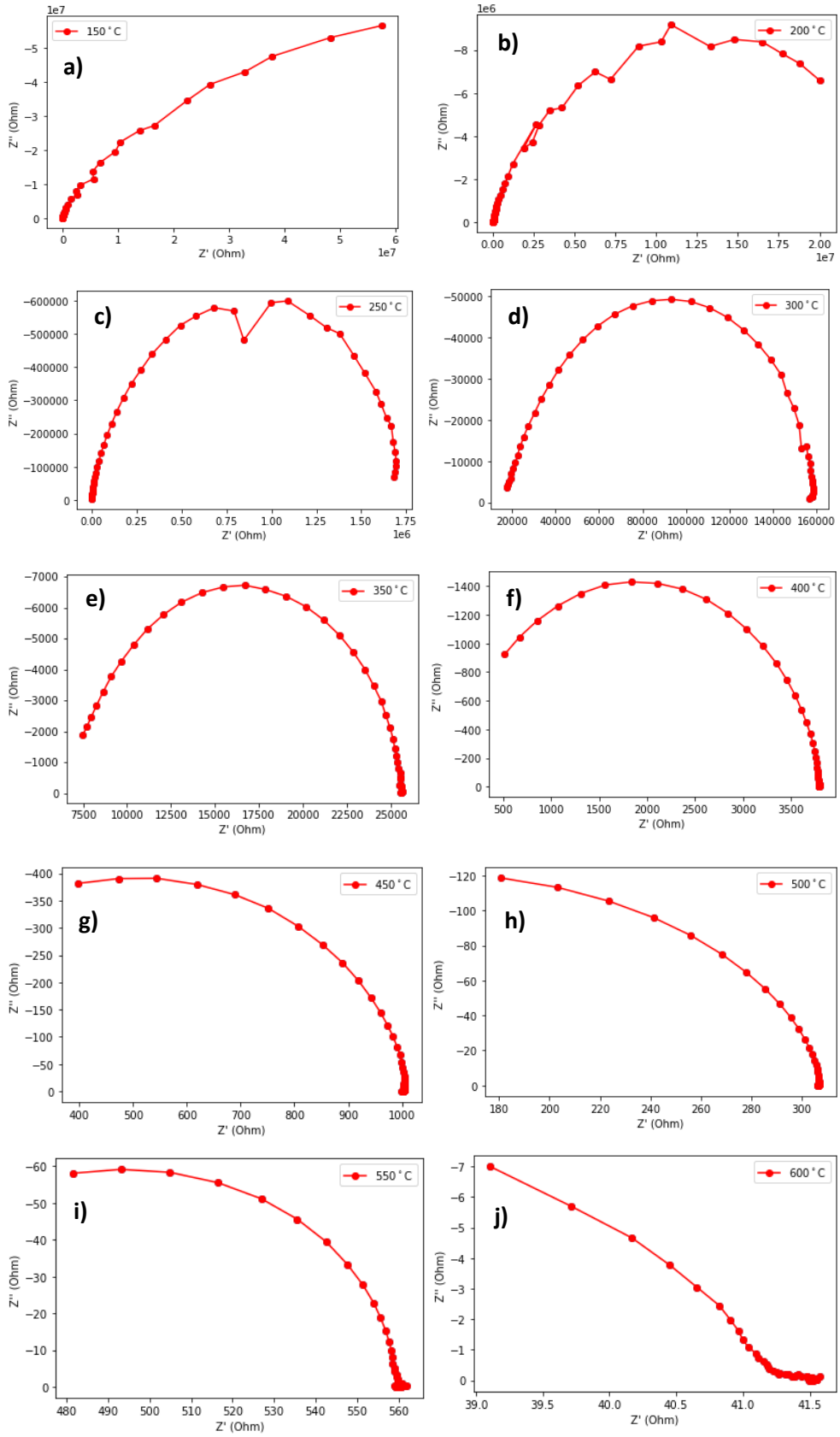

Figure B.3: Cole-Cole Impedance Plots of unquenched BF-BT-Mn taken at different temperatures. a) 150°C, b) 200°C, c) 250°C, d) 300°C, e) 350°C, f) 400°C, g) 450°C, h) 500°C, i) 550°C and j) 600°C.

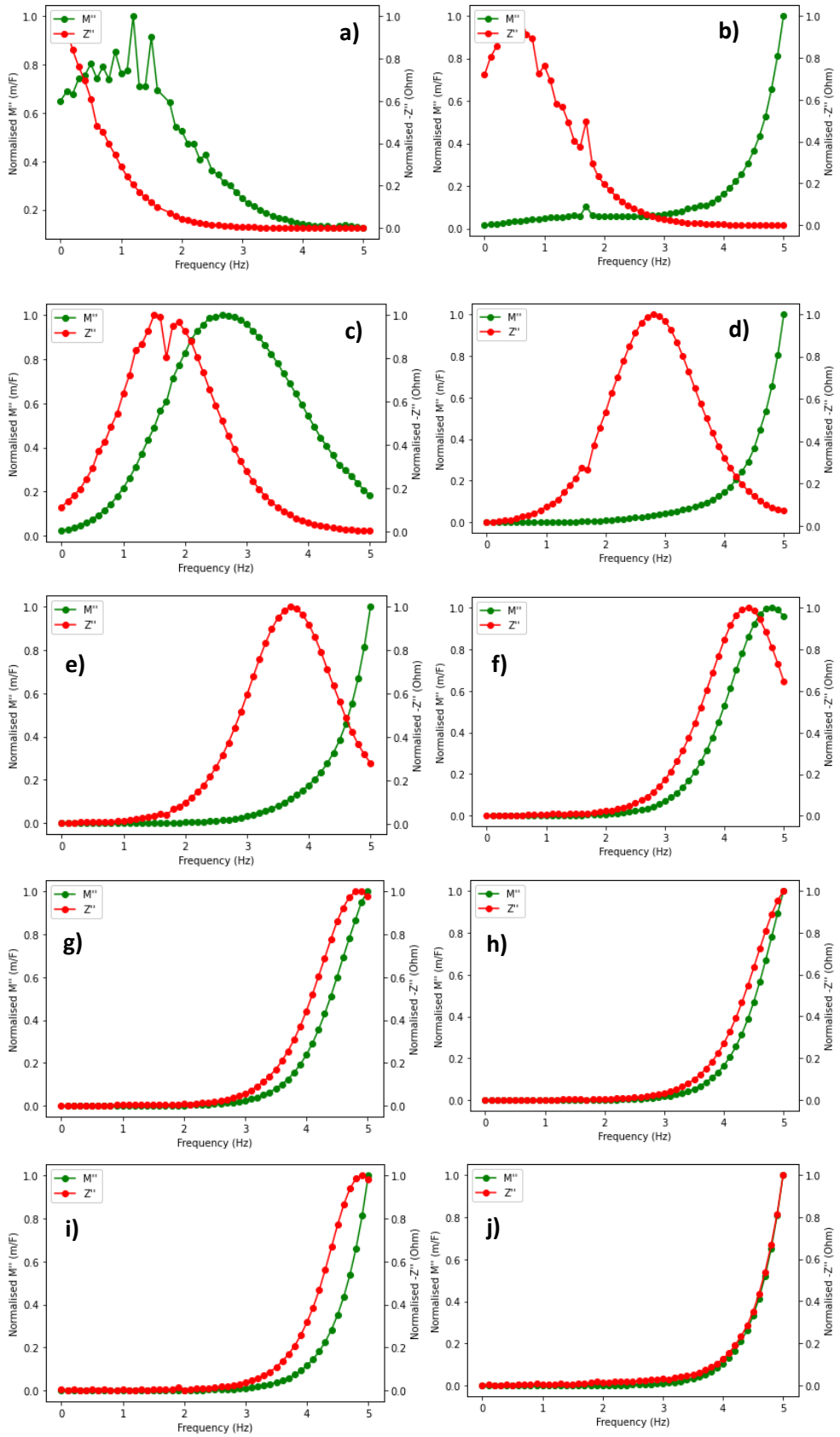

Figure B.4: Cole-Cole Impedance Plots of unquenched BF-BT-Mn taken at different temperatures. a) 150°C, b) 200°C, c) 250°C, d) 300°C, e) 350°C, f) 400°C, g) 450°C, h) 500°C, i) 550°C and j) 600°C.

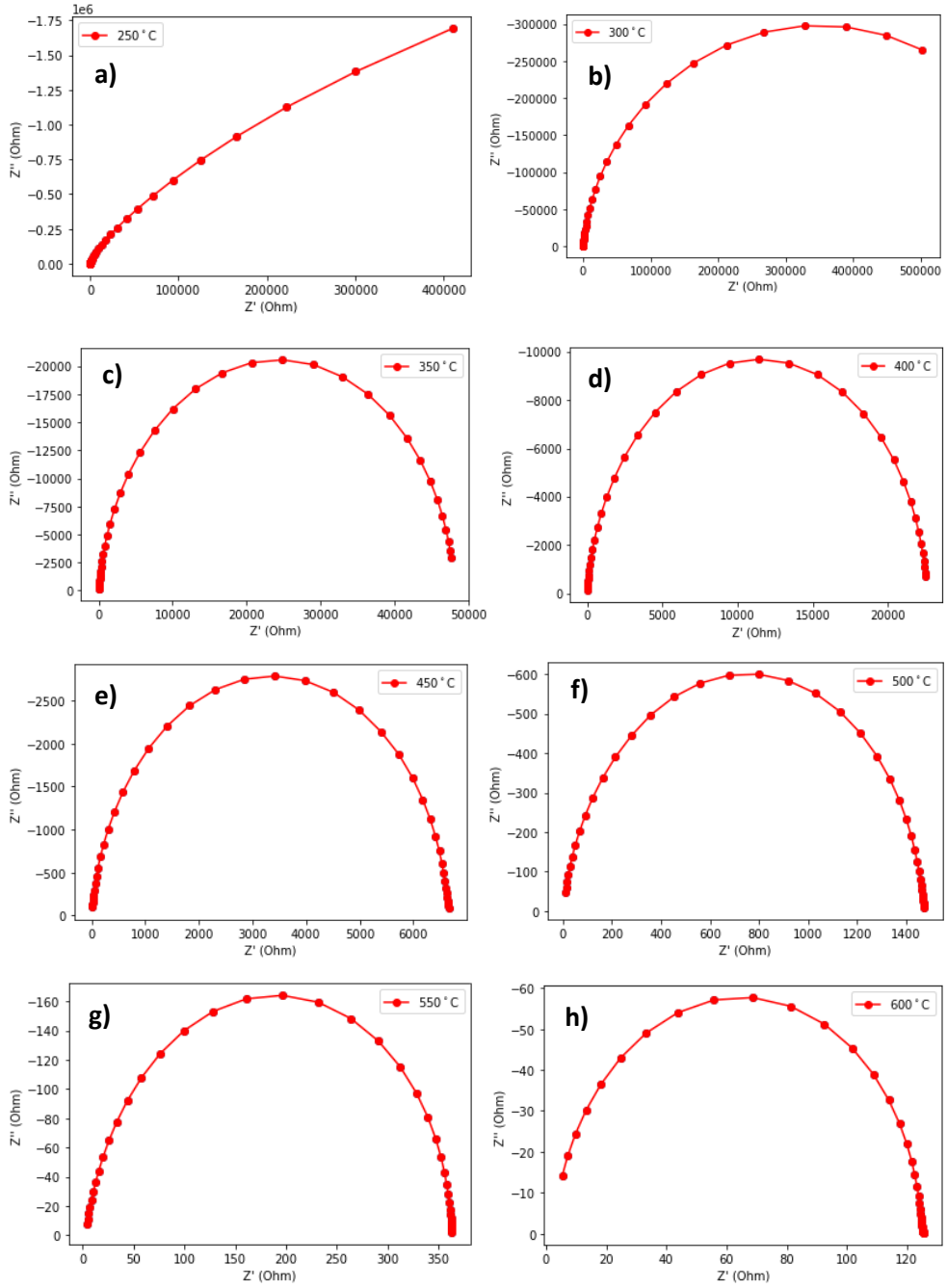

Figure B.5: Cole-Cole plots of air-quenched BF-BT-Mn taken at different temperatures. a) 250°C, b) 300°C, c) 350°C, d) 400°C, e) 450°C, f) 500°C, g) 550°C and h) 600°C.

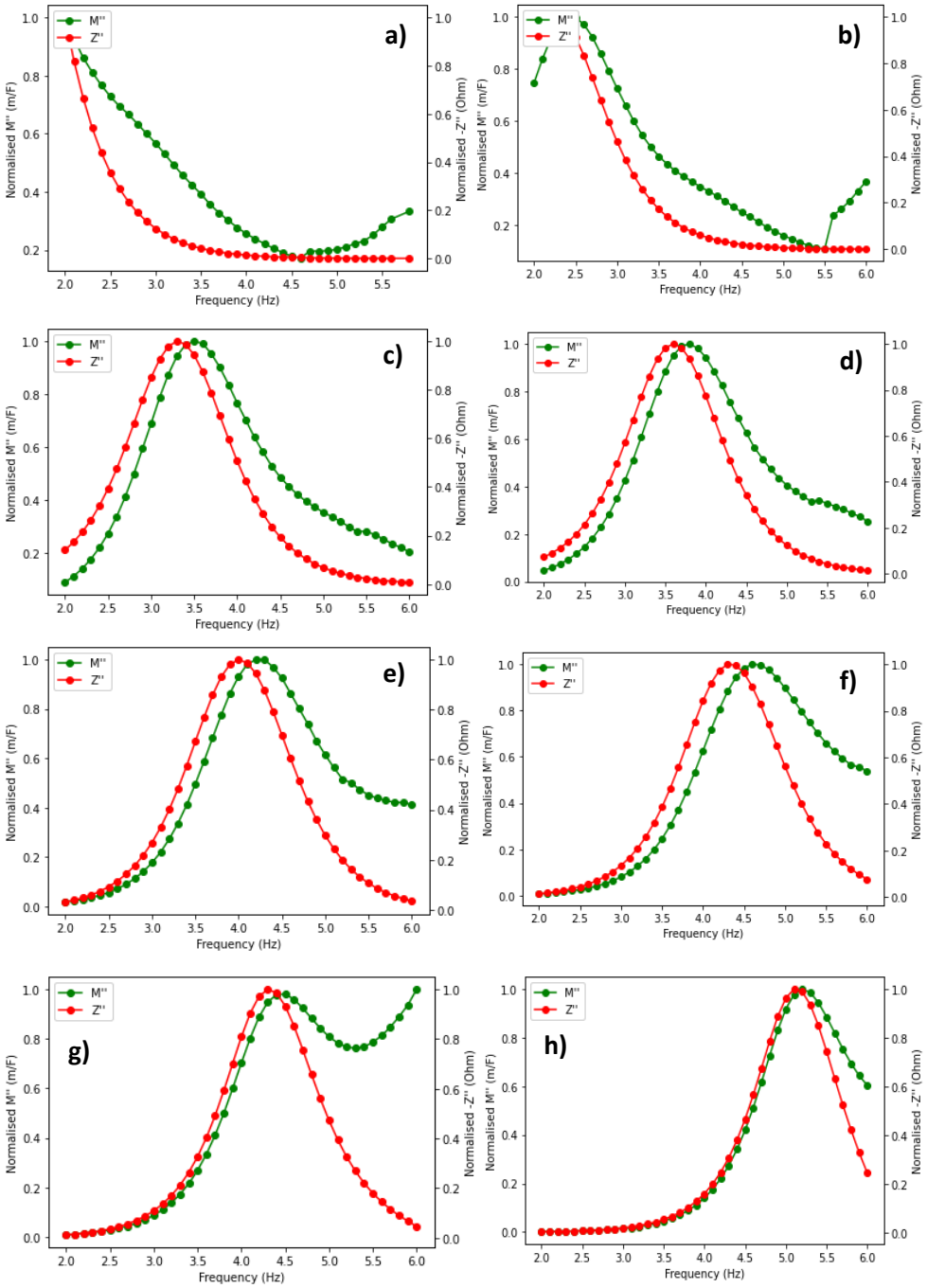

Figure B.6: Bode plots of air-quenched BF-BT-Mn taken at different temperatures. a) 250°C, b) 300°C, c) 350°C, d) 400°C, e) 450°C, f) 500°C, g) 550°C and h) 600°C.

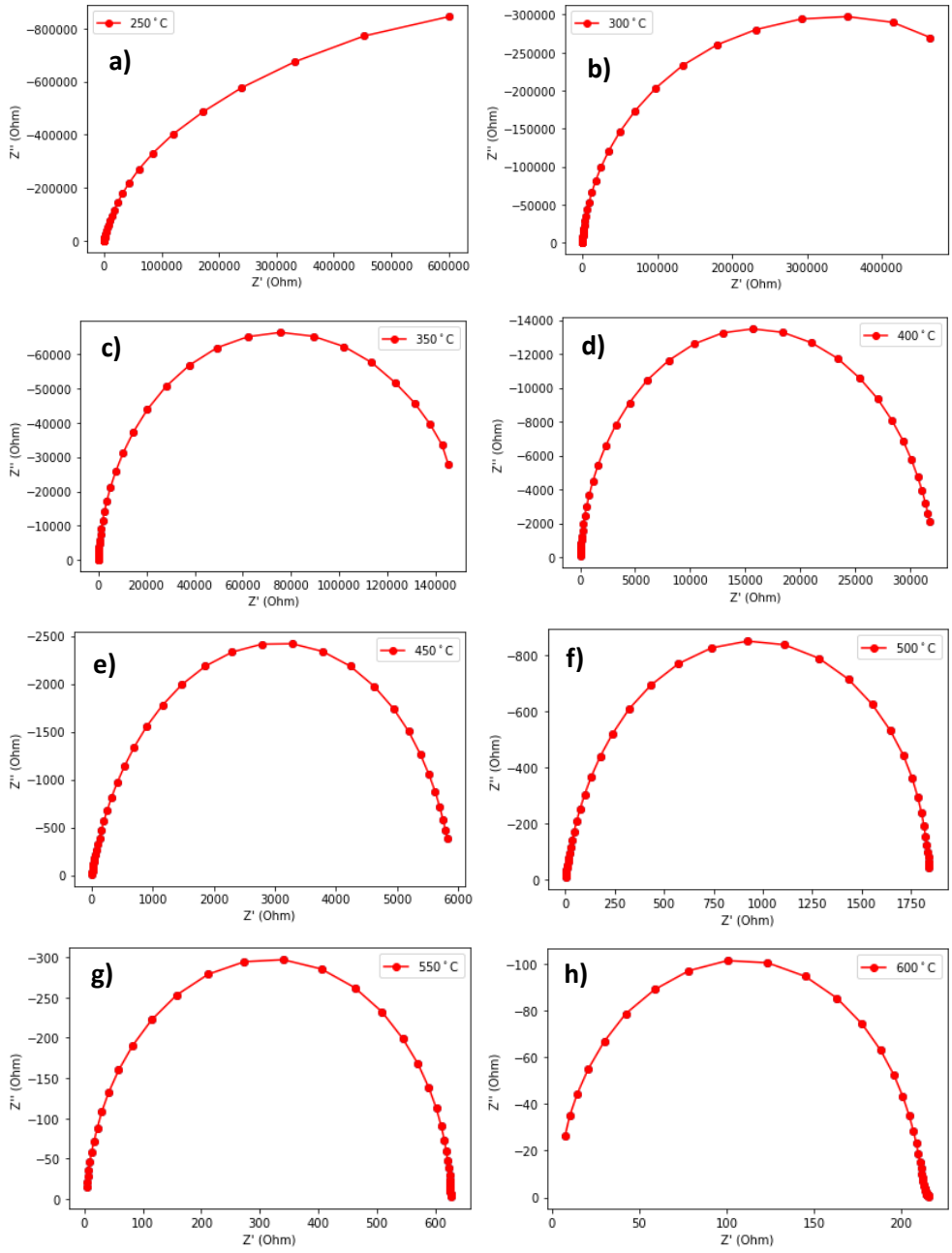

Figure B.7: Cole-Cole plots of water-quenched BF-BT-Mn taken at different temperatures. a) 250°C, b) 300°C, c) 350°C, d) 400°C, e) 450°C, f) 500°C, g) 550°C and h) 600°C.

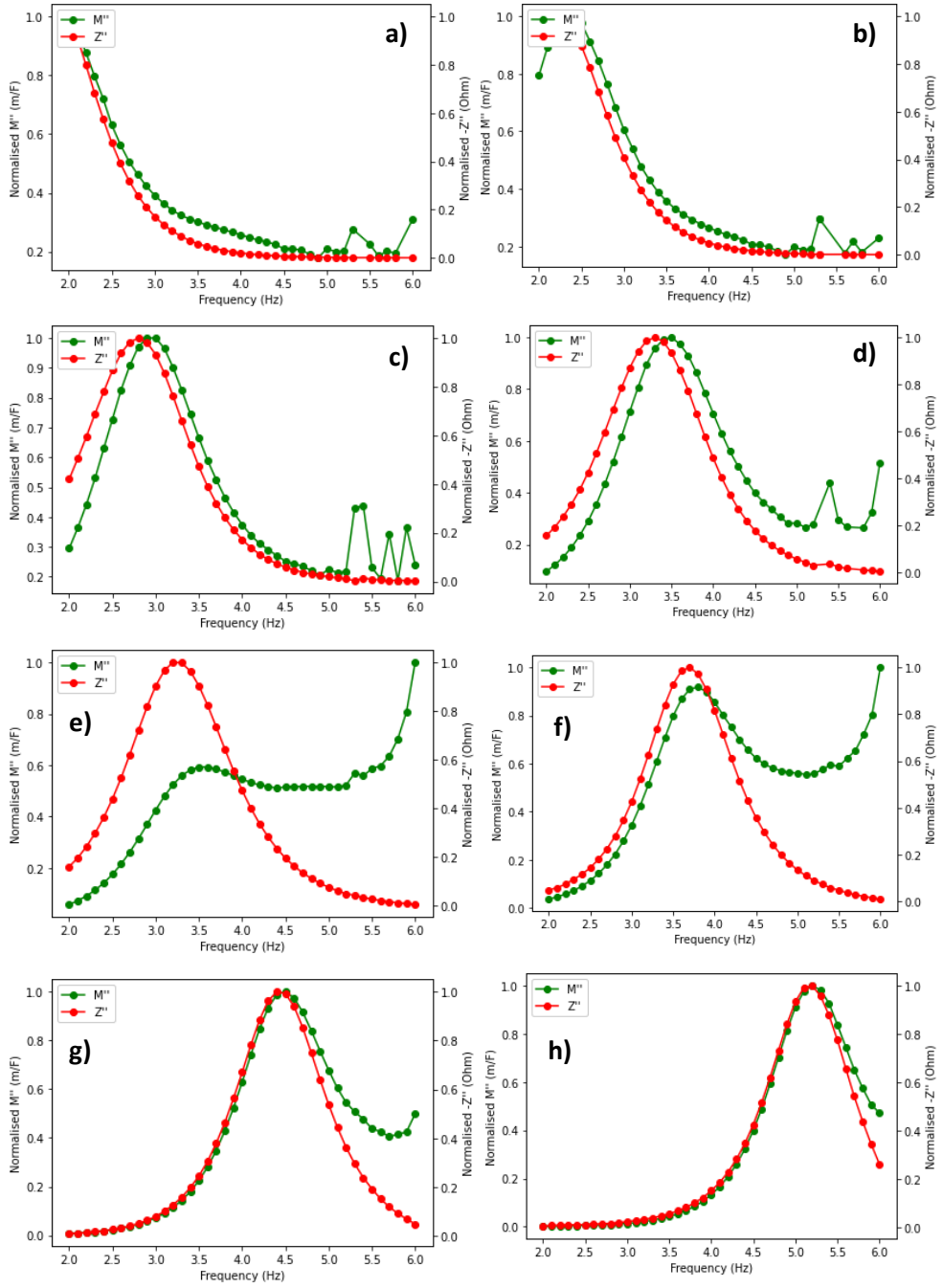

Figure B.8: Bode plots for water-quenched BF-BT-Mn taken at different temperatures. a) 250°C, b) 300°C, c) 350°C, d) 400°C, e) 450°C, f) 500°C, g) 550°C and h) 600°C.

Appendix B3: BF-BT-Mn-Sm

Table B.4: Resistances obtained from impedance spectroscopy for unquenched BF-BT-Mn-Sm

Temp. (°C)	Resistance (Ohm)	Circuit	Conductivity (S/cm)
150	3.14×10^{8}	a	4.23×10^{-10}
200	2.62×10^{7}	c	5.07×10^{-9}
250	1.74×10^{6}	a	7.64×10^{-8}
300	1.60×10^{5}	a	8.31×10^{-7}
350	2.57×10^{4}	a	5.17×10^{-6}
400	3.75×10^{3}	c	3.55×10^{-5}
450	1.01×10^{3}	a	1.32×10^{-4}
500	3.08×10^{2}	a	4.32×10^{-4}
550	1.54×10^{2}	b	8.63×10^{-4}
600	4.13×10^{1}	c	3.22×10^{-3}

Table B.5: Resistances obtained from impedance spectroscopy for air-quenched BF-BT-Mn-Sm

Temp. (°C)	Resistance (Ohm)	Circuit	Conductivity (S/cm)
150	3.59×10^{8}	c	4.66×10^{-10}
200	4.06×10^{7}	a	4.12×10^{-9}
250	6.90×10^{6}	c	2.42×10^{-8}
300	7.10×10^{5}	c	2.35×10^{-7}
350	2.82×10^{5}	c	5.93×10^{-7}
400	5.53×10^{4}	c	3.02×10^{-6}
450	1.02×10^{4}	d	1.63×10^{-5}
500	3.50×10^{3}	b	4.77×10^{-5}
550	1.04×10^{3}	b	1.61×10^{-4}
600	4.23×10^{2}	b	3.95×10^{-4}

Table B.6: Resistances obtained from impedance spectroscopy for water-quenched BF-BT-Mn-Sm

Temp. (K)	Resistance (Ohm)	Circuit	Conductivity (S/cm)
150	4.15×10^{7}	c	4.10×10^{-9}
200	1.14×10^{7}	c	1.49×10^{-8}
250	2.00×10^{6}	c	8.50×10^{-8}
300	3.13×10^{5}	c	5.43×10^{-7}
350	4.54×10^{4}	c	3.75×10^{-6}
400	1.07×10^{4}	b	1.59×10^{-5}
450	3.27×10^{3}	c	5.20×10^{-5}
500	1.05×10^{3}	c	1.62×10^{-4}
550	3.44×10^{2}	b	4.94×10^{-4}
600	1.12×10^{2}	b	1.52×10^{-3}

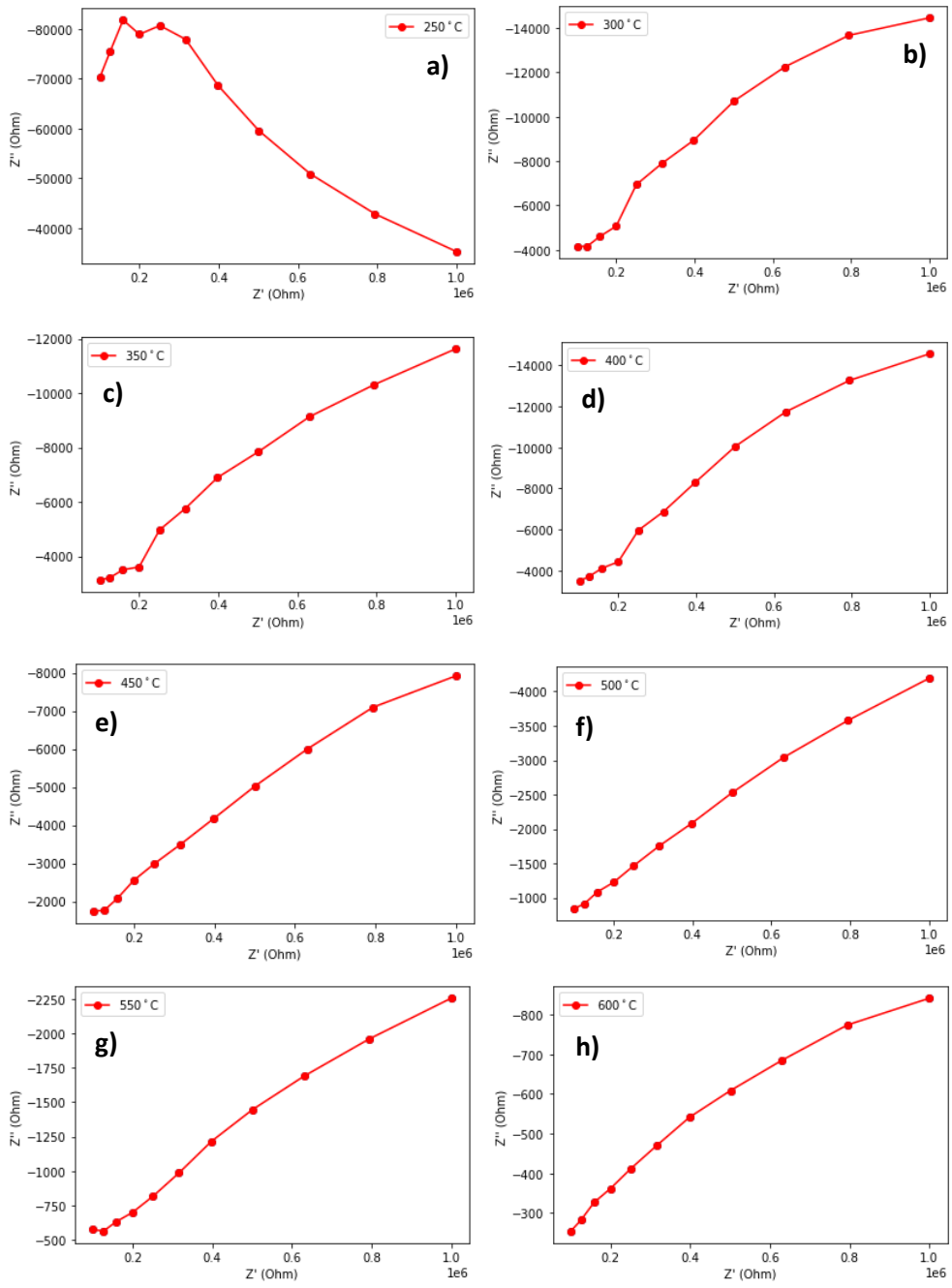

Figure B.9: Cole-Cole plots of unquenched BF-BT-Mn-Sm taken at different temperatures. a) 250°C, b) 300°C, c) 350°C, d) 400°C, e) 450°C, f) 500°C, g) 550°C and h) 600°C.

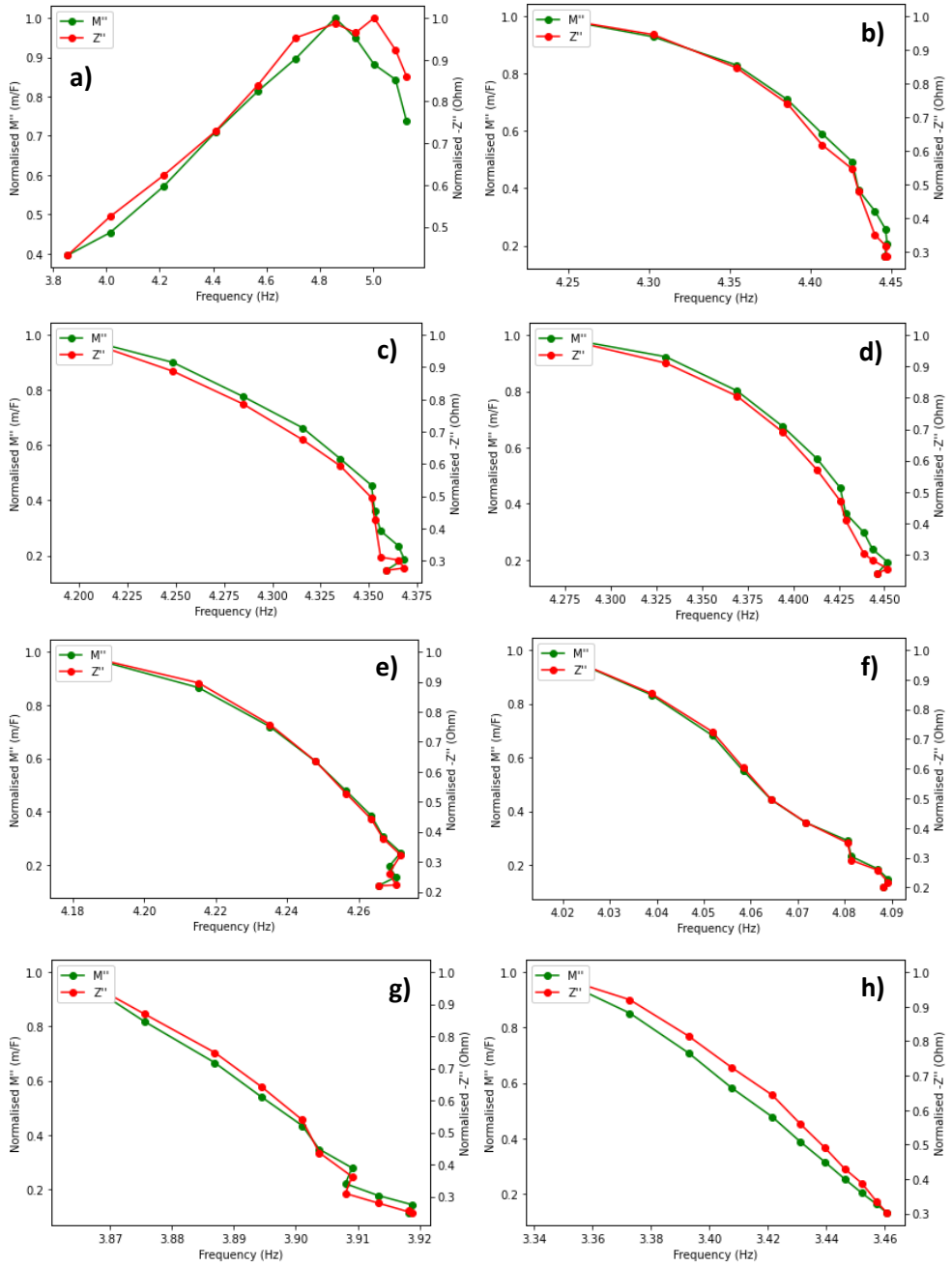

Figure B.10: Bode plots of unquenched BF-BT-Mn-Sm taken at different temperatures. a) 250°C, b) 300°C, c) 350°C, d) 400°C, e) 450°C, f) 500°C, g) 550°C and h) 600°C.

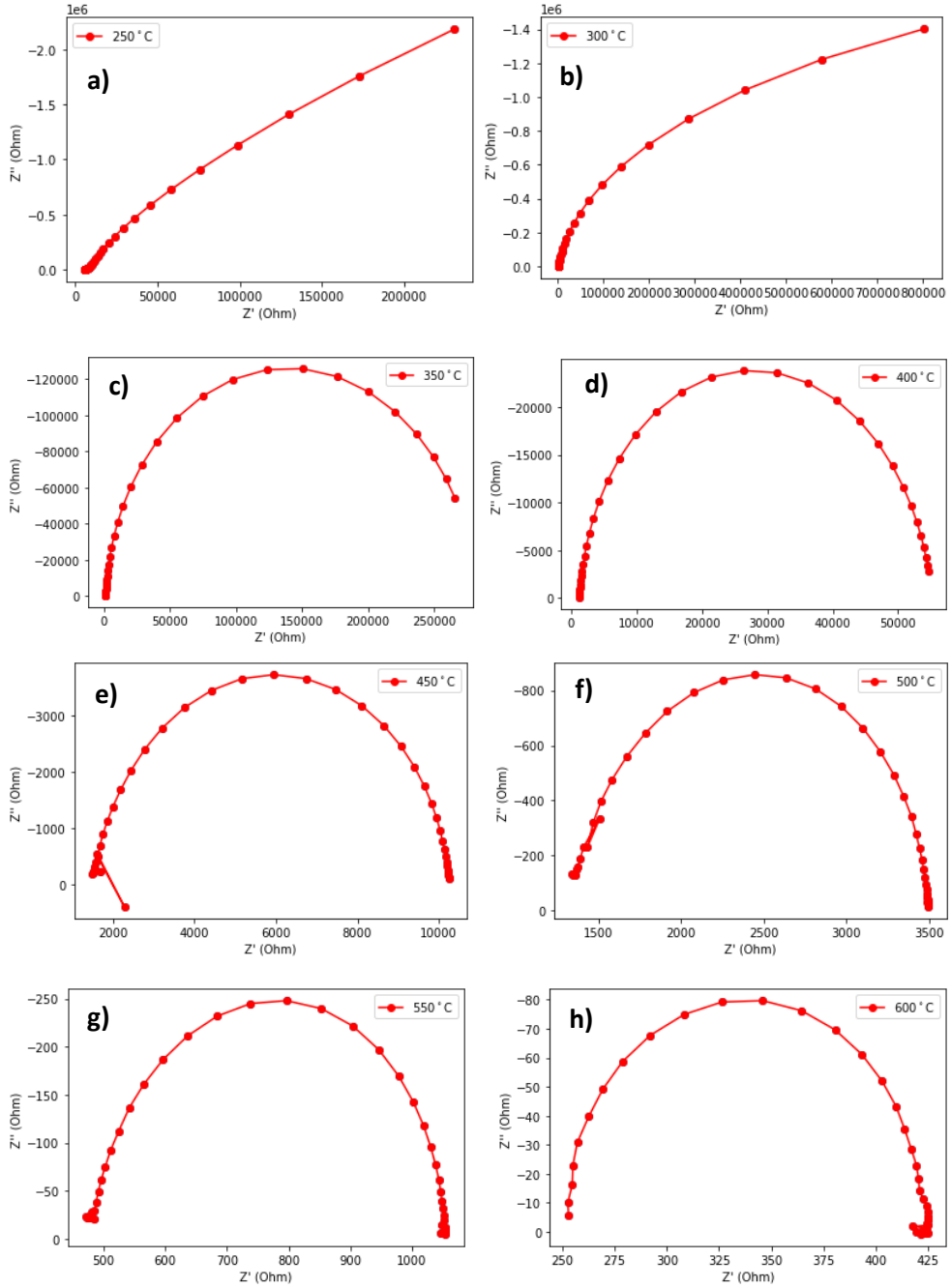

Figure B.11: Cole-Cole plots of air-quenched BF-BT-Mn-Sm taken at different temperatures. a) 250°C, b) 300°C, c) 350°C, d) 400°C, e) 450°C, f) 500°C, g) 550°C and h) 600°C.

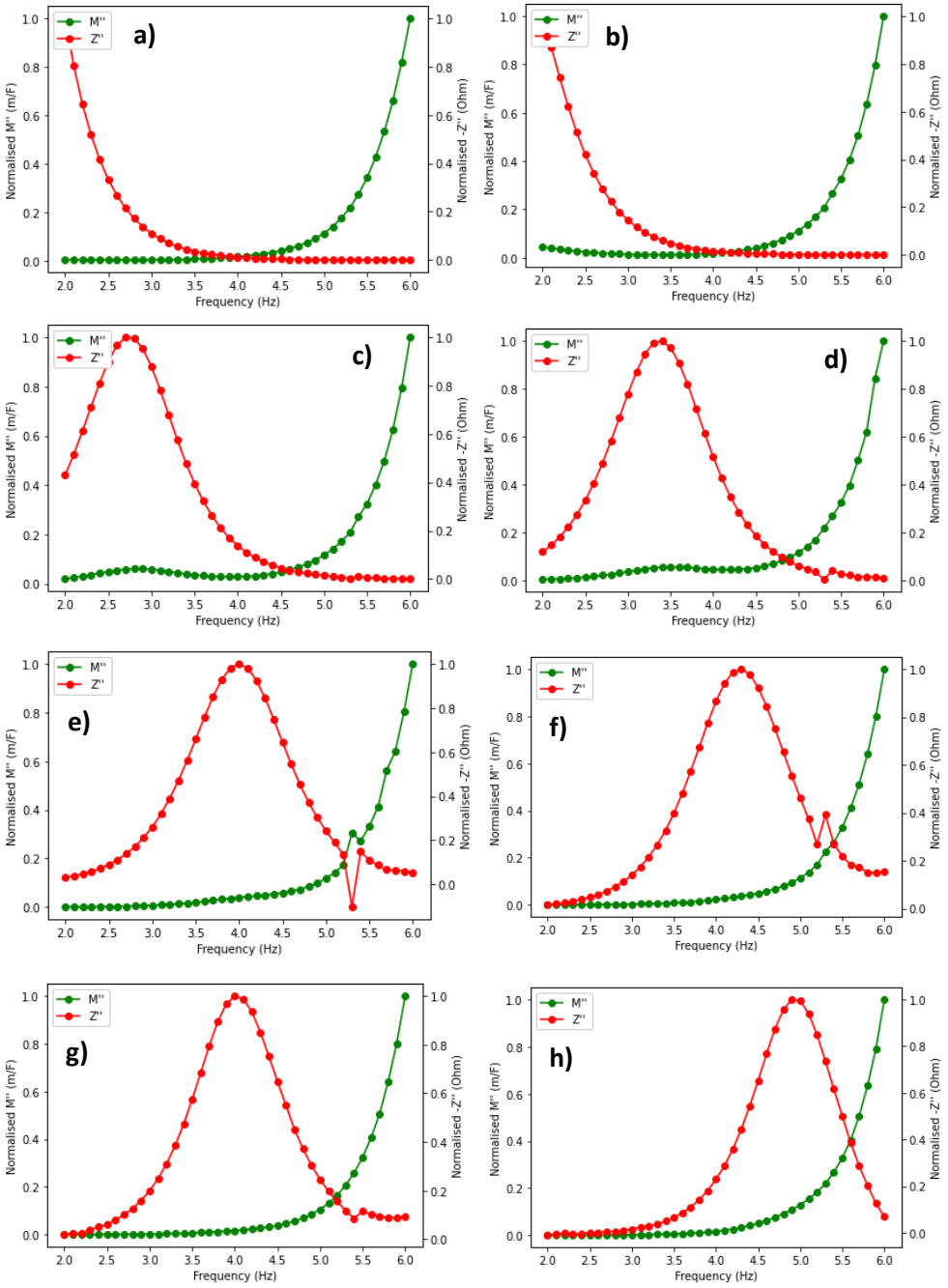

Figure B.12: Bode plots of air-quenched BF-BT-Mn-Sm taken at different temperatures. a) 250°C, b) 300°C, c) 350°C, d) 400°C, e) 450°C, f) 500°C, g) 550°C and h) 600°C.

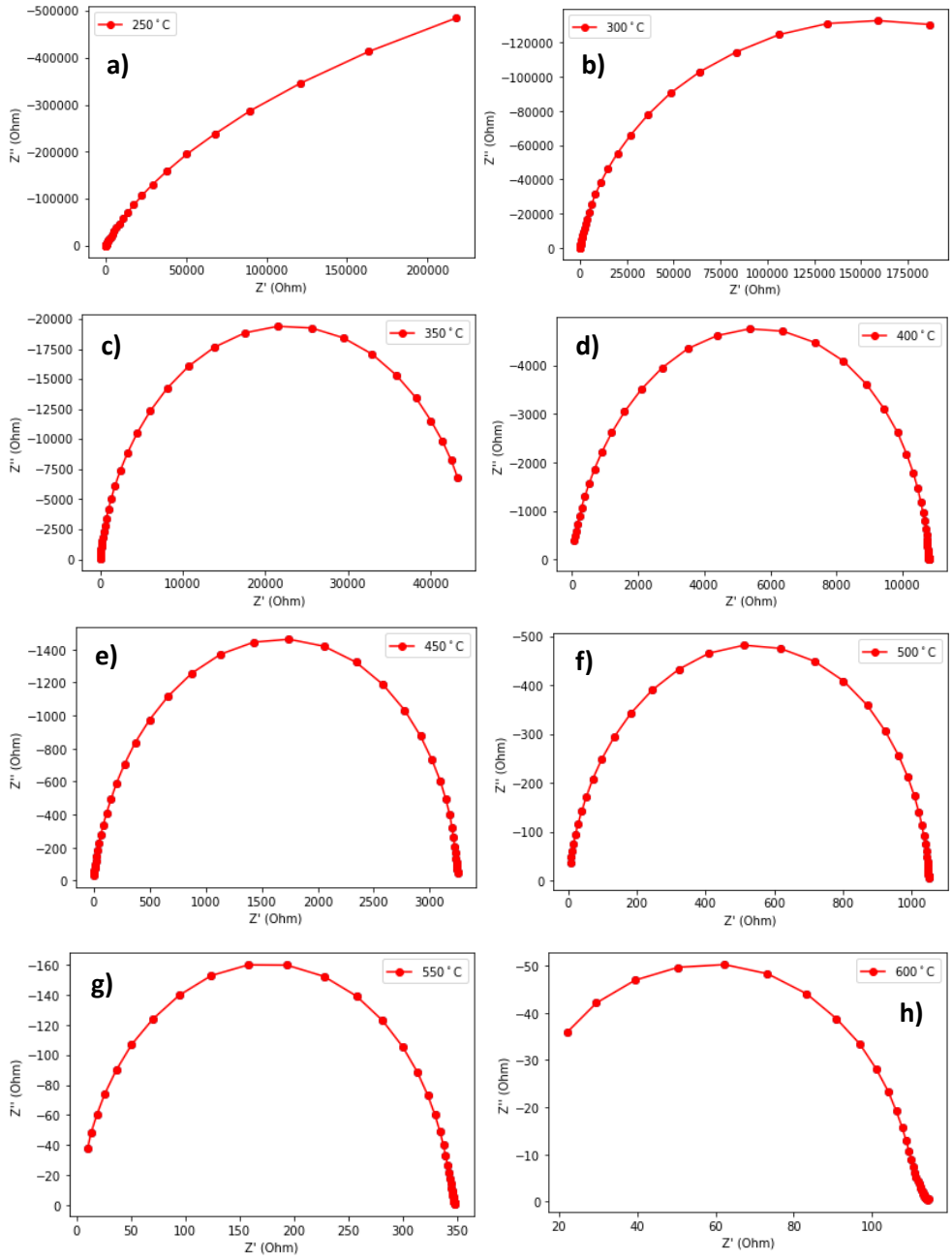

Figure B.13: Cole-Cole plots of water-quenched BF-BT-Mn-Sm taken at different temperatures. a) 250°C, b) 300°C, c) 350°C, d) 400°C, e) 450°C, f) 500°C, g) 550°C and h) 600°C.

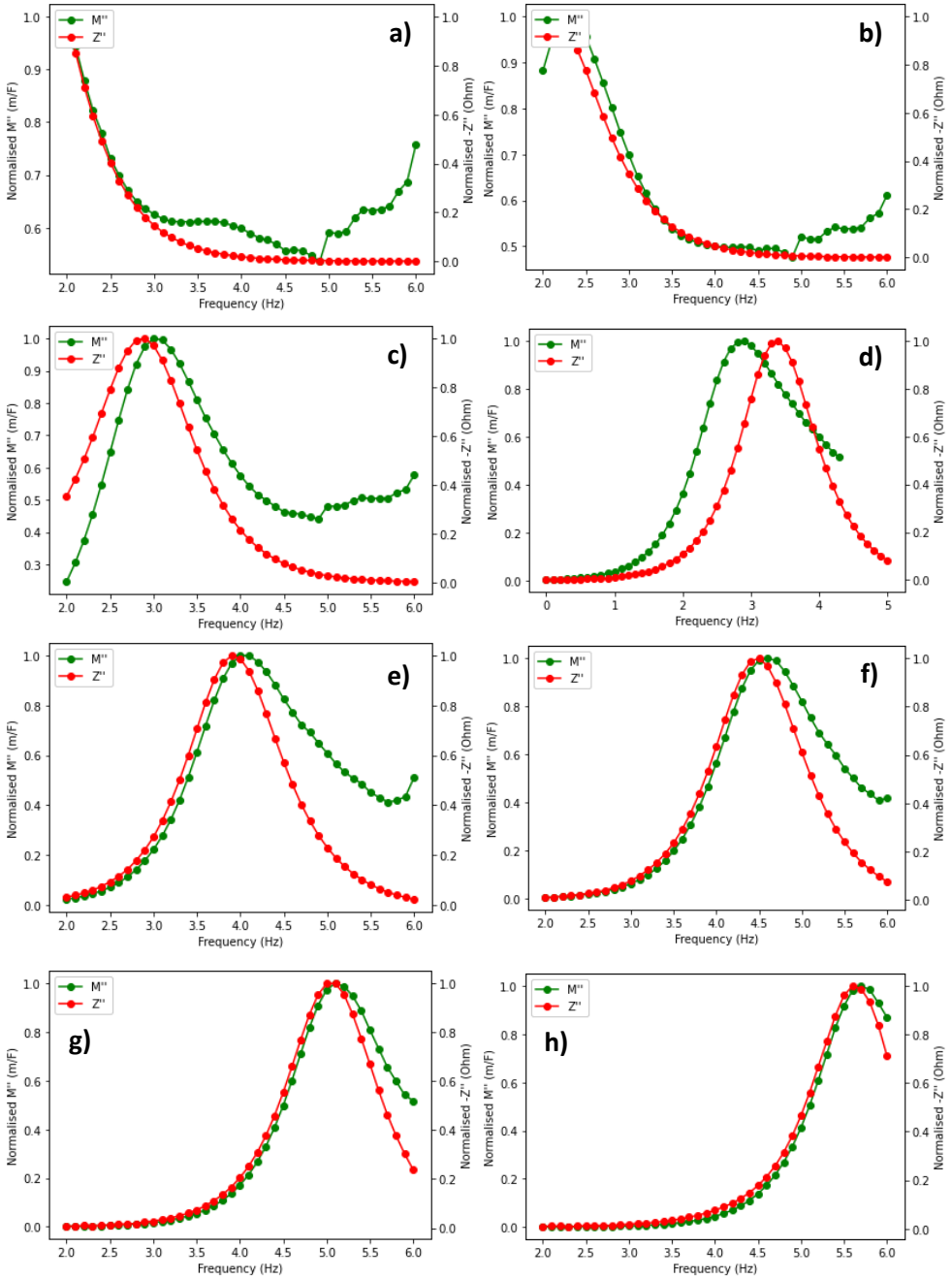

Figure B.14: Bode plots of water-quenched BF-BT-Mn-Sm taken at different temperatures. a) 250°C, b) 300°C, c) 350°C, d) 400°C, e) 450°C, f) 500°C, g) 550°C and h) 600°C.

Appendix C1: PRAP Supplementary Data

Table C.1: Full matrix of unquenched BF-BT-Mn

Length Extensional	
f_a (Hz)	3.143 x 10^5
f_r (Hz)	3.117 x 10^5
k_{33}	0.1443
s^D_{33} (m^2/N)	3.613 x 10^{-12}
s^E_{33} (m^2/N)	3.69 x 10^{-12}
d_{33} (C/N)	6.831 x 10^{-11}
g_{33} (Vm/N)	1.122 x 10^{-3}
$\varepsilon^{S3=0}_{33}$ (F/m)	5.905 x 10^{-8}
ε^X_{33} (F/m)	6.031 x 10^{-8}
Longitundinal Thickness Extensional	
f_a (Hz)	7.78547 x 10^5
f_r (Hz)	7.78589 x 10^5
k_{31}	0.01674
s^E_{11} (m^2/N)	5.882 x 10^{-13}
ε^X_{33} (F/m)	-3.197 x 10^{-10}
d_{31} (C/N)	1.798 x 10^{-13}
g_{31} (Vm/N)	-5.533 x 10^{-4}
Radial Extensional	
f_{r1} (Hz)	1.626 x 10^5
f_{a1} (Hz)	1.6503 x 10^5
f_{r2} (Hz)	4.287 x 10^5
s^E_{11} (m^2/N)	1.476 x 10^{-11}
s^E_{12} (m^2/N)	-4.293 x 10^{-12}
d_{31} (C/N)	3.367 x 10^{-11}
ε^X_{33} (F/m)	5.919 x 10^{-9}
k_p	0.1915
ε^p_{33} (F/m)	5.704 x 10^{-9}
c^p_{11} (N/m^2)	7.395 x 10^{10}
e^p_{31} (C/m^2)	3.219
s^E_{66} (m^2/N)	3.812 x 10^{-11}

Table C.2: Full matrix of air-quenched BF-BT-Mn

Length Extensional	
f_a (Hz)	1.6504×10^{5}
f_r (Hz)	1.6262×10^{5}
k_{33}	0.1888
s^{D}_{33} (m^2/N)	1.311×10^{-11}
s^{E}_{33} (m^2/N)	1.359×10^{-11}
d_{33} (C/N)	1.805×10^{-10}
g_{33} (Vm/N)	2.676×10^{-4}
$\varepsilon^{S3=0}_{33}$ (F/m)	6.499×10^{-6}
ε^{X}_{33} (F/m)	6.737×10^{-7}
Longitundinal Thickness Extensional	
f_a (Hz)	1.398×10^{5}
f_r (Hz)	1.396×10^{5}
k_{31}	0.1048
s^{E}_{11} (m^2/N)	1.829×10^{-9}
ε^{X}_{33} (F/m)	4.794×10^{-8}
d_{31} (C/N)	1.04×10^{-9}
g_{31} (Vm/N)	0.02005
Radial Extensional	
f_{r1} (Hz)	1.705×10^{5}
f_{a1} (Hz)	1.707×10^{5}
f_{r2} (Hz)	4.465×10^{5}
s^{E}_{11} (m^2/N)	1.056×10^{-11}
s^{E}_{12} (m^2/N)	-3.341×10^{-12}
d_{31} (C/N)	6.719×10^{-12}
ε^{X}_{33} (F/m)	3.851×10^{-9}
k_p	0.05705
ε^{p}_{33} (F/m)	3.838×10^{-9}
c^{p}_{11} (N/m^2)	1.052×10^{-11}
e^{p}_{31} (C/m^2)	0.9315
s^{E}_{66} (m^2/N)	2.781×10^{-11}

Table C.3: Obtained matrix of unquenched BF-BT-Mn-Sm for the LE mode. The data for the LTE and RE modes were unavailable due to the lack of resonant and anti-resonant frequencies in the PRAP measurements.

Length Extensional	
f_a (Hz)	1.809×10^{5}
f_r (Hz)	1.802×10^{5}
k_{33}	0.0948
s^{D}_{33} (m^2/N)	1.424×10^{-9}
s^{E}_{33} (m^2/N)	1.437×10^{-9}
d_{33} (C/N)	3.529×10^{-12}
g_{33} (Vm/N)	3.627
$\varepsilon^{S3=0}_{33}$ (F/m)	9.464×10^{-13}
ε^{X}_{33} (F/m)	9.55×10^{-13}

Table C.4: Obtained matrix for LE mode of air-quenched BF-BT-Mn-Sm, as the lack of a significant f_r and f_a value for the RE mode made matrix calculations impossible.

Length Extensional	
f_a (Hz)	1.812×10^{5}
f_r (Hz)	1.806×10^{5}
k_{33}	0.0835
s^{D}_{33} (m^2/N)	1.088×10^{-11}
s^{E}_{33} (m^2/N)	1.096×10^{-11}
d_{33} (C/N)	9.556×10^{-11}
g_{33} (Vm/N)	7.93×10^{-4}
$\varepsilon^{S3=0}_{33}$ (F/m)	1.19×10^{-7}
ε^{X}_{33} (F/m)	1.198×10^{-7}